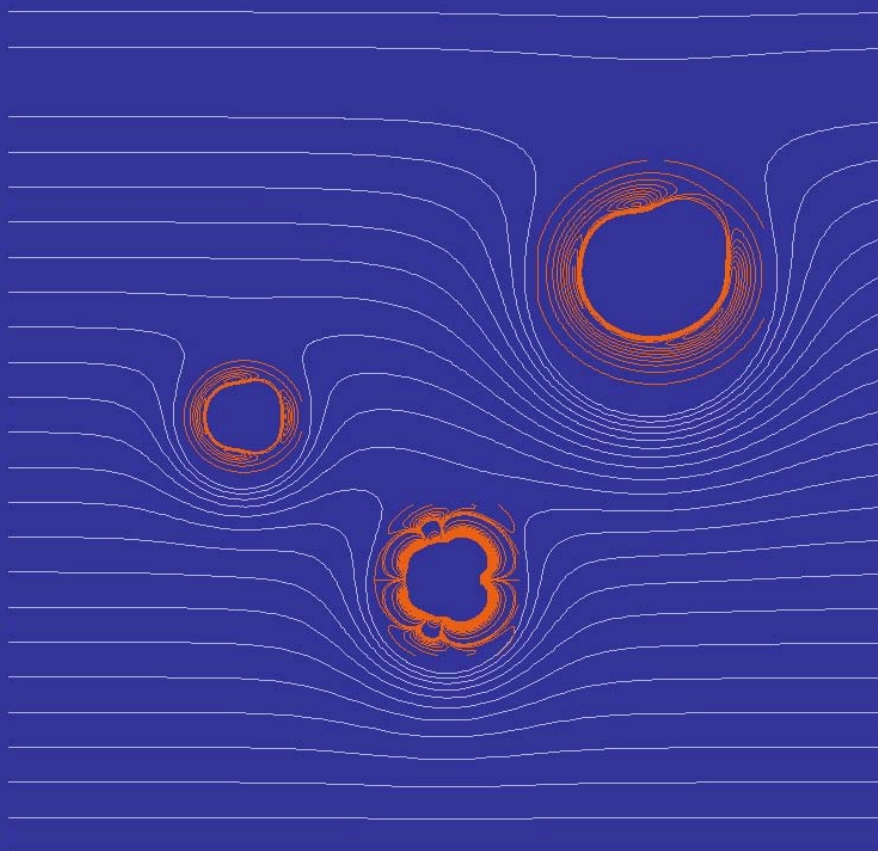


Dynamics of open-Shell van der Waals complexes



Wilfried Zeimen

2004

*Dynamics of open-shell van der Waals
complexes*

Wilfried P. J. B. Zeimen

Dynamics of open-shell van der Waals complexes

een wetenschappelijke proeve op het gebied van de
Natuurwetenschappen, Wiskunde en Informatica

Proefschrift

ter verkrijging van de graad van doctor aan de Katholieke
Universiteit Nijmegen, op gezag van de Rector Magnificus
Prof. Dr. C.W.P.M. Blom, volgens besluit van het College
van Decanen in het openbaar te verdedigen op woensdag
17 maart 2004, des namiddags om 1.30 uur precies

door

Wilfried Patrick Jean-Bernard Zeimen

geboren op 18 Januari 1973
te Toulouse (France)

Promotor: Prof. Dr. ir. A. van der Avoird

Copromotor: Dr. ir. G.C. Groenenboom

Manuscriptcommissie: Prof. Dr. W. J. van der Zande (voorzitter)
Prof. Dr. P. Rosmus (Université de Marne-la-Vallée,
F-77454 Champs sur Marne,
France)
Dr. ir. P.E.S. Wormer

W.P.J.B. Zeimen
Dynamics of open-shell van der Waals complexes
PhD Thesis, University of Nijmegen, The Netherlands
With summary in Dutch
ISBN 90-9017798-1
printed by: PrintPartners Ipskamp, Enschede

This research has been financially supported by the Council for Chemical Sciences of the Netherlands Organization for Scientific Research (CW-NWO).

Acknowledgement

I would like to use this first page to give a little thank you to the people without whom you would not be reading this manuscript today.

First of all of course to my supervisor Ad van der Avoird for giving me the opportunity to do my PhD research in this Lab and also for all his precious help and advice concerning the writing of articles and chapters. I should add that I am grateful that he could bear my south-west of France stubbornness and mood.

Gerrit Groenenboom for solving many theoretical as well as computational problems and for spending so many nights trying or debugging new codes.

Paul Wormer for nice comments and suggestions but particularly for spinning his karnemelk box every day at lunch which gave some thoughts about angular momentum theory.

Jacek Kłos for providing the potential energy surfaces that are used in the calculations throughout this thesis and of course for good fun with *philosophic discussions*, music, poems and table tennis.

All other colleagues in the Lab, Mirjam van Vroonhoven, Gé Vissers, Gilles Verbockhaven, Marc van der Loo and my most recent office-mate Cristina Sanz, rather unforgettable with her BBC radio online. And a special BIG thanks to Mirjam for the *Samenvatting* writing. I am grateful to Ine Meijer for hosting me when I had just arrived and together with Eugenie Miseroy for administrative support.

My thoughts go particularly to Michel Geleijns my first office-mate in Nijmegen University who helped nicely when I arrived.

I can't forget my dear friend Anthony for his eternal, sometimes overdone, support and others for current entertainment for these four years in Nijmegen (Florian, Aidan, Lionel, the Russian gang (they are too many to cite), and the ones I probably forget excuse me).

Finally, I have to say how much I appreciated to work in a Lab with such an obsession for carefulness and precision in calculations and for their highly detailed sense of how to hand out results. This will mark my memories for ever.

“Never forget that 1.47957416524805 isn't 1.47957416524804”

Thanks God for bringing Emma.

Contents

Acknowledgement	1
1 Introduction	7
1.1 Van der Waals and the evidence for intermolecular interactions	7
1.2 Origin of intermolecular interactions	8
1.3 Why study van der Waals interactions?	9
1.4 About this work	9
2 Methodology	11
2.1 Introduction	11
2.2 Coordinate systems	12
2.3 Born-Oppenheimer approximation and non-adiabatic coupling .	13
2.4 Generalized Born-Oppenheimer model and potential expansions	15
2.5 Dynamical calculations	17
3 $F(^2P)$-H_2	19
3.1 Introduction	20
3.2 Diabatic intermolecular potentials	21
3.3 Long range interactions	26
3.4 Refit of the ab initio data	28
3.5 Bound state calculations	35
3.5.1 Computational details	37
3.6 Results and discussion	38
4 He-CO($X^1\Sigma^+$) and He-CO($a^3\Pi$)	47
4.1 Introduction	48
4.2 Potential surfaces	49

4.2.1	Ab initio calculations	49
4.2.2	Expansion of the potentials	50
4.2.3	Analytic fits of the potentials	52
4.2.4	Characteristics of the potentials	54
4.3	Calculation of the vibration-rotation-spin levels	57
4.4	Effective dipole function for singlet-triplet excitation	60
4.5	Computational procedure	62
4.6	Results	63
4.7	Conclusions	66
5	He–CO($X^1\Sigma^+ \rightarrow a^3\Pi$) transitions	71
5.1	Introduction	72
5.2	Photodissociation calculations	73
5.2.1	Coupled-Channel formalism	73
5.2.2	Matching procedure for bound states	75
5.2.3	Photodissociation cross sections	77
5.3	Computational details	79
5.4	Discussion	79
5.5	Conclusions	87
6	Cl(2P)–HCl	91
6.1	Introduction	92
6.2	Bound state calculations	93
6.3	Results	95
6.3.1	One-dimensional calculations	96
6.3.2	Full calculation	106
6.4	Conclusion	113
7	He–HF($^2\Pi$)	115
7.1	Introduction	116
7.2	Calculation of rovibronic states	116
7.2.1	\mathbf{R} -embedding	118
7.2.2	\mathbf{r} -embedding	120
7.2.3	Computational details	122
7.3	Results	123
7.3.1	One-dimensional calculations	123
7.3.2	Full calculation	123
7.3.3	Renner-Teller effect	133
7.4	Conclusion	137
A	Basis transformations	139
	Summary	143
	Samenvatting	147

List of publications 151

Curriculum Vitae 153

Bibliography 155

CHAPTER 1

Introduction

This introductory chapter aims to present in a rather simple way the physical phenomena studied in this thesis such that a reader not acquainted with the subject is able to position this study within the broad diversity of chemical physics research.

1.1 Van der Waals and the evidence for intermolecular interactions

Historically, the idea that matter is constructed of atoms and molecules was born with the kinetic theory of gases and consideration of the stoichiometry of chemical reactions. The existence of the condensed phase of matter is a conclusive proof of attractive forces between molecules. Incompressibility properties are the result of a strong repulsive force at short distances between molecules. J. D. van der Waals was the first to incorporate these ideas into the description of gases, *real gases* as we call them, as opposed to *ideal gases*. In 1873 he proposed the equation that became known as the van der Waals equation which suggests that the volume the molecules occupy reduces the allowed volume for their free path, leading to the conclusion that strong repulsive forces are effective at short distances. Furthermore his main idea was that the gas pressure is decreased by the effect of attractive forces between molecules giving rise to the idea of long range intermolecular forces. The interaction energy V between molecules as a function of the distance between them must then display a minimum for some intermediate distance. It was first believed that these forces were purely of classical electrostatic origin but it was later understood with the advances of quantum mechanics that they have a pure quantum character as

well.

1.2 Origin of intermolecular interactions

Atoms and molecules are composed of electrons and nuclei (the latter consisting of protons and neutrons) which are charged particles. They therefore interact by means of Coulomb forces. When incorporated into the framework of quantum mechanics these Coulomb forces lead to the following intermolecular interactions: electrostatic, induction (or polarization), dispersion, and exchange. In terms of perturbation theory the electrostatic and exchange interactions are found in first order, while the induction and dispersion interactions—and again some exchange effects—occur in second order. The electrostatic and induction contributions can also be described in terms of classical electrostatics, exchange and dispersion are pure quantum mechanical phenomena. The dispersion energy is caused by the quantum fluctuations of the electron distributions (the presence of instantaneous dipole moments in the molecules) leading to the so-called induced dipole-induced dipole interaction. The exchange contribution is due to the Pauli exclusion principle which imposes that two different electrons in a molecule cannot be in the exact same quantum state (a consequence of the antisymmetry of the total electronic wave function). It can be either attractive or repulsive. For a pair of interacting atoms that both have partly filled shells of electrons it is usually attractive and leads to the formation of a stable molecule by strong covalent chemical bonding. Most stable molecules have only closed (completely filled) shells and the exchange forces between them are mostly repulsive. The exchange repulsion, a short-range effect, is responsible for the phenomenon of steric hindrance and for the “excluded volume” in a *real* gas.

At large distances the electronic clouds of the interacting partners do not overlap and the electrostatic, induction, and dispersion interaction terms can be expressed in a multipole expansion. For charged and polar molecules the interaction is dominated by the electrostatic and induction contributions. Electrostatic forces can be either attractive or repulsive, depending on the molecular orientations. Induction forces are always attractive. Hydrogen bonding is a special case of an attraction between polar molecules in which the electrostatic and induction interactions play an important role. For neutral nonpolar species the main long-range interaction is the dispersion energy, which is always attractive too. From the multipole expansion it follows that the leading (induced dipole-induced dipole) term in the dispersion energy is proportional to the inverse sixth power of the intermolecular distance. Around the equilibrium distance, i.e., the distance where the energy of the interacting molecules has its minimum, the overlap of the electron clouds of different molecules is small, the interaction is unable to induce an appreciable modification of the internal structure of the involved species, and the molecules largely retain their

identity. The magnitude of the intermolecular interaction energy ranges from about 8 cm^{-1} for He_2 to several thousands of cm^{-1} for polar or charged species. We can distinguish “true” van der Waals interactions—between molecules that attract each other by dispersion forces and are typically bound by less than a few hundreds of cm^{-1} —from hydrogen bonding which ranges from about 1000 to 2000 cm^{-1} and ionic interactions which can be even much stronger. The strongest interacting system in this thesis is the He-HF^+ complex, with a binding energy of $\approx 1700\text{ cm}^{-1}$. All these interactions are very weak in comparison with chemical bonding, except perhaps when all the interacting molecules are ions.

1.3 Why study van der Waals interactions?

Van der Waals interactions form the basis of a wide range of processes in physics, chemistry and biology and as such have received considerable attention. For instance, they are responsible for the cohesion of molecular crystals and liquids and, as it was recently reported [1, 2], they have prime importance in the mechanics of adhesion. They also play a central role in biology and life sciences, being responsible for DNA site specificities and DNA replication, and they are the mediator of some protein receptor-drug reactions [3, 4, 5]. They sometimes intervene in chemical reactions by formation of so-called van der Waals complexes. These complexes are formed when two or more atoms or molecules are brought together by means of van der Waals interactions. Van der Waals complexes are weakly bound (see the previous section) but their formation in the entrance/exit channel of a chemical reaction can nevertheless strongly affect the outcome of this reaction [6, 7].

Historically, most of the work on van der Waals interactions and complexes was done for systems containing only closed-shell species. Recently more and more attention, both experimental and theoretical, is being given to the study of systems containing open-shell species. Open-shell species are atoms or molecules with one or more unpaired electrons in their electronic ground state, i.e., free radicals, or molecules in electronically excited states. Especially in chemical reactions in the atmosphere and in interstellar clouds collision complexes of open-shell species may be expected to play an important role, because of the relatively low temperature, the occurrence of many free radicals, and the effects of radiation. Also in view of the interest in ultracold molecules and Bose-Einstein condensates [8] they are important because the most promising candidates for molecular cooling and trapping are often open-shell molecules.

1.4 About this work

This thesis focusses on the study of atom-diatom van der Waals complexes in which either the atom or the diatom is an open-shell species. They can be con-

sidered as model systems for interacting open-shell species of a more complex nature. The interactions in these complexes are weak and strongly anisotropic and involve more than one electronic state. For specific (in this case linear) geometries of the complexes and for large distances between the interacting species these electronic states are degenerate and the Born-Oppenheimer approximation or adiabatic hypothesis—that is the decoupling of the electronic and nuclear motions—is not valid. Non-adiabatic coupling becomes important and has to be taken into account in the computation of bound states and spectra of these complexes, as well as in scattering and photodissociation calculations. This, by itself, is interesting because non-adiabatic behaviour is observed in a great number of fundamental molecular processes such as electronic energy transfer, quenching of electronic excitations, and chemical reactions. Also spin-orbit coupling is significant in these open-shell systems and leads to other particular effects.

The thesis is structured as follows. Chapter 2 gives a brief introduction to the methodology applied to calculate the bound and scattering states of open-shell van der Waals complexes, the following chapters treat specific examples. Chapter 3 describes a calculation of the bound states of the $F(^2P)\text{-H}_2$ complex occurring in the entrance channel of the reaction $F + \text{H}_2 \rightarrow \text{H} + \text{HF}$. Chapters 4 and 5 concern the bound states and photodissociation of the ground state and spin-triplet excited He-CO complex and the UV spectrum associated with the spin-forbidden $\text{CO}(X^1\Sigma \rightarrow a^3\Pi)$ excitation of this complex. This study was undertaken to find out what happens to a metastable $a^3\Pi$ excited CO molecule when it interacts with a He atom. It also turned out to be of interest because an experimental attempt to observe the complex of metastable triplet CO with He had failed and our study could explain why and suggest an experiment with a better chance of success. Chapter 6 presents results for the bound states of the $\text{Cl}(^2P)\text{-HCl}$ complex occurring in the entrance and exit channels of the hydrogen exchange reaction $\text{Cl} + \text{HCl} \rightarrow \text{ClH} + \text{Cl}$. Finally, chapter 7 presents a study of the He- $\text{HF}^+(^2\Pi)$ complex, a Renner-Teller system. The Renner-Teller effect, a nonadiabatic coupling phenomenon, has up to now been studied for linear triatomic and polyatomic molecules. It is interesting to observe and theoretically explain this effect in a rather weakly bound complex with large amplitude bending motions.

CHAPTER 2

Methodology

2.1 Introduction

This chapter aims to introduce the analytical and computational methods that we employed to calculate the bound states and photodissociation of several open-shell van der Waals complexes.

For complexes of closed-shell molecules the solution of the quantum mechanical nuclear motion problem (called a dynamical calculation) makes use of a single potential energy surface. This is because only a single electronic state (usually the ground state) is involved and the Born-Oppenheimer approximation — the separation of the electronic and nuclear motion problems — is valid. For open-shell systems the situation is more complicated, however. Atoms or molecules with open shells have degenerate electronic states, which requires the use of multiple potential energy surfaces, and non-zero orbital and/or spin angular momenta, which require the inclusion of spin-orbit, spin-spin, and spin-rotation couplings. The potential surfaces are degenerate at specific geometries (linear in the atom-diatom case) and also for large intermolecular distances where the electronic states tend to the same dissociation limit. At and near these degeneracies non-adiabatic coupling becomes important, which, together with the angular momentum couplings, influences strongly the dynamics of the complex.

We illustrate that the Born-Oppenheimer approximation is valid in the case of a single electronic potential surface calculation and is insufficient when dealing with multiple electronic states. One may handle this problem by including simultaneously all involved surfaces and their corresponding coupling in the dynamical calculation. We call this the “generalised Born-Oppenheimer model”. Instead of explicitly including the non-adiabatic coupling in this model, the

adiabatic electronic states are transformed to a, so-called, diabatic basis. The non-adiabatic coupling that originates from the nuclear kinetic energy operator is removed (or strongly reduced) in this basis. The asymptotically degenerate diabatic states are coupled by off-diagonal potential energy surfaces, so one has to deal with a potential energy matrix rather than a single potential surface. The dimension of this matrix is equal to the number of (a)diabatic states involved. An advantage of this diabatic model is that the corresponding potential energy surfaces are usually smoother functions of the internuclear coordinates and therefore easier to fit to analytic functions. It is often useful to make an expansion of the potentials in terms of functions of a set of angular coordinates. Another advantage of the use of diabatic states is that this expansion takes a specific form that depends on the type of system. This form can be derived in a very general manner from the invariance of the potential energy operator under overall rotations of the system. For atom-diatom complexes with either the atom or the molecule being the open-shell species this derivation is given in chapters 3 and 4, respectively.

2.2 Coordinate systems

This paragraph recalls briefly the definitions used in the thesis for the different frames and coordinate systems. In the study of van der Waals complex formation one preferably uses Jacobi or “scattering” coordinates instead of the valence or hyperspherical coordinates [9, 10] more commonly used in molecular problems and in reaction dynamics. In the present work, we deal with atom-diatom systems for which the Jacobi coordinates are defined by the intermolecular axis \mathbf{R} pointing from the atom to the center of mass of the diatom and the diatom axis \mathbf{r} . The vector \mathbf{R} is defined by its norm R and orientation (polar angles β, α) in a laboratory frame, as \mathbf{r} is defined by its norm r and its orientation (angles θ, ϕ) with respect to the same frame. In many cases, the coordinate r can be fixed at the vibrational ground state expectation value because the frequencies of the diatom vibrations are much higher than those of the intermolecular modes. One can make an adiabatic separation between the diatom vibrations and the intermolecular modes and treat only the latter explicitly.

Various coordinate systems might be useful for different types of complexes and the derivation of their properties. Three different coordinate systems and frames are mainly used in this thesis. The first one is the already mentioned laboratory or space-fixed (SF) frame. It consists of three orthogonal cartesian axes X, Y, Z fixed in space. The reference orientation of these axes can be the direction of an external electric field, the incident molecular beam direction, or any abstract reference that fixes a direction in space. The Hamiltonian for the nuclear motion problem in atom-diatom systems is easily derived in SF coordinates [see eq. (4.12)]. The angular and spin basis to solve this problem

should be expressed in the same coordinates. Different angular momentum coupling schemes can be chosen for this basis, depending on the importance of the various couplings in a given system. See eq. (4.15) for an example. This SF basis is also the most convenient one for scattering and photodissociation calculations.

The two other frames are fixed within the complex. The first one is called body-fixed (BF) and is defined such that its z -axis coincides with the intermolecular axis \mathbf{R} . This frame is related to the SF frame by a rotation $\mathbb{R}(\alpha, \beta)$ with (β, α) being the polar angles of the intermolecular vector \mathbf{R} in the SF frame. Such a frame fixed by two rotation angles is called two-angle embedded. The vector \mathbf{r} is given with respect to the BF frame by $\mathbf{r}^{\text{BF}} = \mathbb{R}(\alpha, \beta)^{-1}\mathbf{r}$. When (θ', ϕ') are the polar angles of \mathbf{r}^{BF} with respect to the BF frame the rotation $\mathbb{R}(\alpha, \beta, \phi')$ defines a fully or three-angle embedded BF frame. The rotation over ϕ' keeps the BF z -axis parallel to the vector \mathbf{R} and puts the diatom in the xz -plane. The use of a BF frame is convenient in bound state calculations because the potential surface is already expressed in internal (BF) coordinates and the expansion of the bound state wave functions in a BF basis gives a direct physical interpretation of the results.

The third coordinate system used in the literature is called molecule-fixed (MF). It is defined such that its z -axis is parallel to the diatom axis \mathbf{r} and obtained by a rotation $\mathbb{R}(\phi, \theta)$. The MF frame is convenient in specific cases such as atom-diatom systems having a strongly bound linear equilibrium geometry (Renner-Teller systems) or complexes containing a diatom with very strong spin-orbit coupling which make the diatomic axis a good projection axis. For examples of the Hamiltonian, the basis, and the matrix elements for an atom-diatom nuclear motion problem in BF and MF coordinates, see chapter 7. The transformation of the basis from BF or MF coordinates to SF coordinates, and vice versa, is derived in the Appendix A.

2.3 Born-Oppenheimer approximation and non-adiabatic coupling

Quantum chemistry is based on the approximate solution of the Schrödinger equation. Current computer technology is powerful enough to perform *ab initio* variational or perturbational calculations reducing the approximation to a high level of accuracy and yielding data that may be compared to experimental results. This thesis concentrates on bound states and scattering calculations which requires the solution of the following time-independent equation

$$\left(-\frac{\nabla_{\mathbf{Q}}^2}{2M} + H_{\text{el}}(\mathbf{q}, \mathbf{Q}) \right) \Psi(\mathbf{q}, \mathbf{Q}) = E\Psi(\mathbf{q}, \mathbf{Q}). \quad (2.1)$$

where \mathbf{q} represents the coordinates of all the electrons, \mathbf{Q} represents the coordinates of the nuclei, H_{el} is the electronic Hamiltonian which includes the

electron kinetic operator as well as the electron-electron, electron-nuclear, and nuclear-nuclear Coulomb interactions. The generic symbol M represents the masses of the different nuclei involved in the problem. $\Psi(\mathbf{q}, \mathbf{Q})$ and E are the total wave function and the total energy of the complex, respectively.

The nuclear masses are larger than the electron mass by at least a factor of 1800 and Born and Oppenheimer proposed in 1927 [11] to solve the Schrödinger equation by separating the electronic motion from the nuclear motion. This decoupling allows the calculation of the molecular bound or scattering states in a two-step procedure. The total wave function $\Psi(\mathbf{q}, \mathbf{Q})$, which is the solution of eq. (2.1), can be expanded in products of functions $\phi_i(\mathbf{q}; \mathbf{Q})$ of the electronic coordinates that depend parametrically on the nuclear coordinates \mathbf{Q} and functions $\chi_i(\mathbf{Q})$ of the nuclear coordinates only

$$\Psi(\mathbf{q}, \mathbf{Q}) = \sum_{i=1}^{\infty} \phi_i(\mathbf{q}; \mathbf{Q}) \chi_i(\mathbf{Q}). \quad (2.2)$$

The functions ϕ_i are eigenfunctions of the electronic hamiltonian H_{el}

$$H_{\text{el}}(\mathbf{q}, \mathbf{Q}) \phi_i(\mathbf{q}; \mathbf{Q}) = V_i(\mathbf{Q}) \phi_i(\mathbf{q}; \mathbf{Q}). \quad (2.3)$$

Since the electronic equation (2.3) does not contain the nuclear kinetic energy operator it can be solved for clamped nuclei, i.e., nuclei fixed at positions \mathbf{Q} . This provides the eigenvalues $V_i(\mathbf{Q})$ and eigenfunctions $\phi_i(\mathbf{q}; \mathbf{Q})$. Substitution of the expansion (2.2) into eq. (2.1), use of eq. (2.3), multiplication with one of the functions ϕ_i , integration over the electron coordinates \mathbf{q} , and use of the orthogonality of the functions ϕ_i leads to a set of coupled equations for the nuclear wave functions

$$\left(-\frac{\nabla_{\mathbf{Q}}^2}{2M} + V_i(\mathbf{Q}) - E \right) \chi_i(\mathbf{Q}) = \sum_{k=1}^{\infty} (\mathbf{F}_{ik} \cdot \nabla_{\mathbf{Q}} + \frac{1}{2} G_{ik}) \chi_k(\mathbf{Q}) \quad (2.4)$$

with coupling coefficients

$$\begin{aligned} \mathbf{F}_{ik}(\mathbf{Q}) &= \frac{1}{M} \langle \phi_i(\mathbf{q}; \mathbf{Q}) | \nabla_{\mathbf{Q}} \phi_k(\mathbf{q}; \mathbf{Q}) \rangle \\ G_{ik}(\mathbf{Q}) &= \frac{1}{M} \langle \phi_i(\mathbf{q}; \mathbf{Q}) | \nabla_{\mathbf{Q}}^2 \phi_k(\mathbf{q}; \mathbf{Q}) \rangle \end{aligned} \quad (2.5)$$

that depend on the nuclear coordinates \mathbf{Q} .

An alternative expression for $\mathbf{F}_{ik}(\mathbf{Q})$ can be derived by acting with the differentiation operator $\nabla_{\mathbf{Q}}$ on the matrix element $\langle \phi_i(\mathbf{q}; \mathbf{Q}) | H_{\text{el}} | \phi_k(\mathbf{q}; \mathbf{Q}) \rangle$. With the use of the eigenvalue equation (2.3) and the orthogonality of the functions $\phi_i(\mathbf{q}; \mathbf{Q})$ which implies that $\nabla_{\mathbf{Q}} \langle \phi_i(\mathbf{q}; \mathbf{Q}) | \phi_k(\mathbf{q}; \mathbf{Q}) \rangle = \nabla_{\mathbf{Q}} \delta_{ik} = 0$ one obtains

$$\mathbf{F}_{ik}(\mathbf{Q}) = \frac{1}{M} \frac{\langle \phi_i(\mathbf{q}; \mathbf{Q}) | \nabla_{\mathbf{Q}} H_{\text{el}} | \phi_k(\mathbf{q}; \mathbf{Q}) \rangle}{V_k(\mathbf{Q}) - V_i(\mathbf{Q})}. \quad (2.6)$$

Both the nuclear mass and the energy separation $V_k - V_i$ between different electronic states i and k are in the denominator of eq. (2.6) and in normal cases this energy separation is large, so that the coupling term $\mathbf{F}_{ik}(\mathbf{Q})$ is very small. A similar reasoning can be applied to $G_{ik}(\mathbf{Q})$. The Born-Oppenheimer approximation consists of neglecting the coupling between different electronic states ϕ_i altogether and solving the nuclear Schrödinger equation obtained by setting the right hand side of eq. (2.4) equal to zero. Note that the potential energy operator in this equation for the nuclear motion is the electronic energy $V_i(\mathbf{Q})$. In the adiabatic approximation one includes only diagonal couplings \mathbf{F}_{ii} and G_{ii} . The off-diagonal terms \mathbf{F}_{ik} and G_{ik} with $k \neq i$ are called non-adiabatic couplings.

In the neighborhood of configurations \mathbf{Q} where different electronic states become degenerate, i.e., when $V_i(\mathbf{Q}) \approx V_k(\mathbf{Q})$, the non-adiabatic coupling term $\mathbf{F}_{ik}(\mathbf{Q})$ becomes important and the Born-Oppenheimer approximation fails. This occurs, for example, at the (avoided) crossings of multiple potential surfaces, conical intersections, and in open-shell van der Waals complexes.

2.4 Generalized Born-Oppenheimer model and potential expansions

For open-shell complexes where one of the monomers has a degenerate electronic state multiple potential energy surfaces will coincide when the intermolecular distance becomes large. We say that the electronic states of the complex are asymptotically degenerate. In such cases one can apply a “Generalized Born-Oppenheimer model” that includes the set of all asymptotically degenerate electronic states and the non-adiabatic coupling $\mathbf{F}_{ik}(\mathbf{Q})$ and $G_{ik}(\mathbf{Q})$ between these states. The wave function of the complex is written as in eq. (2.2)

$$\Psi(\mathbf{q}, \mathbf{Q}) = \sum_{i=1}^n \phi_i(\mathbf{q}; \mathbf{Q}) \chi_i(\mathbf{Q}), \quad (2.7)$$

but with the summation restricted to the set of n asymptotically degenerate states. The condition of validity for the Born-Oppenheimer approximation must then apply to these states collectively, i.e., the energy separation between this set of n states and all other electronic states of the complex must be large.

Even in this model there is a problem, however. Equation (2.6) shows that the non-adiabatic coupling term \mathbf{F}_{ik} becomes singular whenever the energies V_i and V_k are the same. This problem can be avoided by not including the non-adiabatic coupling explicitly, but instead transforming the adiabatic states ϕ_i to a diabatic basis ψ_i in which, by definition, this coupling is removed (or strongly reduced) [12, 13]. Definitions of such diabatic basis sets are presented throughout the following chapters. The price one pays is that these diabatic states are not eigenfunctions of the electronic Hamiltonian H_{el} , which yields

off-diagonal potential energy matrix elements. In the nuclear motion problem one has to deal with a full $n \times n$ potential energy matrix rather than with a single potential surface. The potential energy operator can formally be written as

$$\widehat{V}(\mathbf{Q}) = \sum_{i,k=1}^n |\psi_i\rangle V_{i,k}(\mathbf{Q}) \langle \psi_k| \quad (2.8)$$

where $|\psi_i\rangle$ are the diabatic states. They are defined according to the type of complex studied; for large distances they become direct products of the electronic states of the monomers. See paragraphs 3.2 and 4.2.2 for examples. The matrix elements $V_{i,k}$ of the electronic Hamiltonian in the set of functions $\{|\psi_i\rangle\}$, are called diabatic potential surfaces. When the matrix \mathbf{V} would be diagonalized we recapture, by definition, the adiabatic electronic states of the complex. The eigenvalues of the matrix $\mathbf{V}(\mathbf{Q})$ are the adiabatic potential surfaces.

In the case of interacting closed-shell molecules the Born-Oppenheimer approximation holds and the intermolecular potential is a scalar function. That is, it is invariant under overall rotation of the complex. The anisotropy of the potential (for an atom-diatom complex in BF coordinates) can be described by the well known expansion in Legendre polynomials $P_l(\cos \theta')$

$$V(R, r, \theta') = \sum_l v_l(R, r) P_l(\cos \theta') \quad (2.9)$$

with the angle θ' as defined in section 2.2. The expansion coefficients $v_l(R, r)$ depend on the intermolecular distance R and on the diatom bond length r . They are usually fitted to analytical functions of these coordinates, see for example eqs. (4.6) and (4.7).

Similar expansions can be derived for open-shell systems. The correct form of the angular expansion in this case can be determined by using the invariance of the total potential energy operator—eq. (2.8)—under overall rotation and inversion of the system, as well as the hermiticity of this operator. Details can be found in chapters 3 and 4. It turns out that for an atom-diatom complex the diabatic potentials $V_{i,k}(R, r, \theta')$ should be expanded in associated Legendre functions $P_{l,m}(\theta')$, rather than in Legendre polynomials. Or, equivalently, in Racah normalized spherical harmonics $C_m^l(\theta', 0)$ with $m = 0$ for the diagonal matrix elements $V_{i,i}$ and $m \neq 0$ for the off-diagonal elements $V_{i,k}$ with $i \neq k$. For an open-shell atom interacting with a closed-shell diatom the diabatic states of the complex may be written as $|\lambda, \mu\rangle$. The quantum number λ refers to the electronic angular momentum of the open-shell atom and $\mu = -\lambda, \dots, \lambda$ is the projection of this angular momentum on the z -axis of the BF dimer frame. The expansion of the diabatic potentials reads

$$V_{\mu'\mu}(R, r, \theta') = \langle \lambda\mu' | \widehat{V} | \lambda\mu \rangle = \sum_l v_l^{\mu'\mu}(R, r) C_{\mu-\mu'}^l(\theta', 0). \quad (2.10)$$

As demonstrated in chapter 3 [see eq. (3.10)] invariance under overall rotation implies that m only takes the values $\mu - \mu'$. Chapters 3 and 6 deal with atoms in a P state, with $\lambda = 1$ and $\mu = -1, 0, 1$. In this case, m will take the values $0, \pm 1, \pm 2$.

2.5 Dynamical calculations

Once the first step of the generalized Born-Oppenheimer model is completed, i.e., the adiabatic potential energy surfaces are obtained, the second step consists of solving the quantum mechanical nuclear motion problem

$$\hat{H}\chi(\mathbf{Q}) = \left(-\frac{\nabla_{\mathbf{Q}}^2}{2M} + \hat{V}(\mathbf{Q}) \right) \chi(\mathbf{Q}) = E\chi(\mathbf{Q}) \quad (2.11)$$

with the potential energy operator $\hat{V}(\mathbf{Q})$ of eq. (2.8). This operator contains the diabatic potential energy surfaces, rather than the adiabatic ones obtained from the solution of the electronic Schrödinger equation, so one should first determine the adiabatic to diabatic transformation appropriate for a given system. In this Hamiltonian it is assumed that the kinetic coupling terms $\mathbf{F}_{ik}(\mathbf{Q})$ and $G_{ik}(\mathbf{Q})$ are negligible, because of the choice of the diabatic basis $\{ | \psi_i \rangle \}$.

For an atom-diatom system the (SF) nuclear coordinates \mathbf{Q} are the Jacobi coordinates \mathbf{R} and \mathbf{r} defined in section 2.2. With the inclusion of spin-orbit coupling in the open-shell atom, the nuclear motion Hamiltonian (in atomic units) reduces to

$$\hat{H} = \frac{-1}{2\mu_{\text{tot}}R} \frac{\partial^2}{\partial R^2} R + \frac{\hat{L}^2}{2\mu_{\text{tot}}R^2} + b_0 \hat{j}^2 + A_0 \hat{\lambda} \cdot \hat{\mathbf{S}} + \sum_{\mu'\mu} | \lambda, \mu \rangle V_{\mu, \mu'}(\mathbf{R}, \hat{\mathbf{r}}) \langle \lambda, \mu' | \quad (2.12)$$

with the kinetic energy operator now expressed in spherical polar coordinates. The operator \hat{L} is the end-over-end angular momentum operator and μ_{tot} is the reduced mass of the complex, \hat{j} and b_0 are the angular momentum and the rotational constant of the diatom, $\hat{\lambda}$ and $\hat{\mathbf{S}}$ the electronic orbital and spin angular momenta of the atom and A_0 is the atomic spin-orbit coupling constant. The kinetic energy term $-(2\mu_{\text{diatom}}r)^{-1} (\partial^2/\partial r^2) r$ is omitted from this equation because the r coordinate is kept frozen at a fixed value (see section 2.2). The unit vector $\hat{\mathbf{r}}$ denotes the orientation of \mathbf{r} with respect to the SF frame. The rotational constant b_0 of the diatom is equal to $\langle v=0 | (2\mu_{\text{diatom}}r^2)^{-1} | v=0 \rangle$ and $| v=0 \rangle$ is the vibrational ground state of the diatom.

The effect of the non-adiabatic coupling is implicitly included in the diabatic potentials $V_{\mu, \mu'}(\mathbf{R}, \hat{\mathbf{r}})$. To obtain the energies E , i.e., the eigenvalues of the nuclear motion Hamiltonian, and the corresponding eigenfunctions $\chi(\mathbf{R}, \hat{\mathbf{r}})$, we expand the functions $\chi(\mathbf{R}, \hat{\mathbf{r}})$ in direct products of angular momentum and spin

basis functions $A_{\{l\}}$ and radial functions f_n

$$\chi(\mathbf{R}, \hat{\mathbf{r}}) = \sum_{\{l\}, n}^{\infty} c_{\{l\}, n} A_{\{l\}}(\hat{\mathbf{R}}, \hat{\mathbf{r}}) f_n(R). \quad (2.13)$$

The set of quantum numbers $\{l\}$ represents all angular momentum and spin quantum numbers in eq. (2.12) which refer to the electronic and nuclear wave functions, and n labels radial basis functions. The symbols $\hat{\mathbf{R}}$ and R denote the orientation and norm of the vector \mathbf{R} , respectively. The Hamiltonian matrix is constructed from this, properly truncated, set of basis functions $A_{\{l\}}$ and f_n and then diagonalized. The angular momentum and spin basis functions $A_{\{l\}}(\hat{\mathbf{R}}, \hat{\mathbf{r}})$ are chosen as (coupled) products of eigenfunctions of the angular momentum operators present in the Hamiltonian operator. Integrals involving these angular functions are well known expressions in terms of $3n-j$ symbols [14] and are easily computed.

In calculations of the bound states of a van der Waals complex one may choose an analytical basis for the radial functions $f_n(R)$, e.g. Laguerre functions, and compute the radial integrals by means of a numerical Gauss-Laguerre quadrature. The second derivative occurring in the kinetic energy operator can then be evaluated analytically. Another possibility is to use the sinc-DVR formalism, which provides an analytical and computationally cheap expression for the second derivative [15]. The third alternative is to use propagation procedures that are normally used to obtain scattering states but are also applicable to bound state calculations (see chapter 5). In order to obtain photodissociation cross sections one needs to compute both bound and dissociating states; the latter are obtained by a propagation method as used in scattering calculations. Diagonalization of the Hamiltonian matrix provides the energy levels and wave functions of the van der Waals complex. Also various properties of the complex can then be calculated, as well as excitation spectra. Excitation may lead to dissociation and one can compute photodissociation cross sections, life times (spectral line widths), and state distributions of the fragments. The reader will meet all this in the following chapters, with the complexes He-CO($a^3\Pi$) and He-HF⁺($X^2\Pi$) as examples where the diatom is the open-shell species, and the complexes F(2P)-H₂ and Cl(2P)-HCl as examples with an open-shell atom.

CHAPTER 3

Calculation of the bound states of the $F(^2P)\text{-H}_2$ Van der Waals complex on ab initio diabatic potential energy surfaces

We present a general derivation of the expansion of diabatic intermolecular potentials for an open-shell atom interacting with a closed-shell molecule and the multipolar expansion of these potentials in the long range. It is outlined how to compute bound states of the open-shell atom - molecule complex from the set of asymptotically degenerate diabatic potentials in a body-fixed basis of rovibrational wavefunctions with the inclusion of spin-orbit coupling. This method is applied to produce all the bound energy levels of the $F(^2P)\text{-H}_2$ Van der Waals complex with recent diabatic potentials obtained from *ab initio* calculations by Kłos *et al.* [Int. J. Quant. Chem. **90**, 1038 (2002)]. The binding energy D_0 is 14.6 cm^{-1} for the *para*- H_2 complex and 19.3 cm^{-1} for the *ortho*- H_2 complex. The *para*- $\text{H}_2\text{-F}$ complex does not possess any bound states for rotational quantum numbers J larger than $\frac{9}{2}$, the *ortho*- $\text{H}_2\text{-F}$ complex has a maximum J of $\frac{11}{2}$.

3.1 Introduction

In the more familiar case of two interacting closed-shell molecules the intermolecular potential obtained by solving the first step of the Born-Oppenheimer (BO) or adiabatic approximation is a scalar function. That is, it is invariant under rotations of the whole system, as well as under space-inversion. When the dependence of the potential on the molecular orientations is expressed by an expansion in a basis of angular functions also these functions should be invariant under overall rotations [16]. Such an expansion is convenient for the application of intermolecular potential surfaces in dynamical calculations, computations of second virial coefficients, etc. The coefficients in the expansion depend on the intermolecular distance R and, for nonrigid molecules, on the intramolecular coordinates [16, 17].

For open-shell systems the situation is more complicated. The electronic states of open-shell atoms and molecules are often degenerate, and for a given electronic state of the interacting species there exist multiple adiabatic intermolecular potential surfaces that are asymptotically degenerate. Nonadiabatic coupling between the electronic states involved becomes important. In dynamical calculations it is useful to define a “generalized BO model” which includes the nonadiabatic coupling, but only between the set of electronic states that are asymptotically degenerate. This model works well when the energy separation between the electronic states included in the model and all other states is large with respect to the intermolecular interactions that split the model states.

Formulas for intermolecular potentials between an open-shell atom and a closed-shell diatomic molecule have been presented by Alexander [18] and by Dubernet and Hutson [19, 20]. Alexander obtained his formulas [18] by writing the intermolecular interaction operator in the form of the multipole expansion. However, this expansion is valid only in the long range, when there is no overlap between the wavefunctions of the interacting species. Dubernet and Hutson derived their formulas by starting from the well-known expansion of diatom-diatom potentials, replacing the polar angles of one of the diatom axes by the coordinates of the electrons in the atom, and taking matrix elements with respect to the degenerate electronic substates of the open-shell atom. In Sec. 3.2 we will show that the same formulas can be obtained by defining a general intermolecular potential energy operator \hat{V} for interacting open-shell species and using only the property that this operator is invariant under rotations and inversion. We also define a set of asymptotically degenerate diabatic states and we show how to expand the corresponding diabatic potentials in the appropriate angle-dependent functions. The formulas are first derived for open-shell atom - diatom systems and then generalized to atom - nonlinear molecule systems. Furthermore, it is shown in Sec. 3.3 how the diabatic interaction potentials can be expressed in closed analytic form by the use of the multipole expansion that holds in the long range. An important long range interaction term in the coupling potential between diabatic states of the same

symmetry was overlooked in Ref. [18].

Next, we outline the procedure to include the set of asymptotically degenerate intermolecular potentials for open-shell atom - molecule dimers in bound state calculations. The theory is applied to the $F(^2P)\text{-H}_2(^1\Sigma_g^+)$ complex. The interaction of $F(^2P)$ atoms with H_2 molecules has received much attention from experimentalists and theoreticians [21, 22, 23, 24, 25, 26, 27, 28, 29, 30, 31, 32, 33, 34, 35, 36]. Most studies address the chemical reaction $F + \text{H}_2 \rightarrow \text{H} + \text{HF}$ or one of its isotopic equivalents, theoretically by quantum scattering calculations or quasiclassical trajectory studies and experimentally by crossed molecular-beam studies. Theory and experiment have reached a fair level of agreement. In the similar reaction $\text{Cl} + \text{H}_2 \rightarrow \text{H} + \text{HCl}$ it was found [6, 7] that the occurrence of a weakly bound Cl-H_2 complex in the entrance channel of the reaction is of great importance. In the $F + \text{H}_2$ reaction the role of such an entrance channel complex $F\text{-H}_2$ has not yet been established, but it is certainly worthwhile to study this complex in detail. Lately, Takayanagi and coworkers [37] reported the presence of Van der Waals resonances in the $F + \text{H}_2$ reaction probability, and they used an approximate approach to calculate $F\text{-H}_2$ bound states from one-dimensional effective potential curves. Aquilanti *et al.* [31, 32] measured elastic $F\text{-D}_2$ scattering cross sections and used these data to construct diabatic $F\text{-H}_2$ potential surfaces. Rotationally inelastic $F\text{-H}_2$ scattering cross sections were measured in the Toennies group [34, 35, 36].

We report the first detailed study of the bound states of $F\text{-H}_2$. We employed the accurate three-dimensional diabatic potential energy surfaces for $F(^2P)\text{-H}_2$ system that were recently reported by Kłos *et al.* [38]. They were obtained from *ab initio* unrestricted coupled cluster calculations with single, double, and non-iterative triple excitations [UCCSD(T)]. The *ab initio* data of Kłos *et al.* was refitted—see Sec. 3.4—with the use of the formulas derived in Secs. 3.2 and 3.3. This was necessary because the original fit of this potential had some unphysical artefacts at large distances. These were overlooked in Ref. [38], and they constitute a serious problem in bound state calculations. For comparison, we also computed the bound states of $F\text{-H}_2$ from the empirical potentials of Aquilanti *et al.* [32]. The method for the calculation of the Van der Waals levels on the three asymptotically degenerate diabatic potential energy surfaces with the inclusion of the potential that couples them is presented in Sec. 3.5. The spin-orbit interaction in the $F(^2P)$ atom is included as well. In Sec. 3.6 we discuss the results.

3.2 Diabatic intermolecular potentials for open-shell atom—molecule complexes

We consider an open-shell atom (A) interacting with a closed-shell molecule (B). The degenerate states of the open-shell atom A are denoted as $|\lambda, \mu\rangle^A$ with fixed λ and $\mu = -\lambda, \dots, \lambda$. These quantum numbers may refer to the

orbital angular momentum of the atom or, more generally, to the total electronic angular momentum J, M_J of a spin-orbit coupled state. In the latter case λ can adopt half-integer values. We assume that the states $|\lambda, \mu\rangle^A$ are of well-defined parity p under inversion: $\widehat{i}|\lambda, \mu\rangle^A = (-1)^p|\lambda, \mu\rangle^A$. Molecule B is a closed-shell molecule in state $|0\rangle^B$ with no electronic degeneracy. We may define a set of asymptotically degenerate diabatic states of the interacting system A–B and denote these by $|\lambda, \mu\rangle$. Although these wavefunctions are labeled with the quantum numbers of A, the functions depend on the electronic coordinates of both A and B. For large distance R between A and B they may be written as products $|\lambda, \mu\rangle^A|0\rangle^B$ and the mixing of the diabatic electronic states $|\lambda, \mu\rangle$ of system A–B induced by overall rotation of the whole system follows the transformation of the states $|\lambda, \mu\rangle^A$ of the atom. Since these states are well separated in energy from other electronic states of the interacting system and do not mix with other electronic states, we may assume that this transformation property holds for all relevant distances.

Subsystem B may be a general closed-shell molecule (or atom), but we will first write the formulas for a diatomic molecule. The intermolecular vector \mathbf{R} points from the nucleus of atom A to the center-of-mass of molecule B and the vector \mathbf{r} is the diatom bond axis. The intermolecular potential energy is a linear operator in the vector space spanned by the set of diabatic states and may be expanded as

$$\widehat{V}^{(\lambda)} = \sum_{\mu'\mu} |\lambda, \mu'\rangle^{\text{SF}} \langle \lambda, \mu | V_{\mu'\mu}^{(\lambda)}(R, \beta, \alpha, r, \theta^{\text{SF}}, \phi^{\text{SF}}). \quad (3.1)$$

The functions $V_{\mu'\mu}^{(\lambda)}$ are the diabatic potentials with respect to a space-fixed (SF) coordinate system. They depend on the atom-diatom coordinates: R, β, α , the length and the polar angles of the vector \mathbf{R} with respect to the SF frame and $r, \theta^{\text{SF}}, \phi^{\text{SF}}$, the length and polar angles of \mathbf{r} . These potentials may be expanded

$$V_{\mu'\mu}^{(\lambda)}(R, \beta, \alpha, r, \theta^{\text{SF}}, \phi^{\text{SF}}) = \sum_{LQ;l_B} \mathcal{C}_{(l_B)L,Q}(\beta, \alpha, \theta^{\text{SF}}, \phi^{\text{SF}}) v_{l_B;l_B;LQ}^{(\lambda)\mu'\mu}(R, r) \quad (3.2)$$

in a complete set of angular functions

$$\begin{aligned} \mathcal{C}_{(l_B)L,Q}(\beta, \alpha, \theta^{\text{SF}}, \phi^{\text{SF}}) &= \sum_{m m_B} C_{l,m}(\beta, \alpha) C_{l_B, m_B}(\theta^{\text{SF}}, \phi^{\text{SF}}) \\ &\times \langle l, m; l_B, m_B | L, Q \rangle, \end{aligned} \quad (3.3)$$

which are products of two Racah normalized spherical harmonics $C_{l,m}(\theta, \phi)$ coupled by means of Clebsch-Gordan coefficients $\langle l, m; l_B, m_B | L, Q \rangle$ [39].

The operators $|\lambda, \mu'\rangle \langle \lambda, \mu |$ are also coupled to a Clebsch-Gordan series to produce irreducible tensor operators

$$\widehat{T}_{L',Q'}^{(\lambda)} = \sum_{\mu'\mu} |\lambda, \mu'\rangle \langle \lambda, \mu | (-1)^{\lambda-\mu} \langle \lambda, \mu'; \lambda, -\mu | L', Q' \rangle. \quad (3.4)$$

The above definition holds both with respect to the SF frame and with respect to a body-fixed (BF) frame introduced below. The quantum number L' has always integer values, even if λ is half-integer. From the invariance of the total potential energy operator under overall rotations of the system A–B it follows then that the quantum numbers L' and Q' must be related to the quantum numbers L and Q of the coupled angular expansion functions as $L' = L$ and $Q' = -Q$. The expansion of the rotationally invariant potential energy operator reads

$$\widehat{V}^{(\lambda)} = \sum_{LQ} (-1)^Q \widehat{T}_{L,-Q}^{(\lambda)\text{SF}} \sum_{l_B} \mathcal{C}_{(l_B)L,Q}(\beta, \alpha, \theta^{\text{SF}}, \phi^{\text{SF}}) v_{l_B;L}^{(\lambda)}(R, r). \quad (3.5)$$

The choice of rotationally invariant expansion operators implies that the expansion coefficients do not depend on Q .

The intermolecular potential depends only on the internal coordinates which can be explicitly defined with the introduction of a body-fixed (BF) frame. A two-angle embedded BF frame is obtained by putting the z -axis along the vector \mathbf{R} , i.e., by rotation of the SF frame over the angles β, α . The diatom axis \mathbf{r} has the polar angles θ, ϕ in this frame, where θ is the angle between the vectors \mathbf{R} and \mathbf{r} . A fully embedded BF frame is obtained by a third rotation over the angle ϕ , which ensures that the diatom axis \mathbf{r} lies in the BF xz -plane. The coupled angular functions of Eq. (3.3), when transformed to the BF frame, are given by [17, 40]

$$\mathcal{C}_{(l_B)L,Q}(\beta, \alpha, \theta^{\text{SF}}, \phi^{\text{SF}}) = \sum_K \langle l, 0; l_B, K | L, K \rangle D_{Q,K}^{(L)}(\alpha, \beta, \phi) C_{l_B,K}(\theta, 0). \quad (3.6)$$

The function $D_{Q,K}^{(L)}(\alpha, \beta, \phi)$ is an element of the Wigner rotation matrix [39]. The diabatic basis $|\lambda, \mu\rangle$ and the irreducible tensors in Eq. (3.4) transform from the SF to the BF frame by the standard rotation rules. Substitution of these results into Eq. (3.5) and use of the properties [39] of Wigner D -functions yields the expansion of the potential with respect to the BF frame

$$\widehat{V}^{(\lambda)} = \sum_{LK} \widehat{T}_{L,-K}^{(\lambda)\text{BF}} \sum_{l_B} C_{l_B,K}(\theta, 0) v_{l_B;L,K}^{(\lambda)}(R, r). \quad (3.7)$$

The expansion coefficients in Eq. (3.7) are related to those in Eq. (3.5) as

$$v_{l_B;L,K}^{(\lambda)}(R, r) = (-1)^K \sum_l \langle l, 0; l_B, K | L, K \rangle v_{l;L}^{(\lambda)}(R, r). \quad (3.8)$$

The diabatic potentials that occur in a nonadiabatic dynamical treatment according to the ‘‘generalized BO model’’ are the matrix elements of the rotationally invariant potential energy operator $\widehat{V}^{(\lambda)}$ over the diabatic states $|\lambda, \mu\rangle$ with $\mu = -\lambda, \dots, \lambda$. They are most conveniently expressed in BF coordinates.

With the aid of Eq. (3.4) it follows from Eq. (3.7) that the diabatic potentials can be expanded as

$$V_{\mu',\mu}^{(\lambda)}(R, r, \theta) = \langle \lambda, \mu' | \widehat{V}^{(\lambda)} | \lambda, \mu \rangle^{\text{BF}} = \sum_{l_B} C_{l_B, \mu - \mu'}(\theta, 0) v_{l_B}^{(\lambda)\mu', \mu}(R, r) \quad (3.9)$$

with coefficients

$$v_{l_B}^{(\lambda)\mu', \mu}(R, r) = \sum_{LK} (-1)^{\lambda - \mu} \langle \lambda, \mu'; \lambda, -\mu | L, -K \rangle v_{l_B; L, K}^{(\lambda)}(R, r). \quad (3.10)$$

Only terms with $K = \mu - \mu'$ occur in this summation and the expansion of a given diabatic potential $V_{\mu',\mu}^{(\lambda)}(R, r, \theta)$ in Eq. (3.9) contains only spherical harmonics $C_{l_B, K}(\theta, 0)$ with $K = \mu - \mu'$. The index l_B runs from $|K|$ to infinity.

We also require that the potential energy operator is invariant under inversion: $\widehat{i} \widehat{V}^{(\lambda)} \widehat{i}^\dagger = \widehat{V}^{(\lambda)}$. The effect of inversion on the BF diabatic states is given in Ref. [41], cf. Sec. 5 in the Appendix of this publication. The irreducible tensor operators defined in Eq. (3.4) behave under inversion as $\widehat{i} \widehat{T}_{L, Q}^{(\lambda)\text{BF}} \widehat{i}^\dagger = (-1)^{L-Q} \widehat{T}_{L, -Q}^{(\lambda)\text{BF}}$. The angle θ does not change by inversion and the real angular functions in Eq. (3.7) obey the relation $C_{l_B, -K}(\theta, 0) = (-1)^K C_{l_B, K}(\theta, 0)$. When we apply inversion invariance to the expansion of the potential energy operator in Eq. (3.7) and use these relations, it becomes clear that the expansion coefficients must satisfy

$$v_{l_B; L, -K}^{(\lambda)}(R, r) = (-1)^L v_{l_B; L, K}^{(\lambda)}(R, r). \quad (3.11)$$

Then, with the aid of Eq. (3.10), one can show that the expansion coefficients of the diabatic potentials in Eq. (3.9) have the property

$$v_{l_B}^{(\lambda) - \mu', -\mu}(R, r) = v_{l_B}^{(\lambda)\mu', \mu}(R, r). \quad (3.12)$$

Finally, from the requirement that the potential energy operator $\widehat{V}^{(\lambda)}$ must be Hermitian it follows that

$$v_{l_B; L, K}^{(\lambda)}(R, r)^* = v_{l_B; L, -K}^{(\lambda)}(R, r) \quad (3.13)$$

and the expansion coefficients of the diabatic potentials in Eq. (3.9) obey the additional relation

$$v_{l_B}^{(\lambda)\mu', \mu}(R, r)^* = (-1)^{\mu' - \mu} v_{l_B}^{(\lambda)\mu, \mu'}(R, r). \quad (3.14)$$

Instead of the diabatic wavefunctions $|\lambda, \mu\rangle^{\text{BF}}$ one may use wavefunctions that are even or odd with respect to inversion \widehat{i} . This chapter deals with atom-diatom systems, the diabatic states $|\lambda, \mu\rangle$ are pure orbital angular momentum states, and the quantum number λ adopts integer values only. In the Appendix

of Ref. [41] it is shown that inversion with respect to the SF system is equivalent to the operation $\widehat{R}_y(\pi)\widehat{i}$ in the BF system. For purely spatial wavefunctions this operation is a reflection σ_{xz} with respect to the plane through the nuclei. It follows directly that the combinations

$$\left. \begin{aligned} |0\rangle &= |\lambda, 0\rangle^{\text{BF}} \quad \text{for } p + \lambda \text{ even} \\ |\mu+\rangle &= (|\lambda, -\mu\rangle^{\text{BF}} + (-1)^{p+\lambda-\mu} |\lambda, \mu\rangle^{\text{BF}}) / \sqrt{2} \end{aligned} \right\} \quad A' \text{ symmetry} \quad (3.15)$$

$$\left. \begin{aligned} |0\rangle &= |\lambda, 0\rangle^{\text{BF}} \quad \text{for } p + \lambda \text{ odd} \\ |\mu-\rangle &= i(|\lambda, -\mu\rangle^{\text{BF}} - (-1)^{p+\lambda-\mu} |\lambda, \mu\rangle^{\text{BF}}) / \sqrt{2} \end{aligned} \right\} \quad A'' \text{ symmetry}$$

(with $\mu > 0$) are symmetric (A') or antisymmetric (A'') under this reflection σ_{xz} . If the atom is in a P state, then $\lambda = 1$ and $\mu = -1, 0, 1$. For linear geometries ($\theta = 0$) the first function of A' symmetry describes a Σ state with respect to the intermolecular axis \mathbf{R} . The second function of A' symmetry and the function of A'' symmetry form the components of a twofold degenerate Π state. With the aid of Eqs. (3.12) and (3.14) one finds that the matrix elements, i.e., the diabatic potentials, in this basis are related (for $p + \lambda$ even) to the matrix elements in Eq. (3.9) by

$$\begin{aligned} \langle 0 | \widehat{V}^{(\lambda)} | 0 \rangle &= \langle \lambda, 0 | \widehat{V}^{(\lambda)} | \lambda, 0 \rangle^{\text{BF}} \\ \langle \mu'+ | \widehat{V}^{(\lambda)} | \mu+\rangle &= (-1)^{\mu'+\mu} \langle \lambda, \mu' | \widehat{V}^{(\lambda)} | \lambda, \mu \rangle^{\text{BF}} \\ &\quad + (-1)^{p+\lambda-\mu'} \langle \lambda, \mu' | \widehat{V}^{(\lambda)} | \lambda, -\mu \rangle^{\text{BF}} \\ \langle 0 | \widehat{V}^{(\lambda)} | \mu+\rangle &= (-1)^{p+\lambda-\mu} \sqrt{2} \langle \lambda, 0 | \widehat{V}^{(\lambda)} | \lambda, \mu \rangle^{\text{BF}} \\ \langle \mu'+ | \widehat{V}^{(\lambda)} | \mu-\rangle &= 0 \\ \langle 0 | \widehat{V}^{(\lambda)} | \mu-\rangle &= 0 \\ \langle \mu'- | \widehat{V}^{(\lambda)} | \mu-\rangle &= (-1)^{\mu'+\mu} \langle \lambda, \mu' | \widehat{V}^{(\lambda)} | \lambda, \mu \rangle^{\text{BF}} \\ &\quad - (-1)^{p+\lambda-\mu'} \langle \lambda, \mu' | \widehat{V}^{(\lambda)} | \lambda, -\mu \rangle^{\text{BF}}. \end{aligned} \quad (3.16)$$

So, when the diabatic states are adapted to symmetry A' and A'' the matrix $\mathbf{V}^{(\lambda)}(R, r, \theta)$ with elements given by the diabatic potentials becomes block-diagonal, with a 2×2 block of A' symmetry and a single matrix element of A'' symmetry. For odd values of $p + \lambda$ the state $|\lambda, 0\rangle^{\text{BF}}$ is of A'' symmetry and the nonzero matrix elements of this symmetry form a 2×2 block, while the A' symmetry block contains only one element in that case. Adiabatic potentials are, by definition, the eigenvalues of this matrix. The adiabatic states have either A' or A'' symmetry and can be obtained by separate diagonalizations of the corresponding symmetry blocks.

Sometimes, see Section 3.5, it is convenient to use the two-angle embedded BF frame instead of the BF frame obtained by the rotation $\widehat{R}(\alpha, \beta, \phi)$. Such a frame is obtained by the rotation $\widehat{R}(\alpha, \beta, 0)$ that directs the BF z -axis along

the vector \mathbf{R} . The irreducible tensor operators that correspond to the diabatic states in these two BF systems are related as

$$\widehat{T}_{L,-K}^{(\lambda)\text{BF}} = \exp(iK\phi)\widehat{T}_{L,-K}^{(\lambda)\text{BF},2}. \quad (3.17)$$

This additional factor depending on the angle ϕ can be put into the spherical harmonics $C_{l_B,K}(\theta, 0)$ in Eq. (3.7). Recalling that Eq. (3.10) yields $K = \mu - \mu'$ one finds that the expansion of the diabatic potentials

$$V_{\mu',\mu}^{(\lambda)}(R, r, \theta, \phi) = \langle \lambda, \mu' | \widehat{V}^{(\lambda)} | \lambda, \mu \rangle^{\text{BF},2} = \sum_{l_B} C_{l_B, \mu - \mu'}(\theta, \phi) v_{l_B}^{(\lambda)\mu', \mu}(R, r) \quad (3.18)$$

differs only slightly from the expansion in Eq. (3.9) for the fully BF system.

When molecule B is a general nonlinear molecule instead of a diatom we write \mathbf{q} for the internal coordinates instead of r . The diatom axis \mathbf{r} must be replaced by one of the molecule's principal axes, preferentially a symmetry axis (if present). An extra angle χ is needed to define the orientation of the molecule with respect to the BF frame. This angle corresponds to the rotation of the molecule about the principal axis chosen. When the molecule is a symmetric top its rotational states are labeled with an extra quantum number k_B , but also for a general nonlinear molecule the symmetric rotor functions labeled with (l_B, m_B, k_B) form a basis. The expansion of the intermolecular potential requires an extra summation over k_B . This quantum number is a spectator quantum number that is not involved in the angular momentum coupling. We obtain the same formula for the BF expansion of the diabatic potentials as in Eq. (3.18), except for the Racah spherical harmonics $C_{l_B,K}(\theta, \phi)$ that must be replaced by Wigner rotation functions $D_{K, k_B}^{(l_B)}(\phi, \theta, \chi)^*$

$$\begin{aligned} V_{\mu',\mu}^{(\lambda)}(R, \mathbf{q}, \phi, \theta, \chi) &= \langle \lambda, \mu' | \widehat{V}^{(\lambda)} | \lambda, \mu \rangle^{\text{BF},2} \\ &= \sum_{l_B k_B} D_{\mu - \mu', k_B}^{(l_B)}(\phi, \theta, \chi)^* v_{l_B, k_B}^{(\lambda)\mu', \mu}(R, \mathbf{q}). \end{aligned} \quad (3.19)$$

3.3 Long range interactions

For large distances R between the atom A and the (general) molecule B we can write the diabatic wavefunctions as $|\lambda, \mu\rangle^A |0\rangle^B$. For the intermolecular interaction operator \widehat{V} we can use the multipole expansion in spherical tensor form [16]. The diabatic potentials in the long range region are obtained by taking the $(2\lambda + 1)$ -dimensional matrix of the operator \widehat{V} over the diabatic basis $|\lambda, \mu\rangle^A |0\rangle^B$ with $\mu = -\lambda, \dots, \lambda$. The matrix elements [42] contain the atomic integrals $\langle \lambda, \mu' | \widehat{Q}_{m_A}^{(l_A)} | \lambda, \mu \rangle^A$ over the components ($m_A = -l_A, \dots, l_A$) of the multipole operator $\widehat{Q}_{m_A}^{(l_A)}$ with the basis $|\lambda, \mu\rangle^A$ on the open-shell atom A. These integrals can all be expressed in terms of a single atomic multipole

moment $Q^{(l_A)} = \langle \lambda, 0 | \widehat{Q}_0^{(l_A)} | \lambda, 0 \rangle^A$ by means of the Wigner-Eckart theorem [39]. They also contain expectation values of the multipole operators $\widehat{Q}_{k_B}^{(l_B)}$ over the ground state wavefunction $|0\rangle^B$, which are the permanent multipole moments $Q_{k_B}^{(l_B)}$ of molecule B. These multipole moments $Q_{k_B}^{(l_B)}$ are defined with respect to a reference frame on monomer B and are given with respect to the dimer BF frame by the equation $\widetilde{Q}_{m_B}^{(l_B)} = \sum_{k_B} Q_{k_B}^{(l_B)} D_{m_B, k_B}^{(l_B)}(\phi, \theta, \chi)^*$. The Euler angles (ϕ, θ, χ) relate the monomer frame on B to the two-angle embedded dimer BF frame. Finally, the multipole expansion contains spherical harmonics $C_{l_A+l_B, -m_A-m_B}(\beta, \alpha)$, which in the dimer BF frame with its z -axis along the vector \mathbf{R} are simply $C_{l_A+l_B, -m_A-m_B}(0, 0) = \delta_{m_A+m_B, 0}$. Substitution of the above relations into the multipole expanded diabatic potentials yields precisely Eq. (3.19) with expansion coefficients expressed in closed form

$$\begin{aligned} v_{l_B, k_B}^{(\lambda)\mu', \mu}(R, \mathbf{q}) &= \sum_{l_A} \left[\frac{(2l_A + 2l_B + 1)!}{(2l_A)!(2l_B)!} \right]^{\frac{1}{2}} (-1)^{l_A - \mu'} \begin{pmatrix} \lambda & l_A & \lambda \\ 0 & 0 & 0 \end{pmatrix}^{-1} \\ &\times \begin{pmatrix} l_A & l_B & l_A + l_B \\ \mu' - \mu & \mu - \mu' & 0 \end{pmatrix} \begin{pmatrix} \lambda & l_A & \lambda \\ -\mu' & \mu' - \mu & \mu \end{pmatrix} \\ &\times Q^{(l_A)} Q_{k_B}^{(l_B)} R^{-l_A - l_B - 1}. \end{aligned} \quad (3.20)$$

The quantities in large round brackets are 3- j symbols. Note that the molecular multipole moments $Q_{k_B}^{(l_B)}$ depend on the internal coordinates \mathbf{q} of B. For linear molecules B only terms with $k_B = 0$ are present and one obtains the expansion of Eq. (3.9).

For atom A in a P state, such as $F(2P)$, $Cl(2P)$, $Br(2P)$, the only non-vanishing multipole moment is the quadrupole Q_A , with $l_A = 2$. When B is a linear molecule with dipole d_B and quadrupole Q_B the dipole-quadrupole interaction matrix for the diabatic basis $|\lambda, \mu\rangle^{BF}$ with $\lambda = 1$ and $\mu = -1, 0, 1$ is

$$\mathbf{V}^{dq} = \begin{bmatrix} \frac{3}{2} P_{1,0} & \frac{3}{4} P_{1,1} \sqrt{2} & 0 \\ \frac{3}{4} P_{1,1} \sqrt{2} & -3 P_{1,0} & -\frac{3}{4} P_{1,1} \sqrt{2} \\ 0 & -\frac{3}{4} P_{1,1} \sqrt{2} & \frac{3}{2} P_{1,0} \end{bmatrix} \frac{Q_A d_B}{R^4} \quad (3.21)$$

with the associated Legendre functions $P_{1,0} = \cos \theta$ and $P_{1,1} = \sin \theta$. The quadrupole-quadrupole interaction matrix is

$$\mathbf{V}^{qq} = \begin{bmatrix} -3 P_{2,0} & -P_{2,1} \sqrt{2} & -\frac{1}{4} P_{2,2} \\ -P_{2,1} \sqrt{2} & 6 P_{2,0} & P_{2,1} \sqrt{2} \\ -\frac{1}{4} P_{2,2} & P_{2,1} \sqrt{2} & -3 P_{2,0} \end{bmatrix} \frac{Q_A Q_B}{R^5} \quad (3.22)$$

with the associated Legendre functions $P_{2,0} = \frac{1}{2}(3 \cos^2 \theta - 1)$, $P_{2,1} = 3 \sin \theta \cos \theta$, and $P_{2,2} = 3 \sin^2 \theta$.

For the diabatic basis $|0\rangle$, $|1+\rangle$ and $|1-\rangle$ adapted to inversion symmetry and with the assumption that $|0\rangle$ is of even parity the dipole-quadrupole interaction matrix is

$$\mathbf{V}^{dq} = \begin{bmatrix} -3P_{1,0} & \frac{3}{2}P_{1,1} & 0 \\ \frac{3}{2}P_{1,1} & \frac{3}{2}P_{1,0} & 0 \\ 0 & 0 & \frac{3}{2}P_{1,0} \end{bmatrix} \frac{Q_A d_B}{R^4}. \quad (3.23)$$

The quadrupole-quadrupole interaction matrix in the symmetry-adapted basis is

$$\mathbf{V}^{qq} = \begin{bmatrix} 6P_{2,0} & -2P_{2,1} & 0 \\ -2P_{2,1} & -3P_{2,0} + \frac{1}{4}P_{2,2} & 0 \\ 0 & 0 & -3P_{2,0} - \frac{1}{4}P_{2,2} \end{bmatrix} \frac{Q_A Q_B}{R^5}. \quad (3.24)$$

Observe that the off-diagonal matrix element V_{12} , called V_{xz} in Ref. [18], contains important long-range contributions which were overlooked in that reference.

3.4 Refit of the *ab initio* data

Three-dimensional diabatic potentials for $F(^2P)\text{-H}_2$ were calculated in Ref. [38]. After careful checking we found, however, that the analytical fit of these potentials given in Ref. [38] revealed unphysical behavior in the region with $R > 5.5 \text{ \AA}$ not covered by the *ab initio* calculations. Since this behavior would cause problems in the calculation of bound Van der Waals levels we decided to refit the *ab initio* data for $V_{0,0}^{(\lambda)}$, $V_{1,1}^{(\lambda)} = V_{-1,-1}^{(\lambda)}$ and $V_{1,-1}^{(\lambda)} = V_{-1,1}^{(\lambda)}$. The $V_{0,1}^{(\lambda)}$ diabatic surface of Ref. [38] behaves correctly and was kept. The quantum number λ is always 1 in the remainder of this chapter and from here on will be omitted from the notation of the potentials. Note that $-1 \leq \mu, \mu' \leq 1$.

The *ab initio* calculation of the potentials in Ref. [38] was performed for linear and T-shaped $F\text{-H}_2$ for a range of distances R and r . Three adiabatic (clamped nuclei) potential surfaces were obtained for each of these geometries. For the linear geometry these were labeled V^Σ and V^Π , the latter being twofold degenerate. For the T-shaped geometry they were labeled V^{A_1} , V^{B_1} , and V^{B_2} according to their C_{2v} symmetry. The procedure to fit the R and r dependence of the potentials $V^s(R, r)$ for each of these symmetries s was previously applied to the Cl-H_2 Van der Waals complex and described in detail in Ref. [43]. Briefly, the *ab initio* points for each value of r were fitted to the Esposti-Werner [44] functions of the variable R

$$V(R) = G(R) \exp(-a_1 R - a_2) - T(R) \sum_{n=5}^9 C_n R^{-n}, \quad (3.25)$$

where

$$G(R) = \sum_{j=0}^8 g_j R^j \quad (3.26)$$

and

$$T(R) = \frac{1}{2} \left(1 + \tanh(1 + tR) \right) \quad (3.27)$$

is a damping function. The parameters a_i , g_j , t , and C_n were optimized for each value of r with the modified Levenberg-Marquardt algorithm from the MINPACK set of routines for nonlinear least squares fitting. The smallest root mean square (rms) value of the fit was on the order of 0.001 cm^{-1} and usually the rms did not exceed 0.1 cm^{-1} . Then the potentials $V^s(R, r)$ for each symmetry $s = \Sigma, \Pi, A_1, B_1, B_2$ were expanded in a power series of fractional extensions $z = (r - r_e)/r_e$ of the H_2 bond length with respect to the equilibrium value $r_e = 1.400 \text{ a}_0$

$$V^s(R, r) = \sum_{p=0}^4 v_p^s(R) z^p. \quad (3.28)$$

Results for $V^s(R, r)$ were available for four values of z (in addition to $z = 0$) and to obtain the coefficients $v_p^s(R)$ for a given value of R we solved a system of four linear equations.

At the linear ($\theta = 0^\circ$) and T-shaped ($\theta = 90^\circ$) geometries, where the *ab initio* calculations were made, the symmetry is higher than the general C_s symmetry of the planar triatomic species that was used to adapt the diabatic states according to their reflection (A' or A'') behavior, see Eq. (3.15). The Σ state and the in-plane Π state of the linear geometry obtain A' symmetry when the system is bent and the out-of-plane Π state obtains A'' symmetry. For the T-shaped (C_{2v}) geometry the A_1 and B_2 states correlate with A' symmetry in C_s and the B_1 state with A'' symmetry. Because of the higher symmetry at these specific geometries there is no coupling between the two diabatic states of A' symmetry, i.e., the coupling potential $V_{0,1}(R, r, \theta)$ must vanish for $\theta = 0^\circ$ and 90° , cf. Eq. (3.16). Therefore, the diabatic states at these geometries are the same as the adiabatic states. For the linear geometry the diabatic potentials $V_{0,0}$ and $V_{1+,1+}$ of A' symmetry correspond to the adiabatic potentials V^Σ and V^Π , respectively, and the diabatic potential $V_{1-,1-}$ of A'' symmetry also corresponds to V^Π . For the T-shaped geometry the two diabatic potentials of A' symmetry correspond to the adiabatic potentials V^{A_1} and V^{B_2} and the A'' diabatic potential to V^{B_1} .

The expansion of the diabatic potentials $V_{\mu',\mu}(R, r, \theta)$ in Racah normalized spherical harmonics $C_{l_B, \mu-\mu'}(\theta, 0)$ is given in Eq. (3.9). Only terms with even values of l_B occur in this expansion because H_2 is homonuclear. On the basis of experience with rare gas- H_2 complexes [45, 46, 47, 48] the terms with $l_B \geq 4$ in this expansion may be neglected. When the terms with $l_B = 0$ and $l_B = 2$ are substituted into the righthand side of Eq. (3.16) with the values of the Racah

spherical harmonics $C_{l_B, \mu-\mu'}(\theta, 0)$ at $\theta = 0^\circ$ and $\theta = 90^\circ$ for the linear and T-shaped geometries, respectively, the diabatic potentials of A' and A'' symmetry become simple linear combinations of the expansion coefficients $v_{l_B}^{\mu', \mu}(R, r)$. Setting these potentials equal to the corresponding adiabatic potentials and using the symmetry relations for the expansion coefficients—Eqs. (3.12) and (3.14)—gives simple sets of linear equations that are easily solved to find

$$\begin{aligned} v_0^{0,0}(R, r) &= \frac{1}{3} \left[2V^{A_1}(R, r) + V^\Sigma(R, r) \right] \\ v_2^{0,0}(R, r) &= \frac{2}{3} \left[V^\Sigma(R, r) - V^{A_1}(R, r) \right] \end{aligned} \quad (3.29)$$

$$\begin{aligned} v_0^{1,1}(R, r) &= v_0^{-1,-1}(R, r) = \frac{1}{3} \left[V^{B_1}(R, r) + V^{B_2}(R, r) + V^\Pi(R, r) \right] \\ v_2^{1,1}(R, r) &= v_2^{-1,-1}(R, r) = \frac{1}{3} \left[2V^\Pi(R, r) - V^{B_1}(R, r) + V^{B_2}(R, r) \right] \end{aligned} \quad (3.30)$$

$$v_2^{1,-1}(R, r) = v_2^{-1,1}(R, r) = \frac{2}{\sqrt{6}} \left[V^{B_1}(R, r) - V^{B_2}(R, r) \right]. \quad (3.31)$$

Hence, the expansion coefficients of the diabatic potentials $V_{\mu', \mu}(R, r, \theta)$ can be directly obtained from the fitted adiabatic potentials $V^s(R, r)$.

The diabatic coupling potential,

$$V_{0,1}(R, r, \theta) = V_{-1,0}(R, r, \theta) = -V_{1,0}(R, r, \theta) = -V_{0,-1}(R, r, \theta),$$

cannot be extracted from these calculations, because it vanishes both at the linear and T-shaped geometries. It was calculated for a number of angles θ and expanded in spherical harmonics $C_{l_B, 1}(\theta, 0)$ by means of Gauss-Legendre quadrature. Note, however, that the potential expanded in Ref. [38] refers to a diabatic basis adapted to symmetry A' and A'' and corresponds to the matrix element $V_{0,1+}(R, r, \theta)$ of Eq. (3.16). Equation (3.16) shows that $V_{0,1}(R, r, \theta) = -V_{0,1+}(R, r, \theta)/\sqrt{2}$.

The refitted potentials are plotted in Figs. 3.1, 3.2, 3.3, and 3.4. They are free from artifacts in the long range and can be safely used in bound state calculations. They are available upon request from J. Klos; also requests for the potential from Ref. [38] will be fulfilled by sending the refitted ones. In these figures we also plotted the empirical potentials of Aquilanti *et al.* [32] obtained from elastic F-H₂ scattering cross sections. The diabat $V_{0,0}$ has a global minimum for the T-shaped geometry. In our potential the position of this minimum is at $R_e = 4.71$ a₀ with well depth $D_e = 141.4$ cm⁻¹, whereas in the potential of Aquilanti *et al.* this minimum occurs at $R_e = 5.08$ a₀ and is deeper with $D_e = 157.03$ cm⁻¹. The global minimum in the diabat $V_{1,1}$ occurs for the collinear geometry. In our potential this minimum is located at

Figure 3.1: Contour plots of the diabatic potentials $V_{0,0}$ Upper panel: Klos *et al.* [38] and this work. Lower panel: Aquilanti *et al.* [32].

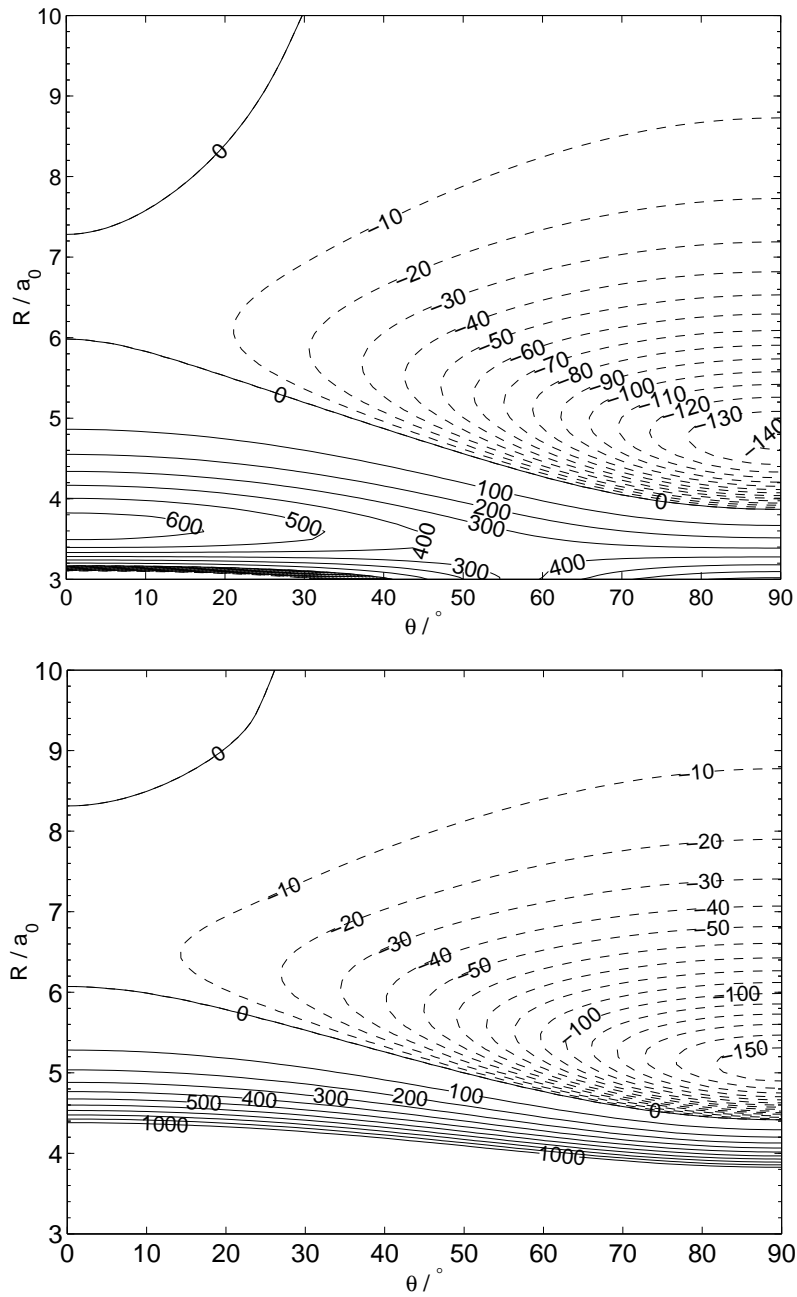


Figure 3.2: Contour plots of the diabatic potentials $V_{1,1} = [V_{1+,1+} + V_{1-,1-}]/2$. Upper panel: Kłos *et al.* [38] and this work. Lower panel: Aquilanti *et al.* [32].

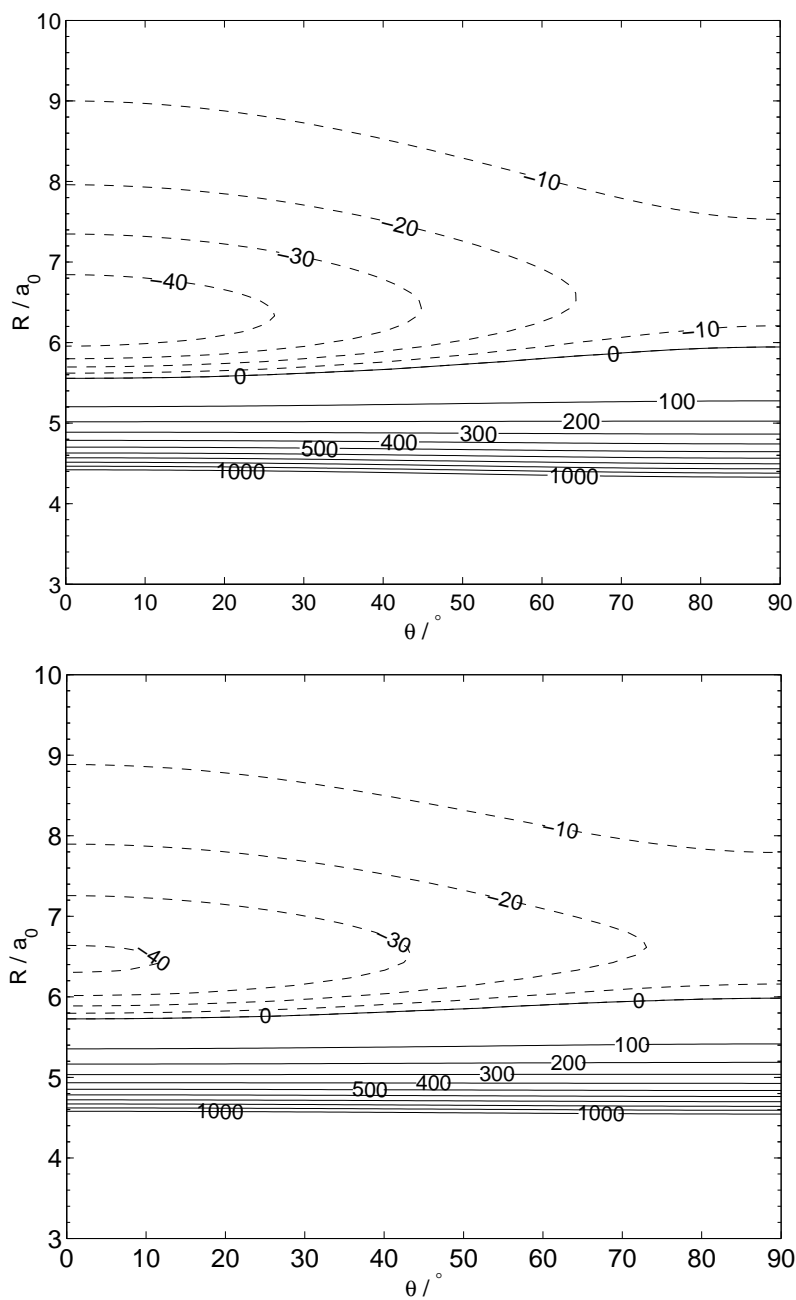


Figure 3.3: Contour plots of the diabatic potential $V_{1,-1} = [V_{1+,1+} - V_{1-,1-}]/2$. Upper panel: Klos *et al.* [38] and this work. Lower panel: Aquilanti *et al.* [32].

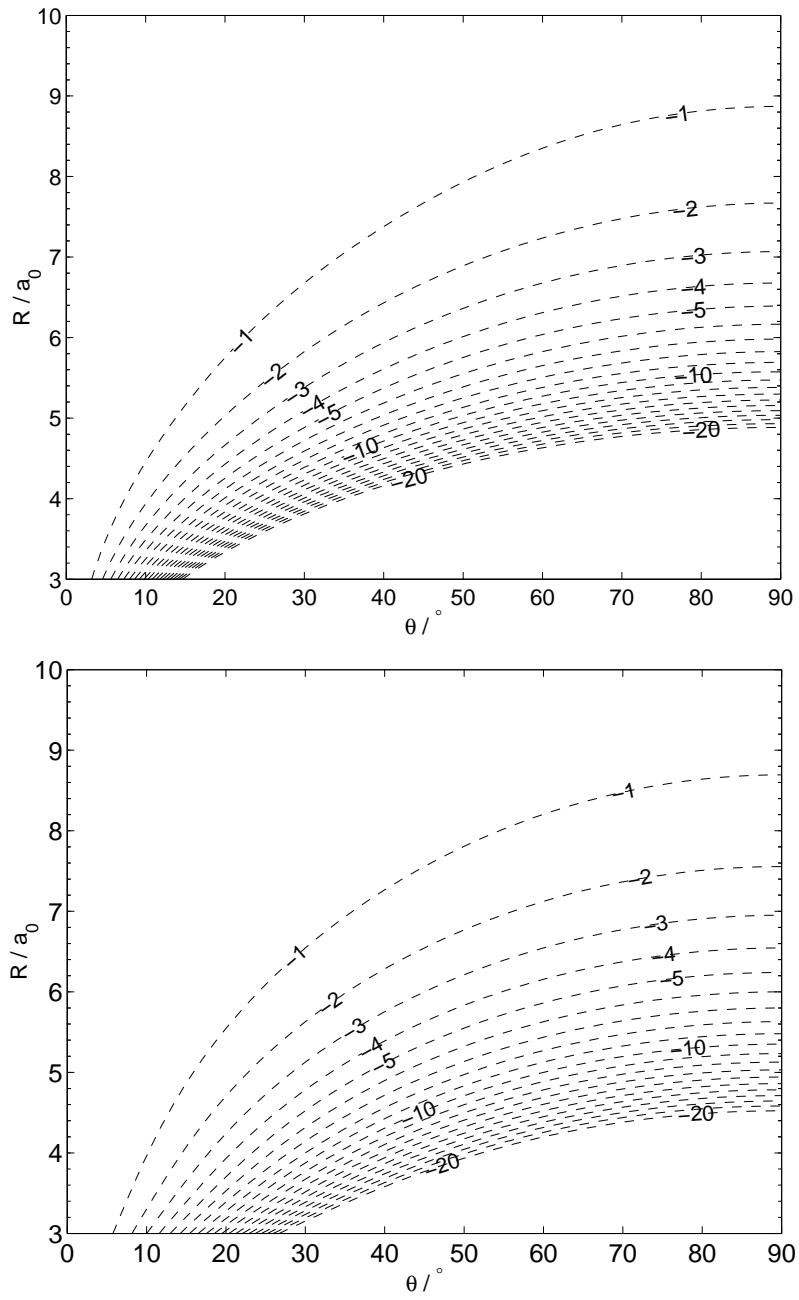
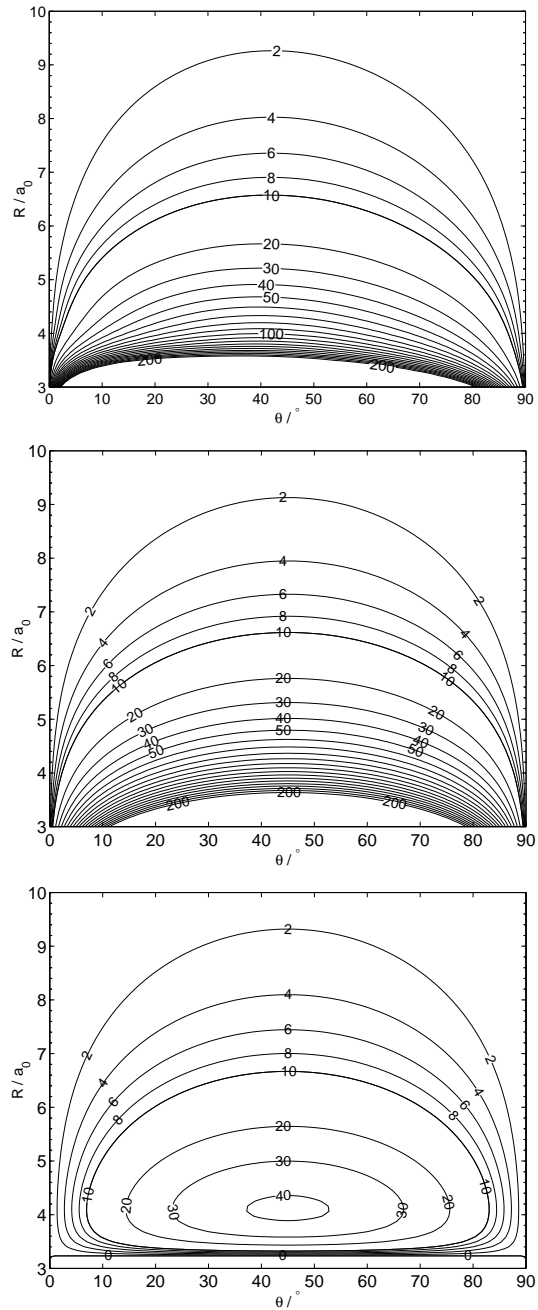


Figure 3.4: Contour plots of the diabatic coupling potential $V_{0,1} = -V_{0,1+}/\sqrt{2}$. Top panel: Klos *et al.* [38] and this work. Middle panel: Long range quadrupole-quadrupole term only. Bottom panel: Aquilanti *et al.* [32].



$R_e = 6.33 \text{ a}_0$ with $D_e = 46.76 \text{ cm}^{-1}$, while the potential of Aquilanti *et al.* has its minimum at $R_e = 6.46 \text{ a}_0$ with $D_e = 41.05 \text{ cm}^{-1}$. The diabat $V_{1,-1}$ in Fig. 3.3 is the small difference $[V_{1+,1+} - V_{1-,1-}]/2$. Also this diabat is quite similar for the two potentials. The off-diagonal coupling term $V_{0,1}$ in Fig. 3.4 again shows larger differences between our potential and that of Aquilanti *et al.*. Comparison of the upper two panels of this figure makes it clear that the behavior of this diabatic coupling potential is completely dominated by the long range quadrupole-quadrupole interaction—see Eq. (3.22)—a contribution that was overlooked in Ref. [18].

3.5 Bound state calculations

The bound state calculations on $F(^2P)\text{-H}_2$ are most conveniently performed in a two-angle embedded BF frame with the z -axis along the vector \mathbf{R} from the F-atom to the H_2 center of mass. The H–H bond axis \mathbf{r} has the polar angles (θ, ϕ) with respect to this frame. The H_2 vibration is very fast and can be adiabatically separated from the intermolecular motions in the $F\text{-H}_2$ complex. Actually, which is almost equivalent [49], we froze the H–H bond length at its ground state vibrationally averaged value $r = 1.44836 \text{ a}_0$ and used the vibrationally averaged value $b_0 = 59.336322 \text{ cm}^{-1}$ of the H_2 rotational constant. For comparison we also performed some calculations with the potential averaged over the H_2 ground state ($v = 0$) vibration and with the H–H bond length frozen at its equilibrium value $r_e = 1.40112 \text{ a}_0$ and $b_e = 60.853119 \text{ cm}^{-1}$.

In the two-angle BF representation the nuclear motion Hamiltonian reduces to

$$\begin{aligned} \hat{H} &= \frac{-\hbar^2}{2\mu_{AB}R} \frac{\partial^2}{\partial R^2} R + \frac{(\hat{\mathbf{j}}_A + \hat{\mathbf{j}}_B)^2 - 2(\hat{\mathbf{j}}_A + \hat{\mathbf{j}}_B) \cdot \hat{\mathbf{J}} + \hat{\mathbf{J}}^2}{2\mu_{AB}R^2} + b_0 \hat{j}_B^2 + A \hat{\boldsymbol{\lambda}} \cdot \hat{\mathbf{S}} \\ &+ \sum_{\mu', \mu} | \lambda, \mu' \rangle V_{\mu', \mu}(R, \theta, \phi) \langle \lambda, \mu | \end{aligned} \quad (3.32)$$

where μ_{AB} is the reduced mass of the complex and $A = -2D_{\text{SO}}/3$ is the spin-orbit coupling constant of the $F(^2P)$ atom. The operators $\hat{\boldsymbol{\lambda}}$ and $\hat{\mathbf{S}}$ are the orbital and spin angular momentum of the F-atom, $\hat{\mathbf{j}}_A = \hat{\boldsymbol{\lambda}} + \hat{\mathbf{S}}$ represents the total atomic angular momentum. The operator $\hat{\mathbf{j}}_B$ is the rotational angular momentum of the H_2 molecule and $\hat{\mathbf{J}}$ the total angular momentum of the complex. The diabatic states of the $F(^2P)\text{-H}_2$ complex that correlate with the corresponding states of the $F(^2P)$ atom are labeled with the quantum numbers (λ, μ) , where $\lambda = 1$ and $\mu = -1, 0, 1$ is the projection of $\hat{\boldsymbol{\lambda}}$ on the BF z -axis \mathbf{R} . The potentials $V_{\mu', \mu}(R, \theta, \phi)$ are the diabatic interaction potentials in a two-angle embedded BF frame described in Section 3.2, Eq. (3.18). The expansion coefficients are the same as in the three-angle embedded frame, cf. Eq. (3.9). These expansion coefficients are obtained from the expansion of the three-dimensional potentials in Section 3.4 by fixing r at 1.40112 a_0 .

Because of the large spin-orbit coupling $D_{SO} = 404 \text{ cm}^{-1}$ of $F(^2P)$ we used a coupled atomic basis set

$$|j_A \omega_A\rangle \equiv |(\lambda S) j_A \omega_A\rangle = \sum_{\mu, \sigma} |\lambda, \mu\rangle |S, \sigma\rangle \langle \lambda, \mu; S, \sigma | j_A, \omega_A\rangle \quad (3.33)$$

in which the spin-orbit term in the Hamiltonian $\widehat{\boldsymbol{\lambda}} \cdot \widehat{\boldsymbol{S}} = (\widehat{j}_A^2 - \widehat{\lambda}^2 - \widehat{S}^2)/2$ is diagonal. Since $\lambda = 1$ and $S = \frac{1}{2}$, one finds that $j_A = \frac{1}{2}$ or $\frac{3}{2}$. The two-angle embedded BF basis for the complex reads

$$|n, j_A, \omega_A, j_B, \omega_B, \Omega\rangle = |n\rangle \left[\frac{2J+1}{4\pi} \right]^{1/2} |j_A \omega_A\rangle Y_{j_B, \omega_B}(\theta, \phi) D_{M, \Omega}^{(J)}(\alpha, \beta, 0)^* \quad (3.34)$$

The spherical harmonics $Y_{j_B, \omega_B}(\theta, \phi)$ describe the rotation of the H_2 monomer and the symmetric rotor functions $D_{M, \Omega}^{(J)}(\alpha, \beta, 0)^*$ the overall rotation of the complex. The exact quantum numbers J, M are omitted from the shorthand notation on the lefthand side. Remember that (β, α) are the polar angles of the BF z -axis \boldsymbol{R} with respect to a SF coordinate system. The components along this axis obey the relation $\Omega = \omega_A + \omega_B$. The radial basis functions $|n\rangle = \chi_n(R)$ are Morse oscillator type functions defined in Ref. [50].

The matrix elements of the Hamiltonian in Eq. (3.32) over the basis in Eq. (3.34) are

$$\begin{aligned} & \langle n', j'_A, \omega'_A, j'_B, \omega'_B, \Omega' | \widehat{H} | n, j_A, \omega_A, j_B, \omega_B, \Omega \rangle \quad (3.35) \\ &= \delta_{j'_A, j_A} \delta_{j'_B, j_B} \delta_{\omega'_A, \omega_A} \delta_{\omega'_B, \omega_B} \delta_{\Omega', \Omega} \left[\langle n' | \frac{-\hbar^2}{2\mu_{AB}R} \frac{\partial^2}{\partial R^2} R | n \rangle \right. \\ &+ \langle n' | \frac{1}{2\mu_{AB}R^2} | n \rangle \left(j_A(j_A+1) + j_B(j_B+1) + J(J+1) - \omega_A^2 - \omega_B^2 - \Omega^2 \right) \\ &+ \delta_{n', n} \left\{ b_0 j_B(j_B+1) + \frac{1}{2} A \left(j_A(j_A+1) - \lambda(\lambda+1) - S(S+1) \right) \right\} \Big] \\ &+ \delta_{j'_A, j_A} \delta_{j'_B, j_B} \langle n' | \frac{1}{2\mu_{AB}R^2} | n \rangle \left[C_{\omega'_A, \omega_A+1}^{j'_A} C_{\omega'_B, \omega_B-1}^{j'_B} + C_{\omega'_A, \omega_A-1}^{j'_A} C_{\omega'_B, \omega_B+1}^{j'_B} \right. \\ &- C_{\Omega', \Omega+1}^J \left(C_{\omega'_A, \omega_A+1}^{j'_A} + C_{\omega'_B, \omega_B+1}^{j'_B} \right) - C_{\Omega', \Omega-1}^J \left(C_{\omega'_A, \omega_A-1}^{j'_A} + C_{\omega'_B, \omega_B-1}^{j'_B} \right) \Big] \\ &+ \sum_{\mu', \mu} \langle n', j'_A, \omega'_A, j'_B, \omega'_B, \Omega' | \lambda, \mu' \rangle V_{\mu', \mu}(R, \theta, \phi) \langle \lambda, \mu | n, j_A, \omega_A, j_B, \omega_B, \Omega \rangle \end{aligned}$$

with $C_{\omega', \omega \pm 1}^j = \delta_{\omega', \omega \pm 1} [j(j+1) - \omega(\omega \pm 1)]^{1/2}$.

The expansion of the diabatic potential surfaces $V_{\mu', \mu}(R, \theta, \phi)$ in terms of Racah normalized spherical harmonics $C_{l, m}(\theta, \phi)$ is given by Eq. (3.18). With

Eq. (3.33) for the coupled atomic basis the potential matrix elements are

$$\begin{aligned}
& \langle n', j'_A, \omega'_A, j'_B, \omega'_B, \Omega' | \lambda, \mu' \rangle V_{\mu', \mu}(R, \theta, \phi) \langle \lambda, \mu | n, j_A, \omega_A, j_B, \omega_B, \Omega \rangle \\
& = (-1)^{2(\lambda-S)+\omega'_B+\omega'_A+\omega_A} [(2j'_A+1)(2j_A+1)(2j'_B+1)(2j_B+1)]^{1/2} \\
& \times \begin{pmatrix} \lambda & S & j'_A \\ \mu' & \sigma & -\omega'_A \end{pmatrix} \begin{pmatrix} \lambda & S & j_A \\ \mu & \sigma & -\omega_A \end{pmatrix} \\
& \times \sum_{l_B} \langle n' | v_{l_B}^{\mu', \mu}(R) | n \rangle \begin{pmatrix} j'_B & l_B & j_B \\ 0 & 0 & 0 \end{pmatrix} \begin{pmatrix} j'_B & l_B & j_B \\ -\omega'_B & \mu - \mu' & \omega_B \end{pmatrix}. \quad (3.36)
\end{aligned}$$

In addition to J and M there are two exact quantum numbers: the parity of the states of the complex under inversion \hat{i} and the even/odd parity of j_B . Even j_B refers to *para*-H₂, odd j_B to *ortho*-H₂ states. The effect of inversion on the basis is

$$\hat{i} | n, j_A, \omega_A, j_B, \omega_B, \Omega \rangle = (-1)^{\lambda-j_A+J} | n, j_A, -\omega_A, j_B, -\omega_B, -\Omega \rangle. \quad (3.37)$$

This property can be used to construct a parity-adapted basis or to inspect the parity of the wavefunctions obtained by diagonalization of the Hamiltonian matrix when the basis is not parity-adapted beforehand.

3.5.1 Computational details

The bound states were obtained from a full diagonalization of the Hamiltonian matrix using the LAPACK routines of MATLAB 6 [51] and optimization toolboxes. Calculations were performed for J up to $\frac{11}{2}$ inclusive, which provides all the bound states. The levels were converged to within about 10^{-4} cm⁻¹ with a basis truncated at $j_{B_{\max}} = 5$. This gives $j_B = 0, 2, 4$ for *para*-H₂ and $j_B = 1, 3, 5$ for *ortho*-H₂. The radial basis $\chi_n(R)$ consisted of 50 functions ($n_{\max} = 49$); the nonlinear parameters $R_e = 13.5$ a₀, $D_e = 132.5$ cm⁻¹ and $\omega_e = 35.0$ cm⁻¹ in this basis were optimized in energy minimizations with smaller values of n_{\max} .

We tested our program by constructing simple model diabatic potentials that consist of an isotropic Morse potential and the anisotropic electrostatic quadrupole-quadrupole term. This model produces directly the analytical form of the diabatic potentials $V_{\mu', \mu}(R, \theta, \phi)$ for all μ' and $\mu = -1, 0, 1$, see Eq. (3.22) in Section 3.3. We coded the computation of the Hamiltonian matrix and its eigenvalues in a fully coupled basis in space-fixed coordinates with the formulas from Ref. [19, 20], as well as in the spin-orbit coupled BF basis of Eqs. (3.33) and (3.34). The eigenvalues agree to machine accuracy. Furthermore, we performed the calculation of the bound levels in this model potential and the levels of F-H₂ with the HIBRIDON 4.1 [52] suite of programs. The definitions of the diabatic potentials that HIBRIDON needs as input are given in Ref. [18]. We discovered that the potential $V_{xz}(R, \theta)$ occurring in Table I of Ref. [18] should

be divided by $2^{1/2}$ instead of multiplied by this factor, and that the HIBRIDON input potential $V_d(R, \theta)$ does not correspond to $(V_{yy} - V_{xx})/2$ as in Eq. (23) of Ref. [18] but, instead, to $(V_{xx} - V_{yy})/2$. With these changes in the input HIBRIDON produced results that were in perfect agreement with those from our programs.

3.6 Results and discussion

The complete set of rovibrational energies of the F–H₂ Van der Waals complex is given in Table 3.1. Figure 3.5 represents the levels graphically. The potential that we used produces no bound states for quantum numbers J larger than $\frac{9}{2}$ for *para*-H₂ and for J larger than $\frac{11}{2}$ for *ortho*-H₂. The binding energy D_0 of the *para*-H₂ complex is 14.6 cm^{-1} ; the *ortho*-H₂ complex is bound by 19.3 cm^{-1} . For comparison we note that the well depth D_e of the lowest adiabatic potential (with $\theta = 90^\circ$) is 141.4 cm^{-1} and the well depth of the lowest adiabatic potential with the spin-orbit coupling included is 67.8 cm^{-1} (also for $\theta = 90^\circ$) [38]. Hence, this complex contains a substantial amount of zero-point energy.

In order to test the effect of freezing the H₂ bond length at the vibrationally averaged value $r_0 = 1.44836 a_0$ we also performed computations with the H₂ bond length frozen at $r_e = 1.40112 a_0$ and with the three-dimensional diabatic potentials averaged over the ground vibrational ($v = 0$) wavefunction of H₂. The well depth of the lowest adiabatic potential without spin-orbit coupling is 133.1 cm^{-1} for $r = r_e$, 141.4 cm^{-1} for $r = r_0$, and 142.3 cm^{-1} for the vibrationally averaged case. With the inclusion of spin-orbit coupling the well depths of the lowest adiabatic potential are 64.5 cm^{-1} , 67.8 cm^{-1} , and 68.2 cm^{-1} , respectively. The lowest bound levels are higher by about 1.2 cm^{-1} than the levels reported in Table 3.1 and Fig. 3.5 when we change r from r_0 to r_e and lower by about 0.2 cm^{-1} for the vibrationally averaged potential. These changes become smaller when the levels approach the dissociation threshold. Especially the changes in going from r_e to r_0 are substantial; this is related to the presence of a chemically bound energy minimum for the linear F–H–H geometry. The depth of this chemical minimum and the barrier that separates it from the Van der Waals minimum are strongly dependent on r [38] and also the depth of the latter minimum depends rather sensitively on r .

Takayanagi and Kurosaki [37] reported Van der Waals resonances in the cumulative reaction probabilities for the F–H₂ system. In order to characterize these resonances they employed the Stark-Werner potential [53] for F–H₂, obtained one-dimensional potential curves by averaging the diabatic potentials over the $^2P_{3/2}$ ground state of the free F-atom and over the rovibrational states (v, j) of free H₂, and then solved the one-dimensional Schrödinger equation for each curve separately. From Fig. 3 of their paper [37] one can estimate their value of D_0 . It is 12 to 14 cm^{-1} for the *para*-H₂ complex which, in spite of

Figure 3.5: Bound levels of $F(^2P)\text{-H}_2$ for *para* and *ortho* H_2 and both \pm parities.

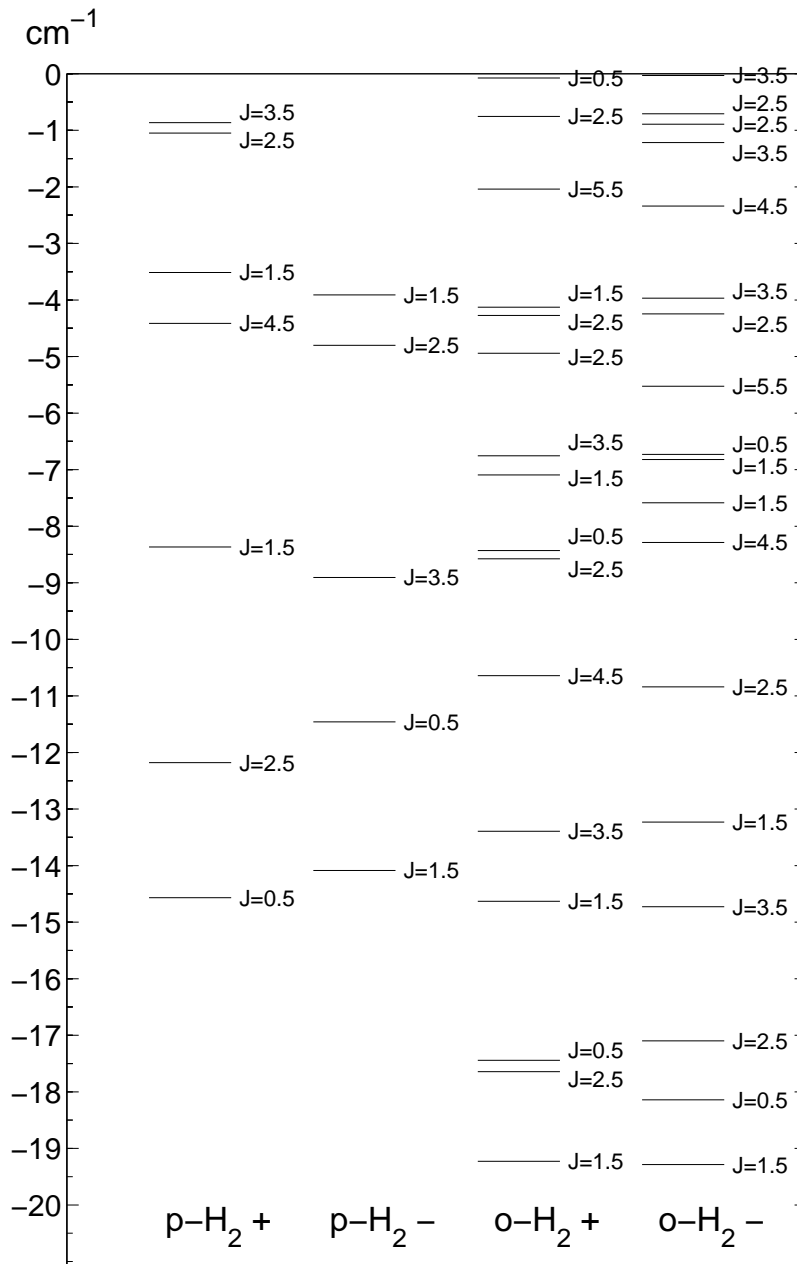


Table 3.1: Bound states of $F\text{-H}_2$ for $J = \frac{1}{2}$ up to $\frac{11}{2}$. Energies are in cm^{-1} relative to the energy of separated $F(^2P_{3/2})$ and $\text{H}_2(j = 0)$ in the case of *para* states and $\text{H}_2(j = 1)$ for *ortho* states. Parities (+/-) of the eigenstates are indicated in parentheses.

$J = \frac{1}{2}$	$J = \frac{3}{2}$	$J = \frac{5}{2}$	$J = \frac{7}{2}$	$J = \frac{9}{2}$	$J = \frac{11}{2}$
<i>para</i> - H_2					
-14.568 (+)	-14.086 (-)	-12.179 (+)	-8.907 (-)	-4.414 (+)	
-11.460 (-)	-8.367 (+)	-4.802 (-)	-0.864 (+)		
	-3.912 (-)	-1.050 (+)			
	-3.515 (+)				
<i>ortho</i> - H_2					
-18.140 (-)	-19.287 (-)	-17.644 (+)	-14.728 (-)	-10.642 (+)	-5.525 (-)
-17.442 (+)	-19.227 (+)	-17.098 (-)	-13.393 (+)	-8.287 (-)	-2.039 (+)
-8.431 (+)	-14.632 (+)	-10.841 (-)	-6.755 (+)	-2.340 (-)	
-6.731 (-)	-13.230 (-)	-8.576 (+)	-3.967 (-)		
-0.074 (+)	-7.586 (-)	-4.941 (+)	-1.216 (-)		
	-7.094 (+)	-4.273 (+)	-0.031 (-)		
	-6.820 (-)	-4.245 (-)			
	-4.129 (+)	-0.893 (-)			
		-0.756 (+)			
		-0.707 (-)			

their approximations, is quite close to our result. But they find a substantially smaller value of D_0 for the *ortho*- H_2 complex, whereas we find a larger value. This must be due to their rotational averaging over the unperturbed $j = 1$ state of *ortho*- H_2 , while in our treatment the *ortho*- H_2 monomer can use its $\omega = -1, 0, 1$ components to adopt the most favorable orientation in the complex. Table 3.2 gives the character of the eigenvectors for $J = \frac{1}{2}, \frac{3}{2},$ and $\frac{5}{2}$ expressed in the spin-orbit coupled basis and Figs. 3.6 and 3.7 show density contours of the $J = \frac{1}{2}$ bound states of the *para* and *ortho* $\text{H}_2\text{-F}$ complex. These densities are obtained by integration of the absolute square of the wavefunction over all coordinates except R and θ . They are displayed as functions of $z = R \cos \theta$ and $x = R \sin \theta$, the Cartesian coordinates of the F atom, with the horizontal z axis representing the H_2 bond axis and the origin at the center of mass of the hydrogen molecule. We show only the densities of the bound states of + parity, as there is very little difference with the corresponding states of -

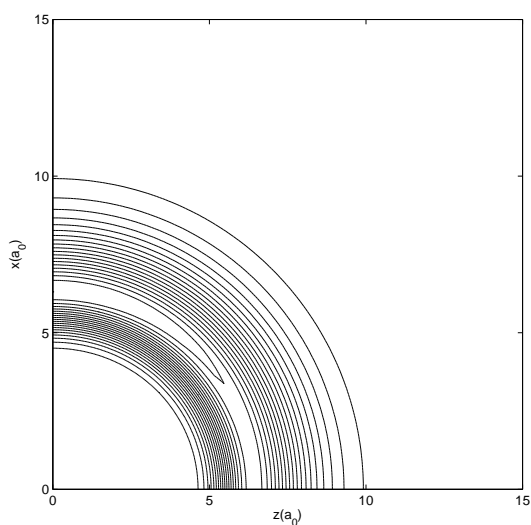
Table 3.2: Character of the bound states in Table 3.1 for $J = \frac{1}{2}$ up to $\frac{5}{2}$, in terms of the parity-adapted basis with quantum numbers $|\omega_A|, |\omega_B|, |\Omega|, \pm\rangle$. All these low lying states have $j_A = \frac{3}{2}$, with $j_B = 0$ for *para*-H₂ and $j_B = 1$ for *ortho*-H₂. Only the most important basis functions are indicated. The label \pm denotes the overall parity of the eigenvector.

	<i>para</i> -H ₂	<i>ortho</i> -H ₂
$J = \frac{1}{2}$	99% $ \frac{1}{2}, 0, \frac{1}{2}, +\rangle$ 99% $ \frac{1}{2}, 0, \frac{1}{2}, -\rangle$	96% $ \frac{1}{2}, 1, \frac{1}{2}, -\rangle$ 98% $ \frac{1}{2}, 1, \frac{1}{2}, +\rangle$ 69% $ \frac{1}{2}, 0, \frac{1}{2}, +\rangle$, 31% $ \frac{3}{2}, 1, \frac{1}{2}, +\rangle$ 54% $ \frac{1}{2}, 0, \frac{1}{2}, -\rangle$, 46% $ \frac{3}{2}, 1, \frac{1}{2}, -\rangle$ 77% $ \frac{3}{2}, 1, \frac{1}{2}, +\rangle$, 21% $ \frac{1}{2}, 0, \frac{1}{2}, +\rangle$
$J = \frac{3}{2}$	96% $ \frac{1}{2}, 0, \frac{1}{2}, -\rangle$ 86% $ \frac{1}{2}, 0, \frac{1}{2}, +\rangle$ 97% $ \frac{3}{2}, 0, \frac{3}{2}, -\rangle$ 87% $ \frac{3}{2}, 0, \frac{3}{2}, +\rangle$	66% $ \frac{1}{2}, 1, \frac{3}{2}, -\rangle$, 28% $ \frac{1}{2}, 1, \frac{1}{2}, -\rangle$ 60% $ \frac{1}{2}, 1, \frac{3}{2}, +\rangle$, 37% $ \frac{1}{2}, 1, \frac{1}{2}, +\rangle$ 55% $ \frac{1}{2}, 1, \frac{1}{2}, +\rangle$, 31% $ \frac{1}{2}, 1, \frac{3}{2}, +\rangle$ 69% $ \frac{1}{2}, 1, \frac{1}{2}, -\rangle$, 22% $ \frac{1}{2}, 1, \frac{3}{2}, -\rangle$ 51% $ \frac{3}{2}, 0, \frac{3}{2}, -\rangle$, 34% $ \frac{1}{2}, 0, \frac{1}{2}, -\rangle$ 90% $ \frac{3}{2}, 0, \frac{3}{2}, +\rangle$ 39% $ \frac{3}{2}, 0, \frac{3}{2}, -\rangle$, 35% $ \frac{1}{2}, 0, \frac{1}{2}, -\rangle$, 27% $ \frac{3}{2}, 1, \frac{1}{2}, -\rangle$ 56% $ \frac{3}{2}, 1, \frac{1}{2}, +\rangle$, 43% $ \frac{1}{2}, 0, \frac{1}{2}, +\rangle$
$J = \frac{5}{2}$	93% $ \frac{1}{2}, 0, \frac{1}{2}, +\rangle$ 60% $ \frac{1}{2}, 0, \frac{1}{2}, -\rangle$, 40% $ \frac{3}{2}, 0, \frac{3}{2}, -\rangle$ 93% $ \frac{3}{2}, 0, \frac{3}{2}, +\rangle$	58% $ \frac{1}{2}, 1, \frac{3}{2}, +\rangle$, 30% $ \frac{1}{2}, 1, \frac{1}{2}, +\rangle$ 55% $ \frac{1}{2}, 1, \frac{3}{2}, -\rangle$, 40% $ \frac{1}{2}, 1, \frac{1}{2}, -\rangle$ 44% $ \frac{1}{2}, 1, \frac{1}{2}, -\rangle$, 24% $ \frac{1}{2}, 1, \frac{3}{2}, -\rangle$, 17% $ \frac{3}{2}, 0, \frac{3}{2}, -\rangle$ 57% $ \frac{1}{2}, 1, \frac{1}{2}, +\rangle$, 15% $ \frac{3}{2}, 0, \frac{3}{2}, +\rangle$ 60% $ \frac{3}{2}, 0, \frac{3}{2}, +\rangle$, 22% $ \frac{1}{2}, 1, \frac{3}{2}, +\rangle$ 52% $ \frac{1}{2}, 0, \frac{1}{2}, +\rangle$, 27% $ \frac{3}{2}, 1, \frac{1}{2}, +\rangle$ 70% $ \frac{3}{2}, 0, \frac{3}{2}, -\rangle$, 14% $ \frac{1}{2}, 1, \frac{3}{2}, -\rangle$ 87% $ \frac{3}{2}, 1, \frac{5}{2}, -\rangle$ 84% $ \frac{3}{2}, 1, \frac{5}{2}, +\rangle$ 65% $ \frac{3}{2}, 1, \frac{1}{2}, -\rangle$, 29% $ \frac{1}{2}, 0, \frac{1}{2}, -\rangle$

parity.

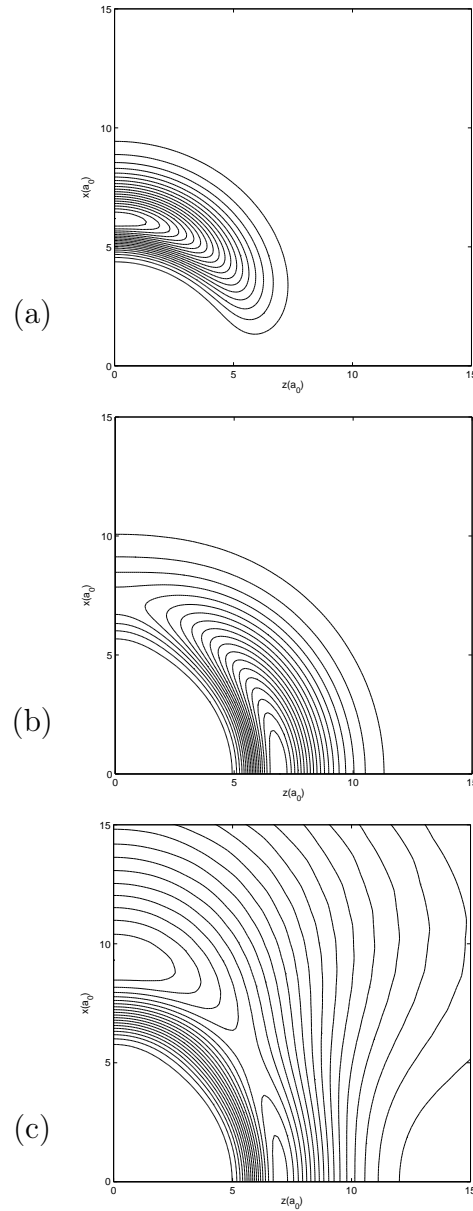
In Fig. 3.6 one observes that the *para*-H₂ molecule in the F-H₂ complex is very nearly spherical, in agreement with the observation in Table 3.2 that the bound state wavefunction has almost exclusively $j_B = 0$ character and little admixture of the basis functions with higher (even) j_B . This is a consequence of the large rotational constant $b_0 = 59.34 \text{ cm}^{-1}$ of H₂, which causes a gap of 356 cm^{-1} between the levels with $j_B = 2$ and $j_B = 0$ that is large with respect to the anisotropy in the F-H₂ potential.

Figure 3.6: Density of the $J = \frac{1}{2}$ bound state of *para*-H₂-F of + parity as function of the F-atom position in the BF xz plane, with the hydrogen molecule lying along the horizontal z axis and the origin at the center of mass of H₂. Energy: -14.570 cm^{-1} .



Also the bound states of *ortho*-H₂-F contain almost exclusively the lowest rotational H₂ wavefunction which has $j_B = 1$ in this case. Since the $j_B = 1$ state has degenerate components with $\omega_B = -1, 0, 1$, the H₂ molecule in the bound *ortho*-H₂-F complex has the possibility to adopt its most favorable orientation. Figure 3.7(a) shows that a T-shaped complex with primarily $|\omega_B| = 1$ (see Table 3.2) has the lowest energy. It is somewhat more compact, with maximum density at $R = 6.19 a_0$, than the bound state of *para*-H₂-F with maximum density at $R = 6.31 a_0$. This is in agreement with the binding energy D_0 being larger for *ortho*-H₂-F than for *para*-H₂-F: the states with $J = \frac{1}{2}$ and + parity that are displayed lie at -17.4 and -14.6 cm^{-1} , respectively. The next higher *ortho*-H₂-F bound state with $J = \frac{1}{2}$ has mainly $\omega_B = 0$ character with some

Figure 3.7: Density of the $J = \frac{1}{2}$ bound states of *ortho*-H₂-F of + parity as function of the F-atom position in the BF xz plane, with the hydrogen molecule lying along the horizontal z axis and the origin at the center of mass of H₂. Energies: (a) -17.442 , (b) -8.431 , (c) -0.074 cm⁻¹.



admixture of $|\omega_B| = 1$ components and it adopts primarily the linear geometry, see Fig. 3.7(b), with maximum density at $R = 6.85 a_0$. The highest level of *ortho*- $\text{H}_2\text{-F}$ is bound by only 0.074 cm^{-1} and it is quite diffuse. Figure 3.7(c) shows that it has two maxima in the density, one for the T-shaped geometry at $R = 9.31 a_0$ and one for the linear geometry at $R = 6.99 a_0$. For higher J values the densities do not present new features. The radius of maximum density changes slightly from one state to another but the pattern observed for $J = \frac{1}{2}$ remains.

The electronic quantum number corresponding to these low lying states is always $j_A = \frac{3}{2}$. The large spin-orbit splitting in the $F(^2P)$ atom makes the $j_A = \frac{1}{2}$ states nearly inaccessible. The ω_A quantum number which corresponds to the projection of j_A on the intermolecular axis \mathbf{R} may vary from one state to another, however. The *para*- $\text{H}_2\text{-F}$ bound state with $J = \frac{1}{2}$ must have $|\omega_A| = \frac{1}{2}$ because $j_B = \omega_B = 0$ for this state and $\Omega = \omega_A + \omega_B$ must be $\pm\frac{1}{2}$ for $J = \frac{1}{2}$. For the *para*- $\text{H}_2\text{-F}$ states with $J \geq \frac{3}{2}$ and for the *ortho*- $\text{H}_2\text{-F}$ states $|\omega_A|$ can be either $\frac{1}{2}$ or $\frac{3}{2}$. Table 3.2 shows that most of the lower bound states have $|\omega_A| = \frac{1}{2}$, whereas the higher states obtain more and more $|\omega_A| = \frac{3}{2}$ character. This quantum number $|\omega_A|$ is related to the orientation of the “ p -hole” in the electron distribution of the $F(^2P)$ atom. For $|\omega_A| = \frac{3}{2}$ the projection of the orbital angular momentum $\lambda = 1$ can only be $\mu = \pm 1$ and, hence, the p -hole is directed perpendicular to the F-H_2 axis \mathbf{R} . States with $|\omega_A| = \frac{1}{2}$ and $j_A = \frac{3}{2}$ contain two thirds of $\mu = 0$ character and one third of $\mu = \pm 1$ character, cf. Eq. (3.33), and the p -hole is primarily directed along \mathbf{R} for such states.

Table 3.3 lists the energies of the bound levels computed with the empirical potential of Aquilanti *et al.* [32]. They are lower than the levels in Table 3.1 and Fig. 3.5 and D_0 is larger, due to the deeper well in the diabatic potential $V_{0,0}$. Also the number of bound states is larger for this potential. Additional bound states appear for $J = \frac{11}{2}$ in *para*- $\text{H}_2\text{-F}$ and for $J = \frac{13}{2}$ in *ortho*- $\text{H}_2\text{-F}$. We also analyzed the bound wavefunctions; most of them are similar to the eigenvectors reported in Table 3.2.

At present, there are no experimental data to compare with our predicted levels. We hope that spectroscopists will soon acquire these data. Since the levels depend sensitively on the potential surface, one will then be able to tell which of the potentials is the most accurate. Finally we mention that similar work on the bound states of $\text{Cl}(^2P)\text{-H}_2$ and $\text{Br}(^2P)\text{-H}_2$ is in progress. Also inelastic scattering and photodissociation cross sections are being calculated. All this work makes use of the procedures outlined in the present chapter and the diabatic potentials of Kłos *et al.* [43, 54, 55] calculated with the UCCSD(T) method.

Table 3.3: Bound states of F-H₂ for $J = \frac{1}{2}$ up to $\frac{13}{2}$ calculated with the potential of Aquilanti *et al.* [32]. Explanations, see Table 3.1.

$J = \frac{1}{2}$	$J = \frac{3}{2}$	$J = \frac{5}{2}$	$J = \frac{7}{2}$	$J = \frac{9}{2}$	$J = \frac{11}{2}$	$J = \frac{13}{2}$
<i>para</i> -H ₂						
-17.800 (+)	-17.258 (-)	-15.308 (+)	-11.986 (-)	-7.381 (+)	-1.672 (-)	
-14.768 (-)	-11.423 (+)	-7.190 (-)	-2.429 (+)			
	-3.869 (-)	-1.198 (+)				
	-3.699 (+)	-0.487 (-)				
<i>ortho</i> -H ₂						
-22.795 (-)	-23.877 (-)	-22.094 (+)	-18.976 (-)	-14.621 (+)	-9.145 (-)	-2.725 (+)
-22.270 (+)	-23.868 (+)	-21.757 (-)	-18.071 (+)	-12.925 (-)	-6.467 (+)	
-9.205 (+)	-19.019 (+)	-14.610 (-)	-9.499 (+)	-4.019 (-)		
-7.484 (-)	-17.978 (-)	-12.786 (+)	-6.833 (-)	-0.884 (+)		
-0.445 (+)	-8.249 (-)	-5.984 (+)	-2.369 (-)			
-0.005 (-)	-6.168 (+)	-4.265 (+)	-1.266 (-)			
	-6.126 (-)	-4.180 (-)	-0.837 (+)			
	-4.903 (+)	-1.467 (-)				
		-1.125 (-)				
		-1.057 (+)				

CHAPTER 4

Singlet-triplet excitation spectrum of the CO–He complex; I: Potential surfaces and bound-bound $\text{CO}(a^3\Pi \leftarrow X^1\Sigma^+)$ transitions

The interaction of He with metastable $\text{CO}(a^3\Pi)$ gives rise to two adiabatic potential surfaces of reflection symmetry A' and A'' which were calculated with the partially spin-restricted open-shell single and double excitation coupled cluster method with perturbative triples, RCCSD(T). Two diabatic potentials were constructed and fitted analytically; the appropriate form of the angular expansion functions was derived from general invariance properties. From variational calculations on these diabatic potential surfaces we obtained the quasi-bound vibration-rotation-spin levels of the CO–He complex in its lowest triplet state. Only the lower spin-orbit levels of this complex with approximate quantum number $\Omega = 0$ of the $\text{CO}(a^3\Pi)$ monomer were found to be stable with respect to dissociation into He and triplet CO. The potential and the bound Van der Waals levels of the ground state $\text{CO}(X^1\Sigma^+)$ –He complex were recalculated and used in combination with the triplet excited state wavefunctions to compute the line strengths and the bound-bound part of the singlet-triplet excitation spectrum of the CO–He complex. The spin-forbidden singlet-triplet transitions access mainly the higher spin-orbit levels with $|\Omega| = 1$, but these were found to undergo rapid predissociation. The following chapter (chapter 5) explicitly studies this process, predicts the excited state life times, and generates the bound-continuum part of the CO–He singlet-triplet spectrum.

4.1 Introduction

The CO molecule is of considerable interest. It plays an important role in interstellar molecular clouds in which collisions occur mostly with abundant species such as He and H₂. The lowest triplet state of CO, the $a^3\Pi$ state, is metastable with life times from a few ms to hundreds of ms for the different sublevels of this state [56, 57]. This implies that triplet CO molecules are sufficiently long-lived to perform (surface) scattering experiments [58, 59]. Since an already cold molecular beam of CO($a^3\Pi$) molecules could be decelerated to substantially lower velocity [60], triplet CO is also a good candidate for the study of ultracold molecules. In view of these prospects it is of interest to study what happens to the metastable CO($a^3\Pi$) species when it interacts with other molecules. The simplest possible complex containing CO($a^3\Pi$) is the triplet excited van der Waals molecule CO–He, but the first experimental attempts to detect this species were not successful [61].

The relatively small number of electrons in CO and He allows an accurate theoretical investigation, which is the subject of the present chapter and of the following one. The spin-forbidden $a^3\Pi \leftarrow X^1\Sigma^+$ transition in the CO monomer gives rise to the so-called Cameron band which was analyzed in detail by spectroscopy [62, 63]. Here we study the same transition in the CO–He complex, after characterization of this complex both in its ground and lowest triplet states. The results will show that almost all of the excited triplet CO–He complexes are rapidly destroyed by dissociation. This dissociation does not produce CO in the ground $X^1\Sigma^+$ state, however, but in the lower sublevels of the triplet state. In chapter 5 we will describe how triplet excited CO–He can be detected anyway.

According to the Born-Oppenheimer approximation this theoretical study consists of two steps. The first step involves the calculation of the potential surfaces of the $X^1\Sigma^+$ and $a^3\Pi$ states of CO interacting with He. The $a^3\Pi$ electronic state of CO lies 48473.2 cm⁻¹ above the $X^1\Sigma^+$ ground state. In CO–He this $^3\Pi$ state splits into an A' and an A'' component due to reflection symmetry [64]. The spin-orbit coupling in the $a^3\Pi$ electronic state of CO makes this state a typical Hund's case (a) system [65]. The spin-orbit coupling constant $A_0 = 41.45$ cm⁻¹ is of the same order of magnitude as the CO–He interaction energy and the spin-orbit coupling turns out to play a crucial role in the dynamics of triplet excited CO–He. The second step is the calculation of the bound and quasi-bound levels of the ground and triplet excited CO–He complex. We found that rapid photodissociation occurs in most of the excited states, hence the quasi-bound levels of the triplet species had to be computed by a scattering technique. Dynamical calculations of the triplet states must take the asymptotically degenerate A' and A'' potential surfaces into account simultaneously, and must include the spin-orbit and other coupling terms. Such calculations were performed, after transformation of the adiabatic A' and A'' states to a convenient pair of diabatic states.

The present chapter deals with the calculation and the analytic fit of the potential surfaces. Also the calculation of the ground state and triplet excited bound levels in these potentials is described. An effective transition dipole for the spin-forbidden singlet-triplet transition is constructed and the bound-bound part of the spectrum is generated. Chapter 5 treats the calculation of the triplet states that dissociate upon excitation.

4.2 Potential surfaces

The $\text{CO}(X^1\Sigma^+)$ -He ground state potential energy surface was calculated previously by Heijmen *et al.* [66], who used symmetry-adapted perturbation theory (SAPT). Here we applied the CCSD(T) (coupled cluster singles and doubles with perturbative triples) supermolecule method [67], as we did for the excited triplet state (see below). Since our results for $\text{CO}(X^1\Sigma^+)$ -He agree very well with those of Refs. [68, 66], we describe in more detail the techniques and calculations involved to obtain the $\text{CO}(a^3\Pi)$ -He potential energy surface. The potentials are expressed in Jacobi coordinates (R, θ) defined such that R is the length of the vector \mathbf{R} which points from the center of mass of CO to the He nucleus and θ is the angle between \mathbf{R} and the CO axis. The angle θ equals zero for the linear geometry CO-He.

4.2.1 Ab initio calculations

For both the $\text{CO}(X^1\Sigma^+)$ -He ground state and the $\text{CO}(a^3\Pi)$ -He excited state potential surfaces supermolecule calculations were performed with the MOLPRO-2000 package [69] using the CCSD(T) method for the ground state and the partially spin-restricted RCCSD(T) method [70, 71] for the excited triplet state. In both cases we applied the counterpoise procedure of Boys and Bernardi [72] to correct for the basis set superposition error (BSSE). We used the same basis set, which consists of $(9s7p3d2f)$ contracted functions defined by Partridge [73] for the C and O atoms and $(5s3p2d)$ contracted functions defined by Van Duijneveldt *et al.* [74] for the He atom. Added to this was a $(3s3p2d1f)$ set of midbond functions defined by Tao and Pan [75], centered at the midpoint of \mathbf{R} , with the exponents 0.9, 0.3, 0.1 for the s and p , 0.6 and 0.2 for the d and 0.3 for the f orbitals. Table 4.1 shows that the basis chosen in this work gives results of the same quality as an augmented correlation consistent polarized quadruple zeta (aug-cc-pVQZ) basis [76, 77, 78]. The aug-cc-pVQZ basis has 235 contracted functions, whereas the basis used in this work has only 171 (an augmented triple zeta aug-cc-pVTZ basis has 144). It is thus a very good basis for this problem.

For the ground state we used a coordinate grid of 143 points with R ranging from 5 to 9 a_0 in steps of 0.5 a_0 and from 9 to 12 a_0 in steps of 1 a_0 . The angle

Table 4.1: Basis set test: interaction energies in μE_h . Calculations with the aug-cc-pVTZ and aug-cc-pVQZ bases also used the 3321 bond functions described in the text.

	aug-cc-pVTZ	aug-cc-pVQZ	basis of this work
$R = 6.770 a_0, \theta = 74.150^\circ$			
$X^1\Sigma$	-90.91	-91.36	-91.21
$A'^3\Pi$	-114.56	-115.33	-115.73
$A''^3\Pi$	-100.06	-101.03	-101.02
$R = 12.250 a_0, \theta = 113.380^\circ$			
$X^1\Sigma$	-3.777	-3.768	-3.815
$A'^3\Pi$	-4.340	-4.337	-4.416
$A''^3\Pi$	-3.855	-3.901	-3.966

θ ranges from 0° to 180° in steps of 15° . The intramolecular CO distance was kept fixed at its equilibrium value $r_e = 2.132 a_0$. For the triplet excited state potential surface the CO bond length was fixed at its $a^3\Pi$ equilibrium value $r_e = 2.279 a_0$ and we calculated 224 points on a coordinate grid with R ranging from 3.25 to 20 a_0 . The step size was 0.35 a_0 in the well region and increases for smaller and larger R . The angular grid ranges from 6° to 174° in steps of 12° .

4.2.2 Expansion of the potentials

For the CO–He ground state potential we use the well known Legendre expansion, but the expansion of the A' and A'' potential surfaces that represent the interaction between $\text{CO}(a^3\Pi)$ and He is more complicated. The form of such an expansion for a Π state diatom interacting with an S state atom was first given by Alexander [64]. His derivation of this form is based on the multipole expansion of the interaction energy, which is applicable only for large intermolecular distances and in the case of a neutral S state atom yields an interaction energy that is zero. Here we present a more general derivation, which yields the same result, which is based on the invariance properties of a general intermolecular potential energy operator. We start by defining a partly space-fixed coordinate frame with its z -axis aligned with the CO diatom axis and its xz plane fixed in space, independent of the position of the He atom. The He atom has position vector $\mathbf{R} = (R, \theta, \phi)$ in this frame and the electronic orbital angular momentum of the Π state of CO is $\Lambda = \pm 1$. The corresponding components of this Π state, which we call diabatic because they do not depend on the position of the He atom, are denoted by $|\Lambda\rangle$. The intermolecular potential energy operator \hat{V} of this open-shell complex is a linear operator in the vector space spanned by the

set of diabatic states and may be expanded as

$$\widehat{V} = \sum_{\Lambda_1 \Lambda_2} |\Lambda_1\rangle V_{\Lambda_1, \Lambda_2}(R, \theta, \phi) \langle \Lambda_2|. \quad (4.1)$$

The matrix elements $V_{\Lambda_1, \Lambda_2} = \langle \Lambda_1 | \widehat{V} | \Lambda_2 \rangle$ are the diabatic potentials of CO($a^3\Pi$)–He. Each of these diabatic potentials depends on R , θ , and ϕ and can be expanded in Racah normalised spherical harmonics $C_{lm}(\theta, \phi)$

$$V_{\Lambda_1, \Lambda_2}(R, \theta, \phi) = \sum_{l, m} v_{\Lambda_1, \Lambda_2}^{l, m}(R) C_{lm}(\theta, \phi). \quad (4.2)$$

From the invariance of the electronic Hamiltonian of CO–He under rotations of the whole system (electrons and nuclei) it follows that the operator \widehat{V} must be invariant in particular to rotations \widehat{R}_z about the CO axis. Then, from the transformation properties $\widehat{R}_z(\alpha)|\Lambda\rangle = |\Lambda\rangle \exp(-i\Lambda\alpha)$ of the diabatic states and of the spherical harmonics $\widehat{R}_z(\alpha)C_{lm}(\theta, \phi) = C_{lm}(\theta, \phi - \alpha) = C_{lm}(\theta, \phi) \exp(-im\alpha)$ it can be easily derived that the expansion coefficients $v_{\Lambda_1, \Lambda_2}^{l, m}(R)$ must vanish except when $m = \Lambda_2 - \Lambda_1$. Hence, for the $^3\Pi$ state of CO with $\Lambda = \pm 1$ the expansion is restricted to diagonal terms ($\Lambda_1 = \Lambda_2$) with $m = 0$ and off-diagonal terms with $m = \pm 2$.

Next we define a completely body-fixed frame with the same z -axis and the He atom in the xz plane and consider reflection symmetry with respect to this plane. This frame is related to the partly space-fixed frame by a rotation $\widehat{R}_z(\phi)$. The rotated diabatic states are $|\Lambda\rangle' = |\Lambda\rangle \exp(-i\Lambda\phi)$. The reflection σ_{xz} simply acts on these rotated states as $\sigma_{xz}|\Lambda\rangle' = (-1)^\Lambda |-\Lambda\rangle'$ and the Π states of CO which are symmetric and antisymmetric with respect to reflection are $|A'\rangle = |+\rangle = (|-1\rangle' - |1\rangle')/\sqrt{2}$ and $|A''\rangle = |-\rangle = i(|-1\rangle' + |1\rangle')/\sqrt{2}$, respectively. These A' and A'' states correspond to the adiabatic states of CO–He obtained in electronic structure calculations. Moreover, it follows from the reflection symmetry that the expansion coefficients of the diabatic potentials in Eq. (4.2) obey the relation $v_{\Lambda_1, \Lambda_2}^{l, m}(R) = v_{-\Lambda_1, -\Lambda_2}^{l, -m}(R)$ and, hence, that $v_{1, 1}^{l, 0}(R) = v_{-1, -1}^{l, 0}(R)$ and $v_{1, -1}^{l, -2}(R) = v_{-1, 1}^{l, 2}(R)$. Combining these results one finds that the adiabatic potentials $V_{A'}$ and $V_{A''}$ are related to the (rotated) diabatic potentials as

$$\begin{aligned} V_{A'} &= \langle + | V | + \rangle = V_{1, 1} - V_{1, -1} \\ V_{A''} &= \langle - | V | - \rangle = V_{1, 1} + V_{1, -1}. \end{aligned} \quad (4.3)$$

Hence, the diabatic potentials can be directly obtained from the computed adiabatic potentials $V_{A'}$ and $V_{A''}$ and they should be expanded in spherical

harmonics with fixed values of $m = \Lambda_2 - \Lambda_1$ ($= 0$ or ± 2)

$$\begin{aligned} V_{1,1}(R, \theta) &= \frac{V_{A'} + V_{A''}}{2} = \sum_l v^{l,0}(R) C_{l,0}(\theta, 0) \\ V_{1,-1}(R, \theta) &= \frac{V_{A''} - V_{A'}}{2} = \sum_l v^{l,2}(R) C_{l,2}(\theta, 0). \end{aligned} \quad (4.4)$$

The ϕ dependence in Eq. (4.2) is automatically removed by the rotation $\widehat{R}_z(\phi)$ of the diabatic states and the condition $m = \Lambda_2 - \Lambda_1$. So, finally, the diabatic potentials depend only on the coordinates R and θ defined by the nuclear framework. The spherical harmonics $C_{l,m}(\theta, 0)$ are simply associated Legendre functions $P_l^m(\theta)$, multiplied by a normalization constant. The same expansion, with $m = 0$, holds for the potential of ground state CO($X^1\Sigma^+$)-He.

4.2.3 Analytic fits of the potentials

The preceding section shows that the angular dependence of the potential of ground state CO($X^1\Sigma^+$)-He and of the two diabatic potentials for CO($a^3\Pi$)-He can be represented by a specific series of spherical harmonics $C_{l,m}(\theta, 0)$ with fixed $m = 0$ or ± 2 and $|m| \leq l < \infty$. Here we describe the analytic fit of each of these potential surfaces in terms of these functions $C_{l,m}(\theta, 0)$ and an appropriate set of radial functions that represent both the long and short range interactions

$$V(R, \theta) = V_{\text{sr}}(R, \theta) + V_{\text{lr}}(R, \theta), \quad (4.5)$$

where

$$V_{\text{sr}}(R, \theta) = \sum_{p=0}^{p_{\text{max}}} \sum_{l=m}^{l_{\text{max}}} s_{lp} R^p \exp(-\alpha R) C_{lm}(\theta, 0) \quad (4.6)$$

and

$$V_{\text{lr}}(R, \theta) = \sum_{n=6}^{n_{\text{max}}} \sum_{l=m}^{l_{\text{max}}} f_n(\beta R) c_{ln} R^{-n} C_{lm}(\theta, 0). \quad (4.7)$$

The long range coefficients c_{ln} are nonzero only when $l \leq n - 4$, while l must be even for even n and odd for odd n . The functions f_n are Tang-Toennies damping functions [79]

$$f_n(x) = 1 - \exp(-x) \sum_{k=0}^n \frac{x^k}{k!}. \quad (4.8)$$

The coefficients s_{lp} and c_{ln} and the nonlinear parameters α and β were fit in a two-step procedure [80]. In the first step we fitted the long range data points, i.e., the interaction energies for $R > 10 a_0$, using only the $n = 6, 7, 8, 9$ terms of the expansion function V_{lr} with the damping function set to one. In this

step the coefficients c_{ln} were determined by a weighted least squares fit using the weight function $w(R) = R^6$. In the second step we included also the short range data points, we fixed the coefficients c_{ln} with $n = 6$, and determined all other linear coefficients in V_{lr} and V_{sr} by a least squares procedure. Since, for the range of R that we considered, the interaction energies vary over several orders of magnitude we had to construct a weight function $w(R, \theta)$ such that $w(R, \theta)V(R, \theta)$ is on the order of unity everywhere. Both in the short and long range $w = |V|^{-1}$ would actually work well, but in the intermediate range the interaction potential goes through zero. Following Ref. [80] we used the weight function $\omega = \omega_{sr}\omega_{lr}$ with

$$\begin{aligned}\omega_{sr} &= \left[\ln \left\{ \exp \left(\frac{V}{V_0} \right) + e - 1 \right\} \right]^{-1} \\ \omega_{lr} &= \left[1 + \left(\frac{R}{R_0} \right)^6 \right] V_0^{-1}\end{aligned}\quad (4.9)$$

and $V_0 = c_6/R_0^6$. This parameter V_0 determines where the short range factor of the weight function effectively “switches on”. We set it equal to $V_0 = 5|E_0|$, where $E_0 = -21.29 \text{ cm}^{-1}$ for the ground state potential and $E_0 = -27.52 \text{ cm}^{-1}$ for the triplet state potentials are the most attractive points on the grid. The value of $c_6 = 11.8 E_h a_0^6$ was taken from the long range fit result; it gives $R_0 = 5.16 a_0$.

The nonlinear parameters α and β , as well as the upper limits p_{max} and n_{max} in the summations (i.e., the degrees of the polynomials), were determined by extensive experimentation. The quality of the fit was judged by considering the relative error for points where $V > V_0$, the absolute error for points with $V < 0$, and the relative error for points with $R > 7 a_0$. This test was done not only for the geometries mentioned before, but also for 15 additional random geometries in the range $4 a_0 < R < 14 a_0$ that were not used in the fit. The nonlinear parameters α and β were determined in fits with only low degree polynomials. Once a reasonably good fit was obtained, the nonlinear parameters were fixed and the order of the polynomials was increased step by step as long as this produced a substantial improvement of the fit.

Our final fit for the $\text{CO}(X^1\Sigma^+)$ -He potential (with $m = 0$) has $p_{max} = 1$, $l_{max} = 10$, and $n_{max} = 14$. The root mean square relative error in the short-range region with $V > 0$ is about 0.13%, the root mean square error for the intermediate region with $V < 0$ and $R < 7 a_0$ is 0.04 cm^{-1} , and the root mean square relative error in the long range region with $R > 7 a_0$ is 0.8%. For the $\text{CO}(a^3\Pi)$ -He potentials the parameters are: $p_{max} = 4$, $l_{max} = 9$, and $n_{max} = 13$ for the $V_{1,1}$ surface with $m = 0$, and $p_{max} = 8$, $l_{max} = 9$, and $n_{max} = 11$ for the $V_{1,-1}$ surface with $m = 2$. For the A' and A'' surfaces that are the sum and difference of $V_{1,1}$ and $V_{1,-1}$ the root mean square relative error in the short-range region is 0.26%, the root mean square error in the

intermediate region is 0.03 cm^{-1} , and the root mean square relative error in the long range region is 0.24%.

4.2.4 Characteristics of the potentials

Figure 4.1 shows the (R, θ) contour plot of the ground state $\text{CO}(X^1\Sigma^+)\text{-He}$ potential. This potential has a single minimum with $D_e = 21.35 \text{ cm}^{-1}$ at $R_e = 6.48 a_0$ and $\theta = 69^\circ$. This result agrees quite well with the SAPT potential in Ref. [66] which has a minimum with $D_e = 22.734 \text{ cm}^{-1}$ at $R_e = 6.53 a_0$ and $\theta = 48.9^\circ$. The large difference (20°) in the angle θ is explained by the fact that the potential surface in the well region is very flat along the θ coordinate. Figure 4.1 shows that at -21 cm^{-1} , i.e., only 0.35 cm^{-1} above the minimum, the width of the well in the θ direction is $\approx 40^\circ$.

Figure 4.1: Potential energy surface of $\text{CO}(X^1\Sigma^+)\text{-He}$.

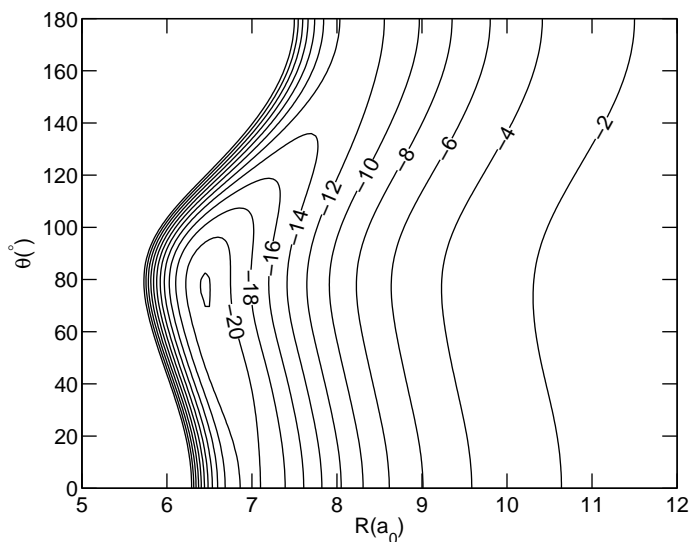


Figure 4.2 shows the A' and A'' potential surfaces of $\text{CO}(a^3\Pi)\text{-He}$, respectively. Minima are found with $D_e = 31.9 \text{ cm}^{-1}$ at $R_e = 6.75 a_0$ and $\theta = 135^\circ$ for the A' surface and $D_e = 30.76 \text{ cm}^{-1}$ at $R_e = 6.22 a_0$ and $\theta = 78^\circ$ for the A'' surface. The two surfaces exhibit a common local minimum with $D_e = 27.44 \text{ cm}^{-1}$ at the linear CO-He geometry with $R = 6.82 a_0$ and $\theta = 0^\circ$.

Figure 4.2: Adiabatic potential energy surface of $\text{CO}(a^3\Pi)\text{-He}$ of A' symmetry (top) and A'' symmetry (bottom).

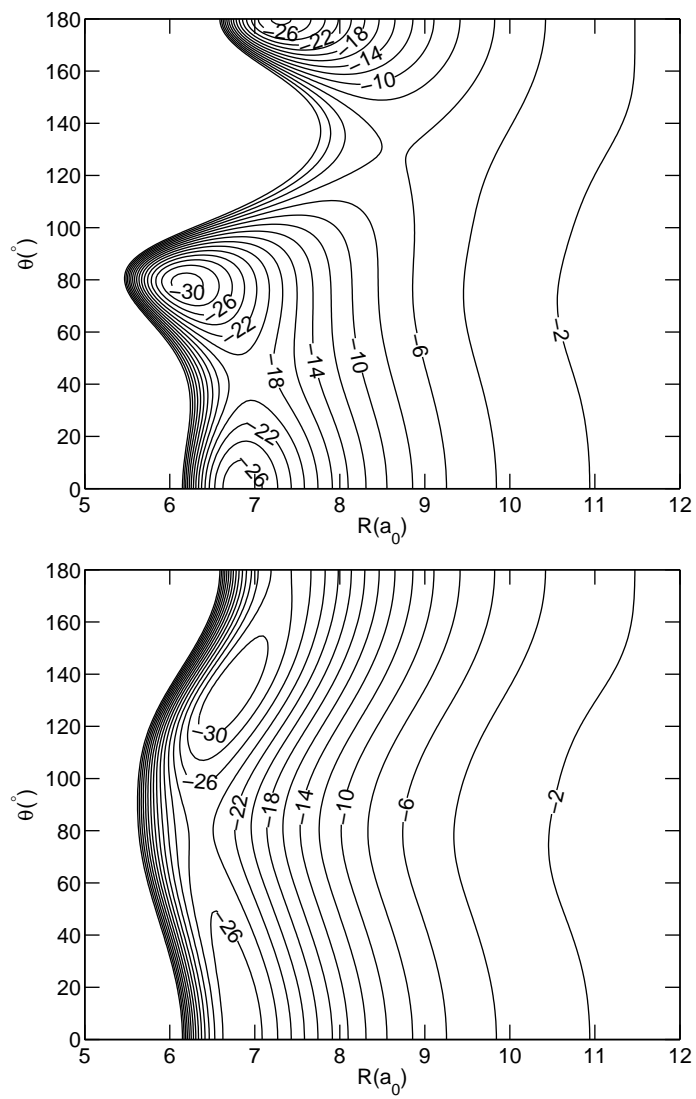
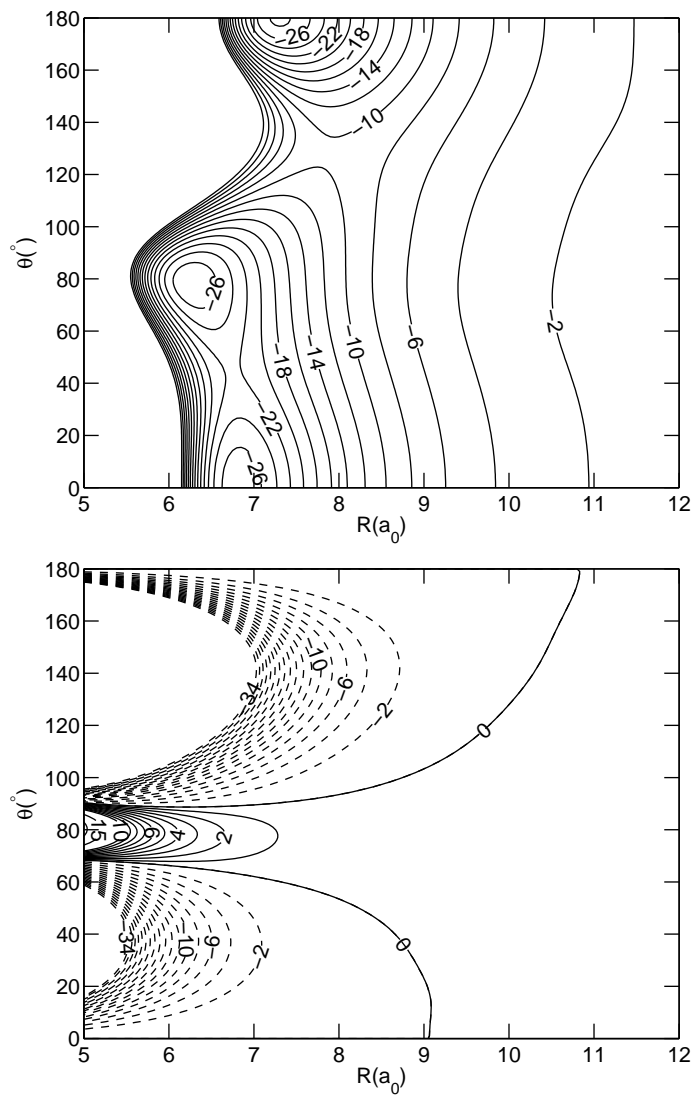


Figure 4.3: Diabatic potential energy surfaces $V_{1,1}$ (top) and $V_{1,-1}$ (bottom) of $\text{CO}(a^3\Pi)\text{-He}$.



4.3 Calculation of the vibration-rotation-spin levels

Different coordinates and basis sets can be used to calculate the vibration-rotation-tunneling (VRT) levels of Van der Waals dimers. In particular, one may choose a space-fixed coordinate frame or various body-fixed frames with the axes fixed by the orientation of the intermolecular vector \mathbf{R} and/or by the orientation of one of the monomers [17, 81]. In the case of ground state CO–He it turned out that a space-fixed frame (SF) is the most convenient, because the quantum numbers J , describing the CO rotation, and L , the end-over-end rotation of the complex—i.e., of the vector \mathbf{R} —are very nearly conserved [66]. Also for triplet excited CO–He we will use a SF frame with the same quantum numbers J and L , since the well depth and anisotropy of the A' and A'' potentials of CO($a^3\Pi$)–He are comparable to those of the ground state CO($X^1\Sigma^+$)–He potential. Before we discuss the calculation of the vibration-rotation-spin levels of the triplet excited CO–He complex, we briefly summarize the fine structure of CO in its $a^3\Pi$ state.

The fine structure of CO in its $a^3\Pi$ state and in some other excited electronic states has been determined in detail by spectroscopy [62, 63]. The dominant term that splits the levels of CO($a^3\Pi$) is the spin-orbit coupling (coupling constant $A_0 = 41.45 \text{ cm}^{-1}$). The best approximate quantum numbers to characterize these energy levels are $\Lambda = \pm 1$ and $\Omega = \Lambda + \Sigma$. The quantum number Λ is the eigenvalue of the electronic orbital angular momentum operator \hat{L}_z and $\Sigma = -1, 0, 1$, the eigenvalue of \hat{S}_z , is the component of the triplet spin ($S = 1$) along the CO bond axis. The total angular momentum is represented by the operator $\hat{\mathbf{J}} = \hat{\mathbf{l}} + \hat{\mathbf{S}} + \hat{\mathbf{R}}$, where $\hat{\mathbf{l}}$, $\hat{\mathbf{S}}$, and $\hat{\mathbf{R}}$ are the electronic orbital, spin, and nuclear (rotation) angular momenta, respectively. The quantum number J that corresponds with the operator $\hat{\mathbf{J}}$ is an exact quantum number. Since the nuclear angular momentum $\hat{\mathbf{R}}$ has a vanishing z component Ω is the eigenvalue of \hat{J}_z as well as of the electronic angular momentum operator $\hat{l}_z + \hat{S}_z$. Relative to the origin of the triplet levels at $48473.201 \text{ cm}^{-1}$ the levels with $\Omega = 0$ are at about -40 cm^{-1} , the levels with $\Omega = \pm 1$ at zero, and the levels with $\Omega = \pm 2$ at about $+40 \text{ cm}^{-1}$ as a result of the spin-orbit coupling and CO($a^3\Pi$) behaves as a typical Hund's coupling case (a) system. Smaller coupling terms are present as well [63]; the effective Hamiltonian that describes the complete level structure of CO($a^3\Pi$) is

$$\begin{aligned} \hat{H}_{\text{CO}} &= B_0 \left[\hat{J}^2 + \hat{S}^2 - \hat{J}_z^2 - \hat{S}_z^2 - \hat{J}_- \hat{S}_- - \hat{J}_+ \hat{S}_+ \right] \\ &+ A_0 \hat{l}_z \hat{S}_z + \frac{2}{3} \lambda_0 \left(3 \hat{S}_z^2 - \hat{S}^2 \right) + C_{\Pi}^{\delta} \hat{P}(\Omega = 0), \end{aligned} \quad (4.10)$$

where $B_0 = 1.6816 \text{ cm}^{-1}$ is the rotational constant of CO($a^3\Pi$) in its vibrational ground state, $A_0 = 41.4500 \text{ cm}^{-1}$ is the spin-orbit coupling constant, $\lambda_0 = 0.0258 \text{ cm}^{-1}$ the spin-spin coupling constant, and $C_{\Pi}^{\delta} = 0.8752 \text{ cm}^{-1}$ the Λ -doubling constant. All these coupling constants have been taken from

experimental work [63]. Terms smaller than 10^{-2} cm^{-1} are omitted. The total angular momentum operator $\hat{\mathbf{J}}$ is given with respect to the molecule-fixed frame and its components have the anomalous commutation relations [82]. The corresponding shift operators are therefore defined as $\hat{J}_{\pm} = \hat{J}_x \mp i\hat{J}_y$, whereas the spin shift operators have the normal definition $\hat{S}_{\pm} = \hat{S}_x \pm i\hat{S}_y$. The last term in Eq. (4.10) is the Λ -doubling term which gives rise to a splitting $\mp C_{\Pi}^{\delta}$ of the $\Omega = 0$ substate into two components with positive and negative parity, see Table IV of Ref. [63]. The origin of this splitting is the spin-orbit coupling of the $a^3\Pi$ state with other electronic states. The Λ -doubling is represented here by an operator that couples the $|\Lambda = -1, \Sigma = +1\rangle$ and $|\Lambda = +1, \Sigma = -1\rangle$ components of the $\Omega = 0$ substate

$$\hat{P}(\Omega = 0) = \sum_{\Lambda=-1,1} |-\Lambda, \Sigma, \Omega = 0\rangle \langle \Lambda, -\Sigma, \Omega = 0|. \quad (4.11)$$

For $J > 0$ Ω is not an exact quantum number and the substates with $\Omega = \pm 1$ and ± 2 are slightly split by the Λ -doubling term, due to some admixture of the $\Omega = 0$ states.

The Hamiltonian of the triplet excited CO($a^3\Pi$)-He complex is easily written now (in atomic units)

$$\hat{H} = \frac{-1}{2\mu R} \frac{\partial^2}{\partial R^2} R + \frac{\hat{L}^2}{2\mu R^2} + \hat{H}_{\text{CO}} + \sum_{\Lambda_1, \Lambda_2} |\Lambda_1\rangle V_{\Lambda_1, \Lambda_2}(R, \theta) \langle \Lambda_2| \quad (4.12)$$

where μ is the reduced mass of the dimer and \hat{L} is the angular momentum operator corresponding to the end-over-end rotation. The diabatic potentials $V_{\Lambda_1, \Lambda_2}(R, \theta)$ are defined in Sec. 4.2.3 and shown in Fig. 4.3. The angle θ between the CO bond axis and the vector \mathbf{R} is not one of the SF coordinates, but after the expansion of the potential $V_{\Lambda_1, \Lambda_2}(R, \theta)$ in spherical harmonics given in Sec. 4.2.3 it is not hard to rewrite this expansion in terms of Wigner D -functions [39] depending on the polar angles of the CO axis and the vector \mathbf{R} with respect to the SF frame. In writing Eq. (4.12) we assumed implicitly that the weak interaction with He does not change the spin-orbit and spin-spin coupling terms in the Hamiltonian of the CO monomer. A similar Hamiltonian for a Π -state diatom interacting with a rare gas atom has been proposed by Dubernet *et al.* [83].

From the discussion on the fine structure of CO in its $a^3\Pi$ state it will be clear that the basis functions for this Hund's coupling case (a) system can be denoted as

$$|\Lambda, S, \Omega, J, M_J\rangle = |\Lambda, S, \Omega\rangle \left[\frac{2J+1}{4\pi} \right]^{1/2} D_{M_J, \Omega}^{(J)}(\phi, \theta, 0)^*, \quad (4.13)$$

where the angles (θ, ϕ) are the polar angles of the CO axis with respect to the SF frame. The function $|\Lambda, S, \Omega\rangle$ is the internal (electronic angular momentum

and spin) part of the $\text{CO}(a^3\Pi)$ wavefunction (with $S = 1$ and $\Sigma = \Omega - \Lambda$) and the symmetric rotor function $D_{M_J, \Omega}^{(J)}(\phi, \theta, 0)^*$ describes the CO rotation. From the basis in Eq. (4.13) we derive a parity adapted basis

$$\begin{aligned} | |\Lambda|, S, \Omega, J, M_J, \epsilon \rangle &= 2^{-1/2} \left[| \Lambda, S, \Omega, J, M_J \rangle \right. \\ &\quad \left. + \epsilon(-1)^{J-S} | -\Lambda, S, -\Omega, J, M_J \rangle \right] \end{aligned} \quad (4.14)$$

consisting of eigenfunctions of the inversion operator with eigenvalues $\epsilon = \pm 1$.

For the $\text{CO}(a^3\Pi)$ -He complex we choose the parity-adapted basis

$$\begin{aligned} | n, |\Lambda|, S, \Omega, J, L; F, M_F, p \rangle &= | n \rangle \sum_{M_J, M_L} | |\Lambda|, S, \Omega, J, M_J, \epsilon \rangle Y_{L, M_L}(\beta, \alpha) \\ &\quad \times \langle J, M_J; L, M_L | F, M_F \rangle. \end{aligned} \quad (4.15)$$

The angles (β, α) are the polar angles of \mathbf{R} with respect to the SF frame. The triplet CO monomer functions with quantum number J and the spherical harmonics $Y_{L, M_L}(\beta, \alpha)$ have been coupled to eigenfunctions of \widehat{F}^2 by means of the Clebsch-Gordan coefficients $\langle J, M_J; L, M_L | F, M_F \rangle$ [39]. The total angular momentum F , with $\widehat{F} = \widehat{J} + \widehat{L}$, and its SF component M_F are exact quantum numbers. Also the parity p , which is related to the parity ϵ of the monomer functions by $p = \epsilon(-1)^L$, is an exact quantum number. The radial basis functions $| n \rangle = \chi_n(R)$ are Morse oscillator type functions of the form defined in Ref. [50].

The wavefunctions of ground state CO-He are also given by Eq. (4.15), but since $\Lambda = S = \Sigma = \Omega = 0$ in this case they are much simpler than the wavefunctions of the triplet state. They are parity-adapted automatically with parity $p = (-1)^{J+L}$. Also the dimer Hamiltonian of Eq. (4.12) is much simpler: the CO monomer term is $\widehat{H}_{\text{CO}} = B_0 \widehat{J}^2$ with $B_0 = 1.9225 \text{ cm}^{-1}$ and the potential energy operator is $\widehat{V} = V(R, \theta)$.

The matrix elements of the Hamiltonian in Eqs. (4.10) and (4.12) over the $\text{CO}(a^3\Pi)$ -He basis are

$$\begin{aligned} \langle n', \Lambda', S', \Omega', J', L' | H | n, \Lambda, S, \Omega, J, L \rangle & \quad (4.16) \\ &= \delta_{\Lambda', \Lambda} \delta_{S', S} \delta_{\Omega', \Omega} \delta_{J', J} \delta_{L', L} \left[\langle n' | \frac{-1}{2\mu R} \frac{\partial^2}{\partial R^2} R + \frac{L(L+1)}{2\mu R^2} | n \rangle \right. \\ &\quad + \delta_{n', n} \left\{ B_0 [J(J+1) + S(S+1) - \Omega^2 - \Sigma^2] \right. \\ &\quad \left. + A_0 \Lambda \Sigma + \frac{2}{3} \lambda_0 [3\Sigma^2 - S(S+1)] \right\} \Big] \\ &\quad - \delta_{n', n} \delta_{S', S} \delta_{J', J} \delta_{L', L} [\delta_{\Lambda', \Lambda} B_0 (\delta_{\Omega', \Omega-1} C^- + \delta_{\Omega', \Omega+1} C^+) - \delta_{\Omega', \Omega} \delta_{\Omega, 0} \delta_{\Lambda', -\Lambda} C_{\Pi}^{\delta}] \\ &\quad + \langle n', \Lambda', S', \Omega', J', L' | V_{\Lambda', \Lambda}(R, \theta) | n, \Lambda, S, \Omega, J, L \rangle \end{aligned}$$

where $\Sigma' = \Omega' - \Lambda'$ and $\Sigma = \Omega - \Lambda$, while $C^{\pm} = [J(J+1) - \Omega(\Omega \pm 1)]^{1/2} [S(S+1) - \Sigma(\Sigma \pm 1)]^{1/2}$. The primitive (non-parity-adapted) basis $| n, \Lambda, S, \Omega, J, L; F, M_F \rangle$

in these matrix elements is not explicitly defined, but is related to the non-parity-adapted CO monomer basis in Eq. (4.13) in the same way as the parity-adapted basis in Eq. (4.15) is related to Eq. (4.14). The exact quantum numbers F and M_F , which must be equal in bra and ket, are omitted from the notation. The matrix elements of the potential are

$$\begin{aligned}
& \langle n', \Lambda', S', \Omega', J', L' | V_{\Lambda', \Lambda}(R, \theta) | n, \Lambda, S, \Omega, J, L \rangle \\
& = \delta_{S', S} \delta_{\Sigma', \Sigma} [(2J+1)(2J'+1)(2L+1)(2L'+1)]^{1/2} (-1)^{J'+J+F-\Omega} \\
& \times \sum_l \langle n' | v^{l, \Lambda' - \Lambda}(R) | n \rangle \begin{pmatrix} L' & l & L \\ 0 & 0 & 0 \end{pmatrix} \\
& \times \begin{pmatrix} J' & l & J \\ -\Omega' & \Lambda' - \Lambda & \Omega \end{pmatrix} \left\{ \begin{matrix} J' & L' & F \\ L & J & l \end{matrix} \right\}. \tag{4.17}
\end{aligned}$$

The expressions in large round brackets are 3- j symbols, the expression in curly braces is a 6- j symbol [39].

4.4 Effective dipole function for singlet-triplet excitation

The spin-forbidden transition $a^3\Pi \leftarrow X^1\Sigma^+$ has been studied in detail for the free CO monomer [62, 63, 84, 56]. This transition becomes weakly allowed due to mixing of the $a^3\Pi$ state with the nearby $A^1\Pi$ state induced by the spin-orbit interaction. The transition from the ground $X^1\Sigma^+$ state to the $A^1\Pi_1$ state is a dipole-allowed perpendicular transition. Since $S = 0$ for the $^1\Pi_1$ state, it has only $|\Omega| = |\Lambda| = 1$ components and it mixes only with the $|\Omega| = 1$ components of the CO($a^3\Pi$) state. Effective wavefunctions for this $|\Omega| = 1$ component of the $^3\Pi$ state may be written as $|a^3\Pi_{\pm 1}\rangle^{\text{eff}} = \sqrt{1 - c_{\text{SO}}^2} |a^3\Pi_{\pm 1}\rangle \pm c_{\text{SO}} |A^1\Pi_{\pm 1}\rangle$. Hence, only the $|\Omega| = 1$ levels of the triplet are directly excited by the $a^3\Pi \leftarrow X^1\Sigma^+$ transition. In reality, Ω is not an exact quantum number, however, and the substates with different $|\Omega|$ are mixed for nonzero J , so that the $^3\Pi_0$ and $^3\Pi_2$ levels obtain some intensity as well. For low values of J this Ω mixing is small and the transition occurs predominantly to the $^3\Pi_1$ levels.

With this knowledge it is possible to write an effective transition dipole moment for the $a^3\Pi \leftarrow X^1\Sigma^+$ transition in CO

$$\begin{aligned}
\mu_k^{\text{trans}} & = \langle a^3\Pi_{\Omega} | \mu_k | X^1\Sigma^+ \rangle^{\text{eff}} \\
& = \delta_{\Omega, \pm 1} \langle \sqrt{1 - c_{\text{SO}}^2} |a^3\Pi_{\pm 1}\rangle \pm c_{\text{SO}} |A^1\Pi_{\pm 1}\rangle | \mu_k | X^1\Sigma^+ \rangle \\
& = \pm c_{\text{SO}} \delta_{\Omega, \pm 1} \langle A^1\Pi_{\pm 1} | \mu_k | X^1\Sigma^+ \rangle, \tag{4.18}
\end{aligned}$$

which has only components with $k = \pm 1$ perpendicular to the CO axis. The two matrix elements $\langle A^1\Pi_{\pm 1} | \mu_{\pm 1} | X^1\Sigma^+ \rangle$ are equal and the effective transition dipole moment is here considered to be a known constant $\mu_{\pm 1}^{\text{trans}} = \pm \mu_{\perp}^{\text{trans}}$.

We assume that the weak interaction with the He atom does not affect this transition dipole moment. It is the spin selection rule, after all, that makes

this transition forbidden, not the spatial symmetry. The closed shell He atom is not expected to affect the spin of the excited CO molecule. The effective singlet-triplet transition dipole function for the CO–He complex is then

$$\mu_m^{\text{SF}} = \sum_k \mu_k^{\text{trans}} D_{m,k}^{(1)}(\phi, \theta, 0)^* \quad (4.19)$$

We remind the reader that the angles (θ, ϕ) are the polar angles of the CO axis with respect to the SF frame. The components $m = -1, 0, 1$ of the dipole function are also defined with respect to this frame.

With the same assumption about the effective CO triplet states we derive for the transition dipole matrix elements $\langle a^3\Pi_\Omega | \mu^{\text{SF}} | X^1\Sigma^+ \rangle^{\text{eff}}$ over the non-parity-adapted CO–He basis

$$\begin{aligned} & \langle n', \Lambda, S, \Omega, J', L'; F', M'_F | \mu_m^{\text{SF}} | n, 0, 0, 0, J, L; F, M_F \rangle \\ &= \delta_{n',n} \delta_{L',L} [(2J' + 1)(2J + 1)(2F + 1)(2F' + 1)]^{1/2} \\ & \times \sum_{k=-1,1} (-1)^{L+M'_F-k} \mu_k^{\text{trans}} \begin{pmatrix} J' & 1 & J \\ -\Omega & k & 0 \end{pmatrix} \\ & \times \begin{pmatrix} F' & 1 & F \\ -M'_F & m & M_F \end{pmatrix} \cdot \left\{ \begin{matrix} 1 & J' & J \\ L & F & F' \end{matrix} \right\} \end{aligned} \quad (4.20)$$

A note of caution regarding the parity is needed. It is obvious from Eq. (4.14) that the transformation of the basis functions under the parity operator involves a phase factor $(-1)^S$. The effective singlet-triplet transition dipole moment function is determined by the admixture of an excited singlet Π state into the triplet Π state considered. This admixture is caused by spin-orbit coupling and was represented in the effective triplet wavefunctions as $\sqrt{1 - c_{\text{SO}}^2} | a^3\Pi_{\pm 1} \rangle \pm c_{\text{SO}} | A^1\Pi_{\pm 1} \rangle$. In the basis functions of Eq. (4.14) the sign of Λ , Ω , and Σ is changed when the parity operator acts upon them, but in addition the triplet ($S = 1$) and singlet ($S = 0$) functions obtain a different sign because of the phase factor $(-1)^{J-S}$. Therefore, parity requires a \pm sign in front of the coefficient c_{SO} , which corresponds to the sign of Ω . With the parity-adapted basis of Eq. (4.14) this ensures that mixing of the singlet and triplet Π functions occurs only when they have the same parity. The parity of the ground state CO–He basis functions is given by $(-1)^{J+L}$. The dipole moment function μ_m^{SF} has odd parity and, hence, the parity of the excited singlet and triplet Π levels must be opposite to the parity of the singlet ground state level.

From the transition dipole moments we calculate the line strengths

$$S(f \leftarrow i) = \sum_{M'_F, m, M_F} |\langle f; F', M'_F | \mu_m^{\text{SF}} | i; F, M_F \rangle|^2, \quad (4.21)$$

where

$$\begin{aligned} |i; F, M_F\rangle &= \sum_{n, J, L} |n, 0, 0, 0, J, L; F, M_F\rangle c_{n, J, L}^{i, F} \\ |f; F', M'_F\rangle &= \sum_{n', \Lambda, \Omega, J', L'} |n', \Lambda, S, \Omega, J', L'; F', M'_F\rangle c_{n', \Lambda, \Omega, J', L'}^{f, F'} \end{aligned} \quad (4.22)$$

are the eigenstates of the ground state and triplet excited CO-He complex, respectively, expanded in the basis of Eq. (4.15). Substitution of Eq. (4.20) into this line strength expression yields

$$\begin{aligned} S(f \leftarrow i) &= (2F' + 1)(2F + 1) \left| \sum_{n', n} \sum_{L', L} \sum_{J', J} \sum_{\Lambda, \Omega} [(2J' + 1)(2J + 1)]^{1/2} \right. \\ &\times \delta_{n', n} \delta_{L', L} c_{n', \Lambda, \Omega, J', L'}^{f, F'} c_{n, J, L}^{i, F} \quad (4.23) \\ &\times \sum_{k=-1, 1} (-1)^{L-k} \mu_k^{\text{trans}} \begin{pmatrix} J' & 1 & J \\ -\Omega & k & 0 \end{pmatrix} \left\{ \begin{matrix} 1 & J' & J \\ L & F & F' \end{matrix} \right\} \Big|^2. \end{aligned}$$

The 6- j coefficient gives the selection rule $\Delta F = 0, \pm 1$. Approximate selection rules that hold for the approximate quantum numbers J and L of the ground and excited levels are $\Delta J = 0, \pm 1$ and $\Delta L = 0$. The approximate selection rule that causes mainly the triplet levels with $|\Omega| = 1$ to be excited was already discussed above. Also the exact parity selection rule was mentioned above.

4.5 Computational procedure

A Fortran program was written to calculate the vibration-rotation-spin levels of ground state CO($X^1\Sigma$)-He and excited CO($a^3\Pi$)-He by diagonalization of the Hamilton matrix derived in Sec. 4.3 with the use of the potential surfaces from Sec. 4.2. Examination of the convergence of both the ground and excited state levels showed that the rotation-spin basis could be truncated at $J_{\text{max}} = 12$, while L is running over all values allowed by the triangular rule for a given quantum number F . The radial basis $|n\rangle$ consisted of 15 functions. The nonlinear parameters $R_e = 11.618 a_0$, $D_e = 14.376 \text{ cm}^{-1}$, and $\omega_e = 9.876 \text{ cm}^{-1}$ in this basis that determine the Morse potential to which it corresponds, were variationally optimized in calculations with smaller basis sets. To avoid a nonorthogonality problem in the computation of the transition dipole moments we used the same basis for ground state CO($X^1\Sigma$)-He and excited CO($a^3\Pi$)-He. The vibration-rotation-spin levels were calculated for $F = 0, 1, 2, 3$, and 4. This provided all the bound states of CO($X^1\Sigma$)-He that are occupied at $T = 5 \text{ K}$ and all the excited triplet states in the desired energy range that are accessible by transitions from the occupied ground state

levels. The temperature of 5 K was chosen after consultation with the experimentalists [61]. The singlet-triplet transition line strengths were computed from the corresponding eigenfunctions with the expressions given in Sec. 4.4. A Boltzmann distribution was taken over the levels of ground state CO–He and combined with the energies of the ground and excited levels and with the line strengths to generate the spectrum that corresponds to the bound-bound transitions.

4.6 Results

Table 4.2: Bound energy levels of CO–He in its $X^1\Sigma^+$ ground state.

Quantum numbers		Energy (cm ⁻¹)	Main character		
F	p		J	L	
0	1	-5.9742	0	0	91.2%
0	1	-0.7161	1	1	76.2%
1	1	-1.6978	1	1	97.1%
2	1	-4.2987	0	2	90.4%
2	1	-1.2728	1	1	86.1%
4	1	-0.5635	0	4	90.3%
1	-1	-5.4115	0	1	90.9%
1	-1	-1.9781	1	0	86.0%
2	-1	-0.5498	1	2	97.3%
3	-1	-2.6645	0	3	90.0%
3	-1	-0.1154	1	2	85.6%

Table 4.2 lists the bound levels of CO($X^1\Sigma^+$)–He. Their energies as well as the contributions of the dominant angular components in the wavefunctions are in good agreement with the results of Refs. [85, 66]. The bound states of CO($a^3\Pi$)–He are listed in Table 4.3. For each bound state we present its energy, the F and p quantum numbers, and the dominant (Ω, J, L) angular function involved in the total wave function. None of the excited CO($a^3\Pi$)–He levels is truly bound, of course, but the life times of the $a^3\Pi$ levels of free CO are on the order of milliseconds. So we expected in first instance that the levels of the $^3\Pi$ excited CO–He complex are similarly long lived and can be calculated with a bound state program. It turned out that this holds only for the $\Omega = 0$ levels, however. As we mentioned already in the discussion of the free CO($a^3\Pi$) levels the $|\Omega| = 1$ levels are about 40 cm⁻¹ above the $\Omega = 0$ levels and the $|\Omega| = 2$ levels are higher by another 40 cm⁻¹, mainly due to spin-orbit coupling. The same picture holds more or less for the CO($a^3\Pi$)–He complex, although there are many more levels due to the Van der Waals vibrations and

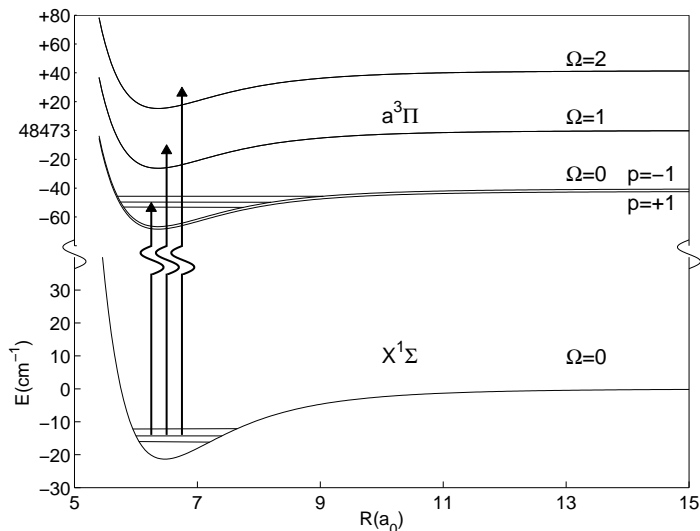
overall rotations of the complex. The wells in the A' and A'' potentials of $\text{CO}(a^3\Pi)\text{-He}$ are about 30 cm^{-1} deep, not much deeper than the well in the ground state $\text{CO}(X^1\Sigma^+)\text{-He}$ potential. In the ground state complex there is a large amount of zero-point energy which leads to a dissociation energy D_0 of only about 7 cm^{-1} . Similarly, the D_0 value for the triplet excited complex is about 8 cm^{-1} , relative to the corresponding Ω levels of free CO. This is schematically shown in Fig. 4.4. Hence, the quasi-bound levels of the triplet CO-He complex with $|\Omega| = 1$ and $|\Omega| = 2$ lie in the continuum of the CO-He state with $\Omega = 0$.

Table 4.3: Bound energy levels of CO-He in its $a^3\Pi$ state. The energy of the two parity levels with $J = \Omega = 0$ of free CO are -40.621 cm^{-1} and -38.871 cm^{-1} . All energies are relative to the CO triplet band origin at 48473.201 cm^{-1} .

Quantum numbers		Energy (cm^{-1})	Main character			
F	p		Ω	J	L	
0	1	-48.2872	0	0	0	83.2%
0	-1	-46.5447	0	0	0	83.0%
0	1	-43.0992	0	1	1	76.2%
1	1	-45.9702	0	0	1	81.6%
1	-1	-47.7129	0	0	1	81.7%
1	1	-44.4316	0	1	1	91.7%
1	-1	-42.6912	0	1	1	91.5%
1	1	-42.9302	0	1	0	75.8%
1	-1	-44.6680	0	1	0	75.9%
1	-1	-42.3730	0	1	2	71.4%
2	1	-46.5759	0	0	2	78.7%
2	-1	-44.8327	0	0	2	78.5%
2	1	-43.8515	0	1	1	72.4%
2	-1	-42.1165	0	1	1	72.2%
2	-1	-43.2249	0	1	2	91.6%
3	1	-43.1565	0	0	3	73.7%
3	-1	-44.9002	0	0	3	73.9%
3	-1	-42.5484	0	1	2	67.2%
4	1	-42.7255	0	0	4	67.4%

We found that they could not be converged with a bound state program; their energies kept going down upon increase of the radial basis $|n\rangle$. After explicit photodissociation studies, which are presented in chapter 5, we concluded that they rapidly predissociate by a spin-orbit coupling mechanism. The dissociation product is not ground state $\text{CO}(X^1\Sigma^+)$ but metastable $\text{CO}(a^3\Pi)$ in its $\Omega = 0$ state. Table 4.3 contains only the $\text{CO}(a^3\Pi)\text{-He}$ levels with $\Omega = 0$ that are

Figure 4.4: Schematic energy level structure of ground state $\text{CO}(X^1\Sigma^+)$ -He and UV excited $\text{CO}(a^3\Pi)$ -He at 48473.201 cm^{-1} .

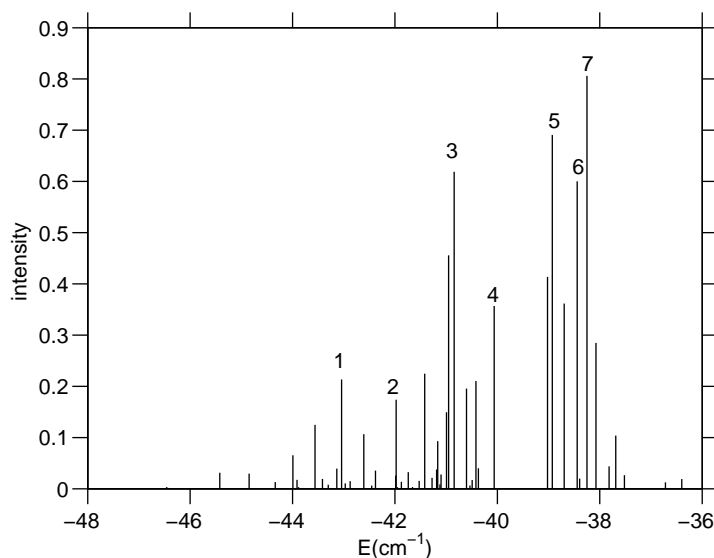


stable with respect to dissociation into He and triplet CO. One clearly observes the Λ -doubling splitting of about 1.75 cm^{-1} between the pairs of levels with opposite parity. Some of the doublets are incomplete, see for example the third row of Table 4.3, because the upper level lies above the dissociation threshold at -41.45 cm^{-1} . One can also observe in Tables 4.2 and 4.3 that the Van der Waals levels of triplet excited CO-He are somewhat more mixed in J and L by the anisotropic potential than those of ground state CO-He. However, this mixing is still sufficiently weak that one can use these approximate quantum numbers as useful labels of the energy levels.

Although the singlet-triplet transition in CO is only allowed by the spin-orbit mixing of the excited $a^3\Pi$ state with the $A^1\Pi_1$ state and most of the excitation intensity goes into the triplet levels with $|\Omega| = 1$, there is also a part of the spectrum that originates from excitations of the levels with $\Omega = 0$. These transitions become allowed by admixture of $|\Omega| = 1$ basis functions into the levels with predominantly $\Omega = 0$. Tables 4.5 and 4.4 list the line strengths of the allowed bound-bound transitions of both parities. The frequencies of these transitions are defined as $\omega_{fi} = E_f - E_i$ relative to the band origin at 48473.201 cm^{-1} of the $a^3\Pi \leftarrow X^1\Sigma^+$ transition in free CO. The intensities are in units of the effective singlet-triplet transition dipole moment $\mu_{\perp}^{\text{trans}}$ squared. We notice that some of the lines do not respect the approximate selection rule

$\Delta L = 0$. The most intense lines obey this rule, however. This confirms that the CO–He complex behaves as a slightly hindered rotor also in its triplet excited state, in spite of the more complex nature of this state which contains two diabatic components and a rather anisotropic potential $V_{1,-1} = V_{A''} - V_{A'}$ coupling these components. Figure 4.5 shows a stick spectrum of this bound-bound part of the spectrum.

Figure 4.5: Theoretical bound-bound spectrum of the $a^3\Pi \leftarrow X^1\Sigma^+$ transition in CO–He. The frequencies are relative to the band origin ($48473.201 \text{ cm}^{-1}$) of the singlet-triplet transition in free CO. Line strength's in units of $0.01(\mu_{\perp}^{trans})^2$. For the assignment of the numbered peaks, see Tables 4.5 and 4.4



4.7 Conclusions

The potential surfaces of the CO–He complex that correspond to the ground $X^1\Sigma^+$ state and the excited $a^3\Pi$ state of CO were calculated by CCSD(T) methods. The interaction of He with CO($a^3\Pi$) gives rise to two potential surfaces which are degenerate at linear geometries of the complex. The Van der Waals bound states of the ground and excited state complex were obtained from variational calculations. The bound states of ground state CO($X^1\Sigma^+$)–He are in good agreement with earlier studies [85, 66]. In the calculation of the bound levels of excited CO($a^3\Pi$)–He we used a diabatic representation of the two potential surfaces and the corresponding vibration-rotation-spin basis.

Only the lowest spin-orbit levels with $\Omega = 0$ were found to be truly metastable quasi-bound states. Since these states can only decay by de-excitation into the ground singlet state, their life times will be comparable to those of free $\text{CO}(a^3\Pi)$. In spite of the more complex nature of the excited state with its two diabatic components coupled by a rather anisotropic potential it behaves as a slightly hindered internal rotor complex, although not quite as weakly hindered as in the ground state.

From the wavefunctions of the ground and excited state vibration-rotation-spin levels of the complex we computed the line strengths of the singlet-triplet transitions and generated that part of the spectrum that corresponds to excitation of the metastable $\Omega = 0$ levels of $\text{CO}(a^3\Pi)\text{-He}$. This is only the lower part of the total spectrum, most of the intensity goes into excitation of the triplet levels with $|\Omega| = 1$. These levels, and also the still higher spin-orbit levels with $|\Omega| = 2$, could not be converged with the bound state program. They couple to the continuum levels of the lowest spin-orbit state with $\Omega = 0$ and predissociate. This spin-orbit dissociation mechanism is the subject of chapter 5, which describes explicit photo-dissociation studies. The life times of the quasi-bound triplet states with $|\Omega| = 1$ and $|\Omega| = 2$, i.e., the spectral line widths, and the principal part of the singlet-triplet excitation spectrum of the CO-He complex will be presented in that chapter.

Table 4.4: Frequencies in cm^{-1} relative to the singlet-triplet band origin of free CO ($48473.201 \text{ cm}^{-1}$) and line strengths $S(f \leftarrow i)$ in units of $0.01 (\mu_{\perp}^{\text{trans}})^2$ of the $a^3\Pi \leftarrow X^1\Sigma^+$ transition for odd parity $X^1\Sigma^+$ states and even parity $a^3\Pi$ states.

Number in Fig. 4.5	$(F', J', L') \leftarrow (F, J, L)$	ω_{fi}	Line strength
	(0, 0, 0) \leftarrow (1, 0, 1)	-42.8757	0.0149
	(0, 1, 1) \leftarrow (1, 0, 1)	-37.6877	0.1039
	(0, 0, 0) \leftarrow (1, 1, 0)	-46.3091	0.0008
	(0, 1, 1) \leftarrow (1, 1, 0)	-41.1211	0.0086
	(1, 0, 1) \leftarrow (1, 0, 1)	-40.5587	0.0013
	(1, 1, 1) \leftarrow (1, 0, 1)	-39.0202	0.4137
	(1, 1, 0) \leftarrow (1, 0, 1)	-37.5187	0.0265
	(1, 0, 1) \leftarrow (1, 1, 0)	-43.9921	0.0653
	(1, 1, 1) \leftarrow (1, 1, 0)	-42.4536	0.0062
	(1, 1, 0) \leftarrow (1, 1, 0)	-40.9521	0.4557
	(2, 0, 2) \leftarrow (1, 0, 1)	-41.1644	0.0929
6	(2, 1, 1) \leftarrow (1, 0, 1)	-38.4400	0.6003
	(2, 0, 2) \leftarrow (1, 1, 0)	-44.5978	0.0000
	(2, 1, 1) \leftarrow (1, 1, 0)	-41.8735	0.0136
	(1, 0, 1) \leftarrow (2, 1, 2)	-45.4204	0.0312
	(1, 1, 1) \leftarrow (2, 1, 2)	-43.8818	0.0030
	(1, 1, 0) \leftarrow (2, 1, 2)	-42.3804	0.0356
	(2, 0, 2) \leftarrow (2, 1, 2)	-46.0261	0.0010
	(2, 1, 1) \leftarrow (2, 1, 2)	-43.3017	0.0080
	(3, 0, 3) \leftarrow (2, 1, 2)	-42.6067	0.1066
	(2, 0, 2) \leftarrow (3, 0, 3)	-43.9114	0.0175
	(2, 1, 1) \leftarrow (3, 0, 3)	-41.1871	0.0377
	(2, 0, 2) \leftarrow (3, 1, 2)	-46.4604	0.0030
	(2, 1, 1) \leftarrow (3, 1, 2)	-43.7361	0.0000
	(3, 0, 3) \leftarrow (3, 0, 3)	-40.4920	0.0170
1	(3, 0, 3) \leftarrow (3, 1, 2)	-43.0411	0.2135
4	(4, 0, 4) \leftarrow (3, 0, 3)	-40.0610	0.3567
	(4, 0, 4) \leftarrow (3, 1, 2)	-42.6100	0.0000

Table 4.5: Frequencies in cm^{-1} relative to the singlet-triplet band origin of free CO ($48473.201 \text{ cm}^{-1}$) and line strengths $S(f \leftarrow i)$ in units of $0.01 (\mu_{\perp}^{\text{trans}})^2$ of the $a^3\Pi \leftarrow X^1\Sigma^+$ transition for even parity $X^1\Sigma^+$ states and odd parity $a^3\Pi$ states.

Number in Fig. 4.5	$(F', J', L') \leftarrow (F, J, L)$	ω_{fi}	Line strength
	(1, 0, 1) \leftarrow (0, 0, 0)	-41.7388	0.0325
	(1, 1, 0) \leftarrow (0, 0, 0)	-38.6938	0.3615
	(1, 1, 1) \leftarrow (0, 0, 0)	-36.7171	0.0125
	(1, 1, 2) \leftarrow (0, 0, 0)	-36.3988	0.0190
	(1, 0, 1) \leftarrow (0, 1, 1)	-46.9968	0.0001
	(1, 1, 0) \leftarrow (0, 1, 1)	-43.9518	0.0016
2	(1, 1, 1) \leftarrow (0, 1, 1)	-41.9751	0.1739
	(1, 1, 2) \leftarrow (0, 1, 1)	-41.6569	0.0033
	(0, 0, 0) \leftarrow (1, 1, 1)	-44.8469	0.0297
	(1, 0, 1) \leftarrow (1, 1, 1)	-46.0151	0.0004
	(1, 1, 0) \leftarrow (1, 1, 1)	-42.9702	0.0106
	(1, 1, 1) \leftarrow (1, 1, 1)	-40.9934	0.1493
	(1, 1, 2) \leftarrow (1, 1, 1)	-40.6752	0.0006
	(2, 0, 2) \leftarrow (1, 1, 1)	-43.1349	0.0393
	(2, 1, 2) \leftarrow (1, 1, 1)	-41.5271	0.0156
	(2, 1, 1) \leftarrow (1, 1, 1)	-40.4187	0.2105
	(1, 0, 1) \leftarrow (2, 0, 2)	-43.4142	0.0192
	(1, 1, 0) \leftarrow (2, 0, 2)	-40.3692	0.0400
	(1, 1, 1) \leftarrow (2, 0, 2)	-38.3925	0.0199
	(1, 1, 2) \leftarrow (2, 0, 2)	-38.0743	0.2847
	(1, 0, 1) \leftarrow (2, 1, 1)	-46.4401	0.0020
	(1, 1, 0) \leftarrow (2, 1, 1)	-43.3951	0.0004
	(1, 1, 1) \leftarrow (2, 1, 1)	-41.4184	0.2246
	(1, 1, 2) \leftarrow (2, 1, 1)	-41.1002	0.0280
	(2, 0, 2) \leftarrow (2, 0, 2)	-40.5339	0.0063
5	(2, 1, 2) \leftarrow (2, 0, 2)	-38.9262	0.6908
	(2, 1, 1) \leftarrow (2, 0, 2)	-37.8177	0.0438
	(2, 0, 2) \leftarrow (2, 1, 1)	-43.5599	0.1248
	(2, 1, 2) \leftarrow (2, 1, 1)	-41.9521	0.0030
3	(2, 1, 1) \leftarrow (2, 1, 1)	-40.8436	0.6189
	(3, 0, 3) \leftarrow (2, 0, 2)	-40.6014	0.1956
7	(3, 1, 2) \leftarrow (2, 0, 2)	-38.2496	0.8061
	(3, 0, 3) \leftarrow (2, 1, 1)	-43.6273	0.0000
	(3, 1, 2) \leftarrow (2, 1, 1)	-41.2756	0.0213
	(3, 0, 3) \leftarrow (4, 0, 4)	-44.3366	0.0131
	(3, 1, 2) \leftarrow (4, 0, 4)	-41.9849	0.0257

CHAPTER 5

Singlet-triplet excitation spectrum of the CO–He complex; II: Photodissociation and bound-free CO($a^3\Pi \leftarrow X^1\Sigma^+$) transitions

The dissociating states of the triplet-excited CO–He complex are studied by means of scattering calculations on *ab initio* diabatic potential energy surfaces introduced in the preceding chapter. With the aid of an effective transition dipole function and the bound states of the CO–He complex in the ground singlet state we obtain the photo-absorption cross section as a function of the excitation energy and generate the full UV spectrum of the singlet-triplet transition. It was found that the dominant contributions to the spectrum, in the energy range from -5 to $+10$ cm^{-1} relative to the band origin at 48473.201 cm^{-1} , originate from resonances that correspond to higher spin-orbit levels of the excited CO($a^3\Pi$)–He complex with approximate quantum number $|\Omega| = 1$. Rapid predissociation, with the triplet CO fragment decaying into its lower spin-orbit levels with $\Omega = 0$, limits the lifetime of these excited levels to, typically, 10 to 700 ps. We also predict the rotational and spin-orbit state distribution of the triplet CO fragment and the maximum deflection angle of the photodissociation products in a molecular beam experiment.

5.1 Introduction

The triplet ($a^3\Pi$) excited CO molecule is an interesting metastable species which has received considerable attention [86, 87, 56, 57, 88]. It can be cooled by electrostatic deceleration [60] of an already cold molecular beam and it lives sufficiently long to be used in scattering experiments [58, 59]. In the preceding chapter we studied the complexation of CO($a^3\Pi$) with a He atom. The presence of this He atom lifts the spatial degeneracy of the CO($a^3\Pi$) state and splits it into an A' state and an A'' state. These states are even and odd, respectively, under reflection in the plane of the nuclei. We computed the adiabatic potential surfaces of CO($a^3\Pi$)-He that correspond to these A' and A'' symmetries by the spin-restricted coupled cluster method with single and double excitations and perturbative triples [RCCSD(T)]. Nonadiabatic coupling is important, because these surfaces are degenerate for linear geometries, and we constructed two diabatic potential surfaces. After making an analytic fit of these diabatic potentials we computed the bound levels of the triplet excited CO-He complex by a variational method, with the inclusion of the spin-orbit and spin-spin couplings.

We also wanted to compute the UV spectrum that corresponds to the singlet-triplet transition in the CO-He complex, but it turned out that for most of the excited upper levels it was impossible to converge the variational bound state calculations. From experimentation with the radial basis we learned that this problem was probably due to a fast dissociative decay of the upper levels, on a time scale that is much shorter than de-excitation of the CO($a^3\Pi$) monomer to its ground singlet ($X^1\Sigma^+$) state. This rapid decay is not caused by the effect that the presence of the He atom accelerates the triplet-singlet de-excitation process, but originates from a completely different mechanism: spin-orbit predissociation. In order to understand this mechanism one should know that the triplet excited CO molecule is a typical Hund's case (a) species with three series of $^3\Pi_\Omega$ levels, characterized by the quantum numbers $|\Omega| = 0, 1, \text{ and } 2$, and split by spin-orbit coupling by approximately 40 cm^{-1} . The quantum number Ω is the projection of the total electronic (orbital plus spin) angular momentum $\mathbf{l} + \mathbf{S}$ of CO($a^3\Pi$) on the CO bond axis and, simultaneously, the axial component of the total angular momentum \mathbf{J} of CO. The spin-forbidden $a^3\Pi \leftarrow X^1\Sigma^+$ transition in CO becomes weakly allowed by some admixture of the singlet $A^1\Pi$ state into the excited triplet $a^3\Pi$ state, caused by spin-orbit coupling, combined with the fact that the $A^1\Pi \leftarrow X^1\Sigma^+$ transition is an allowed (perpendicular) transition. Only the CO($^3\Pi_\Omega$) levels with $\Omega = \pm 1$ would be excited by this transition if Ω were an exact quantum number, but for $J > 0$ it is not. Still, for low J the transitions to the $^3\Pi_{\pm 1}$ levels are by far the most intense. These levels are higher in energy than the $^3\Pi_0$ levels by about 40 cm^{-1} and, since the binding energy D_0 of the CO($a^3\Pi$)-He complex is only about 8 cm^{-1} , they can decay into CO($^3\Pi_0$) and He. This process is called spin-orbit predissociation; the CO fragments produced by it are still in

their metastable triplet state, in the lowest spin-orbit component.

In the present chapter we study this process by means of coupled-channel calculations with photodissociation boundary conditions. These calculations include both diabatic states of $\text{CO}(a^3\Pi)\text{-He}$ simultaneously, and they also include the spin-orbit, spin-spin, an Λ -doubling terms in the Hamiltonian of chapter 4. From the bound levels of ground state $\text{CO}(X^1\Sigma^+)\text{-He}$ (see also chapter 4) and the continuum states obtained from the coupled-channel calculations we compute the photodissociation cross sections. An effective transition dipole function for the spin-forbidden $a^3\Pi \leftarrow X^1\Sigma^+$ transition was constructed in chapter 4. From the widths of the resonances in the photodissociation cross section we extract the lifetimes of the excited upper levels. The partial cross sections yield the distributions of the $\text{CO}(^3\Pi)$ fragments over the rotation (J), spin-orbit (Ω), and parity (ϵ) levels. Finally, we generate the full UV absorption spectrum and suggest how the presence of the excited $\text{CO}(a^3\Pi)\text{-He}$ complex can be detected even though it undergoes rapid predissociation.

5.2 Photodissociation calculations

5.2.1 Coupled-Channel formalism

The CO monomer was considered as a rigid rotor with bond length $r_e = 2.132 a_0$ for the ground $X^1\Sigma^+$ state and $r_e = 2.279 a_0$ for the triplet excited $a^3\Pi$ state. The Hamiltonian of the $\text{CO}(a^3\Pi)\text{-He}$ complex is given by Eq. 4.12 in the previous chapter with the diabatic potentials $V_{1,1}(R, \theta)$ and $V_{1,-1}(R, \theta)$ related to the *ab initio* computed adiabatic A' and A'' potentials by Eq. 4.4. The coordinate R is the length of the vector \mathbf{R} from the CO center of mass to the He nucleus and θ is the angle between the CO bond axis and the vector \mathbf{R} .

The parity-adapted Hund's case (a) basis for the CO monomer is given by

$$\begin{aligned} | |\Lambda|, S, \Omega, J, M_J, \epsilon \rangle &= 2^{-1/2} \left[| \Lambda, S, \Omega, J, M_J \rangle \right. \\ &\quad \left. + \epsilon(-1)^{J-S} | -\Lambda, S, -\Omega, J, M_J \rangle \right] \end{aligned} \quad (5.1)$$

and defined more in detail by Eqs. 4.13 and 4.14. The total angular momentum quantum numbers J and Ω were already defined in the Introduction and ϵ is the parity under inversion. The electronic orbital angular momentum $|\Lambda|$ equals 1 for the $a^3\Pi$ state and the spin S equals 1 as well, so we can introduce the shorthand notation $|\Omega, J, M_J, \epsilon \rangle \equiv | |\Lambda|, S, \Omega, J, M_J, \epsilon \rangle$. The CO monomer Hamiltonian \hat{H}_{CO} is defined by Eq. 4.10. The exact eigenfunctions of this Hamiltonian can be written as

$$| k, J, M_J, \epsilon \rangle = \sum_{\Omega} | \Omega, J, M_J, \epsilon \rangle a_{\Omega, k}^J. \quad (5.2)$$

The corresponding energies are $E_{kJ\epsilon}$. This implies that Ω is not an exact quantum number except for $J = 0$.

For the CO($a^3\Pi$)-He complex we couple the CO monomer basis of Eq. (5.1) to a set of spherical harmonics $|L, M_L\rangle = Y_{L, M_L}(\beta, \alpha)$ that describe the end-over-end rotation of the CO-He complex

$$\begin{aligned} |\Omega, J, L\rangle^{F, M_F, p} &\equiv | |\Lambda|, S, \Omega, J, L, F, M_F, p \rangle \\ &= \sum_{M_J M_L} | |\Lambda|, S, \Omega, J, M_J, \epsilon \rangle | LM_L \rangle \langle JM_J; LM_L | FM_F \rangle. \end{aligned} \quad (5.3)$$

The operator \widehat{L} represents the angular momentum associated with the end-over-end rotation and (β, α) are the polar angles of \mathbf{R} with respect to a space-fixed (SF) frame. The coupled functions, with the Clebsch-Gordan coefficients $\langle JM_J; LM_L | FM_F \rangle$ [39], are eigenfunctions of \widehat{F}^2 and $\widehat{F} = \widehat{J} + \widehat{L}$ is the total angular momentum operator. The quantum number F and its SF component M_F are exact quantum numbers. Also the parity p which is related to the parity ϵ of the monomer functions by $p = \epsilon(-1)^L$ is an exact quantum number. This is the same basis as used in Eq. 4.15, with the exclusion of the radial functions $|n\rangle$.

Scattering wavefunctions for the CO($a^3\Pi$)-He complex for given energy E can be expanded in terms of the channel basis functions of Eq. (5.3) as

$$|k, J, L; E\rangle^{F, M_F, p} = \sum_{\Omega' J' L'} | \Omega', J', L' \rangle^{F, M_F, p} R^{-1} \chi_{\Omega', J', L'}^{k, J, L}(R; E). \quad (5.4)$$

The exact quantum numbers F, p are omitted from the notation of the radial expansion functions $\chi_{\Omega, J, L}^{k, J, L}(R; E)$. Note that the upper label of these functions corresponds to their asymptotic behavior for $R \rightarrow \infty$. It refers to the exact eigenstates $|k, J, \epsilon\rangle$ of the CO monomer with $\epsilon = p(-1)^L$, rather than to the monomer basis functions $|\Omega, J, \epsilon\rangle$.

The expansion functions $\chi_{\Omega', J', L'}^{k, J, L}(R; E)$ satisfy the standard coupled-channel (CC) equations

$$-\frac{d^2 \chi_{\Omega', J', L'}^{k, J, L}(R; E)}{dR^2} = \sum_{\Omega'' J'' L''} W_{\Omega', J', L'; \Omega'', J'', L''}(R) \chi_{\Omega'', J'', L''}^{k, J, L}(R; E), \quad (5.5)$$

where $W_{\Omega', J', L'; \Omega'', J'', L''}(R)$ are the matrix elements of the operator

$$\widehat{W}(R, \theta) = \frac{2\mu}{\hbar^2} \left(E - \widehat{H}_{\text{CO}} - \frac{\widehat{L}^2}{2\mu R^2} - \sum_{\Lambda_1, \Lambda_2} | \Lambda_1 \rangle V_{\Lambda_1, \Lambda_2}(R, \theta) \langle \Lambda_2 | \right) \quad (5.6)$$

over the basis functions of Eq. (5.3) and μ is the reduced mass of the complex. The exact quantum numbers F and p are again omitted from the notation. The W matrix elements are computed with the aid of Eqs. 4.16 and 4.17. The diabatic potentials $V_{\Lambda_1, \Lambda_2}(R, \theta)$ with $\Lambda_1, \Lambda_2 = \pm 1$ are also described in chapter

4. Usually, in the CC method one uses the eigenstates of the monomers as channel functions in the scattering problem. Here, we kept the Hund's case (a) basis $|\Omega, J, L\rangle$ in the propagation because the calculation of the W matrix and the dipole transition matrix is more straightforward. Note that \hat{H}_{CO} is not diagonal in this basis.

The boundary conditions for photodissociation are the reverse of the usual scattering boundary conditions [89]. The asymptotic form of the expansion functions for $R \rightarrow \infty$ is

$$\chi_{k',J',L'}^{k,J,L}(R; E) = v_{k',J',L'}(R; E)\delta_{kk'}\delta_{JJ'}\delta_{LL'} - u_{k',J',L'}(R; E) \left(S_{k',J',L'}^{k,J,L} \right)^* \quad (5.7)$$

where \mathbf{v} represents the outgoing waves, \mathbf{u} the incoming waves and \mathbf{S} the S matrix. The expansion functions should be regular solutions of the coupled equations, i.e. $\chi_{k',J',L'}^{k,J,L}(R=0; E) = 0$ and

$$\begin{aligned} v_{k,J,L}(R; E) &= +i\sqrt{\frac{k_{kJ\epsilon}\mu}{2\pi\hbar^2}} R h_L^{(1)}(k_{kJ\epsilon}R), \\ u_{k,J,L}(R; E) &= -i\sqrt{\frac{k_{kJ\epsilon}\mu}{2\pi\hbar^2}} R h_L^{(2)}(k_{kJ\epsilon}R) \end{aligned} \quad (5.8)$$

where $h_L^{(1)}(k_{kJ\epsilon}R)$ and $h_L^{(2)}(k_{kJ\epsilon}R)$ are modified spherical Bessel functions of the first and second kind, respectively, $E_{kJ\epsilon}$ are the exact energy levels of the free CO monomer, and $k_{kJ\epsilon} = \sqrt{2\mu(E - E_{kJ\epsilon})/\hbar^2}$. The prefactor $\sqrt{k_{kJ\epsilon}\mu/2\pi\hbar^2}$ originates from the energy normalization of the wavefunctions. All open channels ($E_{kJ\epsilon} < E$) and the closed channels ($E_{kJ\epsilon} > E$) with J up to a given value J_{max} were included in the calculation.

The incoming and outgoing waves \mathbf{u} and \mathbf{v} and the radial expansion functions in Eq. (5.7) correspond to the exact CO eigenstates $|k, J, \epsilon\rangle$ rather than to the Hund's case (a) basis $|\Omega, J, \epsilon\rangle$ used in the propagation. Therefore, a transformation of the boundary conditions was included in the procedure to compute the S matrix at the end of the propagation. The elements of the required transformation matrix are the eigenvector coefficients $a_{\Omega,k}^J$ in Eq. (5.2).

5.2.2 Matching procedure for bound states

In order to calculate the radial integrals in the expression of the photodissociation cross section (see below) it is necessary to compute the bound wavefunctions of ground state CO($X^1\Sigma^+$)–He on the same radial grid as the scattering functions of CO($a^3\Pi$)–He. These bound wavefunctions were calculated variationally in chapter 4, and it would be easy to evaluate them on a grid. As an additional check of the convergence of the variational calculations we found it useful, however, to recompute the bound levels with our scattering program. Methods to obtain bound states from a scattering propagation procedure have been known for a long time [90, 91, 92, 93].

The angular basis for ground state CO($X^1\Sigma^+$)-He is given in principle by Eq. (5.3), but it is much simpler than the basis for the triplet state since $\Lambda = S = \Sigma = \Omega = 0$ in the ground state. We denote the basis by $|J, L, F, M_F, p\rangle$ or, for given F, M_F, p , by the shorthand notation $|J, L\rangle$. It is parity-adapted automatically with parity $p = (-1)^{J+L}$. The bound state wavefunctions are

$$|b\rangle = \sum_{J,L} |J, L\rangle R^{-1} f_{J,L}(R). \quad (5.9)$$

The radial expansion functions $f_{J,L}(R)$, put into a column vector $\mathbf{f}(R)$ with components labeled by (J, L) , and the corresponding eigenvalues E_b are obtained from a matching procedure that we now briefly describe.

In the renormalized Numerov method applied in our scattering program one propagates matrices \mathbf{Q}_n outward on a grid $R_n; n = 1, \dots, N$. These matrices \mathbf{Q}_n are defined by

$$\mathbf{f}(R_n) = \mathbf{Q}_{n+1} \mathbf{f}(R_{n+1}). \quad (5.10)$$

and the condition that the radial wavefunctions $\mathbf{f}(R)$ are regular, i.e., that they vanish for $R \rightarrow 0$. Since the bound state wavefunctions must also go to zero for $R \rightarrow \infty$ we define another set of matrices $\tilde{\mathbf{Q}}_n$ by

$$\tilde{\mathbf{f}}(R_{n+1}) = \tilde{\mathbf{Q}}_n \tilde{\mathbf{f}}(R_n). \quad (5.11)$$

with functions $\tilde{\mathbf{f}}(R_n)$ that vanish for $R \rightarrow \infty$. The inward propagation of $\tilde{\mathbf{Q}}_n$ is analogous to the scattering calculation, but is started at a value of R where the bound state wavefunctions may be assumed to be negligibly small. The functions $\mathbf{f}(R)$ and $\tilde{\mathbf{f}}(R)$ match only when the scattering energy E is equal to the energy E_b of one of the (discrete) bound levels. Numerically this is achieved by setting $\tilde{\mathbf{f}}(R_n) = \mathbf{f}(R_n)$ and finding a zero of the norm

$$\|\tilde{\mathbf{f}}(R_{n+1}) - \mathbf{f}(R_{n+1})\| = \|(\tilde{\mathbf{Q}}_n - (\mathbf{Q}_{n+1})^{-1}) \mathbf{f}(R_n)\|. \quad (5.12)$$

We impose the additional condition that the bound state wavefunctions $|b\rangle$ are normalized, i.e.,

$$\langle b | b \rangle = \Delta \sum_{i=1}^N \mathbf{f}^T(R_i) \mathbf{f}(R_i) = 1, \quad (5.13)$$

where Δ is the step size in the propagation. This condition ensures that $\mathbf{f}(R_n)$ cannot be zero since the wavefunctions $\mathbf{f}(R_i)$ for all R_i are linearly related to the wavefunction $\mathbf{f}(R_n) = \tilde{\mathbf{f}}(R_n)$ at the matching point by

$$\mathbf{f}(R_i) = \mathbf{A}_i \mathbf{f}(R_n), \quad (5.14)$$

with $\mathbf{A}_n = \mathbf{1}$ and \mathbf{A}_i defined by the recursion relations

$$\begin{aligned} \mathbf{A}_{i-1} &= \mathbf{Q}_i \mathbf{A}_i & \text{for } i \leq n \\ \mathbf{A}_{i+1} &= \tilde{\mathbf{Q}}_i \mathbf{A}_i & \text{for } i \geq n. \end{aligned} \quad (5.15)$$

These relations follow directly from Eqs. (5.10) and (5.11). After substitution of Eq. (5.14) the normalization condition, Eq. (5.13), can be written as

$$\mathbf{f}^T(R_n)\mathbf{B}\mathbf{f}(R_n) = 1 \quad (5.16)$$

with

$$\mathbf{B} = \Delta \sum_{i=1}^N \mathbf{A}_i^T \mathbf{A}_i. \quad (5.17)$$

The matrix \mathbf{B} , Eqs. (5.17) and (5.15), is computed from the matrices \mathbf{Q}_j and $\tilde{\mathbf{Q}}_j$ at the end of the propagation. We define

$$\mathbf{x} = \mathbf{B}^{1/2}\mathbf{f}(R_n) \quad \text{and} \quad \mathbf{C} = \left(\tilde{\mathbf{Q}}_n - (\mathbf{Q}_{n+1})^{-1} \right) \mathbf{B}^{-1/2} \quad (5.18)$$

in order to rewrite Eqs. (5.12) and (5.16) as

$$\|\tilde{\mathbf{f}}(R_{n+1}) - \mathbf{f}(R_{n+1})\| = \|\mathbf{C}\mathbf{x}\| \quad \text{with} \quad \|\mathbf{x}\| = 1. \quad (5.19)$$

The minimum of $\|\mathbf{C}\mathbf{x}\|/\|\mathbf{x}\|$ over all \mathbf{x} is known as the smallest singular value of the matrix \mathbf{C} , as obtained from a singular value decomposition (SVD) [94] of this matrix. We start with an appropriate set of trial energies and consider the smallest singular value as shown in Fig. 5.1, for example. The energies where the zeros occur, i.e., the bound state energies E_b , are found by linear extrapolation. The accuracy can be improved by iteration, but it turned out that this was not necessary in most cases. The corresponding wavefunctions $|b\rangle$ are obtained from propagation at the energies E_b .

5.2.3 Photodissociation cross sections

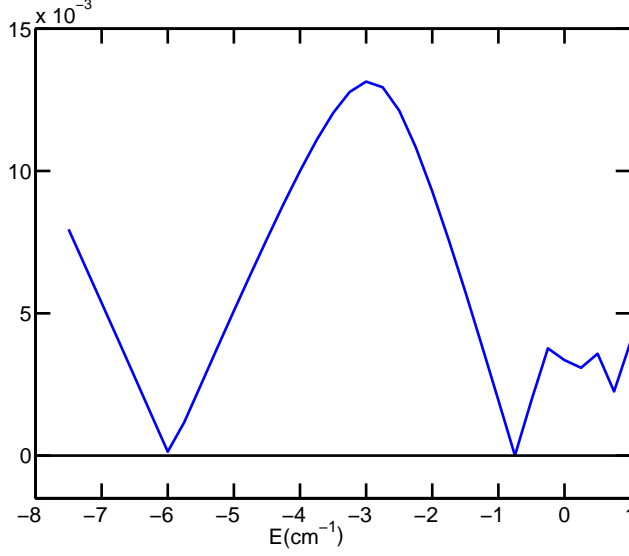
In order to predict the results of future measurements we calculated partial and total photodissociation cross sections and product state distributions. These cross sections are used to generate a theoretical UV absorption spectrum for the singlet-triplet transition in CO–He.

The partial photodissociation cross section for a transition from bound state $|b, F, M_F, p\rangle$ of energy $E_b^{F,p}$ to a dissociating state of energy E with the CO fragment in state $|k, J, \epsilon\rangle$ is [89]

$$\sigma_{k,J,\epsilon \leftarrow b,F,p}(E) = \frac{\pi\omega}{c\epsilon_0} \sum_{F'M'_F L M_F} \left| \langle k, J, L; E | \mathbf{e} \cdot \hat{\boldsymbol{\mu}} | b, F, M_F, p \rangle \right|^2, \quad (5.20)$$

where $\omega = (E - E_b^{F,p})/\hbar$ is the frequency, \mathbf{e} the direction of the electric field vector of the laser beam, c the velocity of light, and ϵ_0 the vacuum dielectric constant. The scattering wavefunctions $|k, J, L; E\rangle^{F',M'_F,p'}$ are defined in Eq. (5.4). The matrix elements of the effective dipole moment operator $\hat{\boldsymbol{\mu}}$

Figure 5.1: Smallest singular value of the matrix C in Eq. (5.18) for $F = 0$ versus the trial energy. Linear extrapolation gives the bound state energies $E_1 = -5.9748 \text{ cm}^{-1}$ and $E_2 = -0.7502 \text{ cm}^{-1}$.



over the basis of Eq. (5.3) and the corresponding selection rules are given in Eq. 4.20. For given parity p of the initial bound state the parity p' of the scattering state must be opposite to p . The parity ϵ of the triplet CO dissociation fragment can be even or odd, because of the relation $p = \epsilon(-1)^L$ and the summation over L occurring in the cross section.

The total photodissociation cross section is a sum over the partial cross sections

$$\sigma_{b,F,p}(E) = \sum_{k,J,\epsilon} \sigma_{k,J,\epsilon \leftarrow b,F,p}(E). \quad (5.21)$$

The singlet-triplet UV absorption spectrum at a given temperature T is obtained by taking a Boltzmann distribution over the initial states $|b, F, p\rangle$

$$\sigma(\omega) = \sum_{b,F,p} \int_E dE \delta(E - E_b^{F,p} - \hbar\omega) \sigma_{b,F,p}(E) \frac{\exp(-E_b^{F,p}/kT)}{Z} \quad (5.22)$$

where $Z = \sum_{b,F,p} (2F+1) \exp(-E_b^{F,p}/kT)$ is the partition function.

The CO product distribution or branching ratio that corresponds to a specific transition $E \leftarrow E_b^{F,p}$ is given by the ratio of the partial and total cross

sections

$$P_{b,F,p}(kJ\epsilon; E) = \frac{\sigma_{k,J,\epsilon \leftarrow b,F,p}(E)}{\sigma_{b,F,p}(E)}. \quad (5.23)$$

The measured branching ratio at a given spectral frequency ω can be obtained again from Boltzmann averaging over the initial states $|b, F, p\rangle$, cf. Eq. (5.22).

5.3 Computational details

Both for the bound and scattering states we used the renormalized Numerov propagation method described in Refs. [91, 92]. The advantage of this algorithm is that it makes it easy to generate the scattering wavefunctions, which was essential in the calculation of the photodissociation cross sections. We propagated on a grid that ranges from $R = 3.5$ to $50 a_0$ with a step size of $0.1373 a_0$. The tails of the bound state wavefunctions vanish between 20 and $30 a_0$.

The angular basis set includes values of J up to $J_{\max} = 8$ with L running according to the triangular rule from $|F - J|$ to $F + J$. F , which is a good quantum number, was fixed at values of 0, 1, 2, 3, 4, 5. At the chosen temperature of 5 K only the ground state levels with F up to 4 have a non-negligible population and the selection rules allow transitions with $\Delta F = -1, 0$, and 1.

The ground state wavefunctions and energies were obtained by the matching procedure described in Sec. 5.2.2 and illustrated in Fig. 5.1, with a set of trial energies ranging from -8 to 0 cm^{-1} in steps of 0.25 cm^{-1} . This choice was based on the knowledge from the variational calculations presented in chapter 4. The matching point was chosen at $R = 7 a_0$, which is close to R_e .

The radial integrations in the transition dipole matrix elements occurring in the photodissociation cross sections, see Eq. (5.20), were performed directly during the propagation procedure. At the end of the propagation when the S matrix was determined the integrals were transformed to the correct S -matrix boundary conditions for the scattering wavefunctions, see Sec. 5.2.1.

The energy level structure of $\text{CO}(a^3\Pi)$ is dominated by the spin-orbit splitting, which leads to a set of levels with $\Omega = 0$ starting at -41.45 cm^{-1} , a set of levels with $|\Omega| = 1$ starting at zero energy, and a set of levels with $|\Omega| = 2$ starting at $+41.45 \text{ cm}^{-1}$. Here, the zero of energy corresponds to the energy of the $\text{CO}(a^3\Pi)$ state calculated without spin-orbit coupling. Hence, the continuum of $\text{CO}(a^3\Pi)\text{-He}$ starts at the $\Omega = 0$ dissociation limit. The photodissociation cross sections were computed for a set of energies E ranging from -41.45 to $+60 \text{ cm}^{-1}$ with a step size of 0.01 cm^{-1} .

5.4 Discussion

Table 5.1 shows the results of the matching calculation for the $\text{CO}(X^1\Sigma^+)\text{-He}$ bound states, compared to the results of the variational calculations performed

in chapter 4. The first four columns of the table contain the exact (F, p) and approximate (J, L) quantum numbers defining the character of these bound states. The populations of the J, L components indicated are given in columns 6 and 8. It is clear from these results that the results of the variational calculations are well reproduced by the scattering calculations with the matching procedure. The largest discrepancies occur for levels close to the dissociation limit; the scattering calculations are more accurate in this case.

Table 5.1: Bound energy levels (cm^{-1}) of the ground state CO($X^1\Sigma$)-He complex; comparison between variational and scattering calculations.

Quantum numbers				Variational		Scattering	
F	p	J	L	energy	population	energy	population
0	+	0	0	-5.9742	91.16%	-5.9748	91.17%
0	+	1	1	-0.7161	76.22%	-0.7502	71.43%
1	+	1	1	-1.6978	97.07%	-1.6990	97.07%
2	+	0	2	-4.2987	90.44%	-4.2996	90.45%
2	+	1	1	-1.2728	86.09%	-1.2759	85.93%
4	+	0	4	-0.5635	90.33%	-0.5724	90.53%
1	-	0	1	-5.4115	90.90%	-5.4121	90.90%
1	-	1	0	-1.9781	85.99%	-1.9798	85.96%
1	-	1	2	-	-	-0.0984	52.97% ¹
2	-	1	2	-0.5498	97.25%	-0.5513	97.25%
3	-	0	3	-2.6645	90.03%	-2.6664	90.07%
3	-	1	2	-0.1154	85.62%	-0.1242	84.42%

¹ This state contains also 43.67% of (J, L) = (0, 1) character

Figure 5.2 displays the spectrum of the $a^3\Pi \leftarrow X^1\Sigma^+$ transition in CO-He calculated at 5 K. The band origin of this transition in free CO is $48473.201 \text{ cm}^{-1}$. The energy in this figure is set to zero at this band origin. The spectrum exhibits clearly the three different regions corresponding to the spin-orbit manifolds of free CO($a^3\Pi$): around -40 cm^{-1} for $\Omega = 0$, around zero for $|\Omega| = 1$, and around $+40 \text{ cm}^{-1}$ for $|\Omega| = 2$. This is illustrated by the schematic diagram in Fig. 4.4. It is clear from Fig. 5.2 that most of the intensity goes into the excited levels with $|\Omega| = 1$. We explained already that this is related to the mechanism which makes the singlet-triplet transition (weakly) allowed: the CO($a^3\Pi$) state has some admixture of the $A^1\Pi$ state and the $A^1\Pi \leftarrow X^1\Sigma^+$ (perpendicular) transition is allowed. It is the $|\Omega| = 1$ component of the $a^3\Pi$ state that mixes with the (purely $|\Omega| = 1$) $A^1\Pi$ state and becomes excited. The fact that also the $\Omega = 0$ and $|\Omega| = 2$ levels receive a small amount of intensity is due to the property that Ω is not an exact quantum number for $J > 0$ even in free CO($a^3\Pi$).

Figure 5.2: UV absorption spectrum of the $\text{CO}(a^3\Pi \leftarrow X^1\Sigma)$ -He transition for a temperature of 5 K. Energy zero corresponds to the band origin at $48473.201 \text{ cm}^{-1}$. The intensity is in units of $0.01 (\mu_{\perp}^{\text{trans}})^2 / \text{cm}^{-1}$.

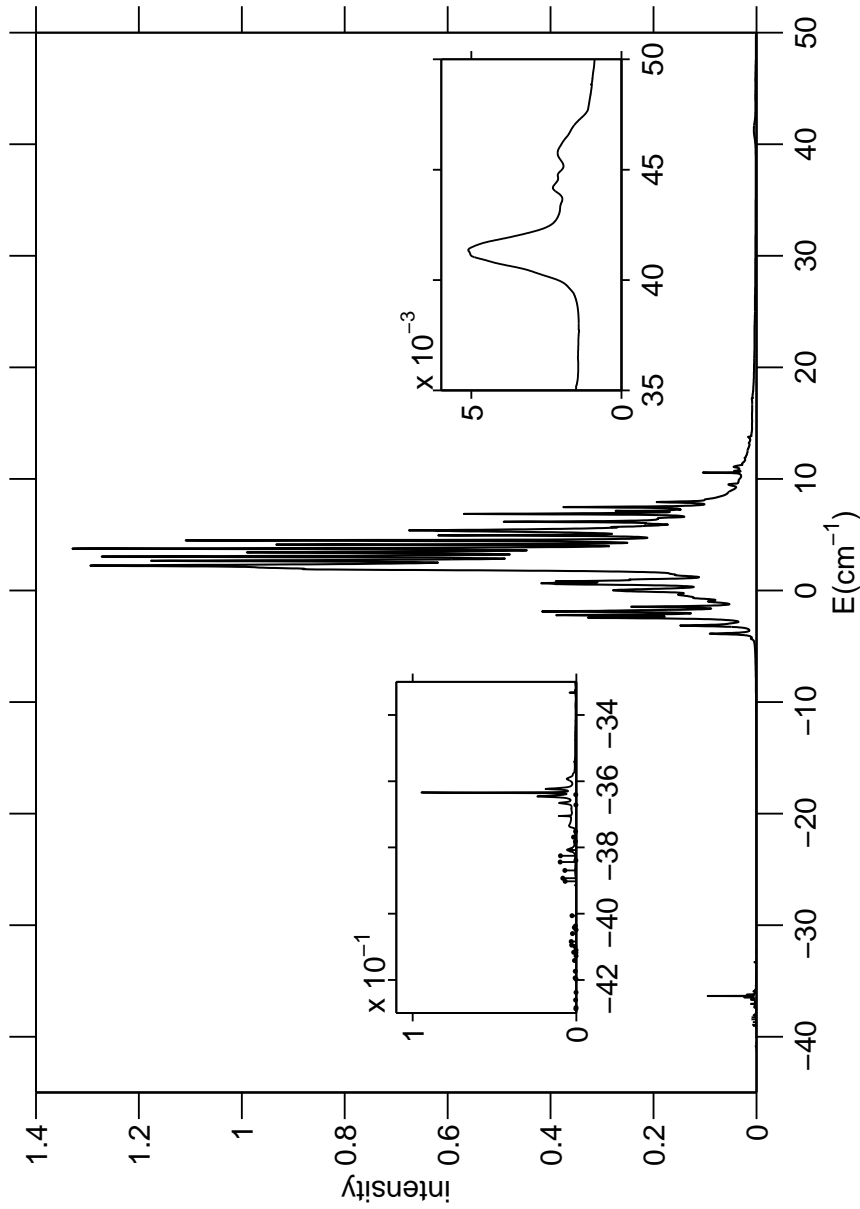


Figure 5.3 shows the intense region of the spectrum that corresponds to the upper levels with $|\Omega| = 1$. From Fig. 5.3(a), which presents the overall structure, it is clear that the spectrum in this region is quite complicated. Figure 5.3(b) which zooms in on part of this region shows the underlying peaks that are responsible for this complicated structure. The individual peaks (dashed lines) are the contributions of different $F' \leftarrow F$ transitions, to which we can assign all quantum numbers and energies of the initial and final states in the complex. In the same manner Figs. 5.4(a) and 5.4(b) present details of the regions in the spectrum that correspond to the upper levels with $\Omega = 0$ and $|\Omega = 2|$, respectively.

In Figs. 5.2 and 5.4(a) one can observe both discrete bound-bound transitions and bound-free resonances; the bound-bound transitions are represented by sticks. The upper levels in these bound-bound transitions are the levels with $\Omega = 0$ in the potential well of CO($a^3\Pi$)-He that have insufficient energy to dissociate. Remember that the zero-point level of CO($a^3\Pi$)-He lies at -48.29 cm^{-1} (see Table 4.3), while the $\Omega = 0$ dissociation limit is at -41.45 cm^{-1} . The intensities of these discrete lines were obtained from the oscillator strengths in chapter 4 and the same Boltzmann averaging procedure as used for the bound-free transitions. The heights of the sticks that mark these bound-bound transitions in Fig. 5.2 were computed by a formula from Ref. [95, 96]

$$\alpha(\omega) = \frac{2\pi\omega}{3c^2} \rho(E_f) S(f \leftarrow i) \frac{\exp(-E_i/kT)}{Z}. \quad (5.24)$$

This formula ensures that the intensities of bound-bound and bound-free transitions join smoothly at the dissociation limit; $\alpha(\omega)$ represents the equivalent cross section of the bound-bound $f \leftarrow i$ transition, $\omega = (E_f - E_i)/\hbar$, c is the velocity of light (in atomic units), $\rho(E_f)$ is the energy density just below the dissociation limit, and $S(f \leftarrow i)$ is the dipole oscillator strength defined in Eq. 4.21. The density $\rho(E_f)$ was calculated by taking into account the highest ten nondissociating states (see Table 4.3). They range from -43.85 to -42.12 cm^{-1} which gives a density $\rho(E_f) = 5.78/\text{cm}^{-1}$. The excited state dissociation threshold lies at -41.45 cm^{-1} , but the transition from bound-bound to bound-free transitions in the spectrum of Fig. 5.2—around -40 cm^{-1} —is blurred by the Boltzmann averaging over the initial bound states. The main peaks in the spectra are labeled and the corresponding transitions are reported in Tables 5.2 and 5.3.

Table 5.2 presents for each of the peaks labeled in the figures (labels in the 1st column): the transition frequency ω (column 2), the quantum numbers of the initial state (column 3), the quantum numbers (F', p'), energy E , and lifetime of the excited scattering state (columns 4, 5, and 6), and the relative intensity of the specified transition at this frequency (column 7). The latter quantity gives an indication of the contribution of the smooth continuum background and of the different transitions that can possibly occur at this frequency (see peaks 9 and 10, for example). The excited state lifetimes were

Figure 5.3: Region of the spectrum corresponding to the excited spin-orbit levels with $|\Omega| = 1$ (a), with more detail given in (b). Labeled peaks are specified in Table 5.2.

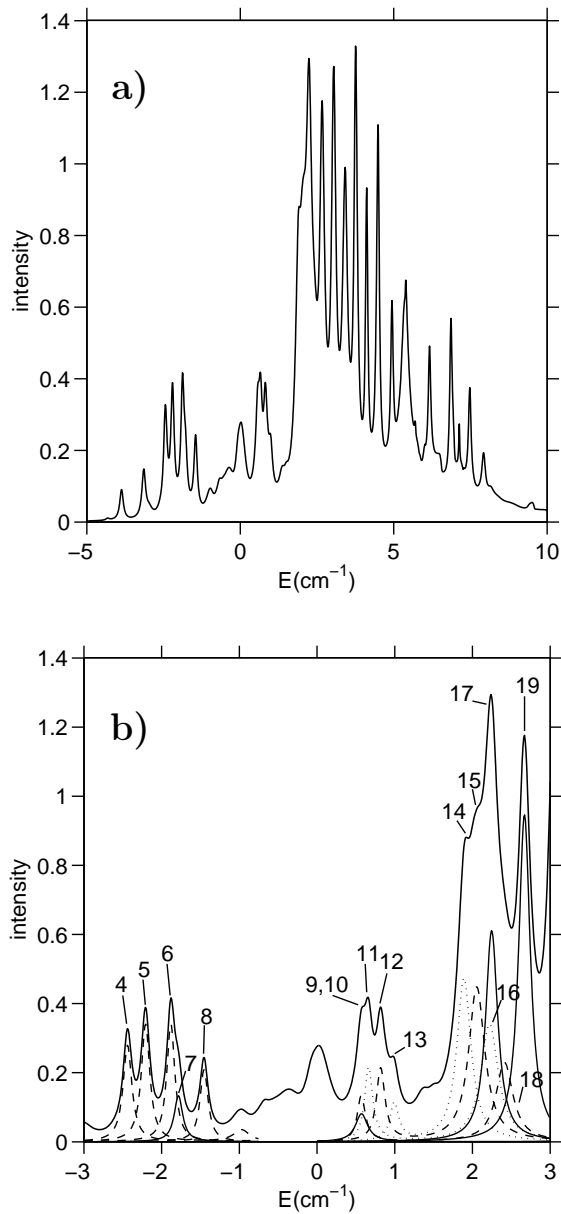
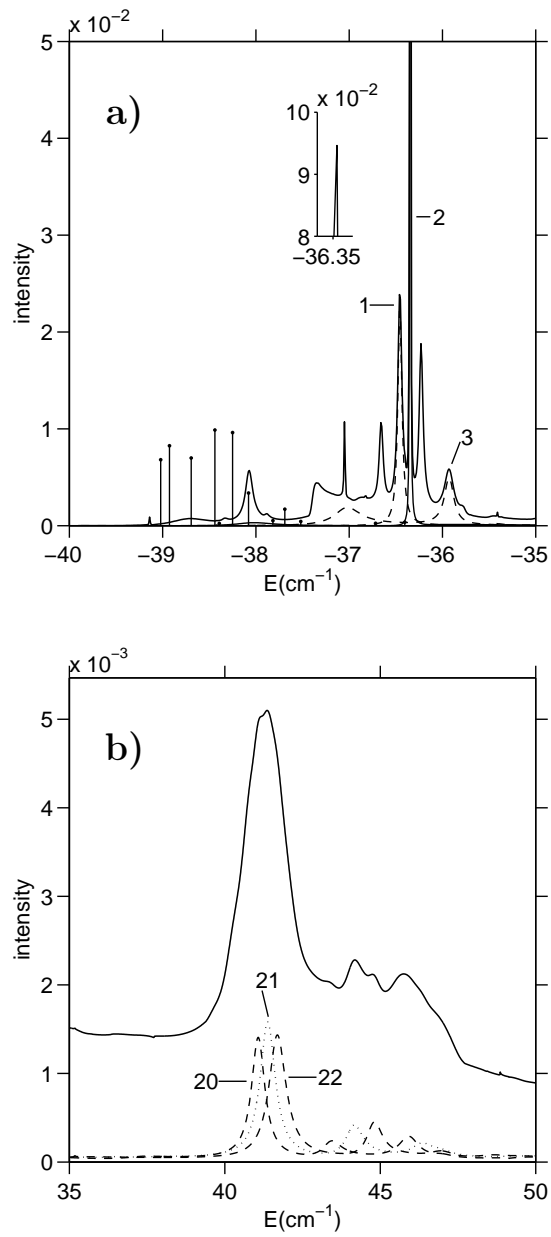


Figure 5.4: Regions of the spectrum corresponding to the excited spin-orbit levels with $\Omega = 0$ (a) and $|\Omega| = 2$ (b). Labeled peaks are specified in Table 5.2.



obtained by fitting the resonances in the photodissociation cross section with a single Lorentzian function. Since this fit was not always perfect, because of the continuum background and because of overlapping resonances, the resulting lifetimes should be considered as estimates. Attempts to correct for this background were not always successful. It is interesting to observe that some of the excited state resonances are probed more than once, at different frequencies and by different transitions. See, for example, peaks 5, 7, and 12. The lifetimes (linewidths) and peak positions of these resonances that result from different fits show only slight variations.

Table 5.2: Peaks in the UV spectrum: transition frequencies ω , initial and final state quantum numbers, final state energy E , lifetime τ , and relative contribution of the transition to the intensity at frequency ω .

peak	ω (cm ⁻¹)	(F_i, p_i, J_i, L_i)	(F_f, p_f)	E (cm ⁻¹)	τ (ps)	%
1	48436.75	(1,-,1,0)	(2,+)	-38.4354	100.42	92.45
2	48436.86	(2,+,1,1)	(3,-)	-37.6211	711.81	97.69
3	48437.27	(3,-,1,2)	(4,+)	-36.0539	42.20	83.25
4	48470.76	(1,-,1,0)	(1,+)	-4.4188	38.66	85.52
5	48470.99	(2,+,1,1)	(2,-)	-3.4823	40.06	87.86
6	48471.32	(3,-,1,2)	(3,+)	-2.0055	42.04	81.65
7	48471.42	(1,+,1,1)	(2,-)	-3.4821	40.08	50.20
8	48471.75	(2,-,1,2)	(3,+)	-2.0053	42.27	85.42
9	48473.77	(4,+,0,4)	(4,-)	-0.0036	43.13	34.56
10	48473.77	(2,+,0,2)	(1,-)	-3.7272	28.14	21.14
11	48473.86	(3,-,0,3)	(3,+)	-2.0025	41.39	52.38
12	48474.02	(2,+,0,2)	(2,-)	-3.4800	38.93	54.84
13	48474.20	(1,-,0,1)	(1,+)	-4.4171	32.16	46.29
14	48475.09	(1,-,0,1)	(1,+)	-3.5214	24.08	53.90
15	48475.26	(2,+,0,2)	(2,-)	-2.2436	20.91	46.27
16	48475.42	(3,-,0,3)	(3,+)	-0.4460	19.71	26.12
17	48475.45	(0,+,0,0)	(1,-)	-3.7269	27.94	46.90
18	48475.61	(4,+,0,4)	(4,-)	1.8396	19.91	31.00
19	48475.87	(1,-,0,1)	(2,+)	-2.7423	29.33	80.45
20	48514.28	(1,-,1,0)	(2,+)	39.1031	9.15	28.01
21	48514.58	(2,+,1,1)	(3,-)	40.1050	8.38	30.94
22	48514.87	(3,-,1,2)	(4,+)	41.5415	6.93	30.72

Table 5.3 lists for a given transition frequency the CO product distribution after dissociation. The 1st column contains again the peak labels corresponding to Table 5.2 and Figs. 5.3 and 5.4. Column 2 shows the exact quantum numbers (k, J, ϵ) of the CO($a^3\Pi$) fragment and column 3 the corresponding energies of

free CO. Note that the quantum number $k = 1$ which is found in all cases tabulated corresponds to an approximate quantum number $\Omega = 0$ of the CO fragment. Column 4 gives the relative contribution of each product according to Eq. (5.23). Percentages of 100% are found at the lowest energies, which implies that only one channel is open at these excitation energies. Column 5 gives the same relative contribution at the given transition frequency after the Boltzmann averaging over the initial states, cf. Eq. (5.22). Only contributions on the order of 10% and higher are listed. Rotational states of CO($a^3\Pi$) with values of J up to 5 are energetically accessible from the higher energy part of the spectrum and such states are indeed found. The results in columns 4 and 5 are mostly similar, but not in all cases. The results in column 5 are observable quantities in terms of counts measured on a detector, whereas the results in column 4 are merely of theoretical importance. It is of importance to note in this respect that the transition listed in Table 5.2 for each peak corresponds to the resonance that yields the most important contribution to the spectrum at the frequency ω of the top of this peak. The relative intensity of that specific transition can be found in the last column of Table 5.2. Some of the numbers in this column are comparatively small, which demonstrates the presence of a large continuum background. Note that the sum of the numbers in column 5 of Table 5.3 is always larger than the number in the last column of Table 5.2, because the same product can arise from transitions other than the one indicated.

The last column of Table 5.3 gives the maximum deflection angle of the CO fragment after dissociation in a beam experiment. After the singlet-triplet excitation of the CO-He complex with the laser beam this complex is very short-lived; the lifetimes are given in Table 5.2. The excess energy released in the complex after dissociation is shared by the spin-orbit and rotational degrees of freedom of the CO monomer and the relative translational motion of CO and He. The CO monomer is not de-excited to its singlet ground state—this is a much slower process—but to a lower spin-orbit level of the metastable $a^3\Pi$ state and the amount of energy available after dissociation is rather small (typically about 40 cm^{-1}). From the distributions of the CO fragment over its spin-orbit and rotational states, with energies $E_{kJ\epsilon}$ given also in Table 5.3, one knows the amount of relative translational energy available

$$T = \hbar(\omega - \omega_0) - E_{kJ\epsilon}, \quad (5.25)$$

where $\omega_0 = 48473.201 \text{ cm}^{-1}$ is the band origin of the singlet-triplet transition. The maximum deflection angle occurs when the fragments fly apart perpendicularly to the molecular beam direction and one finds by simple classical mechanics that the CO velocity equals $v_{\text{CO}} = \sqrt{2\mu T}/m_{\text{CO}}$, where μ is the reduced mass of the complex. In the laboratory frame the center of mass is moving with speed v along the beam axis which implies that the maximum deflection angle is $\theta_{\text{CO}} = \arctan(v_{\text{CO}}/v)$. These angles are presented in Table 5.3 for a benchmark beam velocity of $v = 1000 \text{ m/s}$. For the contributions

that originate from the most intense part of the spectrum (the $|\Omega| = 1$ excited levels) they are typically $\approx 3^\circ$. The lower part of the spectrum (the $\Omega = 0$ excited levels) corresponds to a much smaller deflection angle ($\approx 0.7^\circ$) but its intensity is much lower. The best method to detect the triplet excited CO–He species is probably by aiming for the more intense part and placing the detector sufficiently close to the excitation region.

5.5 Conclusions

This chapter presents a study of the spin-forbidden $a^3\Pi \leftarrow X^1\Sigma^+$ transition in the CO–He complex. With the use of accurate potential energy surfaces for CO($X^1\Sigma$)–He and CO($a^3\Pi$)–He computed in chapter 4 we computed the bound levels of CO($X^1\Sigma$)–He and the bound and scattering states of CO($a^3\Pi$)–He. Then, with the aid of an effective transition dipole function also from chapter 4, we computed photodissociation cross sections and generated a theoretical UV spectrum. The dominant contributions to the spectrum, in the energy range from -5 to $+10$ cm^{-1} relative to the band origin at 48473.201 cm^{-1} , originate from resonances that correspond to the $|\Omega| = 1$ spin-orbit manifold of the excited CO($a^3\Pi$)–He complex. These (overlapping) resonances were assigned to specific transitions between well defined initial and final states and the lifetimes of the excited states were determined. It turns out that the lifetime of the triplet excited CO–He complex is limited by an efficient predissociation process in which the spin-orbit coupling energy of the triplet CO states with $|\Omega| = 1$ is lost by decay into the lower triplet levels with $\Omega = 0$ and the CO–He complex dissociates. The fact that experimental attempts to detect triplet excited CO–He were not successful until now are probably due to this rapid dissociation. We calculated the CO product state distributions resulting from the rapid spin-orbit predissociation process and the corresponding deflection angles of the CO fragments and suggest how the experiment can be repeated with more chance of success.

Table 5.3: CO($a^3\Pi$) fragment state distributions and deflection angles θ_{CO} for the transitions of Table 5.2. Columns 2 and 3 list the quantum numbers and energy of the emerging CO fragment, column 4 the product distribution from Eq. (5.23), and column 5 the same relative contribution after Boltzmann averaging over the initial states. The exact CO quantum number $k = 1$ corresponds to an approximate spin-orbit quantum number $\Omega = 0$.

peak	(k, J, ϵ)	E_{CO} (cm^{-1})	%	%	θ_{CO} ($^\circ$)
1	(1,0,+)	-38.8760	100.00	96.83	0.39
2	(1,0,+)	-38.8760	100.00	98.98	0.67
3	(1,0,+)	-38.8760	32.42	33.53	1.00
	(1,1,-)	-37.5290	67.58	65.54	0.72
4	(1,1,+)	-35.7900	53.29	50.70	3.31
	(1,0,-)	-40.6264	19.94	18.92	3.56
	(1,2,-)	-31.3300	15.73	15.65	3.07
5	(1,1,+)	-35.7900	49.11	47.92	3.36
	(1,0,-)	-40.6264	18.84	18.28	3.61
	(1,2,-)	-31.3300	12.95	13.30	3.12
6	(1,1,+)	-35.7900	41.82	41.76	3.44
	(1,4,+)	-7.9421	17.57	16.10	1.44
	(1,0,-)	-40.6264	15.44	15.48	3.68
	(1,2,-)	-31.3300	11.93	12.54	3.20
7	(1,1,+)	-35.7900	49.01	43.74	3.36
	(1,4,+)	-7.9421	10.11	13.18	1.25
	(1,0,-)	-40.6264	18.78	16.44	3.60
	(1,2,-)	-31.3300	12.85	13.33	3.12
8	(1,1,+)	-35.7900	41.60	39.16	3.44
	(1,4,+)	-7.9421	17.86	16.66	1.44
	(1,0,-)	-40.6264	15.29	14.31	3.68
	(1,2,-)	-31.3300	12.03	13.09	3.20
9	(1,1,+)	-35.7900	32.60	24.03	3.54
	(1,4,+)	-7.9421	26.98	17.93	1.67
	(1,2,-)	-31.3300	11.40	16.05	3.31
10	(1,2,+)	-29.6129	20.03	8.13	3.01
	(1,3,+)	-20.3348	10.75	7.76	2.41
	(1,2,-)	-31.3300	30.71	16.05	3.11
	(1,3,-)	-22.0206	10.85	9.97	2.53
	(1,4,-)	-9.5889	11.92	5.87	1.44
11	(1,1,+)	-35.7900	40.45	28.89	3.44
	(1,4,+)	-7.9421	19.19	17.69	1.44
	(1,0,-)	-40.6264	14.88	9.97	3.68
	(1,2,-)	-31.3300	11.94	14.68	3.20

12	(1,1,+)	-35.7900	47.38	33.65	3.36
	(1,4,+)	-7.9421	11.37	14.38	1.25
	(1,0,-)	-40.6264	18.28	12.32	3.61
	(1,2,-)	-31.3300	12.68	13.31	3.12
13	(1,1,+)	-35.7900	49.77	33.08	3.31
	(1,0,-)	-40.6264	18.73	11.78	3.56
	(1,2,-)	-31.3300	15.79	14.45	3.07
14	(1,2,+)	-29.6129	17.84	16.42	3.02
	(1,3,+)	-20.3348	11.79	11.90	2.43
	(1,2,-)	-31.3300	28.35	25.60	3.12
	(1,3,-)	-22.0206	11.29	12.95	2.55
	(1,4,-)	-9.5889	12.38	11.66	1.46
15	(1,2,+)	-29.6129	16.75	17.12	3.10
	(1,3,+)	-20.3348	13.07	12.33	2.52
	(1,2,-)	-31.3300	26.34	26.07	3.19
	(1,3,-)	-22.0206	13.01	13.37	2.63
	(1,4,-)	-9.5889	12.98	12.52	1.61
16	(1,2,+)	-29.6129	16.85	18.31	3.20
	(1,3,+)	-20.3348	12.39	11.87	2.64
	(1,2,-)	-31.3300	24.51	27.38	3.29
	(1,3,-)	-22.0206	14.71	12.88	2.75
	(1,4,-)	-9.5889	14.29	12.64	1.79
17	(1,2,+)	-29.6129	19.82	18.31	3.01
	(1,3,+)	-20.3348	10.83	11.87	2.41
	(1,2,-)	-31.3300	30.71	27.38	3.11
	(1,3,-)	-22.0206	10.97	12.88	2.53
	(1,4,-)	-9.5889	11.86	12.64	1.43
18	(1,2,+)	-29.6129	17.18	17.98	3.32
	(1,3,+)	-20.3348	15.95	12.89	2.79
	(1,2,-)	-31.3300	18.61	25.01	3.41
	(1,3,-)	-22.0206	16.85	14.11	2.89
	(1,4,-)	-9.5889	14.47	12.86	2.00
19	(1,2,+)	-29.6129	19.42	19.01	3.07
	(1,3,+)	-20.3348	10.83	11.14	2.48
	(1,2,-)	-31.3300	30.00	28.72	3.16
	(1,3,-)	-22.0206	12.33	12.86	2.60
	(1,4,-)	-9.5889	11.05	11.26	1.55
20	(1,4,+)	-7.9421	13.03	9.53	4.06
	(1,4,-)	-9.5889	14.47	9.56	4.13
	(1,5,-)	5.9799	19.29	11.92	3.41
21	(1,4,+)	-7.9421	12.04	9.33	4.10
	(1,4,-)	-9.5889	12.75	9.23	4.17

	(1,5,-)	5.9799	14.41	11.13	3.46
22	(1,4,+)	-7.9421	11.61	8.57	4.16
	(1,4,-)	-9.5889	10.18	8.20	4.23
	(1,5,-)	5.9799	11.17	9.81	3.53

CHAPTER 6

Bound states of the $\text{Cl}(^2P)\text{-HCl}$ van der Waals complex from coupled *ab initio* potential energy surfaces

With the use of recently computed diabatic potential energy surfaces [J. Chem. Phys. **115**, 3085 (2001)] we made a full *ab initio* calculation of the bound energy levels of the $\text{Cl}(^2P)\text{-HCl}$ van der Waals complex for total angular momentum $J = \frac{1}{2}, \frac{3}{2}, \frac{5}{2}$ and $\frac{7}{2}$. The dissociation energy D_0 of the complex was found to be 337.8 cm^{-1} for $J = \frac{1}{2}$ and $|\Omega| = \frac{1}{2}$, where Ω is the projection of \mathbf{J} on the Cl-HCl bond axis. The complex is T-shaped in the ground state and in a series of stretch and bending excited states, with a van der Waals bond length R of approximately 3.2 \AA . We also found a series of states with the linear geometry, however, with $|\Omega| = \frac{3}{2}$ and $R \approx 3.9 \text{ \AA}$, the lowest of which has a binding energy of 276.1 cm^{-1} . The rovibronic levels were analyzed with the help of one-dimensional calculations with R fixed at values ranging from 2.5 to 5.5 \AA and the use of diabatic and adiabatic potential energy surfaces that both include the important spin-orbit coupling. The states of linear geometry are in qualitative agreement with previous work based on more approximate potential energy surfaces, the T-shaped states of considerably lower energy were not predicted earlier. The analysis of the rotational structure and parity splitting of the rovibronic levels leads to the remarkable observation that this T-shaped complex shows several of the typical features of a linear open-shell molecule.

6.1 Introduction

A chemical reaction that has been studied intensively over more than a decade, both by theory [97, 98, 99, 100, 101, 102, 103, 104, 105, 106] and experiment [107, 108, 109, 110, 111, 112, 113, 114, 115, 116], is the hydrogen exchange reaction between a free Cl atom in its ground 2P state and the HCl molecule. A weakly bound $\text{Cl}(^2P)\text{-HCl}$ van der Waals complex is present in the entrance and exit channels of this reaction, which is believed to influence the rate and the outcome of the reaction [6]. Theoretical studies of the bound states of this complex were reported by Dubernet and Hutson [20] and, more recently, by Zdanska *et al.* [117]. Dubernet and Hutson based their studies on diabatic model potentials which they constructed by combining empirical Ar-HCl, Ar-Cl, and Ar-Ar potentials with the electrostatic interactions between the quadrupole moment of the $\text{Cl}(^2P)$ atom and the dipole and quadrupole of HCl. Zdanska and coworkers calculated adiabatic potential energy surfaces at the multi-reference averaged coupled-pair functional (MRACPF) level and reported bound states calculated with and without inclusion of an angular first derivative non-adiabatic coupling term. In their calculations they fixed the orientation of the intermolecular vector \mathbf{R} between the Cl nucleus and the HCl center of mass, which corresponds approximately, but not exactly, to a neglect of the overall rotation of the complex.

Accurate two-dimensional adiabatic and diabatic potential energy surfaces for the $\text{Cl}(^2P)\text{-HCl}$ system were recently reported by Kłos *et al.* [55]. They were obtained from *ab initio* spin-restricted coupled cluster calculations with single, double, and non-iterative triple excitations [RCCSD(T)], combined with multi-reference configuration interaction including single and double excitations [MRCISD] to obtain the non-adiabatic coupling coefficient. In the present work we re-expand these diabatic potentials in the form that was derived in refs [18, 19, 20, 118] and apply them in a detailed study of the bound states of the $\text{Cl}(^2P)\text{-HCl}$ van der Waals complex. The method for the calculation of the van der Waals levels is described in Section 6.2. Also the spin-orbit interaction in the $\text{Cl}(^2P)$ atom is included in this calculation, with the same assumption as in refs [20, 117] that the spin-orbit coupling constant is not affected by the weak interaction with the HCl molecule. We obtain a full solution of the two-dimensional problem with all the six electronic states of $\text{Cl}(^2P)\text{-HCl}$ that correlate asymptotically to the $^2P_{3/2}$ and $^2P_{1/2}$ spin-orbit states of the Cl atom. In order to understand the character of the bound states on the multiple potential surfaces we also perform a set of rigid bender calculations with the Cl-HCl distance R frozen, to a range of values. In Section 6.3 we discuss the results and compare them to previous work. Section 6.4 contains our conclusions.

6.2 Bound state calculations

The bound states of $\text{Cl}(^2P)\text{-HCl}$ are most conveniently calculated in a two-angle embedded body-fixed (BF) frame with the z -axis along the vector \mathbf{R} from the Cl-atom to the HCl center of mass. This frame is related to a space-fixed (SF) frame by a rotation over the angles (β, α) which are the polar angles of \mathbf{R} with respect to the SF frame. The Cl-H bond axis \mathbf{r} has the polar angles (θ, ϕ) with respect to the BF frame; θ is the angle between \mathbf{r} and \mathbf{R} which is zero for the linear Cl-HCl geometry. Since the H-Cl vibration has a much higher frequency than the vibrations of the Cl-HCl complex we froze the H-Cl bond length r and used the experimental value for the ground state rotational constant $b_0 = 10.44019 \text{ cm}^{-1}$ of HCl. The *ab initio* potential was calculated for the equilibrium bond length $r_e = 1.275 \text{ \AA}$. In this representation the Hamiltonian for the nuclear motion on the multiple diabatic potential surfaces reduces to

$$\begin{aligned} \hat{H} &= \frac{-\hbar^2}{2\mu_{AB}R} \frac{\partial^2}{\partial R^2} R + \frac{(\hat{\mathbf{j}}_A + \hat{\mathbf{j}}_B)^2 - 2(\hat{\mathbf{j}}_A + \hat{\mathbf{j}}_B) \cdot \hat{\mathbf{J}} + \hat{\mathbf{J}}^2}{2\mu_{AB}R^2} + b_0 \hat{j}_B^2 + A \hat{\boldsymbol{\lambda}} \cdot \hat{\mathbf{S}} \\ &+ \sum_{\mu', \mu} |\lambda, \mu'\rangle V_{\mu', \mu}(R, \theta, \phi) \langle \lambda, \mu | \end{aligned} \quad (6.1)$$

where $\mu_{AB} = 17.732802 \text{ u}$ is the reduced mass of the complex. The operators $\hat{\boldsymbol{\lambda}}$ and $\hat{\mathbf{S}}$ represent the orbital and spin angular momenta of the Cl-atom, and $\hat{\mathbf{j}}_A = \hat{\boldsymbol{\lambda}} + \hat{\mathbf{S}}$ the total atomic angular momentum. The splitting between the ground $j_A = \frac{3}{2}$ and excited $j_A = \frac{1}{2}$ spin-orbit states of $\text{Cl}(^2P)$ is $D_{\text{SO}} = 882.4 \text{ cm}^{-1}$ and the atomic spin-orbit coupling constant is $A = -2D_{\text{SO}}/3 = -588.27 \text{ cm}^{-1}$. The operator $\hat{\mathbf{j}}_B$ is the rotational angular momentum of the HCl molecule and $\hat{\mathbf{J}}$ the total angular momentum of the complex. The diabatic states of the $\text{Cl}(^2P)\text{-HCl}$ complex that correlate with the corresponding states of the $\text{Cl}(^2P)$ atom are labeled with the quantum numbers (λ, μ) , where $\lambda = 1$ and $\mu = -1, 0, 1$ is the projection of $\hat{\boldsymbol{\lambda}}$ on the BF z -axis \mathbf{R} . The potentials $V_{\mu', \mu}(R, \theta, \phi)$ are the diabatic interaction potentials in a two-angle embedded BF frame as described in chapter 3. The expansion of these diabatic potentials is given by the following expression

$$V_{\mu', \mu}(R, \theta, \phi) = \langle \lambda, \mu' | \hat{V} | \lambda, \mu \rangle = \sum_{l_B} C_{l_B, \mu - \mu'}(\theta, \phi) v_{l_B}^{\mu', \mu}(R). \quad (6.2)$$

The functions $C_{l,m}(\theta, \phi)$ are Racah normalized spherical harmonics. Note that only functions with $m = \mu - \mu'$ occur in the expansion. The same formula (6.2) with identical expansion coefficients holds in a three-angle embedded BF frame with $\phi = 0$ (see chapter 3) and the potentials $V_{\mu', \mu}(R, \theta) \equiv V_{\mu', \mu}(R, \theta, 0)$ do not depend on the angle ϕ in this frame.

Accurate *ab initio* results for the diabatic potential surfaces $V_{\mu', \mu}(R, \theta)$ are given in ref [55]. In order to express their anisotropy in the form of eq (6.2) we

made new fits of the original *ab initio* data. For the diabatic potential surfaces $V_{0,0}$ and $V_{1,1} = V_{-1,-1}$ we fitted the R dependence to an Esposti-Werner [44] function for each value of θ on the grid of 13 angles used in the *ab initio* calculations. Subsequently, we obtained the anisotropic expansion coefficients $v_{l_B}^{\mu',\mu}(R)$ in eq (6.2) for given R from a least squares fit of the values for the 13 angles to a set of spherical harmonics $C_{l_B,m}(\theta, 0)$ with $m = \mu - \mu' = 0$ and $l_B = 0, 1, \dots, 8$. For the diabatic potential $V_{-1,1}$ we made a new global fit of the *ab initio* data similar to the fit made in ref [55], but with the anisotropy expanded in spherical harmonics $C_{l,m}(\theta, 0)$ with $m = 2$ instead of Legendre polynomials $P_l^0(\cos \theta)$. The latter are, of course, equal to $C_{l,m}(\theta, 0)$ with $m = 0$, so this seems only a subtle difference, but a correct description of the anisotropy (see chapter 3) according to eq (6.2) requires that m is fixed at $\mu - \mu' = 2$. The short-range contribution to $V_{-1,1}$ was written as

$$V_{\text{sr}}(R, \theta) = G(R, \theta) \exp \left[d(\theta) - b(\theta)R \right], \quad (6.3)$$

where

$$G(R, \theta) = \sum_{l=|m|}^{l_{\text{max}}} \sum_{i=0}^3 g_{il} R^i C_{l,m}(\theta, 0) \quad (6.4)$$

with $m = 2$ and $l = l_B$ ranging from 2 to 9. The exponents $d(\theta)$ and $b(\theta)$ were expanded in Legendre polynomials $P_l^0(\cos \theta)$ with $l = 0, 1, 2$, just as in ref [55]. The long-range contribution was represented as a damped expansion in powers of R^{-1}

$$V_{\text{lr}}(R, \theta) = \sum_{n=4}^{10} \sum_{l=|m|}^{n-4} f_n(b(\theta)R) C_{nl} R^{-n} C_{l,m}(\theta, 0). \quad (6.5)$$

The electrostatic multipole-multipole contributions start at $n = 4$, the induction and dispersion contributions at $n = 6$, and $f_n(bR)$ is a Tang-Toennies damping function [79]. The coefficients C_{nl} with $n = 4$ and $n = 5$ were not varied in the fit. They were determined from the quadrupole moment of $\text{Cl}(^2P)$ and the dipole and quadrupole of HCl according to the long range formulas in chapter 3. Also for the diabatic coupling potential $V_{0,1}$ we made a new global fit, with the same procedure as applied in the fit of $V_{-1,1}$. In this case, the exponents $d(\theta)$ and $b(\theta)$ in eq (6.3) were chosen to be independent of θ , and we used spherical harmonics $C_{l,m}(\theta, 0)$ with $m = \mu - \mu' = 1$ in the fits of eqs (6.4) and (6.5), with $l = l_B$ ranging from 1 to 6. Finally, we computed the expansion coefficients $v_{l_B}^{-1,1}(R)$ and $v_{l_B}^{0,1}(R)$ for l_B values up to 12 according to eq (6.2) by Gauss-Legendre numerical integration over the fitted potentials $V_{-1,1}$ and $V_{0,1}$. These coefficients obey the relations $v_{l_B}^{-1,1}(R) = v_{l_B}^{1,-1}(R)$ and $v_{l_B}^{0,1}(R) = v_{l_B}^{0,-1}(R) = -v_{l_B}^{1,0}(R) = -v_{l_B}^{-1,0}(R)$, as demonstrated in Sec. 3.2, so that all diabatic potentials $V_{\mu',\mu}(R, \theta, 0)$ with $\mu', \mu = -1, 0, 1$ are known.

Because of the large spin-orbit coupling in the $\text{Cl}(^2P)$ atom it is most convenient for the interpretation of the results to use a coupled atomic basis set

$$|j_A \omega_A\rangle \equiv |(\lambda S) j_A \omega_A\rangle = \sum_{\mu, \sigma} |\lambda, \mu\rangle |S, \sigma\rangle \langle \lambda, \mu; S, \sigma | j_A, \omega_A\rangle \quad (6.6)$$

for which the spin-orbit term in the Hamiltonian $\widehat{\lambda} \cdot \widehat{S} = (\widehat{j}_A^2 - \widehat{\lambda}^2 - \widehat{S}^2)/2$ is diagonal. The expression $\langle \lambda, \mu; S, \sigma | j_A, \omega_A\rangle$ is a Clebsch-Gordan coefficient. Since $\lambda = 1$ and $S = \frac{1}{2}$, one finds that $j_A = \frac{1}{2}$ and $\frac{3}{2}$. The two-angle embedded BF basis for the complex reads

$$|n, j_A, \omega_A, j_B, \omega_B, \Omega\rangle = |n\rangle \left[\frac{2J+1}{4\pi} \right]^{1/2} |j_A \omega_A\rangle Y_{j_B, \omega_B}(\theta, \phi) D_{M, \Omega}^{(J)}(\alpha, \beta, 0)^* \quad (6.7)$$

where the spherical harmonics $Y_{j_B, \omega_B}(\theta, \phi)$ describe the rotation of the HCl monomer with respect to the dimer BF frame and the symmetric rotor functions $D_{M, \Omega}^{(J)}(\alpha, \beta, 0)^*$ the overall rotation of the complex. The exact quantum numbers J, M, λ , and S are omitted from the short notation on the lefthand side. The angular momentum components on the BF z -axis obey the relation $\Omega = \omega_A + \omega_B$. The radial basis functions $|n\rangle = \chi_n(R)$ are Morse oscillator type functions defined in ref [50]. Formulas for the matrix elements of the Hamiltonian over this basis are given in chapter 3.

In addition to J and M , the parity of the states of the complex under inversion \widehat{i} is a good quantum number. The effect of inversion on the basis is

$$\widehat{i} |n, j_A, \omega_A, j_B, \omega_B, \Omega\rangle = (-1)^{\lambda - j_A + J} |n, j_A, -\omega_A, j_B, -\omega_B, -\Omega\rangle \quad (6.8)$$

This property is used to construct a parity-adapted basis

$$|n, j_A, \omega_A, j_B, \omega_B, |\Omega|, p\rangle = 2^{-1/2} \left[|n, j_A, \omega_A, j_B, \omega_B, \Omega\rangle + p(-1)^{\lambda - j_A + J} |n, j_A, -\omega_A, j_B, -\omega_B, -\Omega\rangle \right] \quad (6.9)$$

with parity p . It is customary to define the spectroscopic parity ϵ which is related to the total parity by $\epsilon = p(-1)^{J-S}$. Functions with parities $\epsilon = 1$ and $\epsilon = -1$ are denoted with e and f , respectively.

6.3 Results

The bound states of the complex were obtained from a full diagonalization of the Hamiltonian matrix. Calculations were performed for J up to $\frac{7}{2}$ inclusive. This does not provide all the bound states. A simple extrapolation of the lowest energy level for each J with a second order polynomial shows that there might still be bound states for $J = \frac{123}{2}$. The levels were converged to within

10^{-4} cm^{-1} with an angular basis truncated at $j_{B_{\max}} = 15$ and a radial basis with $n_{\max} = 14$. Test calculations with $j_{B_{\max}} = 20$ gave levels that did not deviate more than 10^{-6} cm^{-1} from the $j_{B_{\max}} = 15$ results.

It is important for understanding the bound levels of $\text{Cl}(^2P)\text{-HCl}$ that one considers also diabatic and adiabatic potential energy surfaces with the large spin-orbit coupling term included. Diabatic states $|j_A\omega_A\rangle$ including spin-orbit coupling are defined which correlate to the atomic states $|j_A\omega_A\rangle \equiv |(\lambda S)j_A\omega_A\rangle$ of eq (6.6). The corresponding diabatic potentials $V_{\omega'_A, \omega_A}^{(j_A)}(R, \theta) \equiv \langle j_A\omega'_A | \hat{V} + \hat{H}_{\text{SO}} | j_A\omega_A \rangle$ are the matrix elements of the operator

$$\hat{V} + \hat{H}_{\text{SO}} = \sum_{\mu', \mu} |\lambda, \mu'\rangle V_{\mu', \mu}(R, \theta) \langle \lambda, \mu | + A\hat{\lambda} \cdot \hat{S}. \quad (6.10)$$

The spin-orbit term is constant and diagonal in this basis. The diagonal elements of the matrix $V_{\omega'_A, \omega_A}^{(j_A)}$ are plotted in Figure 6.1(a,b,c). Adiabatic potentials are obtained by diagonalization of this matrix and plotted in Figure 6.1(d,e,f). Similar pictures of their empirical model potential are shown by Dubernet and Hutson [20]. A few of the most relevant cuts through our potential surfaces are presented in Figures 6.2 and 6.3.

6.3.1 One-dimensional calculations

Before we discuss the full 2d calculation of the bound states it is useful to consider the hindered internal rotation or bending motion of the HCl monomer in the complex in a series of calculations with fixed Cl-HCl distance R . We made such calculations for values of R ranging from 2.5 to 5.5 Å in steps of 0.1 Å; the energy levels for $J = \frac{1}{2}$ and $J = \frac{3}{2}$ are shown in Figure 6.4. An analysis of the wavefunctions of the lowest states of parity e is given in Tables 6.1 and 6.2, for $R = 3.2$ and 3.9 Å, respectively. Many of the curves in Figure 6.4 nearly coincide for $J = \frac{1}{2}$ and $\frac{3}{2}$, which indicates that the corresponding bound states for $J = \frac{3}{2}$ are similar to those for $J = \frac{1}{2}$, except for an additional quantum of overall rotation. In Tables 6.1 and 6.2 one can see that $|\Omega|$ is a good approximate quantum number, also for $J = \frac{3}{2}$, and the nearly coinciding curves correspond to states with $|\Omega| \approx \frac{1}{2}$. The expansion coefficients of these states are indeed very similar, compare, for example, in Table 6.1 the lowest state for $J = \frac{1}{2}$ with the lowest state for $J = \frac{3}{2}$ and the second state for $J = \frac{1}{2}$ with the third state for $J = \frac{3}{2}$. In Table 6.2 the first and second state for $J = \frac{1}{2}$ are very similar to the second and fourth state for $J = \frac{3}{2}$, respectively. The curves in Figure 6.4 that occur for $J = \frac{3}{2}$, but not for $J = \frac{1}{2}$, refer to states with $|\Omega| \approx \frac{3}{2}$.

An interesting feature observed in Figure 6.4 is that the lowest energy curve for $J = \frac{3}{2}$ and $|\Omega| = \frac{3}{2}$ exhibits two minima, for $R = 3.2$ and 3.9 Å. For $R = 3.2$ Å the lowest level with $J = \frac{1}{2}$ and $|\Omega| = \frac{1}{2}$ is the ground state, whereas

Figure 6.1: Diabatic $j_A = \frac{3}{2}, |\omega_A| = \frac{3}{2}$ (a), $j_A = \frac{3}{2}, |\omega_A| = \frac{1}{2}$ (b), and $j_A = \frac{1}{2}, |\omega_A| = \frac{1}{2}$ (c) and adiabatic (d), (e), (f) potential energy surfaces including spin-orbit coupling for Cl(2P)-HCl complex. The surfaces (a), (d), (b), and (e) are given relative to the energy of the $^2P_{3/2}$ state of the Cl atom, the surfaces (c) and (f) relative to the energy of the $^2P_{1/2}$ state.

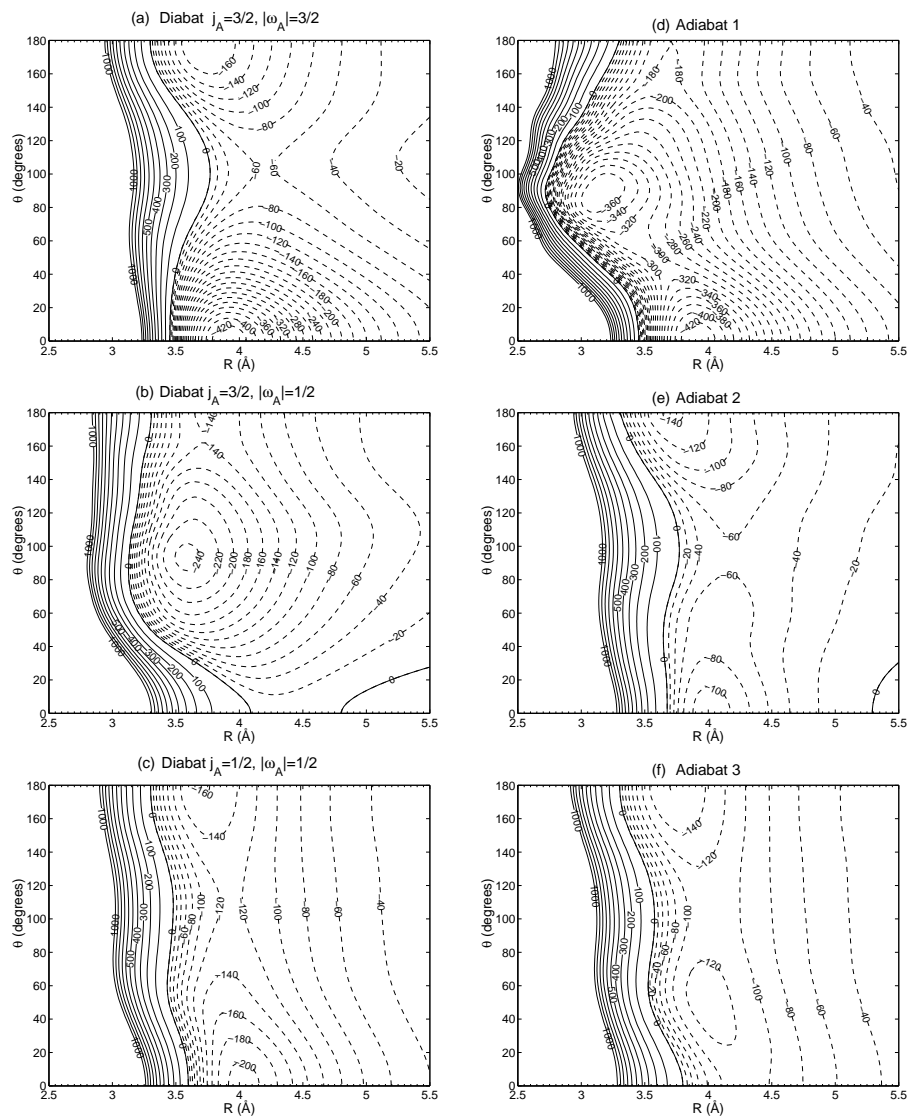
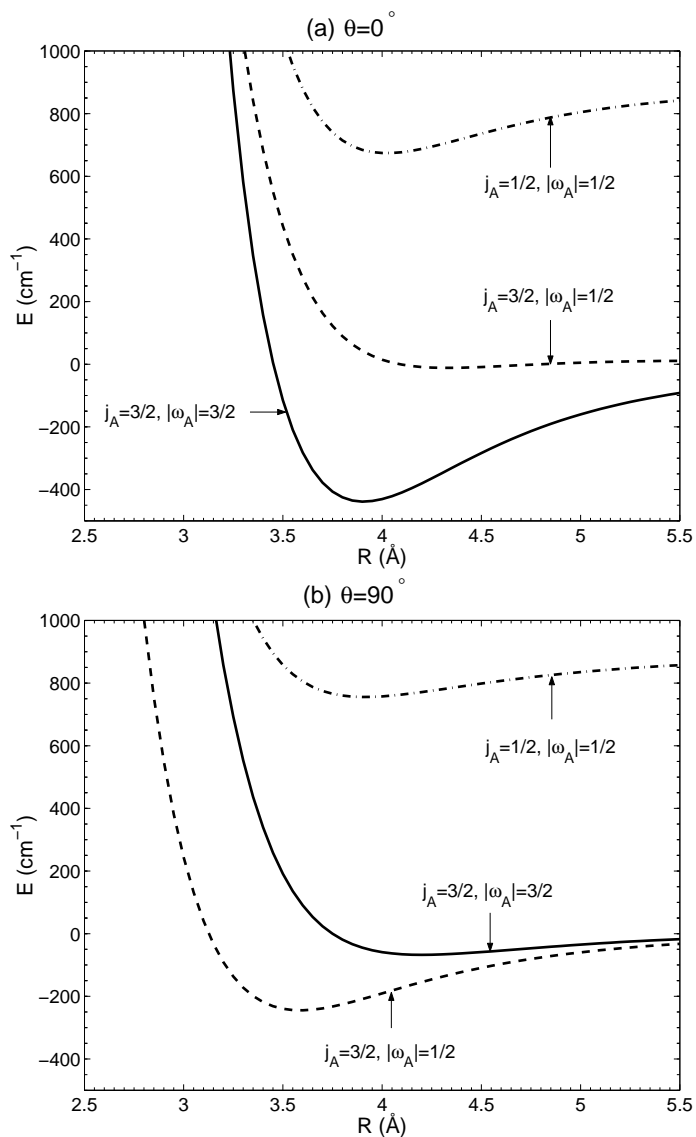


Table 6.2: Energies and wavefunctions from 1d calculations with R fixed at 3.9\AA . The energies E refer to the levels of parity e , $\Delta E = E_f - E_e$ is the parity splitting. The contributions of the basis functions with different quantum numbers are sums of squared coefficients.

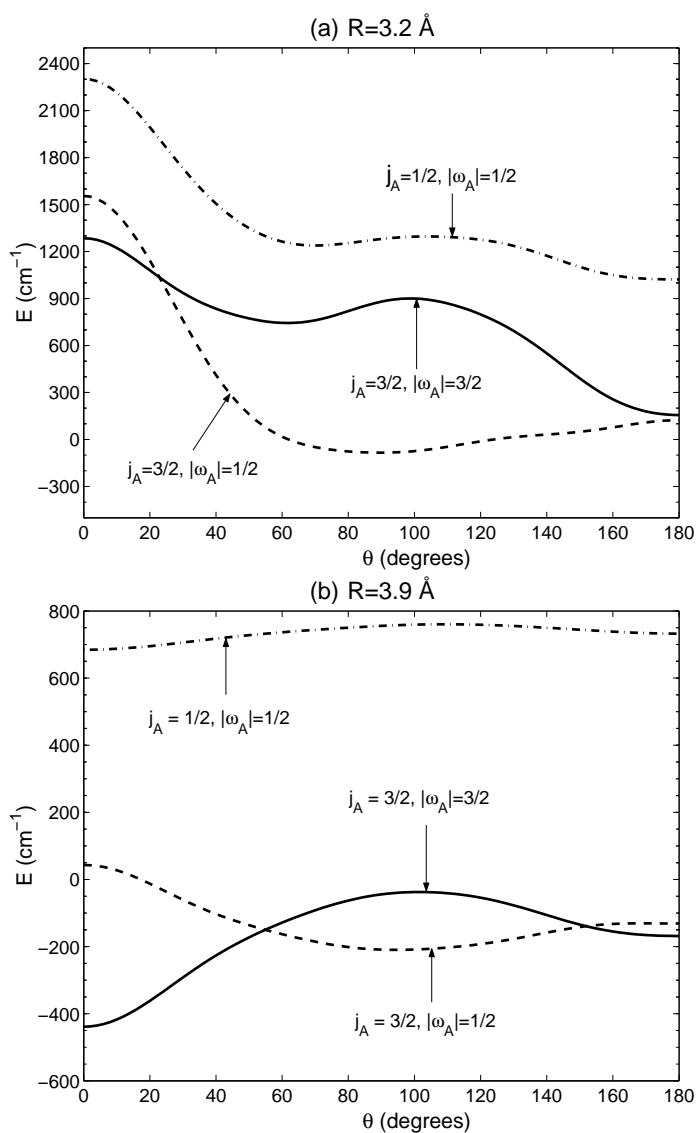
	$J = \frac{1}{2}$			$J = \frac{3}{2}$				
E (cm^{-1})	-255.5538	-227.7538	-193.6043	-305.0698	-255.4367	-231.2392	-227.5604	-182.8490
ΔE (cm^{-1})	0.1383	-0.0013	0.1492	0.0000	0.2766	0.0002	-0.0028	0.0000
$j_A = \frac{1}{2}$	0.013	0.018	0.010	0.001	0.013	0.015	0.018	0.019
$j_A = \frac{3}{2}$	0.987	0.983	0.990	0.999	0.987	0.985	0.983	0.981
$ \omega_A = \frac{1}{2}$	0.599	0.774	0.693	0.069	0.600	0.657	0.774	0.847
$ \omega_A = \frac{3}{2}$	0.400	0.226	0.308	0.931	0.399	0.343	0.226	0.154
$ \Omega = \frac{1}{2}$	1.000	1.000	1.000	0.000	1.000	0.002	0.998	0.000
$ \Omega = \frac{3}{2}$	0.000	0.000	0.000	1.000	0.000	0.998	0.002	1.000
$j_B = 0$	0.445	0.006	0.281	0.220	0.445	0.052	0.006	0.002
$j_B = 1$	0.272	0.679	0.294	0.410	0.271	0.573	0.679	0.008
$j_B = 2$	0.224	0.192	0.173	0.245	0.224	0.169	0.192	0.790
$j_B = 3$	0.055	0.107	0.198	0.085	0.055	0.156	0.107	0.134
$j_B = 4$	0.003	0.015	0.046	0.027	0.003	0.045	0.015	0.059
$j_B = 5$	0.001	0.001	0.006	0.009	0.001	0.005	0.001	0.005
even j_B	0.672	0.213	0.501	0.495	0.673	0.266	0.214	0.852
odd j_B	0.328	0.787	0.499	0.505	0.327	0.734	0.786	0.148
$ \omega_B = 0$	0.597	0.012	0.689	0.930	0.598	0.338	0.013	0.003
$ \omega_B = 1$	0.403	0.767	0.309	0.069	0.402	0.655	0.767	0.013
$ \omega_B = 2$	0.000	0.221	0.001	0.001	0.000	0.007	0.221	0.836
$ \omega_B = 3$	0.000	0.000	0.000	0.000	0.000	0.000	0.000	0.148

Figure 6.2: Cuts through the diabatic potential energy surfaces including spin-orbit coupling. Cuts (a) and (b) for $\theta = 0^\circ$ and 90° , respectively.



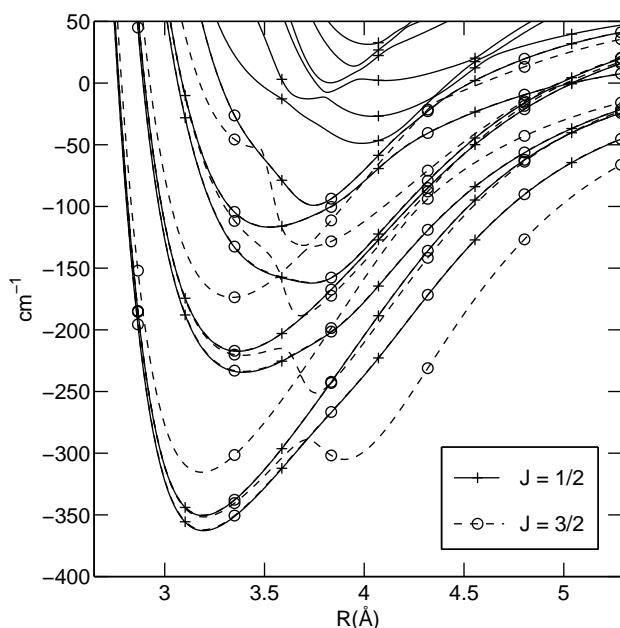
for $R = 3.9 \text{\AA}$ the ground state has $J = \frac{3}{2}$ and $|\Omega| = \frac{3}{2}$. From the potential surface cuts presented in Figure 6.2(a) for $\theta = 0^\circ$ and in Figure 6.2(b) for 90°

Figure 6.3: Cuts through the diabatic potential energy surfaces including spin-orbit coupling. Cuts (a) and (b) for $R = 3.2 \text{ \AA}$ and 3.9 \AA , respectively.



one can see that the ground state at 3.2 \AA corresponds to a minimum in the lowest diabatic potential with $j_A = \frac{3}{2}$ and $|\omega_A| = \frac{1}{2}$ at the T-shaped structure,

Figure 6.4: Bound state energies calculated with R fixed at different values. Closed lines correspond to $J = \frac{1}{2}$ and dashed lines to $J = \frac{3}{2}$.



cf. Figure 6.1(b). It is this diabat that causes the secondary minimum at $\theta = 90^\circ$ in the lowest adiabatic potential energy surface shown in Figure 6.1(d). In Table 6.1 one observes that the ground state at $R = 3.2 \text{ \AA}$ indeed has mostly $j_A = \frac{3}{2}$ and $|\omega_A| = \frac{1}{2}$ character. The ground state at $R = 3.9 \text{ \AA}$ corresponds to the minimum in the lowest diabat with $j_A = \frac{3}{2}$ and $|\omega_A| = \frac{3}{2}$ at the linear structure, see Figure 6.1(a). This diabat is responsible for the minimum at $\theta = 0^\circ$ in the lowest adiabatic potential energy surface shown in Figure 6.1(d). In Table 6.2 one observes that the ground state at $R = 3.9 \text{ \AA}$ indeed has mostly $j_A = \frac{3}{2}$ and $|\omega_A| = \frac{3}{2}$ character.

A striking difference between our results and the results of Dubernet and Hutson [20] is that the ground state with the T-shaped structure and $R \approx 3.2 \text{ \AA}$ was not found in their calculation. Their lowest adiabatic surface including spin-orbit coupling does not display a minimum for the T-shaped geometry. In their lowest spin-free diabat they do find a local minimum at the T-shaped structure, but its relative depth in comparison to the global minimum at the linear structure is smaller than in our case, cf. ref [55]. Hence, their ground state resembles the state of linear geometry that we observe around $R = 3.9 \text{ \AA}$. Zdanska *et al.* [117] did obtain a secondary minimum for the T-shaped struc-

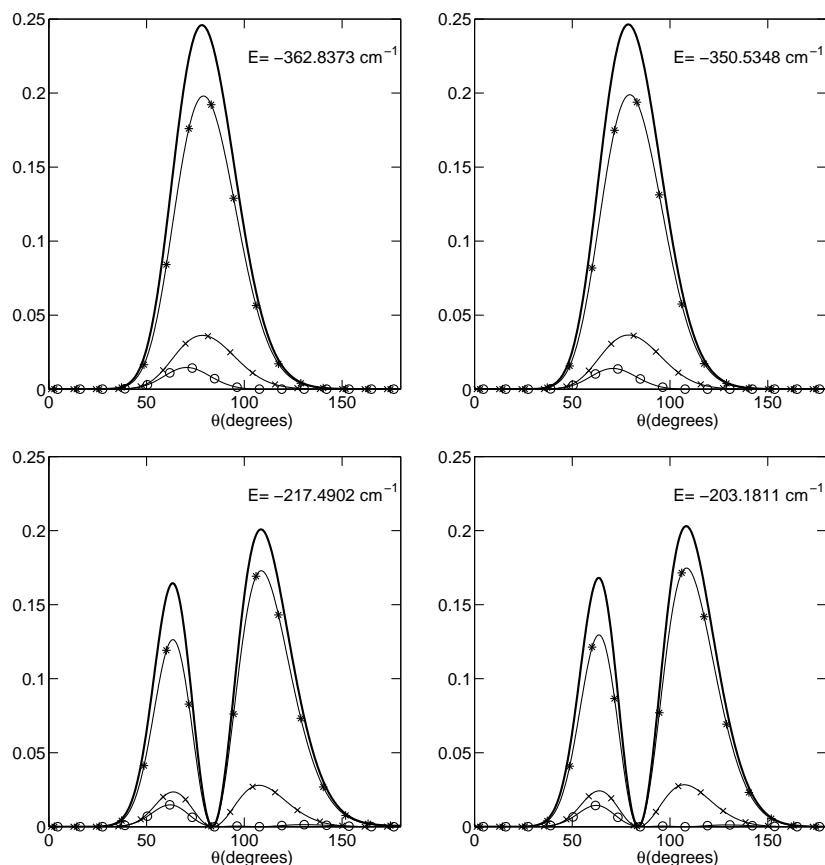
ture in their lowest adiabat including spin-orbit coupling, but apparently this minimum is not sufficiently deep to support the T-shaped ground state that we find.

Inspection of the curves in Figure 6.4 shows an avoided crossing around $R = 3.6 \text{ \AA}$ in the lower curves for $J = \frac{3}{2}, |\Omega| = \frac{3}{2}$. The analysis of the bound states in Tables 6.1 and 6.2 shows that this avoided crossing is accompanied by a switch of $|\omega_A| = \frac{3}{2}$ character at $R = 3.9 \text{ \AA}$, which favors the linear Cl-HCl structure, to $|\omega_A| = \frac{1}{2}$ character at $R = 3.2 \text{ \AA}$, which favors the T-shaped structure. The approximate quantum number j_A is mostly $\frac{3}{2}$ for all the low lying states, because of the large gap between the ${}^2P_{3/2}$ and ${}^2P_{1/2}$ spin-orbit levels in the Cl atom. Still, substantial admixture of the $j_A = \frac{1}{2}$ component is observed at $R = 3.2 \text{ \AA}$. It is somewhat surprising that $|\omega_A|$ is a nearly good quantum number at $R = 3.2 \text{ \AA}$, but not at $R = 3.9 \text{ \AA}$. This can be understood by looking at the potential surface cuts for $R = 3.2 \text{ \AA}$ in Figure 6.3(a) where the $j_A = \frac{1}{2}$ and $j_A = \frac{3}{2}$ curves come close for θ around 90° but the $|\omega_A| = \frac{1}{2}$ and $|\omega_A| = \frac{3}{2}$ curves with $j_A = \frac{3}{2}$ stay far apart for $\theta \approx 90^\circ$. In Figure 6.3(b) one can see that at $R = 3.9 \text{ \AA}$ the $j_A = \frac{1}{2}$ curve stays far above the $j_A = \frac{3}{2}$ curves and the latter stay close together for $|\omega_A| = \frac{1}{2}$ and $|\omega_A| = \frac{3}{2}$ over the whole θ range. The diatom rotational quantum number j_B is definitely not a good quantum number, hence, the rotation of HCl is considerably hindered. Surprisingly, one can clearly distinguish states with even j_B and states with odd j_B at $R = 3.2 \text{ \AA}$. Also $|\omega_B|$ is a nearly good quantum number at $R = 3.2 \text{ \AA}$ but not at $R = 3.9 \text{ \AA}$. The exception is the ground state at $R = 3.9 \text{ \AA}$ which we discussed before. It has a linear geometry and $\omega_B \approx 0$. This state can be considered as a Renner-Teller system, with $|\omega_B|$ being the bending angular momentum that for linear triatomic molecules is commonly denoted as l .

Further understanding of these results can be obtained from a view of the angular density distributions plotted in Figures 6.5 and 6.6. These distributions are obtained by integrating the absolute square of the rovibronic wavefunctions over all coordinates except the angle θ . They contain contributions of the different electronic spin-orbit components ($j_A, |\omega_A|$) which are marked separately. It is clear that the Cl atom and the HCl diatom already have a strong interaction at $R = 3.9 \text{ \AA}$, but this affects mostly the diatom by more or less fixing its orientation (j_B is not a good quantum number anymore). The splitting between the $j_A = \frac{1}{2}$ and $j_A = \frac{3}{2}$ spin-orbit states of the Cl(2P) atom is almost completely preserved. For $R = 3.2 \text{ \AA}$ there is also a strong change in the spin-orbit levels of the Cl atom and j_A is no longer a good quantum number. Instead, the projections $|\omega_A|$ and $|\omega_B|$ on the intermolecular axis \mathbf{R} become good quantum numbers, which shows the more rigid character of the complex.

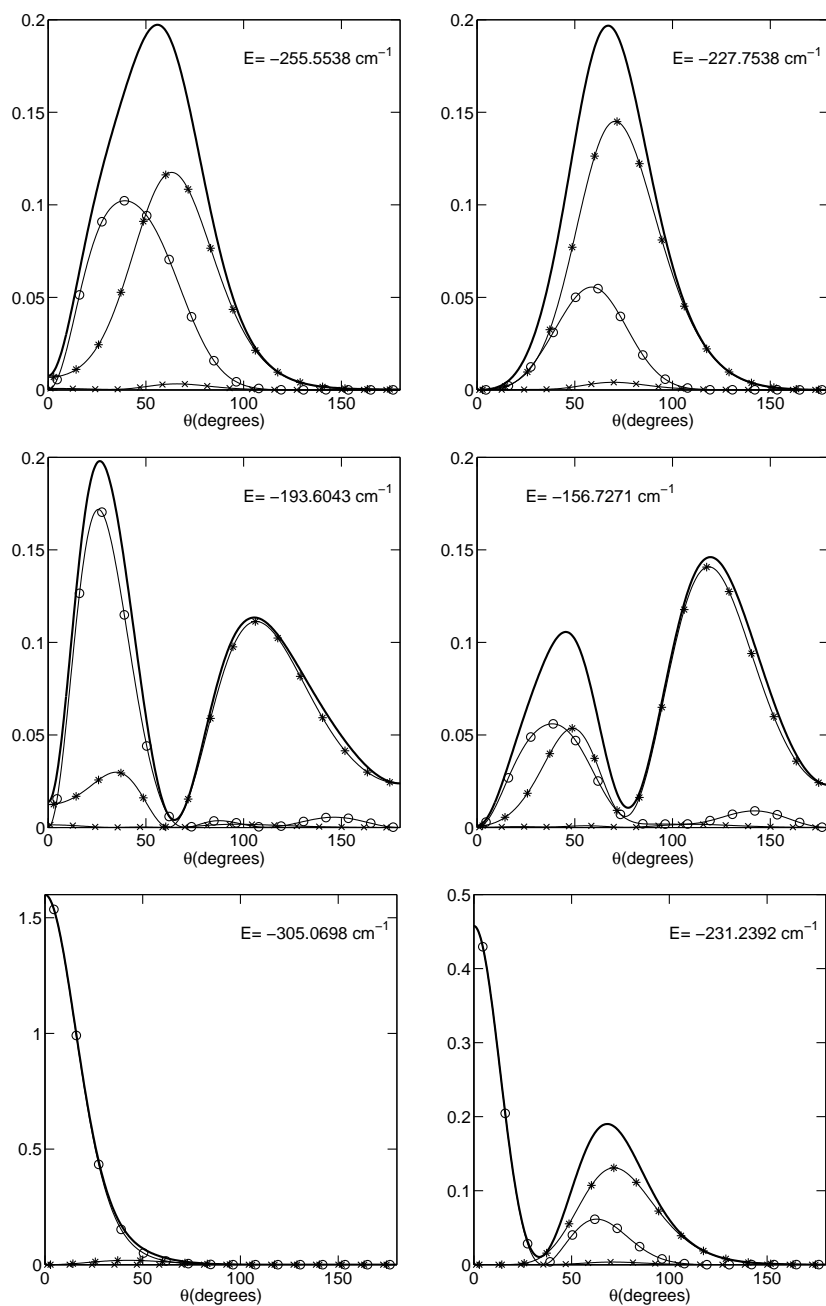
Figure 6.5 demonstrates again that the complex forms in the T-shaped geometry at $R = 3.2 \text{ \AA}$. In the ground state, with $\omega_B \approx 0$ (upper left panel), the diatom orientation is more or less fixed around $\theta = 90^\circ$ by a mixture of basis functions with mainly $j_B = 0$ and $j_B = 2$ (see Table 6.1). In the first

Figure 6.5: Wavefunctions squared from 1d calculations at $R = 3.2 \text{ \AA}$ for $J = \frac{1}{2}$ and $|\Omega| = \frac{1}{2}$, integrated over all coordinates except θ . The contributions of the electronic spin-orbit states ($j_A, |\omega_A|$) are marked by ‘o’ for $(\frac{3}{2}, \frac{3}{2})$, ‘*’ for $(\frac{3}{2}, \frac{1}{2})$, and ‘x’ for $(\frac{1}{2}, \frac{1}{2})$. The energy levels are listed in Table 6.1.



excited state, with $|\omega_B| \approx 1$ (upper right panel), the diatom orientation is equally well localized. We mentioned already that the system at $R = 3.2 \text{ \AA}$ has a strong preference for even or odd values of j_B . This is reminiscent of the para/ortho distinction in H_2 complexes, but quite unexpected as HCl is a strongly heteronuclear diatom. Even values of j_B occur in the ground state and odd values in the first excited state. Figure 6.5 also shows that the second and third excited states are bending excited states. For $R = 3.9 \text{ \AA}$, Figure 6.6, the diatom orientation is clearly more delocalized. This figure contains also the

Figure 6.6: Wavefunctions squared from 1d calculations at $R = 3.9 \text{ \AA}$, integrated over all coordinates except θ , for $J = \frac{1}{2}$ (upper four panels) and $J = \frac{3}{2}$ (lower two panels). The contributions of the spin-orbit states $(j_A, |\omega_A|)$ are marked by ‘o’ for $(\frac{3}{2}, \frac{3}{2})$, ‘*’ for $(\frac{3}{2}, \frac{1}{2})$, and ‘x’ for $(\frac{1}{2}, \frac{1}{2})$. The energy levels are listed in Table 6.2.



lowest two states with $J = \frac{3}{2}$ and $|\Omega| = \frac{3}{2}$. The first one has a linear structure, the second is delocalized over the linear and T-shaped geometries.

6.3.2 Full calculation

We performed full two-dimensional (2d) calculations for the intermolecular degrees of freedom by introducing a radial basis of 15 functions $\chi_n(R)$, with $n_{\max} = 14$, as defined in ref [50]. The nonlinear parameters $R_e = 3.60 \text{ \AA}$, $D_e = 430 \text{ cm}^{-1}$, and $\omega_e = 34.5 \text{ cm}^{-1}$ in this basis were optimized by energy minimizations with smaller values of n_{\max} . The rovibronic levels and parity splittings for $J = \frac{1}{2}, \frac{3}{2}, \frac{5}{2}, \frac{7}{2}$ are given in Tables 6.3 and 6.5. Also the main character of the corresponding wavefunctions is indicated in these tables. As in the calculations with R fixed, $|\Omega|$ is a nearly good quantum number and we can sort the energy levels with respect to $|\Omega|$.

In agreement with the 1d calculations with R fixed at $R = 3.2 \text{ \AA}$ we find that the ground state corresponds to the second diabat with $j_A = \frac{3}{2}$ and $|\omega_A| = \frac{1}{2}$. The density plots for $J = \frac{1}{2}, |\Omega| = \frac{1}{2}$ in Figure 6.7 show that it has a T-shaped geometry. The binding energy D_0 of the complex is 337.8 cm^{-1} for $J = \frac{1}{2}, |\Omega| = \frac{1}{2}$, and spectroscopic parity e . Note that the lowest adiabatic potential including the spin-orbit coupling displays a local minimum with $D_e = 377 \text{ cm}^{-1}$ at the T-shaped geometry with $R_e = 3.2 \text{ \AA}$, and the zero-point level in the calculations with R fixed at 3.2 \AA lies at -362.8 cm^{-1} . The global minimum in this potential with well depth $D_e = 439 \text{ cm}^{-1}$ occurs for the linear geometry at $R_e = 3.9 \text{ \AA}$. The first state with a linear Cl-HCl geometry, see Figure 6.8, is found for $J = \frac{3}{2}, |\Omega| = \frac{3}{2}$, and lies at -276.1 cm^{-1} . This is in good agreement with the ground state energy of -273.7 cm^{-1} that Dubernet and Hutson [20] calculated with their empirical model potential. Note that this potential does not support the T-shaped ground state structure, however, which we find much lower in energy. Also the *ab initio* potential of Zdanska *et al.* [117] does not support the T-shaped ground state structure and, moreover, the well depth and binding energy of the complex are considerably smaller in this potential.

We observe in the figures 6.7 and 6.8 that the angular distributions are in good agreement with the results of the 1d calculations represented in Figures 6.5 and 6.6. The states with $J = \frac{1}{2}$ and $|\Omega| = \frac{1}{2}$ in Figure 6.7 correspond to the T-shaped states computed at $R = 3.2 \text{ \AA}$, the states with $J = \frac{3}{2}$ and $|\Omega| = \frac{3}{2}$ in Figure 6.8 to the states of linear geometry found for $R = 3.9 \text{ \AA}$. The states with energies $E = -293.65$ and -279.43 cm^{-1} in Figure 6.7 are clearly stretch fundamentals which have no counterpart in the 1d calculations with R fixed. The states with energies $E = -215.32$ and -197.01 cm^{-1} in Figure 6.7 are bending fundamentals in nice correspondence with the third and fourth state in Figure 6.5.

It is clear from Figure 6.7 that the Cl-HCl complex has two series of states with a T-shaped geometry and $|\Omega| = \frac{1}{2}$ with very similar internal motion, one with $\omega_B \approx 0$ that includes the ground state at -337.80 cm^{-1} , and one

Figure 6.7: Density distributions from full 2d calculations for $J = \frac{1}{2}$ and $|\Omega| = \frac{1}{2}$. These distributions are the squares of the rovibronic wavefunctions, integrated over the electronic coordinates and the overall rotation angles of the complex (α, β, ϕ) . The corresponding energy levels are listed in Table 6.3.

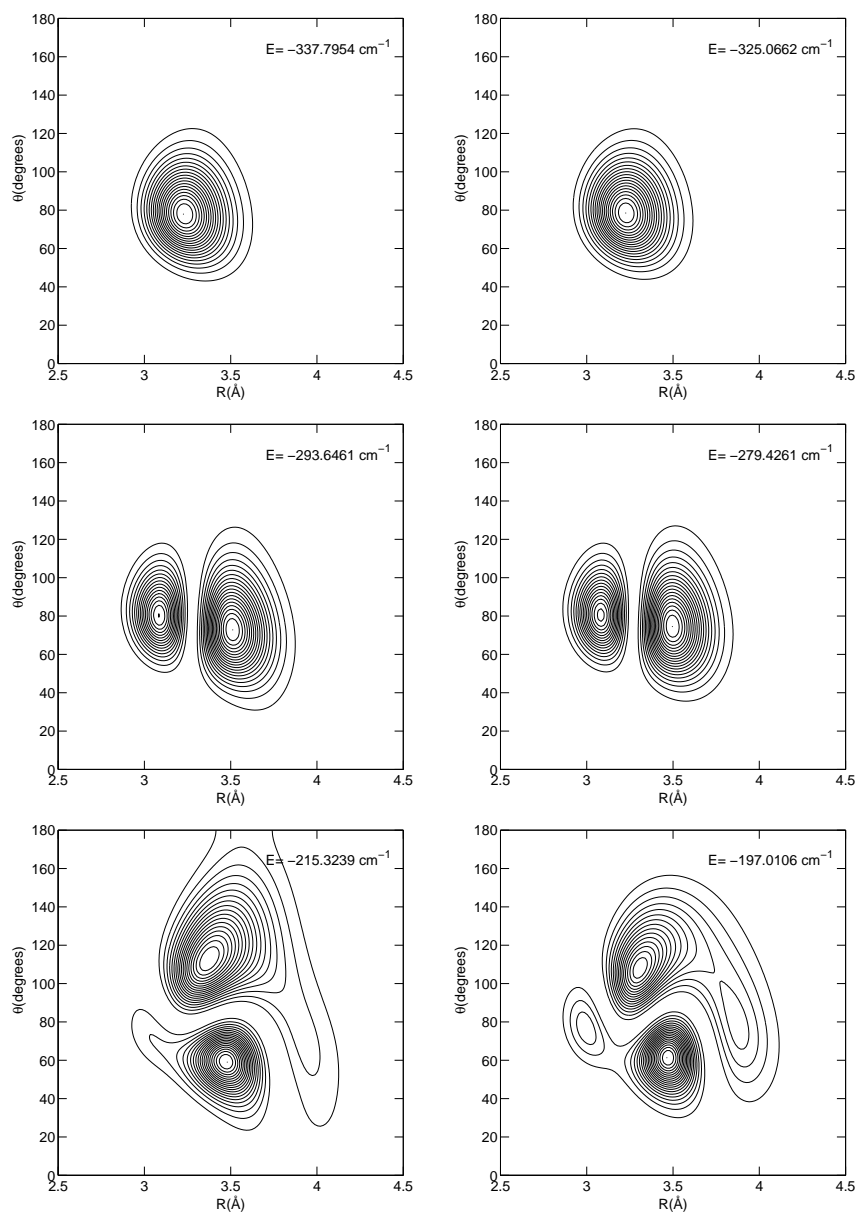
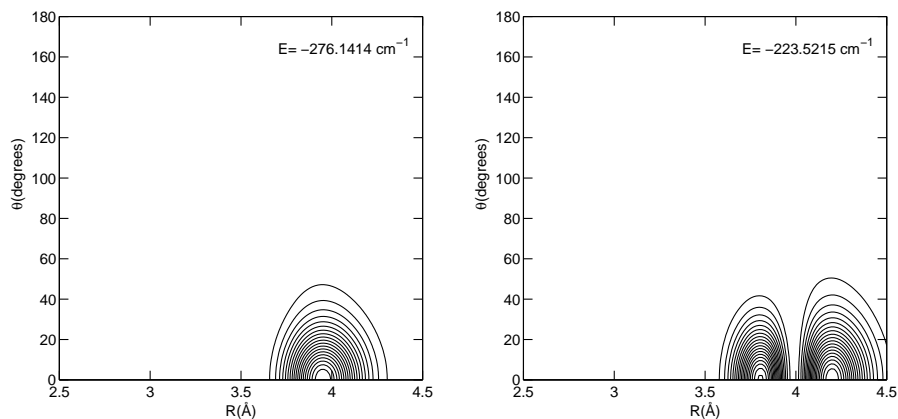


Table 6.3: Lowest bound states of e parity for $J = \frac{1}{2}$ up to $\frac{7}{2}$. Energies in cm^{-1} relative to the energy of $Cl(^2P_{3/2})$ and HCl , v_b and v_s are bending and stretch quantum numbers.

$ \omega_A $	$ \omega_B $	v_b	v_s	$J = \frac{1}{2}$	$J = \frac{3}{2}$	$J = \frac{5}{2}$	$J = \frac{7}{2}$
				$ \Omega = \frac{1}{2}$			
1	0	0	0	-337.7954	-337.6639	-337.3530	-336.8627
1	1	0	0	-325.0662	-324.7655	-324.2682	-323.5761
0	0	0	1	-293.6461	-293.5216	-293.2286	-292.7672
1	0	0	1	-279.4261	-279.1678	-278.7404	-278.1451
0	0	0	2	-254.3481	-254.2233	-253.9404	-253.4994
1	0	0	2	-237.2569	-237.0075	-236.5930	-236.0137
0	0	0	3	-220.0136	-219.8837	-219.6032	-219.1720
0	1	0	0	-215.3239	-215.2127	-214.9421	-214.5123
1	0	0	3	-198.2722	-197.9996	-197.5585	-196.9534
1	1	0	0	-197.0106	-196.7601	-196.3435	-195.7608
0	0	0	4	-187.2257	-187.0933	-186.8135	-186.3863
0	1	1	1	-182.5825	-182.4678	-182.2048	-181.7934
1	0	0	4	-161.6095	-161.3869	-161.0068	-160.4702
				$ \Omega = \frac{3}{2}$			
1	1	0	0	-326.9326	-326.5281	-325.9594	
2	0	0	0	-289.5309	-289.0560	-288.3921	
1	0	0	1	-286.1012	-285.7228	-285.1937	
0	0	0	0	-276.1414	-275.7858	-275.2856	
1	0	0	2	-243.4595	-243.0580	-242.4980	
2	0	0	1	-241.6363	-241.2266	-240.6514	
0	0	0	1	-223.5215	-223.2030	-222.7569	
1	1	1	1	-202.7512	-202.3781	-201.8561	
1	0	0	3	-200.4761	-200.1142	-199.6072	
2	0	0	2	-198.1769	-197.7996	-197.2593	
0	0	0	2	-181.9647	-181.6557	-181.2231	
1	0	0	4	-165.4738	-165.1164	-164.6162	
				$ \Omega = \frac{5}{2}$			
1	2	0	0			-292.9108	-292.3186
2	0	0	1			-250.0382	-249.4693
3	0	0	0			-231.1916	-230.5332
2	0	0	2			-214.2311	-213.6980
2	0	0	3			-184.7843	-184.2657
3	0	0	1			-182.8027	-182.1994
2	1	0	0			-161.2700	-160.7185
				$ \Omega = \frac{7}{2}$			
1	3	0	0				-236.0136
3	0	0	1				-192.5597

Figure 6.8: Density distributions from full 2d calculations for for $J = \frac{3}{2}$ and $|\Omega| = \frac{3}{2}$. For explanations, see Figure 6.7.



with $|\omega_B| \approx 1$ that starts at the slightly higher energy of -325.07 cm^{-1} . In Table 6.3 one observes two similar series of levels for $|\Omega| = \frac{3}{2}$, one with $|\omega_B| \approx 1$ starting at -326.93 cm^{-1} , and one with $|\omega_B| \approx 2$ starting at -289.53 cm^{-1} . Comparison of the energy levels from the 2d calculation in Table 6.3 to the levels from the 1d calculation in Table 6.1 shows that for each of these series of states the stretch zero-point energy of the complex is about 25 cm^{-1} . In the harmonic approximation this corresponds to a stretch frequency of about 50 cm^{-1} . In the full 2d calculation we could identify stretch progressions with quantum numbers up to $v_s = 4$. Fits of these progressions to the usual formula with anharmonic corrections

$$E(v_s) = D_e + \omega_e(v_s + \frac{1}{2}) - \omega_e x_e(v_s + \frac{1}{2})^2 + \omega_e y_e(v_s + \frac{1}{2})^3 \quad (6.11)$$

yield the spectroscopic parameters listed in Table 6.4. Two sets of such parameters are given for the T-shaped states with $|\Omega| = \frac{1}{2}$, one for the states with $\omega_B \approx 0$, and one for the states with $|\omega_B| \approx 1$. The third set of parameters refers to the states with $|\Omega| = \frac{3}{2}$ and $|\omega_B| \approx 2$. All values of D_e from these fits agree well with the corresponding energies of the 1d calculations at $R = 3.2 \text{ \AA}$. From a comparison of Tables 6.3 and 6.2 we extracted a stretch zero-point energy of 29 cm^{-1} for the states of linear geometry with $|\Omega| = \frac{3}{2}$ and we could identify a stretch progression with the first and second excited states lying at 52.6 and 94.2 cm^{-1} above the linear ground state at -276.14 cm^{-1} . A fit of this progression to eq (6.11) yields a set of parameters for the states of linear geometry with $\omega_B \approx 0$. Again, the value of D_e from the fit agrees well

Table 6.4: Spectroscopic parameters in cm^{-1} from fits of the stretch progressions.

$ \omega_B $	$ \Omega $	D_e	ω_e	$\omega_e x_e$	$\omega_e y_e$
0	$\frac{1}{2}$	-362.6657	51.5924	4.0430	0.2754
1	$\frac{1}{2}$	-349.4424	49.8261	2.2280	0.0957
2	$\frac{3}{2}$	-315.1439	52.5612	2.6273	0.1378
0	$\frac{3}{2}$	-306.6001	63.6830	5.5315	-

with the lowest energy of the 1d calculation at $R = 3.9 \text{ \AA}$, as it should. The corresponding 2d and 1d bending fundamentals of the T-shaped structure in Tables 6.3 and 6.1 do not show a simple stretch zero-point energy shift, nor do the levels in Table 6.3 show a clear stretch progression on top of the bending excited levels.

The parity splittings of the levels with $J = \frac{1}{2}, \frac{3}{2}, \frac{5}{2},$ and $\frac{7}{2}$ are presented in Table 6.5. They agree very well with the results of the fixed- R calculation at 3.2 \AA in Table 6.1. The largest splittings occur for $|\Omega| = \frac{1}{2}$ and they are nicely proportional to $J + \frac{1}{2}$. This simple linear dependence on $J + \frac{1}{2}$ is well known for λ doubling in linear molecules [119] and it was also found in $\text{Cl}(^2P)\text{-HCl}$ by Dubernet and Hutson [20]. For the lowest levels with $\omega_B = 0$ the proportionality constant is on the order of the end-over-end rotational constant (see below). It is remarkable, however, that the $\omega_B = 0$ states for which we find this type of parity splitting in $\text{Cl}(^2P)\text{-HCl}$ are not linear, but have a T-shaped geometry. Another characteristic feature is that the parity splitting is much smaller for the levels with $|\omega_B| = 1$. Also these smaller splittings are proportional to $J + \frac{1}{2}$, except for the second stretch overtone where some $|\omega_A| = \frac{3}{2}$ character mixes into the mainly $|\omega_A| = \frac{1}{2}$ state.

All these parity splitting characteristics can be understood by considering the Hamiltonian in eq (6.1) and the parity-adapted basis in eq (6.9). From the latter it follows that the energy difference between functions with e and f parity is caused by a coupling between the basis components with $(\omega_A, \omega_B, \Omega)$ and $(-\omega_A, -\omega_B, -\Omega)$. The term in the Hamiltonian that is responsible for this coupling is the Coriolis coupling operator $-2(\hat{j}_A + \hat{j}_B) \cdot \hat{J} / (2\mu_{AB}R^2)$ and, in particular, the step-up and step-down terms with $\hat{j}_A^+ \hat{J}^+$ and $\hat{j}_A^- \hat{J}^-$ in this operator. The operator $[\hat{j}_A^z + \hat{j}_B^z] \hat{J}^z$ gives simply $(\omega_A + \omega_B)\Omega = \Omega^2$ for both components of the parity-adapted basis. The step-up and step-down operators $\hat{j}_B^\pm \hat{J}^\pm$ cannot couple basis functions with ω_B and $-\omega_B$ because this quantum number has integer values and the step-up and step-down operators shift ω_B only by ± 1 . Hence, only the terms $\hat{j}_A^\pm \hat{J}^\pm / (2\mu_{AB}R^2)$ couple basis functions with $(\omega_A, \omega_B, \Omega) = (\frac{1}{2}, 0, \frac{1}{2})$ and $(-\frac{1}{2}, 0, -\frac{1}{2})$. The coupling matrix elements

Table 6.5: Parity splittings $\Delta E = E_f - E_e$ in cm^{-1} .

$ \omega_A $	$ \omega_B $	v_b	v_s	$J = \frac{1}{2}$	$J = \frac{3}{2}$	$J = \frac{5}{2}$	$J = \frac{7}{2}$
$ \Omega = \frac{1}{2}$							
$\frac{1}{2}$	0	0	0	0.2754	0.5508	0.8261	1.1012
$\frac{1}{2}$	1	0	0	-0.0071	-0.0144	-0.0222	-0.0306
$\frac{1}{2}$	0	0	1	0.2564	0.5127	0.7689	1.0248
$\frac{1}{2}$	1	0	1	-0.0065	-0.0129	-0.0192	-0.0252
$\frac{1}{2}$	0	0	2	0.2245	0.4489	0.6730	0.8967
$\frac{1}{2}$	1	0	2	-0.0031	-0.0062	-0.0095	-0.0129
$\frac{1}{2}$	0	0	3	0.1919	0.3836	0.5749	0.7657
$\frac{1}{2}$	0	1	0	0.2557	0.5115	0.7672	1.0230
$\frac{1}{2}$	1	0	3	0.0044	0.0067	0.0076	0.0076
$\frac{1}{2}$	1	1	0	-0.0036	-0.0075	-0.0118	-0.0166
$\frac{1}{2}$	0	0	4	0.1773	0.3544	0.5312	0.7075
$\frac{1}{2}$	0	1	1	0.2158	0.4280	0.6564	0.8709
$\frac{1}{2}$	1	0	4	0.0281	0.0553	0.0809	0.1046
$ \Omega = \frac{3}{2}$							
$\frac{1}{2}$	1	0	0		0.0003	0.0010	0.0024
$\frac{1}{2}$	2	0	0		0.0000	0.0000	0.0000
$\frac{1}{2}$	1	0	1		0.0001	0.0004	0.0009
$\frac{3}{2}$	0	0	0		-0.0001	-0.0005	-0.0012
$\frac{1}{2}$	1	0	2		0.0001	0.0003	0.0008
$\frac{1}{2}$	2	0	1		0.0001	0.0002	0.0005
$\frac{3}{2}$	0	0	1		0.0000	0.0000	0.0000
$\frac{1}{2}$	1	1	1		0.0002	0.0006	0.0015
$\frac{1}{2}$	1	0	3		0.0004	0.0016	0.0039
$\frac{1}{2}$	2	0	2		0.0018	0.0044	0.0073
$\frac{3}{2}$	0	0	2		0.0035	-0.0091	-0.0080
$\frac{1}{2}$	1	0	4		0.0004	0.0017	0.0041

are

$$\begin{aligned}
& \sqrt{\left(j_A(j_A + 1) - \omega_A(\omega_A \pm 1)\right)\left(J(J + 1) - \Omega(\Omega \pm 1)\right)\langle[2\mu_{AB}R^2]^{-1}\rangle} \\
& = \left(j_A + \frac{1}{2}\right)\left(J + \frac{1}{2}\right)\langle[2\mu_{AB}R^2]^{-1}\rangle
\end{aligned} \tag{6.12}$$

and they cause a first-order splitting between the functions of e and f parity, which would otherwise be degenerate. Equation (6.12) shows that this splitting

should indeed be proportional to $J + \frac{1}{2}$ with a proportionality constant that is $2(j_A + \frac{1}{2})$ times the expectation value of $[2\mu_{AB}R^2]^{-1}$ over the radial part of the wavefunction. The quantum number j_A is mostly $\frac{3}{2}$ in the lower levels and the expectation value $\langle [2\mu_{AB}R^2]^{-1} \rangle$ is the end-over-end rotational constant B of the complex. In reality, the parity splitting for the states with $\omega_B \approx 0$ is somewhat smaller than $4B$. Functions with $\omega_B \neq 0$ are not coupled and would not show any parity splitting if ω_B were an exact quantum number. It is not exact, however, so even the wavefunctions with $|\omega_B| \approx 1$ have a small component with $\omega_B = 0$ and show a small parity splitting. For $|\Omega| = \frac{3}{2}$ the splittings are even smaller and they are proportional to $(J - \frac{1}{2})(J + \frac{1}{2})(J + \frac{3}{2})$ as pointed out by Dubernet and Hutson [20]. They are due to a higher order effect of the Coriolis coupling operator $\hat{j}_A^\pm \hat{J}^\pm / (2\mu_{AB}R^2)$. No splittings are shown for $|\Omega| > \frac{3}{2}$, because they are hardly visible at the accuracy of our calculations.

From the levels with $J = \frac{1}{2}, \frac{3}{2}, \frac{5}{2},$ and $\frac{7}{2}$ we extracted rotational constants of the complex. First, we averaged the energies of the e and f states to remove the effect of the parity splitting. We note that the J dependence of the energy levels originates from the term $[(\hat{j}_A + \hat{j}_B)^2 - 2(\hat{j}_A + \hat{j}_B) \cdot \hat{J} + \hat{J}^2] / (2\mu_{AB}R^2)$ in the Hamiltonian. After removal of the parity splitting the energy contribution of this term is $[J(J+1) - \Omega^2] \langle [2\mu_{AB}R^2]^{-1} \rangle$. The band origins E_0 , end-over-end rotational constants B and centrifugal distortion constants D presented in Table 6.6 were obtained by a fit of the levels with $J = \frac{1}{2}, \frac{3}{2}, \frac{5}{2},$ and $\frac{7}{2}$ for each internal state with the formula

$$E(J, |\Omega|) = E_0 + B \left(J(J+1) - \Omega^2 \right) - D \left(J(J+1) - \Omega^2 \right)^2. \quad (6.13)$$

From the wavefunction of each state we also calculated the expectation value of R and the rotational constant $B_{\text{av}} = \langle [2\mu_{AB}R^2]^{-1} \rangle$. In Table 6.6 we compare these results. Especially for the levels with $\omega_B = 0$ we find that the B value from the fit of the rotational levels agrees very well with the expectation value B_{av} . The agreement is somewhat less good for the levels with $|\omega_B| = 1$. In the fit with eq (6.13) it is assumed that the complex is a linear rotor. Hence, we may conclude that the states with $\omega_B = 0$ behave as a linear rotor, whereas the states with $|\omega_B| = 1$ do not. This conclusion is quite remarkable, however, since the complex has clearly a T-shaped geometry, even in the states with $\omega_B = 0$. The same conclusion was reached on the basis of the parity splittings.

In the rotational constants and the values of $\langle R \rangle$ in Table 6.6 one observes a marked distinction between the T-shaped and linear structures. All the states with $|\Omega| = \frac{1}{2}$ have a relatively large rotational constant and $\langle R \rangle$ values between 3.2 and 3.5 Å. They are T-shaped. For $|\Omega| = \frac{3}{2}$ we find T-shaped states with $|\omega_A| \approx \frac{1}{2}$ and linear states with $|\omega_A| \approx \frac{3}{2}$. The latter have a substantially smaller rotational constant B and a value of $\langle R \rangle$ between 3.7 and 4.0 Å. The value of B for the linear geometry agrees fairly well with the value of Dubernet and Hutson [20].

Table 6.6: Expectation values and spectroscopic parameters in cm^{-1} from fits of the rotational levels.

$ \omega_A $	$ \omega_B $	v_b	v_s	$\langle R \rangle$ (Å)	B_{av}	E_0	B	D
$ \Omega = \frac{1}{2}$								
$\frac{1}{2}$	0	0	0	3.26	0.09013	-337.70	0.08972	8.70×10^{-7}
$\frac{1}{2}$	1	0	0	3.25	0.09045	-325.12	0.09912	3.53×10^{-5}
$\frac{1}{2}$	0	0	1	3.38	0.08466	-293.56	0.08423	1.64×10^{-6}
$\frac{1}{2}$	1	0	1	3.36	0.08541	-279.47	0.08511	2.04×10^{-5}
$\frac{1}{2}$	0	0	2	3.51	0.07946	-254.28	0.07901	1.50×10^{-6}
$\frac{1}{2}$	1	0	2	3.47	0.08114	-237.30	0.08263	4.88×10^{-6}
$\frac{1}{2}$	0	0	3	3.61	0.07564	-219.96	0.07526	1.79×10^{-6}
$\frac{1}{2}$	0	1	0	3.47	0.07973	-215.24	0.07970	1.27×10^{-6}
$\frac{1}{2}$	1	0	3	3.53	0.07863	-198.31	0.09134	2.11×10^{-4}
$\frac{1}{2}$	1	1	0	3.46	0.08052	-197.05	0.08286	-1.34×10^{-6}
$\frac{1}{2}$	0	0	4	3.67	0.07392	-187.17	0.07366	1.60×10^{-6}
$\frac{1}{2}$	0	1	1	3.62	0.07446	-182.51	0.07491	2.26×10^{-5}
$\frac{1}{2}$	1	0	4	3.61	0.07593	-161.63	0.07881	1.91×10^{-5}
$ \Omega = \frac{3}{2}$								
$\frac{1}{2}$	1	0	0	3.26	0.08995	-327.05	0.08071	-3.23×10^{-5}
$\frac{1}{2}$	2	0	0	3.25	0.09050	-289.67	0.09506	1.06×10^{-5}
$\frac{1}{2}$	1	0	1	3.54	0.07765	-286.21	0.07573	4.99×10^{-6}
$\frac{3}{2}$	0	0	0	3.75	0.06968	-276.25	0.07090	-2.48×10^{-5}
$\frac{1}{2}$	1	0	2	3.49	0.08054	-243.58	0.08050	2.30×10^{-5}
$\frac{1}{2}$	2	0	1	3.44	0.08237	-241.76	0.08178	-2.07×10^{-5}
$\frac{3}{2}$	0	0	2	3.91	0.06396	-223.62	0.06368	-2.34×10^{-6}
$\frac{1}{2}$	1	1	0	3.55	0.07718	-202.86	0.07468i	1.67×10^{-6}
$\frac{1}{2}$	1	1	1	3.54	0.07789	-200.58	0.07242	-8.87×10^{-6}
$\frac{1}{2}$	2	0	2	3.48	0.08088	-198.29	0.07459	-1.40×10^{-4}
$\frac{3}{2}$	0	0	3	4.00	0.06187	-182.05	0.05964	-1.12×10^{-4}
$\frac{1}{2}$	1	0	4	3.62	0.07532	-165.58	0.07159	-1.99×10^{-6}

6.4 Conclusion

Without consideration of the spin-orbit coupling the $\text{Cl}(^2P)\text{-HCl}$ complex has three asymptotically degenerate electronic states. With the use of the accurate *ab initio* adiabatic and diabatic intermolecular potential energy surfaces that were recently computed for these states [55] we calculated the bound levels of this complex for $J = \frac{1}{2}, \frac{3}{2}, \frac{5}{2}$, and $\frac{7}{2}$ with the inclusion of spin-orbit coupling.

After a fit of the diabatic potentials with an appropriate analytic form of the anisotropy we present diabatic and adiabatic potentials including spin-orbit coupling. These were very useful to understand the characteristics of the bound levels calculated. We further elucidated these characteristics by a series of one-dimensional calculations on the hindered rotation or bending motion of the HCl monomer with the Cl–HCl distance R fixed at values ranging from 2.5 to 5.5 Å. The ground state of the complex turned out to have a T-shaped geometry with $\langle R \rangle \approx 3.2$ Å, and we identified the associated stretch and bending excited levels. We also found a progression of states with a linear geometry of the complex at substantially higher energy with $\langle R \rangle \approx 3.7$ to 4.0 Å. Previous, more approximate, calculations with empirical [20] or *ab initio* [117] potentials led to a ground state of linear geometry; the T-shaped states were not predicted in earlier work. Stretch and bending vibrational frequencies, rotational constants, and parity splittings were obtained from the usual spectroscopic fits of the levels calculated for different values of J ; the rotational constants were also computed from expectation values. It is noteworthy that the Cl–HCl complex displays several series of states with a T-shaped geometry and very similar internal motion, with different values of $|\omega_B|$. This quantum number ω_B is the component of rotational angular momentum j_B of the HCl monomer on the Cl–HCl bond axis. The series of levels with $\omega_B \approx 0$ includes the ground state and has the remarkable feature that the states possess a T-shaped structure, but display several of the properties of a linear open-shell molecule, such as a relatively large parity splitting proportional to $J + \frac{1}{2}$.

CHAPTER 7

Theoretical study of the He–HF⁺ complex. Rovibronic states from coupled diabatic potential energy surfaces

The bound rovibronic levels of the He–HF⁺ complex were calculated for total angular momentum $J = \frac{1}{2}, \frac{3}{2}, \frac{5}{2}, \frac{7}{2},$ and $\frac{9}{2}$ with the use of *ab initio* diabatic intermolecular potentials, presented in ref [120], and the inclusion of spin-orbit coupling. The character of the rovibronic states was interpreted by a series of calculations with the intermolecular distance R fixed at values ranging from 1.5 to 8.5 Å and by analysis of the wave functions. In this analysis we used approximate angular momentum quantum numbers defined with respect to a dimer body-fixed frame (BF) with its z -axis parallel to the intermolecular vector \mathbf{R} and with respect to a molecule-fixed frame (MF) with its z -axis parallel to the HF⁺ bond. The linear equilibrium geometry makes the He–HF⁺ complex a Renner-Teller system. We found both sets of quantum numbers, BF and MF, useful to understand the characteristics of the Renner-Teller effect in this system. In addition to the properties of a “normal” semi-rigid molecule Renner-Teller system it shows typical features caused by large-amplitude internal (bending) motion. We also present spectroscopic data: stretch and bend frequencies, spin-orbit splittings, parity splittings, and rotational constants.

7.1 Introduction

The article of Lotrich *et al.* [120] presents the calculation of the two asymptotically degenerate adiabatic potential surfaces of the He–HF⁺ complex that correlate with the degenerate $X^2\Pi$ ground state of HF⁺. The twofold spatial degeneracy of this Π state is lifted, except when the complex has a linear geometry. The method used for this calculation is a recently proposed [121] *ab initio* method that combines the potential energy surface of the neutral closed-shell complex, He–HF in this case, with the ionization energies of the complex and of one of the monomers (here HF) to obtain the interaction energy of the cationic complex. Multiple (excited state) potential surfaces can be efficiently generated by the computation of higher ionization energies of the neutral species, a feature that is used in this case to obtain simultaneously the lowest two asymptotically degenerate potential surfaces of He–HF⁺. Reference [120] also presents diabatic surfaces obtained from the two adiabatic ones and a full analytic fit of these diabatic surfaces. In the present chapter we proceed by calculating the rovibronic states of the complex on the diabatic potential surfaces, with the inclusion of spin-orbit coupling. In Sec. 7.2 we describe the formalism used to perform these calculations in space-fixed and different body-fixed coordinates. The non-adiabatic coupling that is particularly important near the linear geometry of the complex where the adiabatic states become degenerate is implicitly taken into account in these calculations. In Sec. 7.3 we present and discuss the results, first of one-dimensional calculations with the intermolecular distance R fixed at a range of values, then of the full calculations.

Since the two potential surfaces computed in [120] correspond to a linear equilibrium geometry of He–HF⁺ this complex is a Renner-Teller system. It is much more strongly bound than the neutral Van der Waals complex He–HF, but considerably less rigid than a normal, chemically bound, linear triatomic molecule where Renner-Teller coupling has mostly been studied. Therefore, we will pay special attention, in Sec. 7.3.3, to the way in which the Renner-Teller effect becomes manifest in this system. We will compare our results to those of Schmelz and Rosmus [122], who made a similar study on different potential surfaces.

7.2 Calculation of rovibronic states

Different coordinates and basis sets can be used to calculate the vibration-rotation-tunneling (VRT) levels of Van der Waals dimers. In particular, one may choose a space-fixed (SF) basis or various body-fixed bases [17, 81], as well as different angular momentum coupling schemes [83]. The rovibronic states of He–HF⁺ were first calculated in this work in a coupled SF basis. For the interpretation of the results and the understanding of the Renner-Teller effect it turned out, however, that the expansion of the rovibronic states and the consideration of various approximate quantum numbers with respect to

different body-fixed frames was very useful. So, we also performed calculations with body-fixed bases with angular momentum projection quantum numbers defined either (BF) with respect to the vector \mathbf{R} that points from the HF⁺ center of mass to the He nucleus or (MF) with respect to the HF⁺ bond axis \mathbf{r} . It is not necessary to repeat the computation of the energy levels in the different frames; the transformation from the SF basis to the BF and MF bases is given analytically. Before we discuss the formalism to compute the rovibronic levels of the complex, we briefly summarize the fine structure of HF⁺ in its X²Π ground state.

The dominant term that splits the levels of HF⁺(X²Π) is the spin-orbit coupling (coupling constant $A = -293.14 \text{ cm}^{-1}$). Approximate quantum numbers that characterize these energy levels are $\Lambda = \pm 1$ and $\Omega = \Lambda + \Sigma$. The quantum number Λ is the eigenvalue of the electronic orbital angular momentum operator \hat{l}_z and $\Sigma = -\frac{1}{2}, \frac{1}{2}$ is the eigenvalue of \hat{S}_z , which is the component of the spin ($S = \frac{1}{2}$) along the HF⁺ bond axis. The total angular momentum of the HF⁺ monomer is represented by the operator $\hat{\mathbf{j}} = \hat{\mathbf{l}} + \hat{\mathbf{S}} + \hat{\mathbf{R}}$, where $\hat{\mathbf{l}}$, $\hat{\mathbf{S}}$, and $\hat{\mathbf{R}}$ are the electronic orbital and spin, and the nuclear (rotation) angular momenta, respectively. For free HF⁺ the quantum number j that corresponds with the operator $\hat{\mathbf{j}}$ is an exact quantum number. The eigenvalue Ω of the electronic angular momentum operator $\hat{l}_z + \hat{S}_z$ is also an eigenvalue of \hat{j}_z , because the nuclear angular momentum $\hat{\mathbf{R}}$ has a vanishing z component. As a result of spin-orbit coupling, the levels with $\Omega = \pm\frac{3}{2}$ are lower by about 300 cm^{-1} than the levels with $\Omega = \pm\frac{1}{2}$, which makes HF⁺(X²Π) a typical Hund's coupling case (a) system. For $j > 0$ Ω is not an exact quantum number even for the free monomer, because states with different Ω are slightly mixed by Coriolis coupling. The effective monomer Hamiltonian that describes the complete level structure of HF⁺(X²Π) is

$$\hat{H}_{\text{HF}^+} = B_0 \left[\hat{j}^2 + \hat{S}^2 - \hat{j}_z^2 - \hat{S}_z^2 - \hat{S}_- \hat{j}_- - \hat{S}_+ \hat{j}_+ \right] + A \hat{l}_z \hat{S}_z, \quad (7.1)$$

where $B_0 = 17.5779 \text{ cm}^{-1}$ is the rotational constant and $A = -293.14 \text{ cm}^{-1}$ the spin-orbit coupling constant of HF⁺(X²Π) in its vibrational ground state [123]. The components of the angular momentum operator $\hat{\mathbf{j}}$ are given with respect to the MF z -axis and obey anomalous commutation relations [124]. The corresponding shift operators are therefore defined as $\hat{j}_{\pm} = \hat{j}_x \mp i\hat{j}_y$, whereas the spin shift operators have the normal definition $\hat{S}_{\pm} = \hat{S}_x \pm i\hat{S}_y$.

Since the H-F vibration has a much higher frequency than the vibrations of the He-HF⁺ complex we froze the HF⁺ bond length at the equilibrium value $r_e = 1.0011 \text{ \AA}$ [123]. It was shown in ref [120] that the intermolecular potential depends strongly on the HF⁺ bond length, however. The global minimum in a full three-dimensional potential, which is the sum of the intermolecular potential and the H-F⁺ pair potential, occurs at $r = 1.0273 \text{ \AA}$. We also computed rovibronic levels with r fixed at this value. The Hamiltonian of

the He–HF⁺(²Π) complex in SF coordinates can then be written (in atomic units) as

$$\hat{H} = \frac{-1}{2\mu R} \frac{\partial^2}{\partial R^2} R + \frac{\hat{L}^2}{2\mu R^2} + \hat{H}_{\text{HF}^+} + \hat{V} \quad (7.2)$$

where $\mu = 3.3353$ u is the reduced mass of the dimer and \hat{L} is the angular momentum operator corresponding to the end-over-end rotation. The potential energy operator \hat{V} , given in terms of diabatic states, is most conveniently expressed in body-fixed coordinates and will be specified below. In writing Eq. (7.2) we assumed implicitly that the interaction with He does not change the spin-orbit coupling term in the Hamiltonian of the HF⁺ monomer. The SF dimer basis and the matrix elements of the Hamiltonian in Eqs. (7.1) and (7.2) over this basis can be found in chapter 4.

7.2.1 R-embedding

Since He–HF⁺(²Π) is much more strongly bound than He–CO(³Π) the bound states of He–HF⁺(²Π) are most conveniently calculated and interpreted in a basis with coordinates and angular momentum quantum numbers defined with respect to a BF frame with its z -axis along \mathbf{R} . The BF coordinates are defined by writing the SF components of the vectors \mathbf{R} and \mathbf{r} as

$$\mathbf{R} = R \mathbb{R}_z(\alpha) \mathbb{R}_y(\beta) \mathbf{e}_z \quad (7.3)$$

$$\mathbf{r} = r \mathbb{R}_z(\alpha) \mathbb{R}_y(\beta) \mathbb{R}_z(\phi) \mathbb{R}_y(\theta) \mathbf{e}_z \quad (7.4)$$

with the unit vector \mathbf{e}_z being the column vector (0, 0, 1) and the rotation matrices

$$\mathbb{R}_z(\alpha) = \begin{pmatrix} \cos \alpha & -\sin \alpha & 0 \\ \sin \alpha & \cos \alpha & 0 \\ 0 & 0 & 1 \end{pmatrix}, \quad \mathbb{R}_y(\beta) = \begin{pmatrix} \cos \beta & 0 & \sin \beta \\ 0 & 1 & 0 \\ -\sin \beta & 0 & \cos \beta \end{pmatrix}. \quad (7.5)$$

The BF coordinate θ is the angle between \mathbf{r} and \mathbf{R} which is zero for the linear He–HF⁺ geometry. The elements of the matrix $\mathbb{R}(\alpha, \beta, \phi) = \mathbb{R}_z(\alpha) \mathbb{R}_y(\beta) \mathbb{R}_z(\phi)$ are the direction cosines of the (three-angle embedded) BF frame with respect to the SF frame.

The Hamiltonian for the rovibronic states of the complex on the multiple diabatic potential surfaces reads in BF coordinates as

$$\hat{H} = \frac{-1}{2\mu R} \frac{\partial^2}{\partial R^2} R + \frac{\hat{j}^2 - 2\hat{\mathbf{j}} \cdot \hat{\mathbf{J}} + \hat{J}^2}{2\mu R^2} + \hat{H}_{\text{HF}^+} + \sum_{\Lambda', \Lambda} |\Lambda'\rangle^{\text{BF}} V_{\Lambda', \Lambda}^{\text{BF}}(R, \theta)^{\text{BF}} \langle \Lambda|. \quad (7.6)$$

The monomer Hamiltonian \hat{H}_{HF^+} is the same as in the SF representation, see Eq. (7.1). The diabatic states $|\Lambda\rangle^{\text{BF}}$ of the He–HF⁺(²Π) complex, labeled

by the HF^+ monomer quantum number $\Lambda = \pm 1$, are here expressed in BF coordinates, cf. Eq. (A.8). The expansion of the diabatic potentials is given by

$$V_{\Lambda',\Lambda}^{\text{BF}}(R, \theta) = {}^{\text{BF}}\langle \Lambda' | \widehat{V} | \Lambda \rangle^{\text{BF}} = \sum_l v_l^{\Lambda',\Lambda}(R) D_{0,\Lambda-\Lambda'}^{(l)}(0, \theta, 0). \quad (7.7)$$

The functions $D_{m',m}^{(l)}(\phi, \theta, \chi)$ are Wigner rotation functions [124] with two of the angles being zero in this case; note that only functions with $m' = 0$ and $m = \Lambda - \Lambda'$ occur in the expansion. We obtained the above expansion from the corresponding expansion in MF coordinates derived in chapter 4.

$$V_{\Lambda',\Lambda}^{\text{MF}}(R, \theta) = \sum_l v_l^{\Lambda',\Lambda}(R) D_{\Lambda-\Lambda',0}^{(l)}(0, \theta, 0) = \sum_l v_l^{\Lambda',\Lambda}(R) C_{\Lambda-\Lambda'}^{(l)}(\theta, 0). \quad (7.8)$$

with the use of the transformation of the electronic wave functions in Eq. (A.9). The functions $C_m^{(l)}(\theta, \phi)$ are Racah normalized spherical harmonics. It was demonstrated in chapter 4 that the restriction of the expansion to functions with $m = \Lambda - \Lambda'$ follows from the invariance of the potential energy operator \widehat{V} under rotations of the complex about the HF^+ bond axis. The expansion coefficients $v_l^{\Lambda',\Lambda}(R)$ can be written, apart from a known normalization constant, as integrals over the diabatic potentials $V_{\Lambda',\Lambda}^{\text{MF}}(R, \theta)$ multiplied with the corresponding spherical harmonic $C_{\Lambda-\Lambda'}^{(l)}(\theta, 0)$. The integration over θ is performed with the analytic fits of the *ab initio* potentials from ref [120] and the use of numerical Gauss-Legendre quadrature.

The BF dimer basis, as derived in Appendix A, reads

$$\begin{aligned} |n, \Lambda, S, \Omega, j, P_R; J, M_J\rangle &= |n\rangle | \Lambda, S, \Omega \rangle^{\text{BF}} \frac{[(2j+1)(2J+1)]^{1/2}}{4\pi} \\ &\times D_{P_R,\Omega}^{(j)}(0, \theta, 0)^* D_{M_J,P_R}^{(J)}(\alpha, \beta, \phi)^*, \end{aligned} \quad (7.9)$$

where the total angular momentum J and its SF z -component M_J are exact quantum numbers and P_R is the projection of both \mathbf{J} and the monomer angular momentum \mathbf{j} on the BF z -axis. The electronic wave function $| \Lambda, S, \Omega \rangle^{\text{BF}}$, labeled by the Hund's case (a) quantum numbers Λ, S, Ω of HF^+ , and implicitly by $\Sigma = \Omega - \Lambda$, is a diabatic wave function of the $\text{He-HF}^+(X^2\Pi)$ complex, here expressed in BF coordinates [Eq. (A.8)]. The symmetric rotor function $D_{P_R,\Omega}^{(j)}(0, \theta, 0)^*$ describes the HF^+ rotation with respect to the dimer BF frame and the function $D_{M_J,P_R}^{(J)}(\alpha, \beta, \phi)^*$ the overall rotation of the complex. The radial basis functions $|n\rangle = \chi_n(R)$ are Morse oscillator type functions of the form defined in Ref. [50].

The matrix elements of the Hamiltonian in the BF basis are

$$\begin{aligned}
& \langle n', \Lambda', S, \Omega', j', P'_R; J, M_J | \widehat{H} | n, \Lambda, S, \Omega, j, P_R; J, M_J \rangle \\
&= \delta_{\Lambda', \Lambda} \delta_{\Omega', \Omega} \delta_{j', j} \delta_{P'_R, P_R} \left[\langle n' | \frac{-1}{2\mu R} \frac{\partial^2}{\partial R^2} R | n \rangle \right. \\
&+ \langle n' | \frac{1}{2\mu R^2} | n \rangle \left(J(J+1) + j(j+1) - 2P_R^2 \right) \\
&+ \delta_{n', n} B_0 \left(j(j+1) + S(S+1) - \Omega^2 - \Sigma^2 \right) + \delta_{n', n} A \Lambda \Sigma \left. \right] \\
&- \delta_{j', j} \delta_{\Lambda', \Lambda} \left[\delta_{\Omega', \Omega} \langle n' | \frac{1}{2\mu R^2} | n \rangle \left(C_{P'_R, P_{R-1}}^J C_{P_R, P_{R-1}}^j + C_{P'_R, P_{R+1}}^J C_{P_R, P_{R+1}}^j \right) \right. \\
&+ B_0 \delta_{P'_R, P_R} \delta_{n', n} \left(C_{\Omega', \Omega-1}^S C_{\Sigma', \Sigma-1}^S + C_{\Omega', \Omega+1}^S C_{\Sigma', \Sigma+1}^S \right) \left. \right] \\
&+ \langle n', \Lambda', S, \Omega', j', P'_R; J, M_J | \widehat{V} | n, \Lambda, S, \Omega, j, P_R; J, M_J \rangle \tag{7.10}
\end{aligned}$$

with shift matrix elements $C_{m', m \pm 1}^j = \delta_{m', m \pm 1} \sqrt{j(j+1) - m(m \pm 1)}$. The matrix elements of the potential energy operator are

$$\begin{aligned}
& \langle n', \Lambda', S, \Omega', j', P'_R; J, M_J | \widehat{V} | n, \Lambda, S, \Omega, j, P_R; J, M_J \rangle \\
&= \sqrt{(2j'+1)(2j+1)} (-1)^{P'_R - \Omega'} \delta_{\Sigma', \Sigma} \tag{7.11} \\
&\times \sum_l \langle n' | v_l^{\Lambda', \Lambda}(R) | n \rangle \begin{pmatrix} j' & l & j \\ -P'_R & 0 & P_R \end{pmatrix} \begin{pmatrix} j' & l & j \\ -\Omega' & \Lambda' - \Lambda & \Omega \end{pmatrix}.
\end{aligned}$$

The expressions in large round brackets are $3j$ -symbols [39].

The parity-adapted basis in the BF embedding is

$$\begin{aligned}
| n, |\Lambda|, S, \Omega, j, P_R; J, M_J, p \rangle &= | n, \Lambda, S, \Omega, j, P_R; J, M_J \rangle \tag{7.12} \\
&+ p(-1)^{J-S} | n, -\Lambda, S, -\Omega, j, -P_R; J, M_J \rangle
\end{aligned}$$

with p being the parity under inversion and $p(-1)^{J-S}$ the spectroscopic parity, e or f .

7.2.2 r -embedding

In order to recognize the characteristic features of a Renner-Teller system it is also useful to express the rovibronic wave functions in coordinates defined with respect to a frame with its z -axis parallel to the HF⁺ monomer bond axis \mathbf{r} . We call this frame molecule-fixed (MF). The MF coordinates are defined by writing the SF components of the vectors \mathbf{r} and \mathbf{R} as

$$\mathbf{r} = r \mathbb{R}_z(\phi') \mathbb{R}_y(\theta') \mathbf{e}_z \tag{7.13}$$

$$\mathbf{R} = R \mathbb{R}_z(\phi') \mathbb{R}_y(\theta') \mathbb{R}_z(\alpha') \mathbb{R}_y(\beta') \mathbf{e}_z. \tag{7.14}$$

The MF coordinate β' , the angle between the vectors \mathbf{R} and \mathbf{r} , is the same as the BF coordinate θ . The matrix $\mathbb{R}(\phi', \theta', \alpha') = \mathbb{R}_z(\phi')\mathbb{R}_y(\theta')\mathbb{R}_z(\alpha')$ contains the direction cosines of the (three-angle embedded) MF frame with respect to the SF frame.

The dimer Hamiltonian in the MF representation is similar to the SF Hamiltonian in Eq. (7.2) except for the appearance of the HF⁺ monomer term. Since the quantum number j is not defined in the MF representation, we write the HF⁺ monomer Hamiltonian as

$$\begin{aligned} \hat{H}_{\text{HF}^+} &= B_0 \left[\hat{J}^2 + \hat{L}^2 + \hat{S}^2 - \hat{J}_z^2 - \hat{L}_z^2 - \hat{S}_z^2 - (\hat{L}_- \hat{J}_- + \hat{L}_+ \hat{J}_+) \right. \\ &\quad \left. - (\hat{S}_- \hat{J}_- + \hat{S}_+ \hat{J}_+) + (\hat{L}_+ \hat{S}_- + \hat{L}_- \hat{S}_+) \right] + A \hat{l}_z \hat{S}_z. \end{aligned} \quad (7.15)$$

The potential energy operator is now

$$\hat{V} = \sum_{\Lambda', \Lambda} | \Lambda' \rangle^{\text{MF}} V_{\Lambda', \Lambda}^{\text{MF}}(R, \beta')^{\text{MF}} \langle \Lambda |. \quad (7.16)$$

with diabatic states $| \Lambda \rangle^{\text{MF}}$ in MF coordinates, cf. Eq. (A.7). The expansion of the diabatic potentials $V_{\Lambda', \Lambda}^{\text{MF}}(R, \beta')$ is given by Eq. (7.8) with $\theta = \beta'$. The dimer basis functions in MF coordinates are, cf. Appendix A

$$\begin{aligned} | n, \Lambda, S, \Omega, L, \Omega_L, P_r; J, M_J \rangle &= | n \rangle | \Lambda, S, \Omega \rangle^{\text{MF}} Y_{L\Omega_L}(\beta', 0) \\ &\quad \times \left[\frac{2J+1}{4\pi} \right]^{\frac{1}{2}} D_{M_J, P_r}^{(J)}(\phi', \theta', \alpha')^*, \end{aligned} \quad (7.17)$$

where Ω_L is the projection of the end-over-end angular momentum \mathbf{L} on the HF⁺ axis and $P_r = \Omega + \Omega_L$ is the projection of the total angular momentum \mathbf{J} on the same axis. The diabatic electronic wave functions $| \Lambda, S, \Omega \rangle^{\text{MF}}$ are defined with respect to the MF frame [Eq. (A.7)]. In Renner-Teller systems it is customary to define also a quantum number K , the projection of the electronic and nuclear orbital angular momenta on the body-fixed z -axis or, in other words, the eigenvalue of the total angular momentum operator \hat{J}_z minus the eigenvalue of the spin operator \hat{S}_z . Here we define $K_r = \Lambda + \Omega_L = P_r - \Sigma$.

The matrix elements of the Hamiltonian in the MF basis read

$$\begin{aligned}
& \langle n', \Lambda', S, \Omega', L', \Omega'_L, P'_r; J, M_J | \hat{H} | n, \Lambda, S, \Omega, L, \Omega_L, P_r; J, M_J \rangle \\
&= \delta_{\Lambda', \Lambda} \delta_{\Omega', \Omega} \delta_{L', L} \delta_{\Omega'_L, \Omega_L} \left[\langle n' | \frac{-1}{2\mu R} \frac{\partial^2}{\partial R^2} R | n \rangle + \langle n' | \frac{L(L+1)}{2\mu R^2} | n \rangle \right. \\
&+ \delta_{n', n} B_0 \left(J(J+1) + L(L+1) + S(S+1) - P_r^2 - \Omega_L^2 - \Sigma^2 \right) + \delta_{n', n} A \Lambda \Sigma \left. \right] \\
&- B_0 \delta_{\Lambda', \Lambda} \delta_{L', L} \delta_{n', n} \left[\left(C_{P'_r, P_r-1}^J C_{\Omega'_L, \Omega_L-1}^L + C_{P'_r, P_r+1}^J C_{\Omega'_L, \Omega_L+1}^L \right) \right. \\
&+ \left(C_{P'_r, P_r-1}^J C_{\Sigma', \Sigma-1}^S + C_{P'_r, P_r+1}^J C_{\Sigma', \Sigma+1}^S \right) \\
&- \left. \left(C_{\Omega'_L, \Omega_L+1}^L C_{\Sigma', \Sigma-1}^S + C_{\Omega'_L, \Omega_L-1}^L C_{\Sigma', \Sigma+1}^S \right) \right] \\
&+ \langle n', \Lambda', S, \Omega', L', \Omega'_L, P'_r; J, M_J | \hat{V} | n, \Lambda, S, \Omega, L, \Omega_L, P_r; J, M_J \rangle. \quad (7.18)
\end{aligned}$$

The matrix elements of the potential are

$$\begin{aligned}
& \langle n', \Lambda', S, \Omega', L', \Omega'_L, P'_r; J, M_J | \hat{V} | n, \Lambda, S, \Omega, L, \Omega_L, P_r; J, M_J \rangle \\
&= \sqrt{(2L'+1)(2L+1)} \delta_{\Sigma', \Sigma} \delta_{P'_r, P_r} \quad (7.19) \\
&\times \sum_l \langle n' | v_l^{\Lambda', \Lambda}(R) | n \rangle (-1)^{\Omega'_L} \begin{pmatrix} L' & l & L \\ 0 & 0 & 0 \end{pmatrix} \begin{pmatrix} L' & l & L \\ -\Omega'_L & \Lambda - \Lambda' & \Omega_L \end{pmatrix}
\end{aligned}$$

The parity-adapted basis in the MF embedding is

$$\begin{aligned}
| n, |\Lambda|, S, \Omega, L, \Omega_L, P_r; J, M_J, p \rangle &= | n, \Lambda, S, \Omega, L, \Omega_L, P_r; J, M_J \rangle \\
&+ p(-1)^{J-S} \quad (7.20) \\
&\times | n, -\Lambda, S, -\Omega, L, -\Omega_L, -P_r; J, M_J \rangle.
\end{aligned}$$

It is also useful to know how to transform the basis from one frame to another. This is derived in Appendix A.

7.2.3 Computational details

The bound states of the complex were obtained from a full diagonalization of the Hamiltonian matrix. We coded the construction of this matrix in the three different sets of coordinates for which the formulas are given above (SF, BF, MF) and used the basis transformations specified in Appendix A to check our codes. Calculations were performed for J up to $\frac{9}{2}$ inclusive. The levels were converged to within 10^{-4} cm^{-1} with an angular basis truncated at $j_{\max} = \frac{35}{2}$ and a radial basis with $n_{\max} = 14$. Test calculations with $j_{\max} = \frac{41}{2}$ gave levels that did not deviate from the $j_{\max} = \frac{35}{2}$ results by more than 10^{-5} cm^{-1} . The nonlinear parameters R_e , D_e , and ω_e of the 15 radial basis functions

$\chi_n(R)$ were optimized by energy minimizations with smaller values of n_{\max} . The final calculation was performed using $R_e = 5.3 a_0$, $D_e = 620 \text{ cm}^{-1}$, and $\omega_e = 140 \text{ cm}^{-1}$.

7.3 Results

7.3.1 One-dimensional calculations

In order to understand how the states of the HF^+ monomer become perturbed and mixed by the interaction with the He atom it is interesting to start with calculations in which the intermolecular distance R is fixed and is reduced from infinity to its equilibrium value. We have performed such fixed- R calculations for a set of distances ranging from 1.5 to 8.5 Å, with a grid spacing of 0.0085 Å for $R < 3.3$ Å and 0.15 Å for larger distances. An analysis of the wave functions for $R = 2.26$ and 3.7 Å in the \mathbf{R} -embedded frame is presented in Table 7.1 for $J = \frac{1}{2}$ and $\frac{3}{2}$. The first observation one can make is that the quantum number P_R , the projection of \mathbf{J} on the BF z -axis \mathbf{R} , is always a nearly good quantum number. The energies are plotted as functions of R in Fig. 7.1 for $P_R = \pm\frac{1}{2}, J = \frac{1}{2}$ and for $P_R = \pm\frac{3}{2}, J = \frac{3}{2}$. The picture exhibits different dissociation limits. The lowest three limits correspond to the $|\Omega| = \frac{3}{2}$ ground state of the HF^+ monomer, the first one at $-114.2138 \text{ cm}^{-1}$ to $j = \frac{3}{2}$, the second one to $j = \frac{5}{2}$, and the third one to $j = \frac{7}{2}$. The fourth asymptote corresponds to the excited spin-orbit state of HF^+ with $|\Omega| = \frac{1}{2}$ and $j = \frac{1}{2}$. We did not plot the energies with $P_R = \pm\frac{1}{2}, J = \frac{3}{2}$ because they only differ from the $P_R = \pm\frac{1}{2}, J = \frac{1}{2}$ energy curves by one quantum of overall rotation and on the scale of Fig. 7.1 would coincide with the latter curves. The corresponding eigenvectors are very similar, cf. Table 7.1. The lowest curve has a global minimum at -1302.37 cm^{-1} for $R = 2.258$ Å and corresponds to $J = \frac{3}{2}$, $P_R = \pm\frac{3}{2}$, $\Omega = \pm\frac{3}{2}$ and e parity.

Figure 7.1 shows that first, from large R inwards to about 3.7 Å, the asymptotic levels of given j split into $2j + 1$ levels with $P_R = -j, -j + 1, \dots, j$ by the anisotropic interaction with the He atom. Monomer states of given Ω that in free HF^+ are mixed only by Coriolis coupling, are now coupled also by the off-diagonal diabatic interaction potentials $V_{\pm 1, \mp 1}$, i.e., by the adiabatic “difference potential” $(V_{A''} - V_{A'})/2$. For smaller distances the interaction with He becomes stronger, the energy curves in Fig. 7.1 show (avoided) crossings, and the monomer spin-orbit states with different $|\Omega|$ start to mix. This is illustrated for $R = 2.26$ Å in Table 7.1. Only the lowest bound state, with $|\Omega| = \frac{3}{2}$, shows negligible mixing with states of $|\Omega| = \frac{1}{2}$, cf. also Fig. 7.1.

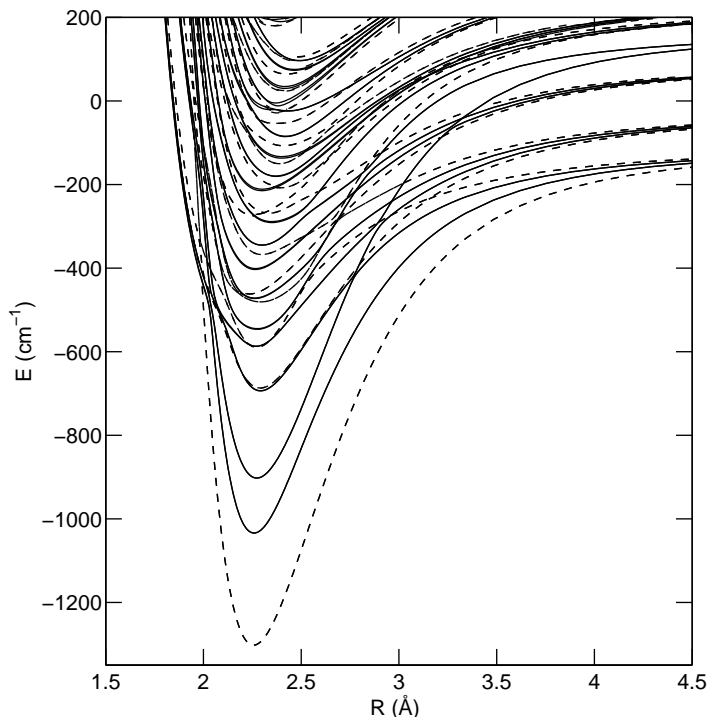
7.3.2 Full calculation

Tables 7.2 and 7.3 contain the rovibronic energy levels and parity splittings from full-dimensional calculations for $J = \frac{1}{2}, \frac{3}{2}, \frac{5}{2}, \frac{7}{2}, \frac{9}{2}$. The first column indicates

Table 7.1: Rovibronic states for $J = \frac{1}{2}$ and $\frac{3}{2}$ from calculations with R fixed. Energies E in the first row correspond to states of e spectroscopic parity, $\Delta E = E_f - E_e$ in the second row is the parity splitting. The other entries are populations (in percent) of basis functions in \mathbf{R} -embedding with approximate quantum numbers P_R, Ω .

		$J = \frac{1}{2}$							
		$R = 2.26 \text{ \AA}$				$R = 3.7 \text{ \AA}$			
E (cm ⁻¹)		-1034.04481	-901.08722	-689.1133	-586.5951	-197.2510	-179.4627	-109.4178	-100.6141
ΔE (cm ⁻¹)		-0.03819	-0.46544	0.40533	-0.13169	-0.01641	0.01662	-0.08587	0.08572
P_R	Ω								
$\frac{1}{2}$	$\frac{1}{2}$	79.56	20.62	2.52	7.56	0.99	0.00	2.15	0.03
$-\frac{1}{2}$	$\frac{1}{2}$	0.07	1.61	37.96	35.96	0.00	0.96	0.02	2.24
$\frac{1}{2}$	$\frac{3}{2}$	20.20	77.38	1.44	37.59	98.89	0.12	96.82	1.01
$-\frac{1}{2}$	$\frac{3}{2}$	0.17	0.39	58.08	18.89	0.12	98.92	1.01	96.72
		$J = \frac{3}{2}$							
		$R = 2.26 \text{ \AA}$				$R = 3.7 \text{ \AA}$			
E (cm ⁻¹)		-1302.3696	-1031.1954	-898.0328	-686.5220	-225.9358	-196.2161	-178.4279	-168.6719
ΔE (cm ⁻¹)		-0.00001	-0.07637	-0.93072	0.78191	-0.00001	-0.03264	0.03286	0.00022
P_R	Ω								
$\frac{1}{2}$	$\frac{1}{2}$	0.00	79.60	20.48	2.47	0.00	0.98	0.01	0.00
$-\frac{1}{2}$	$\frac{1}{2}$	0.00	0.04	1.65	37.37	0.00	0.00	0.94	0.01
$\frac{1}{2}$	$\frac{3}{2}$	0.03	20.10	77.59	1.21	0.14	98.30	0.57	0.00
$-\frac{1}{2}$	$\frac{3}{2}$	0.00	0.22	0.25	57.23	0.00	0.58	97.24	1.23
$\frac{3}{2}$	$\frac{1}{2}$	0.73	0.01	0.01	0.23	0.78	0.00	0.00	0.00
$-\frac{3}{2}$	$\frac{1}{2}$	0.04	0.00	0.00	0.13	0.00	0.00	0.01	0.90
$\frac{3}{2}$	$\frac{3}{2}$	99.20	0.02	0.03	1.28	99.08	0.14	0.00	0.00
$-\frac{3}{2}$	$\frac{3}{2}$	0.00	0.00	0.00	0.09	0.00	0.00	1.23	97.86

Figure 7.1: Energy levels from fixed- R calculations, plotted as functions of R . Closed lines for $|P_R| = \frac{1}{2}$, $J = \frac{1}{2}$ and dashed lines for $|P_R| = \frac{3}{2}$, $J = \frac{3}{2}$



the dominant character of the corresponding eigenstate. The label $^{2S+1}K_P$ is commonly used in Renner-Teller systems; the quantum numbers S , $P = P_r$, and $K = K_r$ were defined in Sec. 7.2.2.

In the linear triatomic open-shell molecules in which Renner-Teller coupling is mostly studied K is the sum of the electronic orbital angular momentum Λ and the vibrational angular momentum, usually called l , generated by the degenerate bending mode. The quantum number that corresponds most closely to l in the He-HF⁺ complex is the quantum number Ω_L defined in the \mathbf{r} -embedding and K is defined in this MF embedding as $K_r = \Lambda + \Omega_L = P_r - \Sigma$. The problem in the BF embedding is that the electronic angular momentum Λ is the projection on the HF⁺ axis \mathbf{r} , the nuclear angular momentum projection Ω_L is not defined, while the total angular momentum projection P_R is defined with respect to the intermolecular vector \mathbf{R} . Still, we write $K_R = P_R - \Sigma$ also in the BF system. This is physically meaningful because the complex has a linear equilibrium geometry with a rather steep well in which the lower rovibronic states are localized and the vectors \mathbf{r} and \mathbf{R} remain nearly parallel. Table 7.4

shows a comparison of the main character of the rovibronic states in terms of the quantum numbers for the two embeddings considered. In all cases except a few, in which the character is quite mixed anyway, we find agreement between the assignments of the two embeddings. The population of the dominant $^{2S+1}K_P$ component is systematically higher in the **R**-embedding, which shows that this embedding yields the better approximate quantum numbers. This seems in contradiction with our previous observation that the quantum number K is more strictly defined in the **r**-embedding, but one should realize that this was a purely formal argument, while the assignment of approximate quantum numbers is of more physical nature.

The binding energy D_0 of the complex is 1125.6 cm^{-1} for $J = \frac{3}{2}$, $|P_r| = \frac{3}{2}$, and spectroscopic parity e . Note, for comparison, that the global minimum in this potential at the linear geometry with $R_e = 2.24 \text{ \AA}$ has well depth $D_e = 1631 \text{ cm}^{-1}$. The analysis of the wave functions using the (BF) **R**-embedding shows that the well is sufficiently deep to considerably hinder the rotation of HF⁺: basis functions with different j are strongly mixed.

Table 7.2 also lists stretch and bend quantum numbers v_s and v_b . The assignment of these quantum numbers was made with the help of the wave functions, some of which are plotted in Figs. 7.2 and 7.3. The stretch quantum number v_s is determined by counting the number of nodes in the wave function along the radial coordinate. The bend quantum number v_b is also determined from the number of nodes, but in a slightly more complicated manner. The bending mode of a semi-rigid triatomic molecule is denoted by v_b^l , where l takes only the values $-v_b, -v_b + 2, \dots, v_b$. Here, the vibrational angular momentum l is equal to $P - \Sigma - \Lambda$. The eigenfunctions of a two-dimensional isotropic harmonic oscillator can be written as $F_{v,l}(q) \exp(il\alpha)$, where q is the amplitude of the bending vibration and α is the phase, and $F_{v,l}(q)$ has $(v - |l|)/2$ nodes. Because l is known, we can count the number of nodes in the wave function along the angular coordinate and deduce the value of v_b .

Comparison of the $v_s, v_b = 0, 0$ energy levels from the full calculation in Table 7.2 with the lower levels from the fixed- R calculation in Table 7.1 shows that the stretch zero-point energy of the complex is about 175 cm^{-1} . In the harmonic approximation this would correspond to a stretch frequency of about 350 cm^{-1} . From the energy differences between the $^2\Pi_{3/2}$ levels with $v_s = 0, 1, 2$ and $v_b = 0$ we find 308 cm^{-1} for the stretch fundamental frequency and 549 cm^{-1} for the first overtone, indicative of strong anharmonicity. This anharmonicity made it difficult to recognize other stretch progressions. Figure 7.4 shows an overview of the calculated rovibronic levels with their successive $v_s = 1, 2, 3$ stretch excited states (as far as they could be identified) separated into different columns. Two of the higher diagonal arrows that refer to stretch excitations do not connect states of the same quantum numbers K and P , but one should realize that these approximate quantum numbers are not always well defined. The states concerned are of mixed character and the character may change upon stretch excitation.

Table 7.2: Rovibronic energy levels (in cm^{-1}) of parity e in \mathbf{r} -embedding. The assignment in terms of ${}^{2S+1}K_P$ with $K = K_r$ and $P = P_r$ and the stretch, bend quantum numbers v_s, v_b is explained in the text. States with $|K| = 0, 1, 2, 3$ are denoted by $\Sigma, \Pi, \Delta, \Phi$.

${}^{2S+1}K_P(v_s, v_b)$	$J = \frac{1}{2}$	$J = \frac{3}{2}$	$J = \frac{5}{2}$	$J = \frac{7}{2}$	$J = \frac{9}{2}$
${}^2\Pi_{3/2}(0, 0)$		-1125.6274	-1121.1001	-1114.7641	-1106.6216
${}^2\Pi_{1/2}(0, 0)$	-862.7696	-860.0766	-855.5705	-849.2533	-841.1274
${}^2\Pi_{3/2}(1, 0)$		-818.1741	-814.0112	-808.1859	-800.7009
${}^2\Sigma_{1/2}(0, 1)$	-750.4286	-747.9311	-743.6468	-737.5769	-729.7240
${}^2\Delta_{5/2}(0, 1)$			-729.9411	-723.7550	-715.8068
${}^2\Pi_{3/2}(2, 0)$		-576.4169	-572.5091	-567.0542	-560.0688
${}^2\Sigma_{1/2}(1, 1)$	-577.1277	-574.9012	-571.0322	-565.5213	-558.3691
${}^2\Pi_{1/2}(0, 2)$	-562.9230	-559.9903	-555.3150	-548.9100	-540.7956
${}^2\Pi_{3/2}(0, 2)$		-556.4190	-552.1326	-546.1146	-538.3456
${}^2\Delta_{5/2}(1, 1)$			-482.6417	-477.1104	-470.0061
${}^2\Pi_{1/2}(1, 0)$	-487.2650	-484.9705	-481.0415	-475.4763	-468.2760
${}^2\Sigma_{1/2}(0, 3)$	-474.7757	-472.2898	-467.9698	-461.8190	-453.8415
${}^2\Delta_{3/2}(0, 1)$		-454.5045	-449.9153	-443.4953	-435.2501
${}^2\Sigma_{1/2}(0, 1)$	-436.7975	-434.3995	-430.1277	-423.9965	-416.0239
${}^2\Phi_{7/2}(0, 2)$				-415.0390	-407.7367
${}^2\Delta_{5/2}(0, 3)$			-391.2582	-385.9204	-379.0634
${}^2\Pi_{3/2}(3, 2)$		-392.7682	-388.2957	-382.2816	-374.9899
${}^2\Pi_{3/2}(3, 0)$		-388.3586	-384.6341	-379.2496	-371.9206
${}^2\Pi_{1/2}(1, 4)$	-383.8626	-381.1165	-376.6832	-370.4884	-362.5129
${}^2\Pi_{3/2}(0, 4)$		-370.8265	-366.8738	-361.7200	-355.0922
${}^2\Pi_{1/2}(2, 2)$	-371.9084	-369.3066	-364.0358	-356.5184	-347.2930
${}^2\Sigma_{1/2}(2, 3)$	-361.7989	-359.1454	-354.8810	-348.9126	-341.0510
${}^2\Pi_{3/2}(1, 2)$		-355.9188	-351.9194	-346.3406	-339.1907
${}^2\Sigma_{1/2}(0, 5)$	-321.0598	-318.9936	-314.9773	-308.9983	-301.0462
${}^2\Delta_{5/2}(1, 3)$			-304.2796	-298.4314	-291.0522
${}^2\Sigma_{1/2}(1, 3)$	-303.9462	-302.4868	-299.4022	-294.6780	-288.3062

The parity splittings of the levels with $J = \frac{1}{2}$ up to $\frac{9}{2}$ presented in Table 7.3 are in reasonable agreement with the results of the fixed- R calculation at 2.26 Å in Table 7.1. The largest splittings occur for the levels with $|P| = \frac{1}{2}$ and these splittings are nicely proportional to $J + \frac{1}{2}$. This simple linear dependence on $J + \frac{1}{2}$ is well known for λ doubling in linear molecules [119]. Here

Table 7.3: Parity splitting $\Delta E = E_f - E_e$ (in cm⁻¹) of the levels in Table 7.2.

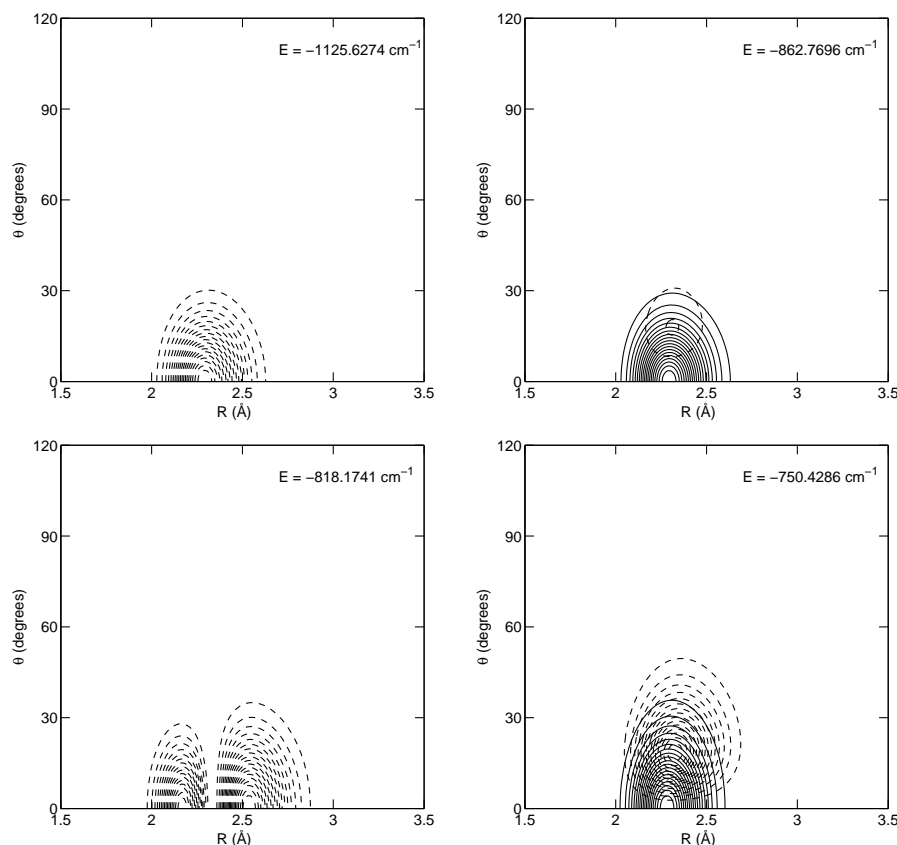
$^{2S+1}K_P(v_s, v_b)$	$J = \frac{1}{2}$	$J = \frac{3}{2}$	$J = \frac{5}{2}$	$J = \frac{7}{2}$	$J = \frac{9}{2}$
$^2\Pi_{3/2}(0, 0)$		0.0000	0.0000	0.0001	0.0002
$^2\Pi_{1/2}(0, 0)$	0.0567	0.1134	0.1701	0.2267	0.2833
$^2\Pi_{3/2}(1, 0)$		0.0000	0.0000	0.0001	0.0002
$^2\Sigma_{1/2}(0, 1)$	0.3675	0.7337	1.0971	1.4565	1.8105
$^2\Delta_{5/2}(0, 1)$			0.0000	0.0000	0.0000
$^2\Pi_{3/2}(2, 0)$		0.0006	0.0016	0.0023	0.0030
$^2\Sigma_{1/2}(1, 1)$	0.4719	0.9376	1.3917	1.8301	2.2484
$^2\Pi_{1/2}(0, 2)$	-0.6069	-1.2053	-1.7859	-2.3363	-2.8391
$^2\Pi_{3/2}(0, 2)$		-0.0004	-0.0031	-0.0133	-0.0426
$^2\Delta_{5/2}(1, 1)$			0.0000	0.0000	0.0000
$^2\Pi_{1/2}(1, 0)$	0.2976	0.5844	0.8510	1.0909	1.3006
$^2\Sigma_{1/2}(0, 3)$	0.5355	1.0680	1.5937	2.1068	2.6000
$^2\Delta_{3/2}(0, 1)$		-0.0022	-0.0086	-0.0213	-0.0420
$^2\Sigma_{1/2}(0, 1)$	0.8638	1.7357	2.6226	3.5299	4.4601
$^2\Phi_{7/2}(0, 2)$				0.0000	0.0000
$^2\Delta_{5/2}(0, 3)$			-0.0023	-0.0065	-0.0070
$^2\Pi_{3/2}(3, 2)$		-0.0006	0.0030	0.0156	0.0283
$^2\Pi_{3/2}(3, 0)$		0.0022	0.0079	0.0184	0.0490
$^2\Pi_{1/2}(1, 4)$	-0.6516	-1.2274	-1.6942	-2.0432	-2.2524
$^2\Pi_{3/2}(0, 4)$	0.2764	0.2233	0.8807	1.3386	1.6524
$^2\Pi_{1/2}(2, 2)$		0.2969	-0.1394	-0.3734	-0.6122
$^2\Sigma_{1/2}(2, 3)$	-0.6501	-1.3329	-2.0817	-2.9202	-3.7046
$^2\Pi_{3/2}(1, 2)$		0.0014	0.0061	0.0158	0.0266
$^2\Sigma_{1/2}(0, 5)$	1.6586	3.2800	4.8236	6.2406	7.4659
$^2\Delta_{5/2}(1, 3)$			0.0014	0.0091	0.0367
$^2\Sigma_{1/2}(1, 3)$	1.8674	3.6779	2.6978	2.9431	3.0847

it can be understood by considering the Hamiltonian in Eq. (7.15) and the parity-adapted basis in Eq. (7.20). From the latter it follows that the energy difference between functions with e and f parity is caused by a coupling between the basis components $|\Lambda, \Sigma, \Omega, \Omega_L, P_r\rangle$ and $|- \Lambda, -\Sigma, -\Omega, -\Omega_L, -P_r\rangle$. The J -dependent coupling operators in the Hamiltonian of Eq. (7.15) are the shift operators $\widehat{J}_\pm \widehat{L}_\pm$ and $\widehat{J}_\pm \widehat{S}_\pm$. The latter operator indeed gives a first-order splitting between the components with $\Sigma, P_r = \pm \frac{1}{2}, \pm \frac{1}{2}$ that is proportional to

Table 7.4: Comparison of the main character (in percent) of the levels in Table 7.2 in \mathbf{R} - vs \mathbf{r} -embedding. Quantum numbers P, K are either P_R, K_R or P_r, K_r ; the label $^{2S+1}K_P$ corresponds to the latter.

Energy (cm ⁻¹)	P	K	$K - \Lambda$		\mathbf{R} -emb	\mathbf{r} -emb
-1125.6274	1	1	0	$^2\Pi_{3/2}(0, 0)$	99.2	93.2
-862.7696	1	1	0	$^2\Pi_{1/2}(0, 0)$	71.4	70.8
-818.1741	1	1	0	$^2\Pi_{3/2}(1, 0)$	99.1	91.9
-750.4286	0	0	-1	$^2\Sigma_{1/2}(0, 1)$	69.2	68.4
-729.9411	2	2	1	$^2\Delta_{5/2}(0, 1)$	97.9	75.4
-576.4169	1	1	0	$^2\Pi_{3/2}(2, 0)$	96.7	82.2
-577.1277	0	0	-1	$^2\Sigma_{1/2}(1, 1)$	50.9	45.0
	1	1	0		35.7	34.5
-562.9230	-1	-1	-2	$^2\Pi_{1/2}(0, 2)$	61.7	55.2
-556.4190	1	1	0	$^2\Pi_{3/2}(0, 2)$	89.0	66.9
-482.6417	2	2	1	$^2\Delta_{5/2}(1, 1)$	97.9	69.5
-487.2650	1	1	0	$^2\Pi_{1/2}(1, 0)$	50.3	47.0
	0	0	-1		46.5	46.5
-474.7757	0	0	-1	$^2\Sigma_{1/2}(0, 3)$	63.2	41.4
	0	0	-1		23.6	15.7
	-1	-1	-2		5.2	27.0
	1	1	0		8.0	15.0
-454.5045	2	2	1	$^2\Delta_{3/2}(0, 1)$	68.6	30.9
-436.7975	0	0	-1	$^2\Sigma_{1/2}(0, 1)$	42.2	45.2
	-1	-1	-2		38.8	10.8
	0	0	-1		10.2	38.1
-415.0390	3	3	2	$^2\Phi_{7/2}(0, 2)$	93.0	45.1
-391.2582	2	2	1	$^2\Delta_{5/2}(0, 3)$	64.8	31.4
-392.7682	-2	-2	-3	$^2\Pi_{3/2}(3, 2)$	38.1	10.8
	1	1	0		36.9	30.8
-388.3586	1	1	0	$^2\Pi_{3/2}(3, 0)$	74.4	63.6
-383.8626	-1	-1	-2	$^2\Pi_{1/2}(1, 4)$	61.0	62.1
-370.8265	1	1	0	$^2\Pi_{3/2}(0, 4)$	47.4	19.1
	0	0	-1		17.3	29.3
	-1	-1	-2		11.7	22.0
-371.9084	0	0	-1	$^2\Pi_{1/2}(2, 2)$	51.4	38.5
	-1	-1	-2		30.3	43.2
-361.7989	-1	-1	-2	$^2\Sigma_{1/2}(2, 3)$	50.0	36.3
	0	0	-1		34.2	48.0
-355.9188	1	1	0	$^2\Pi_{3/2}(1, 2)$	83.5	52.0
-321.0598	0	0	-1	$^2\Sigma_{1/2}(0, 5)$	73.7	58.6
-304.2796	-3	-3	-4	$^2\Delta_{5/2}(1, 3)$	56.6	6.2
	2	2	1		27.1	14.0
-303.9462	0	0	-1	$^2\Sigma_{1/2}(1, 3)$	74.0	67.6

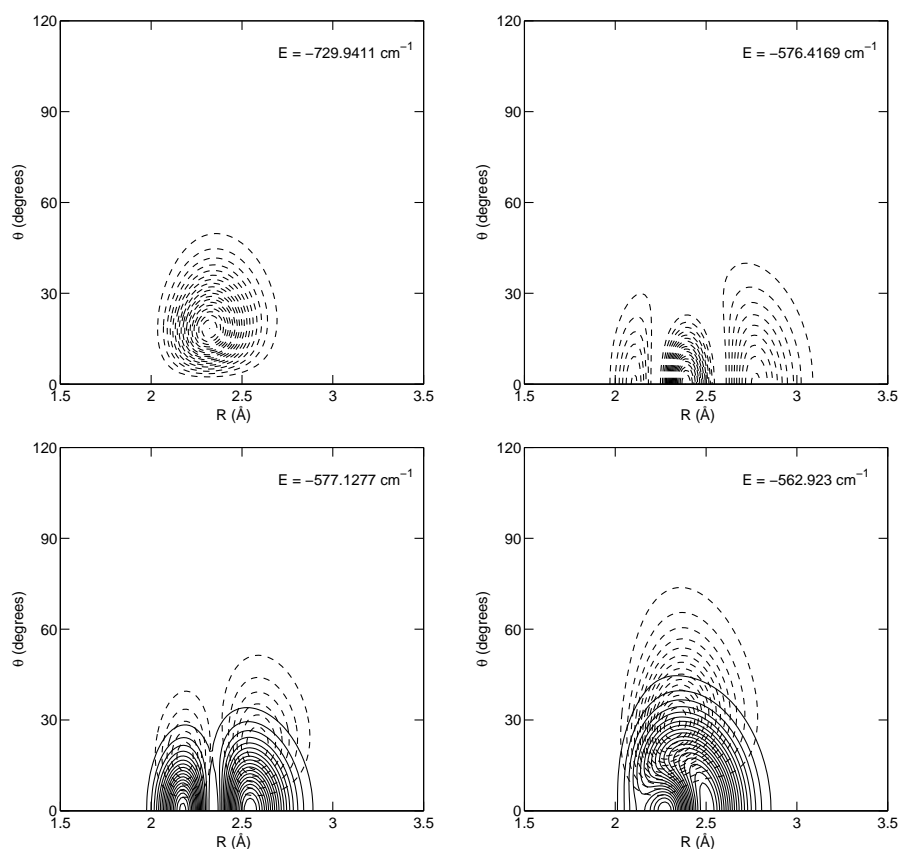
Figure 7.2: Density distributions of the lowest four levels from full calculations. The closed and dashed contours are the $|\Omega| = \frac{1}{2}$ and $|\Omega| = \frac{3}{2}$ contributions, respectively. These distributions are the squares of the rovibronic wavefunctions with $J = |P|$, integrated over all coordinates except R and θ . For the corresponding energy levels and quantum numbers we refer to Table 7.2.



$\sqrt{[J(J+1) + \frac{1}{4}]} \sqrt{[S(S+1) + \frac{1}{4}]} = (J + \frac{1}{2})(S + \frac{1}{2}) = (J + \frac{1}{2})$. The magnitude of the actual splittings in Table 7.3 is on the order of the end-over-end rotational constant of the complex (see below), rather than the size of the monomer rotational constant B_0 that appears in Eq. (7.15). This is a consequence of the quenching of the HF⁺ monomer rotations in the complex.

From the levels with $J = \frac{1}{2}, \frac{3}{2}, \frac{5}{2}, \frac{7}{2}, \frac{9}{2}$ we extracted rotational constants of the complex. First, we averaged the energies of the e and f states to remove

Figure 7.3: Density distributions of the next four levels from full calculations. For explanations, see Fig. 7.2.



the effect of the parity splitting. We note that the J dependence of the energy levels originates from the term $[\hat{J}^2 - 2\hat{j} \cdot \hat{J}]/(2\mu R^2)$ in the Hamiltonian of Eq. (7.6). After removal of the parity splitting caused by the J -dependent shift operators the energy contribution of this term is $[J(J+1) - P^2] \langle [2\mu R^2]^{-1} \rangle$. The expectation value $\langle [2\mu R^2]^{-1} \rangle$ is the end-over-end rotational constant of the complex. The band origins E_0 , end-over-end rotational constants B , and centrifugal distortion constants D presented in Table 7.5 were obtained by a fit of the levels with $J = \frac{1}{2}$ to $\frac{9}{2}$ for each internal state with the formula

$$E(J, P) = E_0 + B[J(J+1) - P^2] - D[J(J+1) - P^2]^2. \quad (7.21)$$

We observe that a substantial decrease of the end-over-end rotational constant B is caused by one or two quanta of stretch excitation, as might be expected, but that also the combination of one stretch and one bend quantum gives a strong reduction of B .

Table 7.5: Band origins E_0 , rotational constants B , and distortion constants D extracted from energy levels with $J = \frac{1}{2}, \frac{3}{2}, \frac{5}{2}, \frac{7}{2}, \frac{9}{2}$.

	E_0	B	D
² Π _{3/2} (0, 0)	-1126.9858	0.9057	0.0000261
² Π _{1/2} (0, 0)	-863.1948	0.9072	0.0000307
² Π _{3/2} (1, 0)	-819.4233	0.8328	0.0000323
² Σ _{1/2} (0, 1)	-750.6916	0.8936	0.0000358
² Δ _{5/2} (0, 1)	-732.1512	0.8842	0.0000363
² Π _{3/2} (2, 0)	-577.5910	0.7832	0.0001951
² Σ _{1/2} (1, 1)	-577.3014	0.8198	0.0000480
² Π _{1/2} (0, 2)	-563.6658	0.8784	0.0001176
² Π _{3/2} (0, 2)	-557.7031	0.8557	-0.0001637
² Δ _{5/2} (1, 1)	-484.6184	0.7908	0.0000515

A similar study of the He-HF⁺ complex was made earlier by Schmelz and Rosmus [122] on the basis of intermolecular potentials computed by the coupled electron pair approximation (CEPA). It was already mentioned in ref [120] that our potentials are somewhat different from theirs and, in particular, that our binding energy D_e is larger. The rovibronic energy level pattern that they obtain from their potentials is different from ours. The character of the ground state is the same, but the order of the excited states is considerably different. Their spin-orbit splitting ²Π_{1/2}(0, 0) - ²Π_{3/2}(0, 0) is 319.6 cm⁻¹, whereas ours is 265.6 cm⁻¹. Their stretch frequency ²Π_{3/2}(1, 0) - ²Π_{3/2}(0, 0) is 311.0 cm⁻¹, ours is 307.5 cm⁻¹. The most striking difference occurs for the bend frequency ²Σ_{1/2}(0, 1) - ²Π_{3/2}(0, 0) that they find to be 223.2 cm⁻¹, substantially lower than our value of 377.7 cm⁻¹.

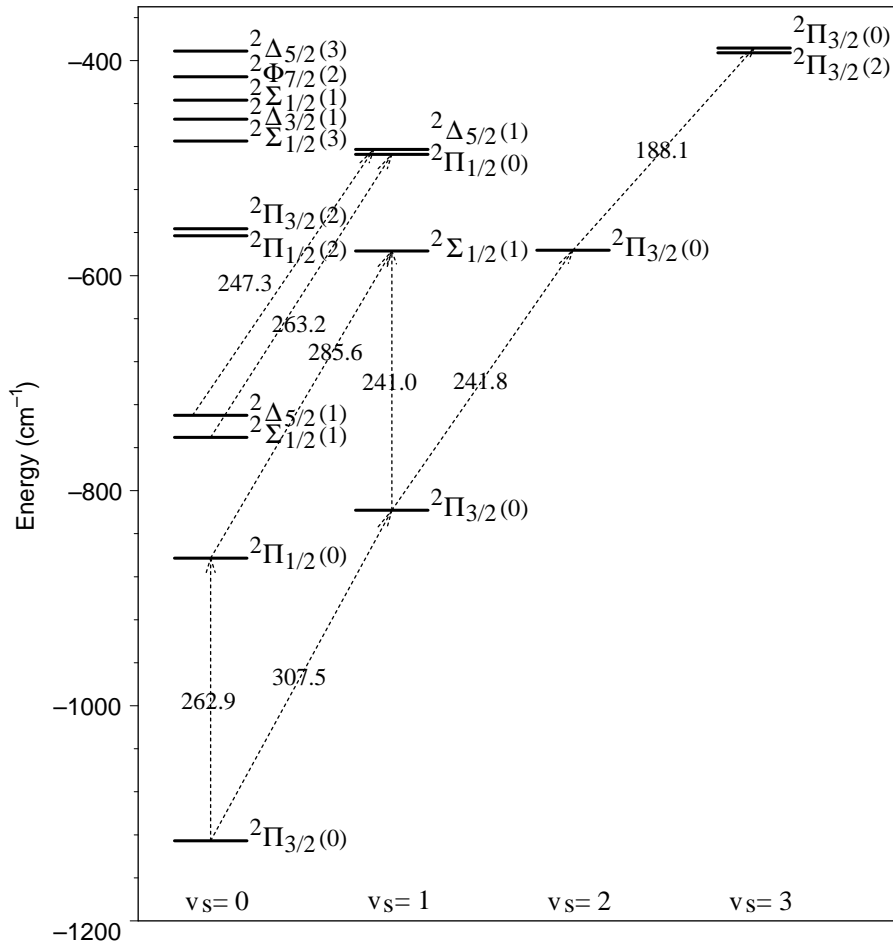
Since the intermolecular potential depends strongly on the HF⁺ bond length, we also computed rovibronic levels with r fixed at the value of 1.0273 Å that corresponds to the global minimum of a full three-dimensional potential surface (see ref [120]). The dissociation energy D_e of the complex with respect to He and the HF⁺ monomer at its equilibrium geometry is increased by 72.3 cm⁻¹ by this relaxation of r . The intermolecular zero-point energy increases by 55.4 cm⁻¹, from 505.7 to 561.1 cm⁻¹, making D_0 increase by 16.9 cm⁻¹. The actual increase of D_0 in full three-dimensional calculations is probably larger, however, because the vibrational zero-point energy of HF⁺ may be lower in the complex. The characteristic excitation energies, 273.1 cm⁻¹ for the spin-orbit splitting, 329.4 cm⁻¹ for the stretch, and 415.5 cm⁻¹ for the bend, are higher than the values calculated for $r = r_e$.

7.3.3 Renner-Teller effect

The Renner-Teller effect is taken into account in our calculations, because our intermolecular potentials refer to coupled diabatic electronic states and we include all of the relevant electronic and nuclear angular momentum couplings in our Hamiltonian. Our basis can accurately describe the internal (stretch and bend) motions and overall rotation of the He-HF⁺ complex, even when these internal motions have large amplitudes. Let us now consider explicitly how the Renner-Teller effect becomes manifest in our results. Figure 7.5 shows the levels calculated for stretch quantum number $v_s = 0$, i.e., the leftmost column of Fig. 7.4. This picture may be directly compared with the energy level diagram of a ²Π triatomic linear molecule shown in Herzberg’s book [125], Fig. 8 of Sec. I.2. This diagram correlates the energy levels obtained from a full calculation with the levels obtained when either the Renner-Teller interaction or the spin-orbit coupling are set to zero. Herzberg’s “full” treatment includes the bending mode only and it defines the Renner-Teller interaction parameter ϵ as the ratio of the harmonic force constants of the coupling or difference potential $V_{1,-1} = (V_{A''} - V_{A'})/2$ and the diagonal or sum potential $2V_{1,1} = V_{A'} + V_{A''}$. The corresponding set of levels from our calculation is shown in the second column of Fig. 7.5. Note that the bend quantum number v_b in our notation is given in parentheses, while Herzberg’s figure shows v_2 on the lefthand side. In Herzberg’s figure the levels of the same $|K|$ with the larger $|P|$ are higher than the levels with smaller $|P|$, whereas in our figure the levels with the larger $|P|$ are lower. The reason for this reversed order is that our spin-orbit constant A has a negative value, while Herzberg’s is positive. Otherwise, the levels from our calculations follow nicely the pattern of the levels in Herzberg’s picture. The gaps between levels with different v_b are smaller in our case, so different v_b manifolds overlap in energy. When we switch off the coupling potential $V_{1,-1}$ we obtain the levels in the first column of Fig. 7.5. They differ from the levels with $\epsilon = 0$ in the first column of Herzberg’s picture in that the lower Σ and Δ levels with $v_b = 1$ do not become degenerate in our case, and neither do the Π and Φ levels with $v_b = 2$. When we set the spin-orbit coupling constant A to zero we produce the levels in the third column of Fig. 7.5 that are very similar to the levels in the third column of Herzberg’s picture, except that the Δ levels with $v_b = 1$ are not centered between the Σ levels, but nearly coincide with the upper Σ level. When we switch off both $V_{1,-1}$ and A we produce—cf. the fourth column of Fig. 7.5—some further degeneracies, but the Δ levels with $v_b = 1$ remain higher than the Σ levels, and so do the Φ levels with $v_b = 2$ relative to the Π levels. These differences in the first and third columns indicate a fundamental deviation from Herzberg’s model, which we will now show to be due to the bending motion being treated as a hindered rotation rather than a harmonic vibration.

This can be understood from an analysis of the matrix elements of the potential $V_{1,1}$ in Eq. (7.11), but it is easier to consider the example of the HF⁺

Figure 7.4: Rovibronic levels from full calculations. The levels are labeled with the approximate quantum numbers $^{2S+1}K_P(v_b)$, and $|K| = 0, 1, 2, 3$ is denoted by $\Sigma, \Pi, \Delta, \Phi$. The overall angular momentum J is always taken equal to $|P|$.



molecule in a homogeneous electric field of strength F parallel to the SF Z -axis. For simplicity we omit the spin, i.e., we put $S = \Sigma = 0$ and $\Omega = \Lambda = \pm 1$. When μ is the dipole moment of HF⁺ the potential energy can be written as $\widehat{V} = -\mu F \cos \theta = -\mu F P_1(\cos \theta)$, with (θ, ϕ) being the SF polar angles of the diatom axis \mathbf{r} and $P_1(\cos \theta)$ the Legendre polynomial P_l with $l = 1$. The basis to describe the hindered rotation of HF⁺ in this example is obtained from Eq. (7.9) by omitting the overall rotation functions with quantum numbers J, M_J and depending on the polar angles (β, α) of \mathbf{R} . This is equivalent to

considering \mathbf{R} (i.e., the direction of the He atom) to be fixed along the SF Z -axis (i.e., the field direction). Furthermore, we replace P_R by K because $\Sigma = 0$ and get the basis

$$|\Lambda, j, K\rangle = |\Lambda\rangle \sqrt{\frac{2j+1}{4\pi}} D_{K,\Lambda}^j(\phi, \theta, 0)^*. \quad (7.22)$$

The matrix elements of the potential read

$$\begin{aligned} \langle j', K', \Lambda' | \hat{V} | j, K, \Lambda \rangle &= -\mu F \sqrt{(2j'+1)(2j+1)} (-1)^{m'-\Lambda'} \\ &\times \begin{pmatrix} j' & 1 & j \\ -K' & 0 & K \end{pmatrix} \begin{pmatrix} j' & 1 & j \\ -\Lambda' & 0 & \Lambda \end{pmatrix}, \end{aligned} \quad (7.23)$$

which is a simplified version of the potential matrix elements with $\Lambda' - \Lambda = 0$ in Eq. (7.11). The kinetic energy operator is given by $\hat{T} = B_0 [\hat{\mathbf{j}} - \hat{\mathbf{l}}]^2$, where $\hat{\mathbf{j}}$ is the total angular momentum operator, and $\hat{\mathbf{l}}$ the electronic angular momentum. Only the projection Λ , the eigenvalue of \hat{l}_z with z being the diatom axis \mathbf{r} , is a good quantum number and we may therefore omit all of the shift terms with \hat{l}_\pm from the kinetic energy operator. The remaining operator $\hat{T} = B_0 [\hat{j}^2 + \hat{l}_z^2 - 2\hat{l}_z \hat{j}_z]$ is diagonal in the basis of Eq. (7.22), with eigenvalue $B_0 [j(j+1) - \Lambda^2]$. Diagonalization of this simple Hamiltonian $\hat{T} + \hat{V}$ in a basis with $j = |\Lambda|, \dots, j_{\max}$ and plotting the eigenvalues as a function of the field strength F gives the energy level correlation diagram in Fig. 7.6. Note, in the first place that for sufficiently strong fields the energy levels are very similar to the levels in the rightmost column of Fig. 7.5. It is clear that the Σ ($K = 0$) and Δ ($|K| = 2$) levels that belong to the first excited ‘‘bending’’ state with $v_b = 1$ and $l = \pm 1$ are not degenerate, and neither are the Π ($|K| = 1$) and Φ ($|K| = 3$) levels of the second excited ‘‘bending’’ state with $v_b = 2$ and $l = 0, \pm 2$. This is related to the finite amplitude of the ‘‘bending’’ motion or, in other words, to the fact that the electronic angular momentum Λ and the total angular momentum K refer to different axes. When the field F becomes stronger, the level pattern becomes more and more similar to that of a harmonic oscillator and the splittings become relatively smaller. In the strong field limit the rotating molecule can hardly bend away from the SF Z -axis, the axes Z and z become parallel, and the splitting pattern is similar to Herzberg’s.

Also in our calculations on He-HF⁺ the energy differences between the Δ and Σ levels with $v_b = 1$ and between the Φ and Π levels with $v_b = 2$ did not disappear, even when we switched off both $V_{1,-1}$ and the spin-orbit coupling. When increasing the steepness of the well at the linear geometry in $V_{1,1}$ we found, also in the full calculations, that these energy differences became relatively small in comparison with the (vibrational) splitting between levels with different v_b . So, in that sense, our results agree with Herzberg’s model for the Renner-Teller coupling in a ² Π triatomic linear molecule.

Figure 7.5: Correlation diagram showing the dependence of the $v_s = 0$ levels on the Renner-Teller interaction potential $V_{1,-1}$ and on the spin-orbit coupling constant A . Labeling of the levels as in Fig. 7.4.

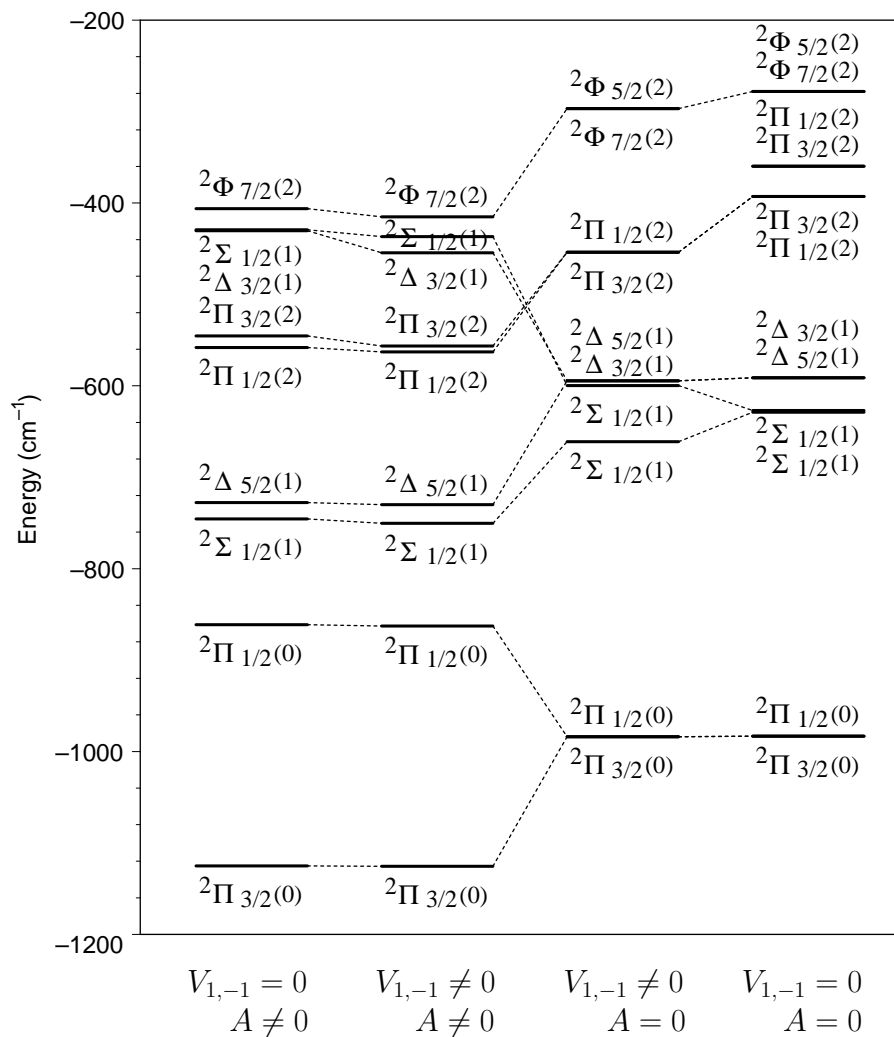
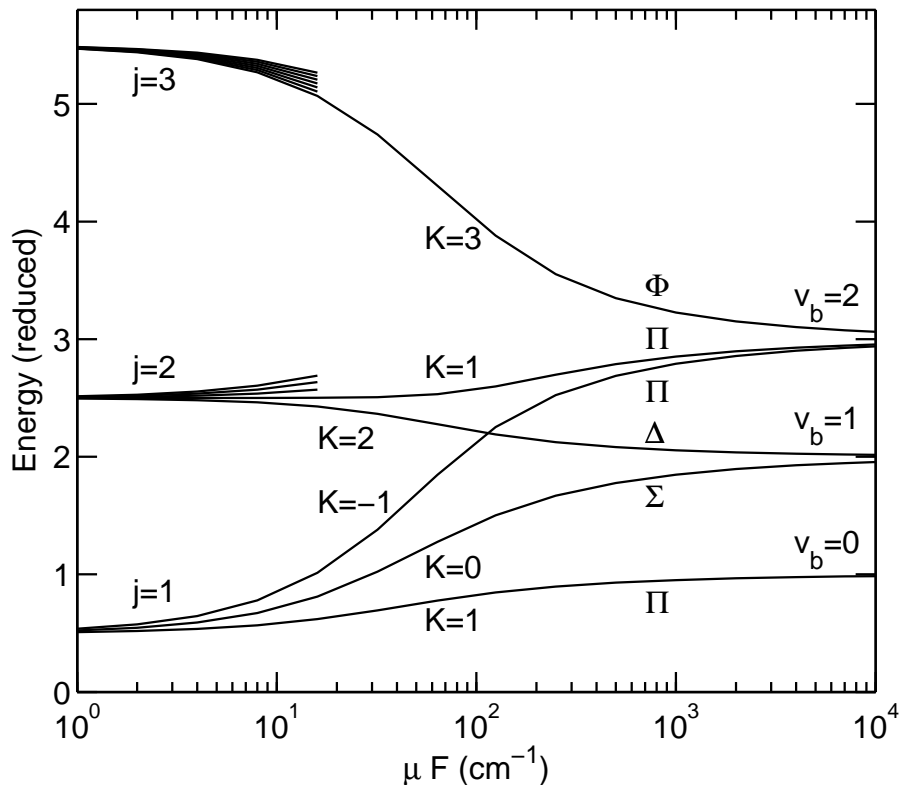


Figure 7.6: Energy levels of model HF^+ (with $\Lambda = \pm 1$ and $S = 0$) in an electric field F as function of the coupling strength μF . The $\Sigma, \Pi, \Delta, \Phi$ labels denote levels with $|K| = 0, 1, 2, 3$, while v_b is the “bending” quantum number. The labels K refer to the $\Lambda = +1$ component. The energies are divided by the fundamental “bending” vibration energy defined as $[E_\Sigma(v_b = 1) + E_\Delta(v_b = 1)]/2 - E_\Pi(v_b = 0)$.



7.4 Conclusion

Without consideration of the spin-orbit coupling the He-HF^+ complex has two asymptotically degenerate electronic states that correlate with the $X^2\Pi$ ground state of free HF^+ . We calculated the bound rovibronic levels of this complex for $J = \frac{1}{2}, \frac{3}{2}, \frac{5}{2}, \frac{7}{2}, \frac{9}{2}$ with the use of diabatic intermolecular potentials that couple these states and the inclusion of spin-orbit coupling. The *ab initio* diabatic potential surfaces and their analytic fits are described in ref [120]. The calculation of rovibronic levels was performed with basis sets defined in different coordinate frames: a BF frame with the z -axis parallel to the vector

\mathbf{R} that points from the center of mass of HF^+ to the He atom, and an MF frame with the z -axis parallel to the HF^+ bond axis \mathbf{r} . We interpreted the character of the rovibronic states by a series of calculations with the He– HF^+ distance R fixed at values ranging from 1.5 to 8.5 Å and by analysis of the wave functions. The approximate quantum numbers corresponding to the various angular momentum components with respect to the BF and MF frames were very useful in this analysis.

The intermolecular potential has a rather deep well at the linear He– HF^+ geometry, which makes this complex a Renner-Teller system. Renner-Teller effects have mostly been studied for semi-rigid triatomic and polyatomic linear molecules. Although the He– HF^+ complex is much more strongly bound than the neutral He–HF Van der Waals complex, it is considerably less rigid than a “normal” molecule held together by covalent bonds. It was, therefore, interesting to analyse the effects of the Renner-Teller coupling in this system and to look for characteristics due to large amplitude internal motions. We made such an analysis and, indeed, found such features. Finally, we extracted from our results some quantitative data that determine the spectroscopy of this complex: stretch and bend frequencies, spin-orbit splittings, parity splittings, rotational constants, and we compare some of these with the results of a previous theoretical study.

APPENDIX A

Basis transformations

Before we discuss the transformation of the different bases, we must derive a relation between the BF and MF frames. For this purpose it is most convenient to take the definition of the BF frame $[\mathbb{R}(\alpha, \beta, \phi)]$ from Sec. 7.2.1 and to *define* the MF rotation angles by

$$\mathbb{R}(\phi', \theta', \alpha') \equiv \mathbb{R}(\alpha, \beta, \phi)\mathbb{R}(0, \theta, \pi). \quad (\text{A.1})$$

Next we verify that this definition is equivalent to the definition of the MF frame given in Sec. 7.2.2. Substituting Eq. (A.1) into Eq. (7.13) and using $\mathbb{R}_z(\chi)e_z = e_z$ for any angle χ we find

$$r \mathbb{R}(\phi', \theta', \alpha')e_z = r \mathbb{R}(\alpha, \beta, \phi)\mathbb{R}_y(\theta)e_z = \mathbf{r}, \quad (\text{A.2})$$

where we used Eq. (7.4) in the last step. To verify Eq. (7.14) we again substitute Eq. (A.1) which gives

$$R \mathbb{R}(\phi', \theta', \alpha')\mathbb{R}_y(\beta')e_z = R \mathbb{R}(\alpha, \beta, \phi)\mathbb{R}(0, \theta, \pi)\mathbb{R}_y(\beta')e_z = \mathbf{R}, \quad (\text{A.3})$$

where we used $\beta' = \theta$, the relation

$$\mathbb{R}_y(\theta)\mathbb{R}_z(\pi) = \mathbb{R}_z(\pi)\mathbb{R}_y(-\theta), \quad (\text{A.4})$$

and Eq. (7.3).

We define electronic basis functions by applying rotation operators of the form $\widehat{R}(\alpha, \beta, \gamma) = \widehat{R}_z(\alpha)\widehat{R}_y(\beta)\widehat{R}_z(\gamma)$ to the wave functions $|\Lambda, S, \Omega\rangle$ with angular momentum projection quantum numbers defined with respect to the SF z -axis. This method is particularly convenient for giving a precise definition of open-shell electronic wave functions, also in the case of half-integral spin. In

the appendix of Ref. [41] it was used to define Hund's case (a) basis functions for open-shell diatoms and more details can be found there. Here we extend the technique to define basis functions for open-shell complexes and to derive the transformations between different basis sets. For this purpose we require the rotation operator analogue of Eq. (A.1)

$$\widehat{R}(\phi', \theta', \alpha') = \widehat{R}(\alpha, \beta, \phi) \widehat{R}(0, \theta, \pi). \quad (\text{A.5})$$

This relation holds for both integral and half-integral angular momentum cases.

Two- and three-angle embedded MF electronic wave functions are defined by

$$|\Lambda, S, \Omega\rangle^{\text{MF},2} \equiv \widehat{R}(\phi', \theta', 0) |\Lambda, S, \Omega\rangle \quad (\text{A.6})$$

and

$$|\Lambda, S, \Omega\rangle^{\text{MF}} \equiv \widehat{R}(\phi', \theta', \alpha') |\Lambda, S, \Omega\rangle = \exp(-i\Omega\alpha') |\Lambda, S, \Omega\rangle^{\text{MF},2}. \quad (\text{A.7})$$

Electronic wave functions defined with respect to the (three-angle embedded) BF frame are given by

$$|\Lambda, S, \Omega\rangle^{\text{BF}} \equiv \widehat{R}(\alpha, \beta, \phi) \widehat{R}(0, \theta, 0) |\Lambda, S, \Omega\rangle, \quad (\text{A.8})$$

where we use the BF label, even though these functions are quantized with respect to the HF^+ axis, just as the MF functions. This can be readily verified since the operator relation in Eq. (A.5) yields

$$|\Lambda, S, \Omega\rangle^{\text{BF}} = \exp(i\Omega\pi) |\Lambda, S, \Omega\rangle^{\text{MF}}. \quad (\text{A.9})$$

In chapter 4 a basis for the He-CO($a^3\Pi$) complex in SF coordinates

$$\begin{aligned} |n, \Lambda, S, \Omega, j, L; J, M_J\rangle &= |n\rangle |\Lambda, S, \Omega\rangle^{\text{MF},2} \left[\frac{2j+1}{4\pi} \right]^{1/2} \\ &\times \sum_{m, M_L} D_{m, \Omega}^{(j)}(\phi', \theta', 0) Y_{L, M_L}(\beta, \alpha) \\ &\times \langle j, m; L, M_L | J, M_J \rangle. \end{aligned}$$

was obtained by coupling the CO monomer functions with total angular momentum j and the spherical harmonics $Y_{L, M_L}(\beta, \alpha)$ by means of the Clebsch-Gordan coefficients $\langle j, m; L, M_L | J, M_J \rangle$ [39]. The two-angle embedded electronic wave function may be replaced by $|\Lambda, S, \Omega\rangle^{\text{MF}}$ if simultaneously the third argument (0) of the function $D_{m, \Omega}^{(j)}$ is set to α' . By a straightforward extension of the definition of the case (a) basis in Ref. [41] we define a MF basis for the complex as

$$\begin{aligned} |n, \Lambda, S, \Omega, L, \Omega_L, P_r; J, M_J\rangle &= |n\rangle \left[\frac{2J+1}{4\pi} \right]^{1/2} D_{M_J, P_r}^{(J)}(\phi', \theta', 0)^* \\ &\times \widehat{R}(\phi', \theta', 0) [Y_{L, \Omega_L}(\beta, \alpha) |\Lambda, S, \Omega\rangle], \quad (\text{A.10}) \end{aligned}$$

where the rotation operator acts on the electronic coordinates, as well as on (β, α) . With the use of Eq. (A.7) and the relation $P_r = \Omega + \Omega_L$ we obtain the MF basis in Eq. (7.17).

Analogously we define the \mathbf{R} -embedded (BF) basis

$$|n, \Lambda, S, \Omega, j, P_R; J, M_J\rangle = |n\rangle \frac{[(2J+1)(2j+1)]^{\frac{1}{2}}}{4\pi} D_{M_J, P_R}^{(J)}(\alpha, \beta, 0)^* \quad (\text{A.11})$$

$$\times \widehat{R}(\alpha, \beta, 0) \left[D_{P_R, \Omega}^{(j)}(\phi', \theta', 0)^* \widehat{R}(\phi', \theta', 0) | \Lambda, S, \Omega \rangle \right].$$

Acting with the rotation operators on the electronic and nuclear coordinates and using the BF electronic wave functions from Eq. (A.8) we obtain Eq. (7.9).

The elements of the unitary matrix that transforms the coupled SF basis into the MF basis are the overlap integrals

$$T_{\Omega_L, j}^{(\Omega, L, J)} = \langle n, \Lambda, S, \Omega, L, \Omega_L, P_r; J, M_J | n, \Lambda, S, \Omega, j, L; J, M_J \rangle \quad (\text{A.12})$$

that can be evaluated by integration over nuclear and electronic coordinates after substitution of Eqs. (7.17) and (A.10). Upon switching to the three-angle MF electronic wave functions introduced in Eq. (A.7) the electronic integral becomes simply ${}^{\text{MF}}\langle \Lambda, S, \Omega | \Lambda, S, \Omega \rangle^{\text{MF}} = 1$. The integration over the nuclear coordinates is performed most easily in the MF coordinates θ', ϕ', β' , and α' . We substitute

$$Y_{L, M_L}(\beta, \alpha) = \widehat{R}^{-1}(\phi', \theta', 0) Y_{L, M_L}(\beta', \alpha') \quad (\text{A.13})$$

$$= \sum_{M'_L} Y_{L, M'_L}(\beta', \alpha') D_{M_L, M'_L}^L(\phi', \theta', 0)^*. \quad (\text{A.14})$$

After integration over α' only the term with $M'_L = \Omega_L$ survives, which allows us to integrate over β' . Upon introduction of a dummy third angle χ via $\frac{1}{2\pi} \int_0^{2\pi} d\chi \exp[i(P_r - \Omega - \Omega_L)\chi] = 1$ the remaining integral of the product of three D -matrices over ϕ' and θ' becomes a standard integral [124]. The result is a product of two Clebsch-Gordan coefficients. Finally the summation over m and M_L may be performed by using the orthogonality relation of Clebsch-Gordan coefficients [39] and we obtain

$$T_{\Omega_L, j}^{(\Omega, L, J)} = \left[\frac{2j+1}{2J+1} \right]^{\frac{1}{2}} \langle j, \Omega, L, \Omega_L | J, P_r \rangle. \quad (\text{A.15})$$

The elements of the matrix that transforms the SF basis into the BF basis can be evaluated similarly

$$T_{P_R, L}^{(j, J)} = \langle n, \Lambda, S, \Omega, j, P_R; J, M_J | n, \Lambda, S, \Omega, j, L; J, M_J \rangle. \quad (\text{A.16})$$

Here the electronic integral yields ${}^{\text{BF}}\langle \Lambda, S, \Omega | \Lambda, S, \Omega \rangle^{\text{BF}} = \exp(-i\Omega\pi)$. The nuclear integral is most easily evaluated in BF coordinates, which requires the

substitution

$$D_{m,\Omega}^{(j)}(\phi', \theta', \alpha')^* = \sum_{\Omega'} D_{m,\Omega'}^{(j)}(\alpha, \beta, \phi)^* D_{\Omega',\Omega}^{(j)}(0, \theta, \pi)^*. \quad (\text{A.17})$$

This relation is simply a representation of the operator relation in Eq. (A.5). After integration over ϕ we find that only the term with $\Omega' = P_R$ survives. The argument π in the last D -matrix cancels the factor from the electronic integral and the remaining integrals are readily performed using expressions from Ref. [124]. Again using the orthogonality of the Clebsch-Gordan coefficients in the last step, we find

$$T_{P_R,L}^{(j,J)} = \left[\frac{2L+1}{2J+1} \right]^{\frac{1}{2}} \langle j, P_R, L, 0 | J, P_R \rangle. \quad (\text{A.18})$$

Summary

This thesis deals with open-shell atom-diatom complexes which are of interest for various reasons and can also be considered as model systems for complexes of larger open-shell molecules. Intermolecular potential surfaces were computed by means of *ab initio* electronic structure calculations for a set of frozen nuclear geometries or taken from the literature. The bound levels of the complex were obtained by solving the Schrödinger equation for the nuclear motion problem. The standard harmonic oscillator approach to solve this problem is not applicable here, because of the large amplitude internal motions in these weakly bound complexes. Instead, the bound levels were obtained by solving a coupled-channel problem in Jacobi coordinates either by variational or by DVR (discrete variable representation) methods. Photodissociation of the complex, a half-collision, was studied with the aid of full coupled-channel scattering calculations.

This two-step procedure to treat the electronic and nuclear motion problems is similar to the Born-Oppenheimer model, but it should be emphasized that the standard Born-Oppenheimer or adiabatic approximation is not valid for these open-shell complexes. The electronic states of the complex become degenerate, i.e., the corresponding adiabatic potential energy surfaces coincide, at linear geometries and for a large distance between the interacting molecules. Non-adiabatic coupling between different electronic states that originates from the nuclear kinetic energy operator becomes important especially in these regions. A generalized Born-Oppenheimer model was applied that involves the multiple asymptotically degenerate electronic states simultaneously and takes into account the non-adiabatic coupling between these states. This coupling was not explicitly considered, however, but the adiabatic states were transformed into diabatic states that are no longer coupled by the nuclear kinetic energy operator. These diabatic states are not eigenstates of the electronic

Hamiltonian and they are coupled by off-diagonal potentials. The generalized Born-Oppenheimer model uses a full $n \times n$ matrix of diabatic potential energy surfaces, where n is the number of asymptotically degenerate electronic states. This approach is briefly explained in Chapter 2 of the thesis. It was applied to several atom-diatom complexes with either the atom or the diatom being an open-shell system in Chapters 3 to 7.

In Chapter 3 we show, for the case of an open-shell atom interacting with a closed-shell diatom, the transformation from adiabatic to diabatic states and the derivation of a generalized Legendre expansion for the diabatic potentials from invariance properties of the potential energy operator for the multiple diabatic states. The formalism was used to calculate the bound states of the $F(^2P)\text{-H}_2$ complex that occurs in the entrance channel of the chemical reaction $F + \text{H}_2 \rightarrow \text{HF} + \text{H}$. Results were obtained for both *para* and *ortho* H_2 species. We used this calculation also to compare *ab initio* and semi-empirical potentials for this system. The predicted energy levels have not been measured yet, but several experimental groups are now interested in performing spectroscopic measurements.

In Chapter 4 we present a similar derivation of the form of the diabatic potentials, now for an atom-diatom complex where the diatom is the open-shell system. We computed *ab initio* potentials both for the closed-shell ground state and for an open-shell triplet excited state of the He-CO complex. The $a^3\Pi$ excited CO molecule is a long-lived metastable species and it was interesting to find out what happens when this excited molecule interacts with a He atom and the degeneracy of the triplet Π state is lifted. We computed the bound levels of the ground state and triplet excited He-CO complex and theoretically generated the UV spectrum associated with the $\text{CO}(X^1\Sigma \rightarrow a^3\Pi)$ spin-forbidden transition in the complex. It turned out that the CO monomer in the complex is predominantly excited into a higher spin-orbit level of the $a^3\Pi$ state and can decay into the lowest spin-orbit level. This process releases a sufficient amount of energy to dissociate the complex. Explicit calculation of the dissociating states with the aid of a scattering formalism, described in Chapter 5, shows that this so-called spin-orbit predissociation process leads to rapid fragmentation of the complex, and is much faster than the decay of metastable triplet CO back into the ground singlet state. Chapter 5 presents life times of different excited levels of the complex that can be measured as spectral line widths, as well as photodissociation cross sections and state distributions of the emerging, still triplet excited, CO fragment. Most of the excited triplet "levels" of He-CO are actually resonances in the dissociation continuum and the (calculated) UV spectrum is dominated by bound-to-free transitions. A first experimental attempt to observe triplet excited He-CO had failed; with the aid of our results we suggested a modification of the experimental setup that will have a better chance of success.

Chapter 6 presents bound state calculations for the Cl-HCl complex with the formalism derived in Chapter 3 and the use of *ab initio* potential surfaces.

This complex is formed in the entrance and exit channels of the hydrogen exchange reaction $\text{Cl} + \text{HCl} \rightarrow \text{ClH} + \text{Cl}$. The most stable rovibronic levels of the complex correspond to a T-shaped geometry, but we also found a series of higher levels that correspond to a linear geometry. A remarkable result is that even for the lower lying states with the T-shaped structure a number of the calculated spectral features are typically those that are normally observed for linear molecules. Again, there are some experimental groups that are now interested in performing spectroscopic measurements.

In Chapter 7 we present a study of the He-HF^+ complex. This complex has a linear equilibrium geometry with a degenerate $^2\Pi$ ground state and it is interesting to observe the Renner-Teller effect—a nonadiabatic coupling phenomenon that occurs for linear molecules—in a rather weakly bound complex. Up to now it was only studied for “normal”, i.e., nearly rigid, molecules. The bound states of the complex were calculated and analyzed in different coordinates and angular momentum coupling schemes and compared to the energy level pattern that is normally obtained for Renner-Teller systems. Although this pattern is also found here, we noticed and explained some typical deviations caused by the large amplitude of the bending motion in this complex which cannot be described by the standard harmonic approximation.

Samenvatting

Dit proefschrift behandelt open-schil atoom-diatoom complexen die om verschillende redenen zelf interessant zijn en die tevens kunnen worden beschouwd worden als modelsystemen voor complexen van grotere open-schil moleculen. De benodigde intermoleculaire wisselwerkingspotentialen hebben we berekend met behulp van *ab initio* elektronenstructuur-methoden voor een reeks van vaste kernconfiguraties of we hebben potentiaaloppervlakken uit de literatuur gebruikt. De quantumtoestanden van het gebonden complex vinden we door de Schrödingervergelijking voor de kernbewegingen op te lossen. Omdat de interne bewegingen in deze zwakgebonden complexen grote amplitudes hebben, konden we hiervoor niet de standaard harmonische-oscillator-aanpak gebruiken. We hebben daarom gebruik gemaakt van variationele en DVR (discrete variabele representatie) methoden en een gekoppeld kanalenprobleem opgelost in Jacobi-coördinaten. Ook de fotodissociatie van het complex, die beschouwd kan worden als een halve botsing, hebben we bestudeerd met behulp van verstrooiingsberekeningen met het gekoppelde-kanalen formalisme.

Deze tweetrapsprocedure om de elektronische en kernbewegingen te behandelen lijkt op het Born-Oppenheimer model. Het moet echter benadrukt worden dat de standaard Born-Oppenheimer of adiabatische benadering niet geldig is voor deze open-schil complexen. De elektronische toestanden van het complex zijn ontaard, dat wil zeggen de adiabatische potentiaaloppervlakken voor deze toestanden vallen samen, zowel voor lineaire geometrieën als voor grote afstanden tussen de wisselwerkende moleculen. De niet-adiabatische koppeling tussen verschillende elektronische toestanden, veroorzaakt door de kern-kinetische energie operator, wordt vooral in deze gebieden belangrijk. We hebben een gegeneraliseerd Born-Oppenheimer model toegepast waarin de verschillende asymptotisch ontaarde toestanden en de niet-adiabatische koppeling tussen deze toestanden tegelijkertijd worden behandeld. We hebben echter

deze koppeling niet expliciet meegenomen; in plaats daarvan hebben we de adiabatische toestanden getransformeerd naar diabatische toestanden, die niet gekoppeld worden door de kern-kinetische energie operator. Deze diabatische toestanden zijn geen eigentoestanden van de elektronische Hamiltoniaan, ze worden gekoppeld door niet-diagonale potentialen. Het gegeneraliseerde Born-Oppenheimer model gebruikt een volledige $n \times n$ matrix van diabatische potentiaaloppervlakken, waarbij n het aantal asymptotisch ontaarde elektronische toestanden is. In hoofdstuk 2 van het proefschrift wordt deze aanpak kort uitgelegd. In de hoofdstukken 3 tot en met 7 wordt hij toegepast op een aantal atoom-diatoom complexen, waarin ofwel het atoom ofwel het diatoom in een open-schil toestand is.

In hoofdstuk 3 laten we de transformatie van adiabatische naar diabatische toestanden zien voor het geval van een open-schil atoom dat wisselwerkt met een gesloten-schil diatoom. We geven ook de afleiding van een expansie voor de diabatische potentialen in gegeneraliseerde Legendre-functies die volgt uit de invariantie-eigenschappen van de potentiële energie operator voor de gekoppelde diabatische toestanden. Dit formalisme is gebruikt om de gebonden toestanden te berekenen van het $F(^2P)\text{-H}_2$ complex dat gevormd wordt in het ingangskanaal van de chemische reactie $F + \text{H}_2 \rightarrow \text{HF} + \text{H}$. We presenteren resultaten voor zowel *para* als *ortho* H_2 moleculen. Deze berekening is ook gebruikt om *ab initio* en semi-empirische potentialen voor dit systeem te vergelijken. De voorspelde energieniveaus zijn nog niet gemeten, maar verschillende experimentele groepen hebben nu belangstelling om deze spectroscopische metingen uit te voeren.

In hoofdstuk 4 presenteren we een vergelijkbare afleiding voor de vorm van de diabatische potentialen, voor een atoom-diatoom complex met een open-schil diatoom. We hebben *ab initio* potentialen berekend, zowel voor de gesloten-schil grondtoestand als voor een open-schil triplet aangeslagen toestand van het He-CO complex. Het $a^3\Pi$ aangeslagen CO molecuul is een langlevend metastabiel deeltje. Het was interessant om uit te zoeken wat er gebeurt wanneer dit aangeslagen molecuul wisselwerkt met een heliumatoom, waardoor de ontaarding van de triplet Π toestand opgeheven wordt. We hebben eerst de gebonden energieniveaus van de grond- en de triplet aangeslagen toestand van het He-CO complex berekend. Hiermee hebben we een theoretisch UV spectrum gegenereerd dat geassocieerd is met de $\text{CO}(X^1\Sigma \rightarrow a^3\Pi)$ spinverboden overgang in het complex. Het blijkt dat het CO monomeer in het complex voornamelijk wordt aangeslagen naar een hoger liggend spin-baan niveau van de $a^3\Pi$ toestand, wat daarna kan terugvallen naar het laagste spin-baan niveau. Bij dit proces komt voldoende energie vrij om het complex te dissociëren. Een expliciete berekening van de dissociërende toestanden met behulp van een verstrooiingsformalisme, zoals beschreven in hoofdstuk 5, laat zien dat dit zogenaamde spin-baan predissociatieproces leidt tot snelle fragmentatie van het complex, veel sneller dan de terugval van metastabiel triplet CO naar de singlet grondtoestand. In hoofdstuk 5 presenteren we levensduren van ver-

schillende aangeslagen toestanden van het complex, die experimenteel bepaald kunnen worden uit spectrale lijnbreedtes. Verder hebben we de fotodissociatiewaarschijnlijkheid bepaald als functie van de excitatie-frequentie, evenals de toestandsverdeling van het resulterende, nog steeds triplet aangeslagen, CO fragment. De meeste aangeslagen triplet “niveaus” van He–CO zijn eigenlijk resonanties in het dissociatie-continuum en het (berekende) UV spectrum wordt gedomineerd door gebonden-naar-vrij overgangen. Een eerste experimentele poging om triplet aangeslagen He–CO waar te nemen was mislukt; met behulp van onze resultaten hebben we een modificatie van de experimentele opzet met meer kans van slagen gesuggereerd.

Hoofdstuk 6 beschrijft berekeningen van gebonden toestanden van het Cl–HCl complex, uitgevoerd met het formalisme dat we in hoofdstuk 3 hebben afgeleid, waarbij we *ab initio* potentiaaloppervlakken gebruikt hebben. Dit complex wordt gevormd in het ingangs- en uitgangskanaal van de waterstofuitwisselingsreactie $\text{Cl} + \text{HCl} \rightarrow \text{ClH} + \text{Cl}$. De meest stabiele rotatie-vibratieniveaus van het complex hebben een T-vormige geometrie, maar we hebben ook een serie hogere niveaus met een lineaire geometrie gevonden. Een opmerkelijk resultaat is dat voor de lager gelegen toestanden met T-vormige structuur een aantal berekende spectroscopische eigenschappen typisch zo zijn als normaal waargenomen voor lineaire moleculen. Ook voor dit complex zijn nu experimentele groepen geïnteresseerd om spectroscopische metingen te gaan uitvoeren.

In hoofdstuk 7 wordt een studie van het He–HF⁺ complex beschreven. Dit complex heeft een lineaire evenwichtsgeometrie met een ontaarde ²Π grondtoestand. Het is interessant om het Renner-Teller effect —een niet-adiabatisch koppelingsverschijnsel dat in lineaire moleculen optreedt— te observeren in een tamelijk zwakgebonden complex. Tot nu toe was het alleen bestudeerd voor “normale”, dat wil zeggen bijna starre, moleculen. We hebben de gebonden toestanden berekend en geanalyseerd in verschillende coördinatenstelsels en hoekmomentkoppelingsschema’s. Verder hebben we de berekende energieniveaus vergeleken met het patroon dat normaal optreedt in Renner-Teller systemen. Hoewel we dit patroon hier terugvinden, merken we een aantal karakteristieke afwijkingen op en verklaren deze. Deze afwijkingen worden veroorzaakt door de grote amplitude van de buigbeweging in dit complex, die niet beschreven kan worden in de standaard harmonische benadering.

List of publications

- Chapter 3 of this thesis:
W. B. Zeimen, J. Kłos, G. C. Groenenboom, and A. van der Avoird, *Diabatic intermolecular potentials and bound states of open-shell atom-molecule dimers: Application to the F(2P)-H₂ complex*, J. Chem. Phys. **118**, 7340–7352, (2003),
- Chapter 4 of this thesis:
W. B. Zeimen, G. C. Groenenboom, and A. van der Avoird, *Singlet-triplet excitation spectrum of the CO-He complex I: Potential surfaces and bound-bound CO (a³PX1S⁺) transitions*, J. Chem. Phys. **119**, 131–140, (2003),
- Chapter 5 of this thesis:
W. B. Zeimen, G. C. Groenenboom, and A. van der Avoird, *Singlet-triplet excitation spectrum of the CO-He complex II: Photodissociation and bound-free CO (a³PX1S⁺) transitions*, J. Chem. Phys. **119**, 141–148, (2003),
- Chapter 6 of this thesis:
W. B. Zeimen, J. Kłos, G. C. Groenenboom, and A. van der Avoird, *Bound states of the Cl(2P)-HCl van der Waals complex from coupled ab initio potential energy surfaces*, J. Phys. Chem. A **107**, 5110–5121, (2003),
- Chapter 7 of this thesis:
G. Dhont, W. B. Zeimen, G. C. Groenenboom, and A. van der Avoird, *Theoretical study of the He-HF⁺ complex II: Rovibronic states from coupled diabatic potential energy surfaces*, J. Chem. Phys. **120**, 103–116, (2004),

- in preparation:

J. Kłos, W. B. Zeimen, A. van der Avoird, Millard Alexander, *Bound states of $X(^2P) \cdots H_2(^1\Sigma_g^+)$ [$X=Cl, Br$] Van der Waals complexes on *ab initio* diabatic potential energy surfaces.*

Curriculum Vitae

Name: Wilfried Patrick Jean-Bernard Zeimen
Born: 18 January 1973 in Toulouse (France)

Education:

1999 – 2003: PhD studies in Theoretical Chemistry at the Institute of Theoretical Chemistry, University of Nijmegen, The Netherlands.

supervisor: Prof. Dr. Ir. Ad van der Avoird,
co-supervisor: Dr. Ir. Gerrit C. Groenenboom.

1997 – 1998: DEA in Theoretical Physics
with specialisation in Molecular Physics,
University of Paul Sabatier Toulouse III.
Final project at IRSAMC/CNRS on Computational simulation of ionization and dissociation of neon clusters,
supervisor: Prof. Dr. Nadine Halberstadt.

1996 – 1997: Maîtrise de Physique
With specialisation in quantum physics, solid state physics and fluid dynamics/meteorology.
University of Paul Sabatier Toulouse III.
Project at the LPCM/CNRS on Computational simulation of the magnetization of ultra-thin ferromagnetic films,
supervisor: Dr. Jean-Marc Broto.

- 1996 : Research Assistant at CESR/CNRS
In the group of Prof. J.P. Treihlou, leading the INTERBOA research project, the task was to develop a computer program, in close collaboration with technical staff, to record, recover and analyze stratospheric balloon data of electric and magnetic field measurements.

Bibliography

- [1] K. Autumn et al., PNAS **99**, 12252 (2002).
- [2] A. K. Geim et al., Nature Materials **2**, 461 (2003).
- [3] B. Brutschy and P. Hobza, Chem. Rev. **100** (2000).
- [4] A. H. Krotz, T. P. S. L. Y. Kuo, and J. K. Barton, J. Am. Chem. Soc. **115**, 3877 (1993).
- [5] A. Sitlani and J. K. Barton, Biochemistry **33**, 12100 (1994).
- [6] D. Skouteris et al., Science **286**, 1713 (1999).
- [7] F. J. Aoiz et al., J. Chem. Phys. **115**, 2074 (2001).
- [8] H. Kohguchi, T. Suzuki, and M. H. Alexander, Science **294**, 832 (2001).
- [9] J. M. Hutson and S. Jain, J. Chem. Phys. **91**, 4197 (1989).
- [10] C. Leforestier, K. Yamashita, and N. Moiseyev, J. Chem. Phys. **103**, 8468 (1995).
- [11] M. Born and R. Oppenheimer, Ann. Phys. **84**, 457 (1927).
- [12] C. A. Mead and D. G. Truhlar, J. Chem. Phys. **70**, 2284 (1979).
- [13] B. K. Kendrick, C. A. Mead, and D. G. Truhlar, Chem. Phys. **277**, 31 (2002).
- [14] D. A. Varshalovich, A. N. Moskalev, and V. K. Khersonskii, *Quantum Theory of Angular Momentum*, World Scientific, Singapore, 1988.
- [15] G. C. Groenenboom and D. T. Colbert, J. Chem. Phys. **99**, 9681 (1993).

-
- [16] A. van der Avoird, P. E. S. Wormer, F. Mulder, and R. M. Berns, *Topics Curr. Chem.* **93**, 1 (1980).
- [17] A. van der Avoird, P. E. S. Wormer, and R. Moszynski, *Chem. Rev.* **94**, 1931 (1994).
- [18] M. H. Alexander, *J. Chem. Phys.* **99**, 6014 (1993).
- [19] M.-L. Dubernet and J. Hutson, *J. Chem. Phys.* **101**, 1939 (1994).
- [20] M.-L. Dubernet and J. Hutson, *J. Phys. Chem.* **98**, 5844 (1994).
- [21] D. E. Manolopoulos, *J. Chem. Soc., Faraday Trans.* **93**, 673 (1997).
- [22] M. H. Alexander, D. E. Manolopoulos, and H.-J. Werner, *J. Chem. Phys.* **113**, 11084 (2000).
- [23] D. E. Manolopoulos et al., *Science* **262**, 1852 (1993).
- [24] J. F. Castillo et al., *J. Chem. Phys.* **109**, 7224 (1998).
- [25] J. F. Castillo, D. E. Manolopoulos, K. Stark, and H.-J. Werner, *J. Chem. Phys.* **104**, 6531 (1996).
- [26] M. Baer et al., *J. Chem. Phys.* **104**, 2743 (1996).
- [27] P. Honvault and J.-M. Launay, *Chem. Phys. Lett.* **270**, 287 (1998).
- [28] P. Honvault and J.-M. Launay, *Chem. Phys. Lett.* **303**, 657 (1999).
- [29] J. F. Castillo and D. E. Manolopoulos, *Faraday Discuss. Chem. Soc.* **110**, 119 (1998).
- [30] R. T. Skodje et al., *J. Chem. Phys.* **112**, 4536 (2000).
- [31] V. Aquilanti, R. Candori, D. Cappelletti, E. Luzzatti, and F. Pirani, *Chem. Phys.* **145**, 293 (1990).
- [32] V. Aquilanti, S. Cavalli, F. Pirani, A. Volpi, and D. Cappelletti, *J. Phys. Chem. A* **105**, 2401 (2001).
- [33] V. Aquilanti et al., *Phys. Chem. Chem. Phys.* **4**, 401 (2002).
- [34] M. Faubel et al., *J. Chem. Soc. Faraday Trans.* **89**, 1475 (1993).
- [35] F. A. Gianturco et al., *Chem. Phys.* **200**, 405 (1995).
- [36] M. Ayabakan et al., *Chem. Phys.* **229**, 21 (1998).
- [37] T. Takayanagi and Y. Kurosaki, *J. Chem. Phys.* **109**, 8929 (1998).

- [38] J. Kłos, G. Chałasiński, and M. M. Szczęśniak, *Int. J. Quant. Chem.* **90**, 1038 (2002).
- [39] D. M. Brink and G. R. Satchler, *Angular Momentum*, Clarendon, Oxford, third edition, 1993.
- [40] G. Brocks, A. van der Avoird, B. T. Sutcliffe, and J. Tennyson, *Mol. Phys.* **50**, 1025 (1983).
- [41] M. C. G. N. van Vroonhoven and G. C. Groenenboom, *J. Chem. Phys.* **117**, 5240 (2002).
- [42] A. J. H. M. Meijer, G. C. Groenenboom, and A. van der Avoird, *J. Chem. Phys.* **101**, 7603 (1994).
- [43] J. Kłos, G. Chałasiński, and M. M. Szczęśniak, *J. Chem. Phys.* **117**, 4709 (2002).
- [44] A. D. Esposti and H.-J. Werner, *J. Chem. Phys.* **93**, 3351 (1990).
- [45] J. W. Riehl, C. J. Fischer, J. D. Baloga, and J. L. Kinsey, *J. Chem. Phys.* **58**, 4571 (1973).
- [46] R. J. Le Roy and J. van Kranendonk, *J. Chem. Phys.* **61**, 4750 (1974).
- [47] U. Buck, H. Meyer, and R. J. Le Roy, *J. Chem. Phys.* **80**, 5589 (1984).
- [48] R. J. Le Roy and J. M. Hutson, *J. Chem. Phys.* **86**, 837 (1987).
- [49] M. Jeziorska, P. Jankowski, K. Szalewicz, and B. Jeziorski, *J. Chem. Phys.* **113**, 2957 (2000).
- [50] J. Tennyson and B. T. Sutcliffe, *J. Chem. Phys.* **77**, 4061 (1982).
- [51] The MathWorks, Inc., 24 Prime Park Way, Natick, MA, *MATLAB Version 6*, 1996, <http://www.mathworks.com/>.
- [52] HIBRIDON is a package of programs for the time-independent quantum treatment of inelastic collisions and photodissociation written by M. H. Alexander, D. Manolopoulos, H.-J. Werner, and B. Follmeg, with contributions by P. Vohralik, G. Corey, B. Johnson, T. Orlikowski, and P. Valiron.
- [53] K. Stark and H.-J. Werner, *J. Chem. Phys.* **104**, 6515 (1996).
- [54] J. Kłos, G. Chałasiński, and M. M. Szczęśniak, *J. Phys. Chem. A* **106**, 7362 (2002).
- [55] J. Kłos, G. Chałasiński, M. M. Szczęśniak, and H.-J. Werner, *J. Chem. Phys.* **115**, 3085 (2001).

-
- [56] R. T. Jongma, G. Berden, and G. Meijer, *J. Chem. Phys.* **107**, 7034 (1997).
- [57] T. Sykora and C. R. Vidal, *J. Chem. Phys.* **110**, 6319 (1999).
- [58] R. T. Jongma et al., *Phys. Rev. Lett.* **78**, 1375 (1997).
- [59] R. T. Jongma et al., *J. Chem. Phys.* **107**, 252 (1997).
- [60] H. Bethlem, G. Berden, and G. Meijer, *Phys. Rev. Lett.* **83**, 1558 (1999).
- [61] G. Meijer, (2001), private communication.
- [62] T. James, *J. Chem. Phys.* **55**, 4118 (1971).
- [63] R. Field, S. Tilford, R. Howard, and J. Simmons, *J. Mol. Spec.* **44**, 347 (1972).
- [64] M. H. Alexander, *Chem. Phys.* **92**, 337 (1985).
- [65] G. Herzberg, *Molecular Spectra and Molecular Structure, Vol. 1: Spectra of Diatomic Molecules*, Van Nostrand, New York, 1950.
- [66] T. G. A. Heijmen, R. Moszynski, P. E. S. Wormer, and A. van der Avoird, *J. Chem. Phys.* **107**, 9921 (1997).
- [67] J. D. Watts, J. Gauss, and R. J. Bartlett, *J. Chem. Phys.* **98**, 8718 (1993).
- [68] R. Moszynski, T. G. A. Heijmen, and A. van der Avoird, *Chem. Phys. Lett.* **247**, 440 (1995).
- [69] MOLPRO is a package of *ab initio* programs written by H.-J. Werner and P. J. Knowles, with contributions from J. Almlöf, R. D. Amos, *et al.*
- [70] P. J. Knowles, C. Hampel, and H.-J. Werner, *J. Chem. Phys.* **99**, 5219 (1993).
- [71] P. J. Knowles, C. Hampel, and H.-J. Werner, *J. Chem. Phys.* **112**, E3106 (2000).
- [72] S. F. Boys and F. Bernardi, *Mol. Phys.* **19**, 553 (1970).
- [73] H. Partridge, *J. Chem. Phys.* **90**, 1043 (1989).
- [74] J. H. van Lenthe and F. B. van Duijneveldt, *J. Chem. Phys.* **81**, 3168 (1984).
- [75] F. M. Tao and Y. K. Pan, *J. Chem. Phys.* **97**, 4989 (1992).
- [76] T. H. Dunning, *Chem. Phys.* **90**, 1007 (1989).

- [77] R. A. Kendall, T. H. Dunning, and R. J. Harrison, *J. Chem. Phys.* **96**, 6796 (1992).
- [78] D. E. Woon and T. H. Dunning, *J. Chem. Phys.* **100**, 2975 (1994).
- [79] K. T. Tang and J. P. Toennies, *J. Chem. Phys.* **80**, 3726 (1984).
- [80] G. C. Groenenboom and I. M. Struniewicz, *J. Chem. Phys.* **113**, 9562 (2000).
- [81] P. E. S. Wormer and A. van der Avoird, *Chem. Rev.* **100**, 4109 (2000).
- [82] R. N. Zare, *Angular Momentum*, Wiley, New York, 1988.
- [83] M.-L. Dubernet, D. Flower, and J. M. Hutson, *J. Chem. Phys.* **94**, 7602 (1991).
- [84] M. Drabbels, W. L. Meerts, and J. J. ter Meulen, *J. Chem. Phys.* **99**, 2352 (1993).
- [85] R. Moszynski, T. Korona, P. E. S. Wormer, and A. van der Avoird, *J. Chem. Phys.* **103**, 321 (1995).
- [86] M. Drabbels, S. Stolte, and G. Meijer, *Chem. Phys. Lett.* **200**, 108 (1992).
- [87] R. T. Jongma, M. G. H. Boogaarts, and G. Meijer, *J. Mol. Spec.* **165**, 303 (1994).
- [88] A. Wada and H. Kanamori, *J. Mol. Spec.* **200**, 196 (2000).
- [89] R. Schinke, *Photodissociation Dynamics*, Cambridge University Press, Cambridge, 1993.
- [90] R. G. Gordon, *J. Chem. Phys.* **51**, 14 (1969).
- [91] B. R. Johnson, *J. Chem. Phys.* **69**, 4678 (1978).
- [92] B. R. Johnson, National Resource for Computation in Chemistry, University of California, Berkeley, *Proceedings* **5**, 86 (1979).
- [93] A. E. Thornley and J. M. Hutson, *J. Chem. Phys.* **101**, 5578 (1994).
- [94] G. H. Golub and C. Van Loan, *Matrix Computations*, Johns Hopkins University Press, Baltimore, third edition, 1996.
- [95] A. C. Allison and A. Dalgarno, *J. Chem. Phys.* **55**, 4342 (1971).
- [96] A. L. Smith, *J. Chem. Phys.* **55**, 4344 (1971).
- [97] G. C. Schatz, *J. Chem. Phys.* **90**, 3582 (1989).

- [98] B. Gadzy and J. M. Bowman, *J. Chem. Phys.* **91**, 4615 (1989).
- [99] G. C. Schatz, D. Sokolovski, and J. N. L. Connor, *Faraday Discuss. Chem. Soc.* **91**, 17 (1991).
- [100] K. Yamashita and K. Morokuma, *J. Chem. Phys.* **93**, 3716 (1990).
- [101] O. Hahn, J. M. L. Gomez, and S. H. Taylor, *J. Chem. Phys.* **94**, 2608 (1991).
- [102] T. W. J. Whiteley, A. J. Dobbyn, J. N. L. Connor, and G. C. Schatz, *Phys. Chem. Chem. Phys.* **2**, 549 (2000).
- [103] A. J. Dobbyn, J. N. L. Connor, N. A. Besley, P. J. Knowles, and G. C. Schatz, *Phys. Chem. Chem. Phys.* **1**, 957 (1999).
- [104] M. González, J. Hijazo, J. J. Novoa, and R. Sayós, *J. Chem. Phys.* **108**, 3168 (1998).
- [105] G. C. Schatz, P. McCabe, and J. N. L. Connor, *Faraday Discuss.* **110**, 139 (1998).
- [106] C. S. Maierle, G. C. Schatz, M. S. Gordon, P. McCabe, and J. N. L. Connor, *J. Chem. Soc., Faraday Trans.* **93**, 709 (1997).
- [107] D. K. Bondi, J. N. L. Connor, J. Manz, and J. Römel, *Mol. Phys.* **50**, 467 (1983).
- [108] J. N. L. Connor and W. Jakubetz, in *Supercomputer Algorithms for Reactivity, Dynamics and Kinetics of Small Molecules*, edited by A. Laganà, pages 395–411, Kluwer Dordrecht, The Netherlands, 1989.
- [109] Q. Sun, J. M. Bowman, G. C. Schatz, J. R. Sharp, and J. N. L. Connor, *J. Chem. Phys.* **92**, 1677 (1990).
- [110] G. C. Schatz, B. Amaee, and J. N. L. Connor, *J. Chem. Phys.* **92**, 4893 (1990).
- [111] J. P. Fulmer and P. M. Aker, *J. Chem. Phys.* **96**, 4252 (1992).
- [112] W. Jakubetz, D. Sokolovski, J. N. L. Connor, and G. C. Schatz, *J. Chem. Phys.* **97**, 6451 (1992).
- [113] M. J. Cohen, A. Willets, and N. C. Handy, *J. Chem. Phys.* **99**, 5885 (1993).
- [114] R. B. Metz, T. Kitsopoulos, A. Weaver, and D. M. Neumark, *J. Chem. Phys.* **88**, 1463 (1988).

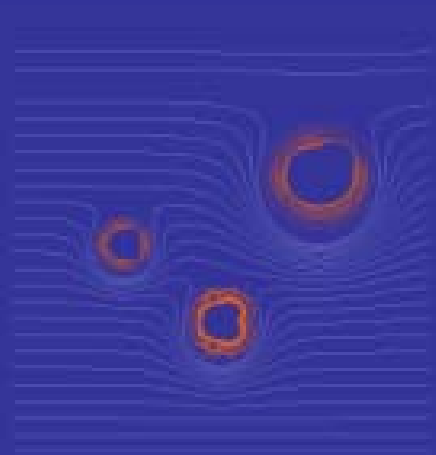
-
- [115] R. B. Metz, A. Weaver, S. E. Bradforth, T. N. Kitsopoulos, and D. M. Neumark, *J. Phys. Chem.* **94**, 1377 (1990).
- [116] D. M. Neumark, *Annu. Rev. Phys. Chem.* **43**, 153 (1992).
- [117] P. Žďánska, D. Nachtigallová, P. Nachtigall, and P. Jungwirth, *J. Chem. Phys.* **115**, 5974 (2001).
- [118] W. B. Zeimen, J. A. Kłos, G. C. Groenenboom, and A. van der Avoird, *J. Chem. Phys.* **118**, 7340 (2003).
- [119] H. Lefebvre-Brion and R. W. Field, *Perturbations in the spectra of diatomic molecules*, Academic Press, New York, 1986.
- [120] V. F. Lotrich, P. E. S. Wormer, and A. van der Avoird, *J. Chem. Phys.* **120**, 1200 (2004).
- [121] V. F. Lotrich and A. van der Avoird, *J. Chem. Phys.* **118**, 1110 (2003).
- [122] T. Schmelz and P. Rosmus, *Chem. Phys. Lett.* **220**, 117 (1994).
- [123] K. P. Huber and G. Herzberg, *Molecular Spectra and Molecular Structure. IV. Constants of Diatomic Molecules*, Van Nostrand Reinhold, New York, 1979.
- [124] L. C. Biedenharn and J. D. Louck, *Angular Momentum in Quantum Physics*, volume 8 of *Encyclopedia of Mathematics*, Addison-Wesley, Reading, 1981.
- [125] G. Herzberg, *Molecular Spectra and Molecular Structure, Vol. 3: Electronic Spectra and Electronic Structure of Polyatomic Molecules*, Van Nostrand, New York, 1950.

A free society is one where it is safe to be unpopular

Uitnodiging

tot het bijwonen van de
openbare verdediging van
mijn proefschrift

Dynamics of open-shell van der Waals complexes



op woensdag 17 maart 2004
om 13.30 uur in de Aula
van de Katholieke
Universiteit Nijmegen,
Comeniuslaan 2 te Nijmegen

Aansluitend is er een receptie

Wilfried Zeimen
030 2885946
zeimen@theochem.kun.nl